

FLEXIBLE SUPPORT AND ENHANCED GROOVE GEOMETRIES FOR GAS LUBRICATED BEARINGS

Thèse N° 9774

Présentée le 25 octobre 2019

à la Faculté des sciences et techniques de l'ingénieur
Laboratoire de conception mécanique appliquée
Programme doctoral en énergie

pour l'obtention du grade de Docteur ès Sciences

par

Philipp Kaspar BÄTTIG

Acceptée sur proposition du jury

Prof. K. A. J. Mulleners, présidente du jury
Prof. J. A. Schiffmann, directeur de thèse
Prof. N. Hofmann, rapporteur
Prof. I. Santos, rapporteur
Prof. G. Villanueva, rapporteur

2019

De Hans im Schnäggeloch
het alles was är wott.
Und was är het das wott är ned
und was är wott das het är ned,
de Hans im Schnäggeloch. . .

To my uncle Kaspar

Acknowledgements

First of all, I would like to express my sincere gratitude towards my thesis supervisor Prof. Dr. Jürg Schiffmann for giving me the opportunity of doing a PhD at LAMD. Your support was always spot-on, leading me back on track when I was stuck but also letting me work independently as long as things went well.

A big thank you goes to Markus for his friendship and the many funny hours we spent together in the office, singing songs of old German TV commercials or just simply having tee. You most probably saved me months with the support you provided me in Latex, Matlab and all other IT related stuff. Thank you also for giving me tasks that enabled me to leave the office and get my hands dirty.

Thank you Suresh for the great time, your friendship and the delicious food prepared by you and your wife. Your Momos helped me many times to survive an exhausting day in the lab.

A big thank you goes to Dr. Karim Shalash and Eliott Guenat for the technical discussions and for introducing me to the life as a PhD at LAMD.

Julie, thank you for keeping the LAMD in good working order during my time here, all the administrative tasks you helped me with and the recreational events you put in place. To all the other team members I met during my time at LAMD: Kossi, Cyril, Chris, Lili, Kévin, Violette, Wanhui, Thierry, Christophe Darioli, Christophe Pham, Antonio, Tomohiro, Patrick, Nathaniel, Luis and Sajjad. Thank you for the many discussions and making my stay at LAMD an enjoyable adventure. I would also like to thank Cécile Taverney, who always helped me with my last-minute requests and questions regarding the organization of the PhD.

Thanks to Micromécanique SA in Neuchâtel for the manufacturing of the rotors. The discovery of your company was a revelation with regards to high-precision manufacturing. Thanks as well to Joël Currit, who manufactured lots of mechanical parts for this work and let me use his workshop in Microcity, when time was short.

Thank you to my friend Manuel Blaser, who let me know that LAMD has an open PhD position. Without your hint, all this would not have happened.

Furthermore, I would like to thank my jury members Prof. Dr. Norbert Hofmann, Prof. Dr. Ilmar Santos, Prof. Dr. Guillermo Villanueva and Prof. Dr. Karen Mulleners.

Thank you to my family and friends. You all were a great help and supported me all along the way.

A big thank you goes to my uncle Kaspar for his support and for always believing in me.

Acknowledgements

Thank you for the great time we spent during my stay in Romandie and for keeping me occupied with mechanical systems outside of the office hours.

Last but not least, the largest Thank You goes to you, Lorette. Thank you for your support, making me smile after a hard day at work, the countless walks with Boutchette that let me forget the stressful life as a PhD student and the encouraging words you always told me: "Ça va aller!"

Neuchâtel, October 2019

Philipp Bättig

Abstract

Gas lubricated Herringbone-Grooved Journal Bearings (HGJB) are a promising solution to support high-speed rotors in oil-free turbo-machinery due to their compactness, relatively low losses, no need for lubrication and low wear. Gas lubricated bearings, however, generally require very small clearance to diameter ratios to allow stable rotor operation. The consequences are high manufacturing cost, stringent misalignment tolerances and increased specific windage losses. Increasing the bearing clearance while maintaining the performance of the rotor-bearing-system allows to significantly reduce these shortcomings and would help to make the application of HGJBs in products less challenging. Two approaches have been investigated that allow an increase in bearing clearance while maintaining the rotordynamic stability of the system: (1) a flexible support structure for HGJB bushings and (2) enhanced groove geometries. Both approaches suggest a 50% increase in bearing clearance.

A dedicated test-rig was designed to allow the experimental characterization of stiffness and damping of various O-Ring geometries and installation specifications. In a first stage, a Design of Experiments approach enabled the identification of the governing variables on the stiffness and damping of O-Rings. The measurement results of 60 representative O-Ring geometries then allowed the development of data-driven, reduced-order models for the stiffness and damping of O-Rings as a function of the excitation frequency, rubber hardness, O-Ring geometry and squeeze.

A generic flexible bearing bushing support for HGJBs has been developed to address the shortcomings of the commonly used O-Rings to flexibly support the bearing bushings. The novel flexible support is based on membrane shaped disks featuring specific cut-outs, resulting in an independently tunable support stiffness. An alignment procedure has been presented that is able to perform the very challenging task of aligning two bearing bushings separated by a considerable distance. The novel flexible support has been successfully implemented in a base-line prototype and aligned with the presented alignment concept, which showed significantly improved repeatability, lower lift-off speeds and less wear compared to O-Ring supported bearing bushings.

An experimental campaign was conducted to verify the theoretically predicted potential of enhanced groove geometries to increase the bearing clearance of HGJBs. Good agreement between experimentally determined speed of instability onset and

Acknowledgements

prediction was found for the investigated enhanced groove patterns. By using rotors with enhanced groove geometries, it was possible to increase the speed of instability onset by more than a factor three compared to a classically grooved shaft with the same bearing clearance, which confirmed the potential of enhanced groove geometries to stabilize HGJBs.

Keywords: Herringbone-Grooved Journal Bearings, enhanced groove geometries, stability threshold, flexible support, O-Ring model

Zusammenfassung

Genutete, gas-geschmierte Lager sind aufgrund ihrer Kompaktheit, relativ geringen Verlusten, ihrer Fähigkeit ohne Schmierung auszukommen und ihres geringen Verschleisses eine vielversprechende Lösung, um schnelllaufende Rotoren in ölfreien Turbomaschinen zu lagern. Gaslager erfordern jedoch grundsätzlich sehr geringe Lagerpalte, um stabil zu laufen. Die Konsequenzen sind hohe Fertigungskosten, strenge Ausrichttoleranzen und erhöhte spezifische Lagerverluste. Eine Erhöhung des Lagerpaltes unter Beibehaltung der Stabilität des Rotor-Lager-Systems erlaubt eine deutliche Verringerung dieser Nachteile und würde die Anwendung von genuteten Gaslagern in Produkten vereinfachen. Zwei Ansätze zur Erhöhung des Lagerpaltes unter Beibehaltung der rotodynamischen Stabilität des Lagersystems sind untersucht worden: (1) eine flexible Aufhängung der Lagerschalen von genuteten Gaslagern und (2) die Verwendung von verbesserten Nuten-Geometrien. Beide Ansätze zeigen eine mögliche Erhöhung des Lagerpaltes um 50%.

Ein Prüfstand wurde konzipiert, um die Steifigkeit und Dämpfung von verschiedenen O-Ring Geometrien unter unterschiedlichen Einbaubedingungen experimentell zu charakterisieren. In einer ersten Etappe wurde einem experimentellen Plan gefolgt, welcher es erlaubte die wichtigen Einflussgrößen auf die Steifigkeit und die Dämpfung der O-Ringe zu identifizieren. Die Messresultate von 60 repräsentativen O-Ring Geometrien erlaubten anschliessend die Entwicklung von Modellen reduzierter Ordnung für die Steifigkeit und Dämpfung von O-Ringen als Funktion der Anregungsfrequenz, des Polymer Härtegrades, der O-Ring Geometrie und der Einbauvorspannung.

Eine flexible Aufhängung für die Lagerschalen von Gaslagern wurde entwickelt, um die Nachteile, resultierend von den oftmals verwendeten O-Ringen zur flexiblen Aufhängung, zu beseitigen. Die neue flexible Aufhängung basiert auf dünnen, membranförmigen Scheiben, welche über spezifische Ausschnitte verfügen, die die unabhängige Abstimmung von Radial- und Kippsteifigkeit erlaubt. Eine Ausrichtprozedur wurde präsentiert, welche es erlaubt die sehr anspruchsvolle Ausrichtung von Lagerschalen beträchtlicher Distanz auszuführen. Die neuartige flexible Lagerschalenaufhängung wurde erfolgreich in einem Referenz-Prototypen implementiert und mit dem vorgestellten Ausrichtkonzept ausgerichtet. Experimentelle Untersuchungen zeigten eine deutlich verbesserte Wiederholbarkeit, eine verringerte Abhebedrehzahl des Rotors und eine Reduktion des Verschleisses im Vergleich mit Lagerschalen, welche mittels

Acknowledgements

O-Ringen aufgehängt sind.

Eine experimentelle Kampagne wurde durchgeführt, um das theoretisch vorhergesagte Potenzial von verbesserten Nuten-Geometrien zur Erhöhung des Lagerspaltens von Gaslagern zu verifizieren. Für die untersuchten Nuten-Geometrien konnte eine gute Übereinstimmung zwischen prognostizierter und gemessener Instabilitätsdrehzahl festgestellt werden. Die Verwendung von Rotoren mit verbesserten Nuten-Geometrien erlaubte die Erhöhung der Instabilitätsdrehzahl um mehr als einen Faktor drei verglichen mit klassisch genuteten Rotoren die denselben Lagerspalt aufweisen. Dies bestätigte das theoretisch vorhergesagte Potenzial von Rotoren mit verbesserten Nuten-Geometrien zur Stabilisierung von genuteten Gaslagern.

Schlüsselworte: Genutete Gaslager, verbesserte Nuten-Geometrien, Stabilitätsgrenze, flexible Aufhängung, O-Ring Modell

Résumé

Les paliers à gaz rainurés en chevrons représente une solution adaptée au support d'arbres de turbomachines à haute vitesse grâce à leur compacité, des pertes relativement faibles, leur absence de lubrification active et leur faible usure. Néanmoins, ces paliers ont besoin d'un jeu extrêmement faible pour garantir une opération stable. Les conséquences sont un coût de fabrication élevé, des tolérances d'alignement strictes et des pertes élevées. Une augmentation du jeu sans perte de stabilité réduirait ces aspects négatifs et faciliterait l'implémentation pratique de paliers aérodynamiques rainurés. Deux approches permettant d'augmenter le jeu sans diminuer la stabilité du système ont été investiguées : (1) un support flexible pour les douilles de palier et (2) l'utilisation de rainures améliorées. Les deux approches suggèrent qu'une augmentation de 50% du jeu des paliers est possible.

Un banc d'essai dédié a été réalisé pour mesurer la rigidité et le facteur d'amortissement de joints toriques de tailles et de configurations diverses. Dans une première étape, un plan d'expérience a été suivie pour identifier les variables les plus influentes sur la rigidité et l'amortissement des joints. Les résultats expérimentaux de 60 échantillons de tailles caractéristiques ont permis le développement de modèles pour la rigidité et l'amortissement des joints toriques en fonction de la fréquence d'excitation, de la dureté, de la géométrie et du niveau de précontrainte des joints.

Un support flexible pour paliers à gaz a été développé pour répondre aux problèmes identifiés sur les supports des douilles par des joints toriques. Le nouveau support flexible est composé de disques fins spécifiquement découpés et permettant de choisir indépendamment la rigidité radiale et la rigidité de torsion du support. Une méthode d'alignement a été présentée, permettant d'aligner des douilles très espacées. Le nouveau support flexible a été implémenté et aligné avec la nouvelle méthode sur un prototype de référence, ce qui a permis de mettre en évidence une amélioration de la répétabilité, une réduction de la vitesse de décollage du rotor et une usure moindre par rapport aux douilles supportées sur des joints toriques.

Une campagne expérimentale a été menée pour vérifier le potentiel théorique des rainures améliorées afin d'augmenter le jeu des paliers à gaz rainurés en chevron. La vitesse de manifestation de l'instabilité observée expérimentalement est en bon accord avec la prédiction pour toutes les géométries investiguées. En utilisant des arbres avec

Acknowledgements

des rainures améliorées, la vitesse limite de stabilité a pu être augmentée d'un facteur supérieur à trois par rapport à un arbre équipé de rainures classiques. Cela a permis de confirmer le potentiel de stabilité des rainures améliorées pour les paliers rainurés en chevron.

Mots clé : Paliers à gaz en chevron, geometries améliorées, limite de stabilité, support flexible, modèle pour joints toriques

Contents

Acknowledgements	v
Abstract (English/Français/Deutsch)	vii
Contents	xvi
List of figures	xxiii
List of tables	xxvi
List of Symbols	xxxii
Introduction	1
1 Introduction	1
1.1 Prelude	1
1.2 High-speed rotors supported on Herringbone-Grooved Journal Bearings	2
1.3 Problem statement	4
1.4 Goal and objectives	8
1.5 Methodology	9
1.6 Thesis outline	10
1.7 Specific aspects of novelty	12
2 Potential of flexible bearing bushing support and enhanced groove geometries	13
2.1 Introduction	13
2.2 Motivation and nature of the issue	15
2.3 Goals and objectives	15
2.4 Methodology	16
2.4.1 Rotordynamic model	16
2.4.2 Boundary conditions	18
2.4.3 Monte-Carlo simulations	19
2.4.4 Design variables and optimization objectives	20
2.5 Results and discussion	21
	xiii

Contents

2.5.1	Monte-Carlo simulation results - Classical grooves on flexible support	21
2.5.2	Optimization results - Classical grooves on rigid and flexible support	23
2.5.3	Optimization results - Enhanced grooves on rigid support . . .	26
2.5.4	Optimization results - Enhanced grooves on flexible support . .	29
2.6	Summary and chapter conclusions	31
3	Data-driven model for stiffness and damping of O-Rings	35
3.1	Introduction	35
3.2	Motivation and nature of the issue	38
3.3	Goals and objectives	40
3.4	Methodology	40
3.4.1	Experimental setup	40
3.4.2	Experimental procedure	43
3.5	Results and discussion	44
3.5.1	Measurement campaign 1 - Silicone O-Rings	44
3.5.2	Measurement campaign 2 - Pre-assessment of effects with a Design of Experiments (DOE) approach	46
3.5.3	Measurement campaign 2 - Results of extended measurement campaign	48
3.5.4	Development of reduced-order models	50
3.6	Reduced-order model performance and limitations	57
3.7	Summary and chapter conclusions	61
4	Flexible support for Herringbone-Grooved Journal Bearings	63
4.1	Introduction	64
4.2	Motivation and nature of the issue	65
4.3	Goals and objectives	67
4.4	Methodology	68
4.4.1	Experimental methodology to determine stiffness and damping of flexible support	68
4.4.2	Experimental methodology for performance evaluation of flexible support in prototype	69
4.5	An alternative flexible bearing bushing support	73
4.5.1	Design requirements	73
4.5.2	Development of parametric membrane model	73
4.5.3	Verification of parametric membrane model	78
4.6	Results and discussion	80
4.6.1	Monte-Carlo simulations	80
4.6.2	Manufacturing of flexible membranes	83
4.6.3	Experimental validation of the parametric membrane model . .	84
4.6.4	Damping concepts	88

4.6.5	Fatigue failure investigation	90
4.6.6	Bearing bushing alignment	91
4.6.7	Assessment of bearing bushing alignment quality	104
4.6.8	Analysis of the bearing bushing motion	105
4.6.9	Influence of the bearing bushing inertia on the vibration response and the bush tilting stability	110
4.6.10	Influence of the membrane tilting stiffness on the vibration response and the bush tilting stability	116
4.6.11	Influence of the support damping on the bush tilting stability	119
4.6.12	Assessment of long-term flexible support performance	121
4.7	Summary and chapter conclusions	125
5	Enhanced groove geometries for Herringbone-Grooved Journal Bearings	129
5.1	Introduction	129
5.2	Motivation and nature of the issue	130
5.3	Goals and objectives	131
5.4	Methodology	132
5.4.1	Methodology for theoretical investigation	132
5.4.2	Experimental methodology	133
5.5	Results and discussion	135
5.5.1	Results of multi-objective optimizations	135
5.5.2	Identification of common bearing clearance for experimental campaign	141
5.5.3	Manufacturing of bearing bushing and rotors	144
5.5.4	Experimental results	146
5.5.5	Comparison of predicted and experimental results	151
5.6	Summary and chapter conclusions	155
6	Conclusions	157
6.1	Potential of flexible bearing bushing support and enhanced groove geometries	157
6.2	O-Ring model	158
6.3	Flexible support for HGJBs	159
6.4	Experimental exploration of enhanced groove geometries	160
6.5	Future work	160
A	Detailed O-Ring stiffness and damping measurement results	163
B	Timoshenko stiffness matrix for beam element	171
C	Wiring diagram of heating cartridge system	173
D	Error estimation of SIO for enhanced groove geometries	175

Contents

Bibliography	187
Curriculum Vitae	189

List of Figures

1.1	a) Working principle of a fluid film bearing; b) Herringbone-Grooved rotor and bearing bushing	2
1.2	a) Rotor supported on bearing sleeve containing both bearing planes in one part; b) Rotor supported by two separate bearing bushings	5
1.3	Coast-down frictional torque measurement results of O-Ring supported HGJB bushings	8
1.4	Conceptual sketch of LAMD prototype with O-Ring supported HGJB bushings	10
2.1	Rotordynamic model used for multi-objective optimizations	16
2.2	Nomenclature of HGJB including the four interpolation points along the rotor axis to define the enhanced groove geometry	17
2.3	Monte-Carlo simulation results present the effect of support stiffness k_S and damping coefficient c_S on the relative stability change of classical HGJB on a flexible support. Red dots represent lower rotordynamic stability compared to a rigid bushing support.	22
2.4	Influence of the reduced frequency $\bar{\Omega}$ and the relative damping \bar{N} on the stability of a classical HGJB on a flexible support. Red dots represent lower rotordynamic stability compared to a rigid bushing support.	23
2.5	a) Logarithmic decrement Γ against radial clearance C for classical grooves on flexible support; b) Load capacity against radial clearance C	24
2.6	a) Optimum support stiffness k_S against radial clearance C for classical grooves on flexible support; b) Optimum damping coefficient c_S against radial clearance C	25
2.7	a) Groove width ratio α against radial clearance C for classical grooves on flexible support; b) Groove angle β against radial clearance C	25
2.8	a) Groove depth ratio H against radial clearance C for classical grooves on flexible support; b) Bearing length ratio γ against radial clearance C	26
2.9	a) Logarithmic decrement Γ for classical grooves (yellow), fully enhanced grooves (red) and enhanced grooves with constant groove depth H (cyan); b) Load capacity F_L versus radial clearance C	27

List of Figures

2.10	a) Groove width ratio α versus radial clearance C for enhanced grooves with minimal load capacity constraint (dots) and enhanced grooves with constant groove depth ratio H (triangles); b) Groove angle β versus radial clearance C	28
2.11	a) Groove depth ratio H versus radial clearance C for enhanced grooves with minimal load capacity constraint (dots) and enhanced grooves with constant groove depth ratio H (triangles); b) Bearing length ratio γ versus radial clearance C	28
2.12	a) Logarithmic decrement Γ versus radial clearance C for classical grooves on rigid support (yellow), enhanced grooves with load capacity constraint on rigid support (red) and enhanced grooves without and with constant groove depth on flexible support (green cyan); b) Load capacity F_L versus radial clearance C	29
2.13	a) Evolution of groove width ratio α versus radial clearance C for enhanced grooves with load capacity constraint on flexible support (dots) and enhanced grooves with constant groove depth on flexible support (triangles); b) Groove angle β versus radial clearance C	30
2.14	a) Evolution of groove depth ratio H versus radial clearance C for enhanced grooves with load capacity constraint on flexible support (dots) and enhanced grooves with constant groove depth on flexible support (triangles); b) Bearing length ratio γ versus radial clearance C	31
3.1	Measurement of O-Ring supported bearing bushing amplitudes	36
3.2	O-Ring nomenclature	37
3.3	Example of dimensionless stiffness \underline{k} as a function of d and D to illustrate the importance of varying d and D simultaneously for capturing the real dependency of d/D	39
3.4	a) Cut view of ORI1 test section; b) ORI2 test section	41
3.5	ORI2 test section with displacement probes on shaker table	42
3.6	Results of stiffness and damping measurements of a single silicone O-Ring using the measurement setup presented in Fig. 3.4 a)	45
3.7	Pareto chart of relative effects on stiffness and damping for the tested NBR O-Rings	47
3.8	Evolution of the measured stiffness k_1 as a function of excitation frequency for selected Shore 70 and 90 NBR O-Rings	48
3.9	Evolution of the measured damping coefficient c as a function of excitation frequency for selected Shore 70 and 90 NBR O-Rings	49
3.10	Identified storage modulus E' as a function of frequency and Shore hardness	52
3.11	Dimensionless stiffness \underline{k} as a function of d/D and squeeze δ for Shore 70	53
3.12	Dimensionless stiffness \underline{k} as a function of d/D and squeeze δ for Shore 90	54

3.13	Averaged loss factor η for Shore 70 and Shore 90 NBR O-Rings including standard deviations and 2nd order polynomial fit for Shore 70 and Shore 90 NBR O-Rings	56
3.14	Comparison of model prediction and measurement: a) Stiffness k_1 ; b) Damping coefficient c	57
3.15	Residual error of fitted surface of dimensionless stiffness vs d/D and squeeze δ	58
3.16	Plot of static storage modulus E'_0 as a function of Shore hardness according Eqn. (3.18) and Shore hardness tolerance band as given by O-Ring manufacturer	59
3.17	Measured O-Ring stiffness compared to predicted stiffness for Shore 90, $D = 20$ mm, $d = 2$ mm, $\delta = 10\%$. Dashed lines represent measurement uncertainty while dash-dotted lines include measurement and Shore hardness uncertainty.	60
4.1	Wear on HGJB due to misalignment, visible by the accumulation of white dust in the bearing grooves of a silicone-nitride rotor shaft	66
4.2	3/4 cut view of membrane test section	68
4.3	Experimental setup for the determination of the membrane tilting stiffness k_t . a) Initial state b) Additional weight added at end of rod	69
4.4	Location of LionPrecision and Philtec displacement probes on bearing bushing	70
4.5	Transformation of measurement data to a cylindrical and a tilting movement in the center of the bearing bushing	71
4.6	Prototype with implemented flexible membrane bushing support and instrumentation	72
4.7	Available parameters of membrane model for calculating radial and tilting stiffness	74
4.8	Comparison of displacement due to a radial force F_r of 1 N in x-direction from parametric membrane model (left) with 1D ABAQUS (middle) and 3D ABAQUS results (right) (displacements scaled x500).	79
4.9	Results of 500000 Monte-Carlo simulations for PEEK, aluminum and steel membranes according the design variables in Tab. 4.4	81
4.10	Three selected results in design space for low, intermediate and high stiffness	81
4.11	Maximum von-Mises stresses obtained with the membrane tool for a radial force of 1 N for aluminum membranes with a thickness t of 1 mm, inner radius R_i of 9 mm and outer radius R_o of 17.5 mm	82
4.12	Overview of investigated membrane designs	83
4.13	Measurement of radial stiffness k_r for aluminum membrane Var20 and Var45 and steel membrane Var28 using the base excitation-resonant mass method	85

List of Figures

4.14	Measurement of tilting stiffness k_t for aluminum membrane Var19 and steel membranes Var8 and Var23	86
4.15	Overlay of designed geometry in CAD and real geometry of membrane Var23 achieved by laser cutting	87
4.16	Investigated damping concepts: a) Silicone coating (Sil); b) Friction disk (FD); c) Membrane stack (MS)	88
4.17	Comparison of damping coefficient c for aluminum membrane Var45 and Var20 and steel membrane Var28 in combination with the investigated damping concepts silicone coating (Sil), friction disk (FD) and membrane stack (MS)	89
4.18	Maximum von-Mises stress of $\sigma_{nom}=17.85$ MPa as a result of a radial displacement of $5 \mu\text{m}$ on membrane Var6. Displacements are scaled x200	90
4.19	Stress-cycle curve for aluminum AL6082T-6, according to the measured fatigue data by Karolczuk et al.	91
4.20	Alignment concept consisting of electric stator (orange), alignment shaft (gray), thrust bearing disk (blue) and front centering flange (green)	92
4.21	Outer diameter D_o and maximum tangential stress $\sigma_{\theta\theta}$ of a steel shaft with internal diameter $D_i = 7\text{mm}$ as a function of internal pressure p_0	94
4.22	Results of FEM simulation using a cone to radially expand a slotted shaft. Left figure shows the half-model of the slotted shaft and the cone to be inserted. Right figure presents the radial expansion after inserting the cone.	95
4.23	a) Diameter of alignment shaft and bushing as a function of temperature; b) Heat loss of alignment shaft and bearing bushing as a function of uniform temperature	97
4.24	a) FEM results for steady-state temperature distribution of alignment shaft and bushings; b) Simulated distance of defined contact surfaces	98
4.25	a) Selected heating cartridges of ID = 6.5 mm and $P=100$ W; b) Alignment shaft with PT100 temperature probes applied at bearing bushing locations	100
4.26	a) Set temperature at heating cartridge T_{set} versus measured temperature on alignment shaft surface T_{S0} ; b) Measured temperature on alignment shaft surface T_{S0} plotted against measured diameter of alignment shaft	101
4.27	Cut-view of alignment setup featuring electric stator (white), alignment shaft (brown), heating cartridges (gray), front centering cover (orange) and thrust bearing disk (yellow)	102
4.28	a) Alignment station to glue and align bushings to flexible support; b) Aligned and glued bearing bushing supported on flexible membrane and fitted to electric stator	103
4.29	Coast-down measurement results of HGJB bushings supported on flexible membrane	105

4.30	Recorded synchronous and sub-synchronous motion amplitudes of front bearing bushing supported on membrane Var19	106
4.31	Frequency spectrum of cylindrical bushing motion q_{ex} and q_{ey}	107
4.32	Frequency spectrum of bushing tilting angles ϕ and θ	108
4.33	Evolution of measured front bearing bushing motion during a speed ramp from 20 krpm to 116 krpm. The selected speeds for the visualization are marked in Fig. 4.30	109
4.34	Orbits of front, center and back bushing plane at the onset of instability located at a rotational speed of 116 krpm.	110
4.35	Setup for measurements with optical probes: a) Standard setup containing one ring; b) Additional target ring fitted	111
4.36	Reflective target options for measurements with optical probes: a) Low inertia metal foil target; b) Polished metal ring target	112
4.37	Comparison of back bearing bushing motion amplitudes for metal foil and metal ring target	113
4.38	FFT spectrum of back bushing tilt angle θ : a) with metal foil; b) with additional metal ring ($J_{Ttot} + 37\%$)	114
4.39	Influence of the bushing transverse moment of inertia. a) Predicted critical speed of bearing bushing tilting mode; b) Logarithmic decrement Γ_{Bush}	115
4.40	Comparison of back bearing bushing motion amplitudes for membranes Var19, Var8, Var23 and Var6 offering different tilting stiffnesses k_t	117
4.41	Influence of membrane tilting stiffness for membranes Var19, Var8, Var23 and Var6. a) Predicted critical speed of bearing bushing tilting mode; b) Logarithmic decrement Γ_{Bush}	118
4.42	Measured frequency spectrum of bushings supported on flexible membranes Var6 ($k_t = 82.1$ Nm/rad): a) Front bearing bushing; b) Back bearing bushing	119
4.43	Frequency spectrum of back bearing bushing tilt angle θ : a) Membrane Var19, no damping; b) Membrane Var19, friction disk damping concept installed	120
4.44	Measured frictional torque during coast-down: a) O-Ring supported bearing bushings; b) Flexible membrane supported bearing bushings	121
4.45	Photograph of rotor shaft after 15000 performed start-stop cycles: a) O-Ring supported bearing bushings; b) Flexible membrane supported bearing bushings	122
4.46	Measured frictional torque during coast-down after 1, 5000, 15000, 25000, 50000, 75000 and 100000 start-stop cycles for membrane supported bearing bushings	123
4.47	Synchronous bearing bushing motion amplitudes after 1, 1000, 5000 and 15000 start-stop cycles: a) Front bearing bushing; b) Back bearing bushing	124

List of Figures

5.1	Experimental setup for the enhanced groove exploration: a) Fan-side of rotor shaft; b) Turbine-side of rotor shaft	134
5.2	Optimization results for groove width ratio α : a) Rotor <i>classic</i> and <i>beta_var</i> with constant groove width; b) Rotor <i>alpha_var</i> with varying groove width	136
5.3	Optimization results for groove width ratio α : a) Rotor <i>alpha_beta_var</i> ; b) Rotor <i>alpha_beta_hg_var</i>	136
5.4	Optimization results for groove angle β : a) Rotor <i>classic</i> and <i>alpha_var</i> with constant groove angle; b) Rotor <i>beta_var</i> with varying groove angle	137
5.5	Optimization results for groove angle β : a) Rotor <i>alpha_beta_var</i> ; b) Rotor <i>alpha_beta_hg_var</i>	138
5.6	Optimization results for groove depth ratio H : a) Rotor <i>classic</i> , <i>alpha_var</i> , <i>beta_var</i> and <i>alpha_beta_var</i> with constant groove depth; b) Rotor <i>alpha_beta_hg_var</i> with varying groove depth	139
5.7	Optimization results for bearing length ratio γ	139
5.8	Evolution of logarithmic decrement Γ for rotor <i>classic</i> and the four rotors featuring enhanced groove geometries of increasing degree of complexity	140
5.9	Predicted speed of instability onset for the classically grooved rotor and the four rotors featuring enhanced groove geometries	142
5.10	Predicted speed of instability onset for rotor <i>classic</i> and the four rotors featuring enhanced groove geometries	143
5.11	Comparison of groove designs in CAD. From left to right: <i>classic</i> , <i>alpha_var</i> , <i>beta_var</i> , <i>alpha_beta_var</i> , <i>alpha_beta_hg_var</i>	145
5.12	Comparison of groove designs after laser etching onto rotors. From left to right: <i>classic</i> , <i>alpha_var</i> , <i>beta_var</i> , <i>alpha_beta_var</i> , <i>alpha_beta_hg_var</i>	145
5.13	Manufactured bearing bushing (top) and rotor (bottom) for enhanced groove geometry exploration. From left to right: Turbine nut, turbine, axial shim, tie bolt, rotor <i>alpha_beta_var</i> with fan	146
5.14	Measurement of axial rotor clearance using a Tesa IP65 digital dial test indicator	147
5.15	Experimentally captured synchronous and sub-synchronous motion amplitudes of rotor <i>classic</i>	148
5.16	Experimentally captured synchronous and sub-synchronous motion amplitudes of rotor <i>alpha_var</i>	149
5.17	Experimentally captured synchronous and sub-synchronous motion amplitudes of rotor <i>beta_var</i>	149
5.18	Experimentally captured synchronous and sub-synchronous motion amplitudes of rotor <i>alpha_beta_var</i>	150
5.19	Experimentally captured synchronous and sub-synchronous motion amplitudes of rotor <i>alpha_beta_hg_var</i>	151
5.20	Evaluated combinations of clearance uncertainty ΔC and groove depth uncertainty Δhg in uncertainty analysis	152

5.21	Whirl speed map and evolution of logarithmic decrement Γ for rotor <i>classic</i> considering the uncertainty in bearing clearance and groove depth	152
5.22	Evolution of logarithmic decrement Γ for conical forward mode of rotor <i>classic</i>	153
5.23	Comparison of predicted and measured speed of instability onset. Red stars represent experimentally observed instability, red dots represent maximum achieved speed with no observed instability	154
A.1	Measurement results for stiffness k_1 of a Shore 70 NBR O-Ring with $d=1\text{mm}$	163
A.2	Measurement results for stiffness k_1 of a Shore 70 NBR O-Ring with $d=2\text{mm}$	164
A.3	Measurement results for stiffness k_1 of a Shore 70 NBR O-Ring with $d=3\text{mm}$	164
A.4	Measurement results for stiffness k_1 of a Shore 90 NBR O-Ring with $d=1\text{mm}$	165
A.5	Measurement results for stiffness k_1 of a Shore 90 NBR O-Ring with $d=2\text{mm}$	165
A.6	Measurement results for stiffness k_1 of a Shore 90 NBR O-Ring with $d=3\text{mm}$	166
A.7	Measurement results for damping coefficient c of a Shore 70 NBR O-Ring with $d=1\text{mm}$	166
A.8	Measurement results for damping coefficient c of a Shore 70 NBR O-Ring with $d=2\text{mm}$	167
A.9	Measurement results for damping coefficient c of a Shore 70 NBR O-Ring with $d=3\text{mm}$	167
A.10	Measurement results for damping coefficient c of a Shore 90 NBR O-Ring with $d=1\text{mm}$	168
A.11	Measurement results for damping coefficient c of a Shore 90 NBR O-Ring with $d=2\text{mm}$	168
A.12	Measurement results for damping coefficient c of a Shore 90 NBR O-Ring with $d=3\text{mm}$	169
C.1	Wiring diagram of heating cartridge system	173
D.1	Whirl speed maps and evolution of logarithmic decrement for shaft featuring enhanced grooves α_{var} on rigid support	175
D.2	Whirl speed maps and evolution of logarithmic decrement for shaft featuring enhanced grooves β_{var} on rigid support	176
D.3	Whirl speed maps and evolution of logarithmic decrement for shaft featuring enhanced grooves $\alpha_{\beta_{\text{var}}}$ on rigid support	176
D.4	Whirl speed maps and evolution of logarithmic decrement for shaft featuring fully enhanced grooves $\alpha_{\beta_{\text{hg_var}}}$ on rigid support	177

List of Tables

1.1	Specifications of LAMD prototype for PEM fuel cell pressurization . . .	9
2.1	Rotor design properties of LAMD prototype used to investigate the effect of flexible support characteristics	18
2.2	Fluid properties used to investigate the effect of flexible support characteristics	19
2.3	Baseline properties of flexible support for Monte-Carlo simulations . .	19
2.4	Range of investigated support characteristics for Monte-Carlo simulations	20
2.5	Range of design variables for the multi-objective optimization	20
3.1	Investigated O-Ring materials, dimensions and installation specifications in measurement campaign 1&2	42
3.2	List of instrumentation for O-Ring test rig	43
3.3	Measurement points for full factorial design	46
3.4	Coefficients and R^2 for dimensionless stiffness model of Shore 70 and Shore 90 NBR O-Rings	53
3.5	Coefficients and R^2 for 2nd order polynomial fit of loss factor η for Shore 70 and Shore 90 NBR O-Rings	56
4.1	List of instrumentation for membrane characterization and performance assessment of the new flexible support	72
4.2	Rotor design parameters	73
4.3	Radial stiffness k_r and tilting stiffness k_t obtained with the parametric membrane model compared to results from 1D ABAQUS and 3D ABAQUS models	79
4.4	Range of design variables for the performed Monte-Carlo simulations .	80
4.5	Geometrical properties of investigated flexible membrane designs . . .	84
4.6	Overview of advantages and disadvantages of bearing bushing alignment concepts	96
4.7	Masses and transverse moments of inertia of bearing bushing, target ring and membrane center ring	112

List of Tables

4.8	Radial and tilting stiffnesses of membranes tested in prototype. An asterisk * represents measured values with the designed value provided in brackets	116
5.1	Rotor design properties for theoretical and experimental enhanced groove geometry exploration	132
5.2	Range of design variables for the performed multi-objective optimizations	133
5.3	List of instrumentation for enhanced groove geometry exploration . .	135
5.4	Predicted speed of instability onset (SIO) for all five investigated rotors with a radial clearance $C = 8.2 \mu\text{m}$	143
5.5	Measurement results of rotor diameter	144

Nomenclature

Acronyms

BERM	Base-Excitation-Resonant-Mass
CAD	Computer Aided Design
CoG	Center of Gravity
DOE	Design-of-Experiment
DOF	Degree of Freedom
EDM	Electric Discharge Machining
FD	Friction Disk
FE	Finite element
FEM	Finite-Element Method
FFT	Fast-Fourier-Transformation
HGJB	Herringbone-Grooved Journal Bearing
ID	Inner Diameter
LAMD	Laboratory for Applied Mechanical Design
MS	Membrane Stack
NBR	Nitrile-Butadiene-Rubber
OD	Outer Diameter
ORC	Organic-Rankine-Cycle
PEM	Proton-exchange Membrane
SIL	Silicone Coating
SiN	Silicone Nitride

List of Tables

SIO Speed of Instability Onset

WHR Waste-Heat-Recovery

Greek Symbols

α	Amplitude ratio $\frac{A_2}{A_1}$, [-]
α	Convective heat transfer coefficient, $[\frac{W}{m^2K}]$
α	Groove width ratio, [-]
α	Thermal expansion coefficient, $[\frac{1}{K}]$
$\bar{\Omega}$	Reduced frequency, [-]
β	Groove angle, [<i>deg</i>]
δ	Squeeze, [-]
$\Delta\varphi$	Phase angle difference, [<i>rad</i>]
η	Damping factor, [-]
η	Loss factor, [-]
Γ	Logarithmic decrement, [-]
γ	Bearing length ratio, [-]
λ	Real part of eigenvalue s, $[\frac{1}{s}]$
λ	Thermal conductivity, $[\frac{W}{mK}]$
μ	Poisson ratio, [-]
μ	Viscosity, [<i>Pa.s</i>]
Ω	Whirl ratio, [-]
ω	Angular frequency, $[\frac{rad}{s}]$
ϕ	Angular displacement, [<i>rad</i>]
ρ	Density, $[\frac{kg}{m^3}]$
σ	Stress, [<i>Pa</i>]
θ	Angular displacement, [<i>rad</i>]
ε	Emissivity, [-]
ε	Stretch, [-]

Roman Symbols

\bar{N}	Relative damping coefficient, [-]
\dot{q}	Heat flux, $[\frac{W}{m^2}]$
\underline{k}	Dimensionless O-Ring stiffness, [-]
A	Amplitude, [m]
A	Area, [m ²]
A	Main effect matrix, [-]
A	Matrix assembly operator, [-]
a	Main effects, [-]
AW	Inverse section modulus, $[\frac{1}{m^2}, \frac{1}{m^3}]$
B	Damping matrix, $[\frac{Ns}{m}]$
C	Radial bearing clearance, [m]
c	Damping coefficient, $[\frac{Ns}{m}]$
D	Diameter, [m]
d	Cross-sectional diameter, [m]
E	Modulus, [Pa]
E	Young's modulus, [Pa]
F	Force, [N]
f	Frequency, [Hz]
G	Shear modulus, [Pa]
H	Groove depth ratio, [-]
h	Depth, [m]
J	Moment of inertia, [kgm ²]
K	Stiffness matrix, $[\frac{N}{m}]$
k	Stiffness, $[\frac{N}{m}]$
l	Length, [m]
M	Inertia matrix, [kg, kgm ²]

List of Tables

m	Mass, [kg]
N	Amount, [-]
N	Number of cycles, [-]
N	Rotational speed, [$\frac{1}{min}$]
p	Pressure, [Pa]
q	Displacement, [m]
R	Radius, [m]
s	Rotordynamic system Eigenvalue, [$\frac{1}{s}$]
s	Safety factor, [-]
Sh	Shore hardness, [-]
T	Torque, [Nm]
T	Transformation matrix, [-]
t	Thickness, [m]
t	Time, [s]
w	Width, [m]
X	Model matrix, [-]
Y	Response matrix, [-]

Superscripts

'	in local coordinates
'	storage
''	loss
*	complex

Subscripts

θ	Tangential
0	Base-line
1	Housing
2	Mass

a	Front bearing mid-plane
a	preferential
b	Back bearing mid-plane
b	non-preferential
Brg	Bearing
c	constrained
crit	Critical
el	element
eq	equivalent
ext	External
F	Friction
f	Failure
fe	Flexible element
g	Groove
i	Inner
int	Internal
L	Load
Land	Bearing land region
m	Master
max	Maximum
min	Minimum
nom	Nominal
o	Outer
P	Polar
r	Radial
r	Ridge
Rot	Rotor

List of Tables

S	Support
s	Slave
sub	Submatrix, subvector
T	Transversal
t	Tilting

1 Introduction

1.1 Prelude

Recent environmental concerns caused an increased research activity in the energy conversion and transport sector. The increased use of renewable energy sources [1, 2] yields a growing interest in decentralized energy conversion methods [3, 4], where energy is converted locally near the end-user rather than in large centralized power plants, often powered by fossil fuels. Typical examples of decentralized energy conversion systems are domestic heat-pumps [5, 6] and co-generation systems [7], which are able to offer both, electrical energy and heat.

In the transport sector and stationary power generation, much recent research efforts have been devoted on reducing the CO₂ emissions of internal combustion engines. One method to increase the overall net-efficiency is the integration of waste-heat-recovery (WHR) systems, that convert the thermal energy contained in the hot exhaust gases of internal combustion engines, otherwise lost to the environment, into electrical or mechanical energy. One of the promising approaches for efficient waste-heat-recovery systems is the use of an organic Rankine cycle (ORC), which can be applied to both stationary power generation stations [8, 9], as well as motor vehicles [10, 11].

The implementation of fuel cells into moving vehicles is another growing field of research that aims to reduce CO₂ emissions in the transport sector. Fuel cells can be used to power buses [12], passenger cars [13], fork lifts [14] or even cleaning vehicles. In a fuel cell, the electrochemical energy of hydrogen is converted into electrical energy in the presence of an oxidant [15]. The oxidant can be either supplied by means of compressed oxygen directly from a storage tank mounted in the vehicle, or by supplying air from the environment with a compressor.

Amongst other applications, all above presented technologies have one point in common: Their application in decentralized systems or moving vehicles requires efficient,

compact and lightweight compressors and expanders. Small-scale turbomachinery offers a significant advantage compared to conventional low speed positive displacement compressors or expanders, such as much lower volume and weight, but require high rotational speeds in order to achieve the desired pressure ratios and mass flow rates.

Schiffmann [16] has shown that gas lubricated Herringbone-Grooved Journal Bearings (HGJB) are a viable solution to support high-speed rotors in oil-free compressor units due to their compactness, low losses, no need for lubrication, no need for auxiliary systems, low maintenance, low cost and very little wear.

1.2 High-speed rotors supported on Herringbone-Grooved Journal Bearings

Herringbone-Grooved Journal Bearings belong to the family of fluid film bearings. They are of the self-acting type, meaning they do not rely on external pressurized gas supply to provide a lift effect but on dynamic effects caused by the rotation of the shaft. The relative motion between rotor and bearing bushing drags fluid into the resulting wedge between rotor and bushing, which creates a local pressure rise and results in a net lift force acting on the rotor. If the bearing is designed appropriately, the resulting lift force is high enough to carry the weight of the rotor, imbalance forces, as well as radial loads acting on the rotor.

Figure 1.1 a) illustrates how fluid is dragged into the bearing wedge due to relative motion between rotor and bushing and Fig. 1.1 b) presents a picture of a Herringbone-Grooved rotor and the respective bearing bushing.

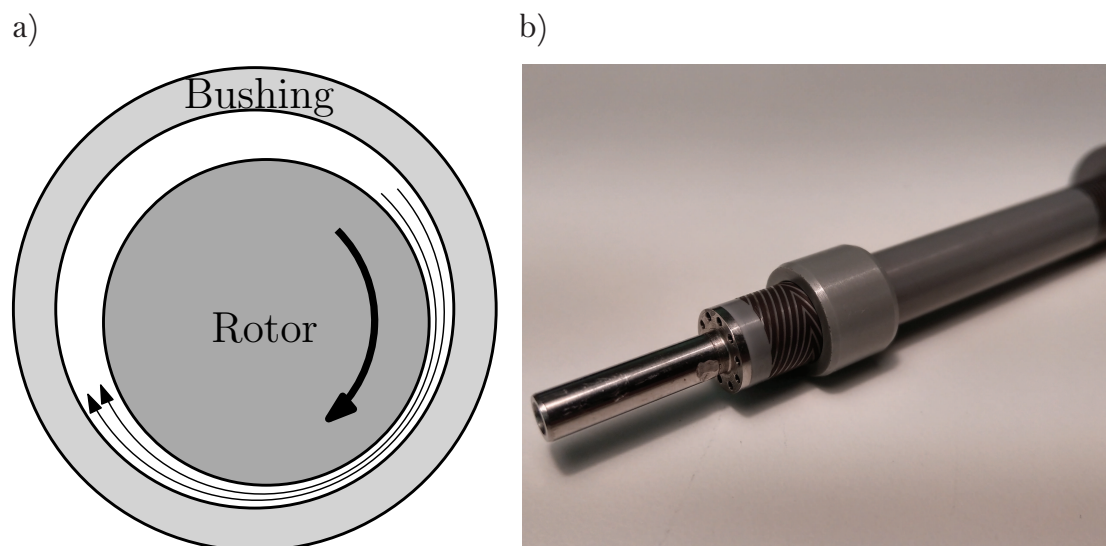


Figure 1.1 – a) Working principle of a fluid film bearing; b) Herringbone-Grooved rotor and bearing bushing

1.2. High-speed rotors supported on Herringbone-Grooved Journal Bearings

Equation (1.1) presents the general form of the stiffness and damping matrices for a fluid film bearing.

$$K = \begin{bmatrix} K_{xx} & K_{xy} \\ K_{yx} & K_{yy} \end{bmatrix}, \quad C = \begin{bmatrix} C_{xx} & C_{xy} \\ C_{yx} & C_{yy} \end{bmatrix} \quad (1.1)$$

A typical characteristic of fluid film bearings is the presence of cross-coupled terms K_{xy} , K_{yx} , C_{xy} and C_{yx} in the stiffness and damping matrices, that are non-zero. The cross-coupling terms cause a coupling between the two main orthogonal directions x and y. A displacement in x-direction, for example, results in a force in x- as well as y-direction.

At stable operation, the imbalance forces of the rotor cause the rotor to whirl around its center axis at a frequency that is identical to the rotational frequency of the rotor and is therefore called the synchronous frequency.

In the absence of high enough damping, the whirling orbit of the rotor in the bearing bushing can start to grow, marking the onset of instability. If the system is not stopped at this point, the growing whirl orbits can become so large as to cause touch-down of the rotor in the bearing bushing, often resulting in a failure of the rotor-bearing system. This unstable whirl phenomena is called half-frequency whirl or fractional-frequency whirl [17], since the frequency of the whirling motion occurs at a fraction of the rotational frequency of the rotor. In general, the appearance of fractional-frequency whirling signals the onset of instability, which can be detected by scanning for sub-synchronous vibrations in the measured frequency spectrum of the rotor motion.

Due to the mentioned cross-coupling terms in the stiffness and damping matrices of HGJBs, as well as their low effective damping as a result of the low viscosity of the gaseous lubricant, rotors supported on Herringbone-Grooved Journal Bearings yield a stability threshold and therefore require careful design of the rotor-bearing-system.

High-speed rotors supported on HGJBs are usually manufactured from materials like high-strength steels, ceramics or tungsten-carbides due to their favorable ratio of elastic modulus to density, as well as high mechanical strength. These mechanical properties are required to obtain high critical rotor bending speeds, which is crucial for HGJB supported rotors due to the low bearing clearances required for HGJB supported rotors to run stable.

The first critical bending speed of the rotor is usually designed to be at least 25% higher than the nominal rotor speed in order to avoid excitation of a critical bending mode in operation. If this criteria is not respected, the resulting deflection from passing a critical bending speed could potentially lead to contact between rotor and bearing bushing and subsequent failure. The risk of contact between rotor and bushings is further reduced by designing the rotor and bearings in such a way that the bearing planes are positioned at the nodes of a potentially excited bending mode.

Another important aspect to be considered in the design of HGJB supported rotors is the careful selection of rotor and bearing bushing materials in terms of thermal expansion coefficient. Due to the often high temperatures occurring in high-speed turbomachinery, materials featuring low thermal expansion coefficients are favored to guarantee thermal stability of the rotor-bearing-system.

Various techniques exist to model the dynamic behavior of HGJBs. The fluid film of a Herringbone-Grooved Journal Bearing is governed by the Reynold's equation, a non-linear differential equation that can be solved numerically by discretizing the grooved bearing clearance and applying finite element/finite difference methods [18, 19, 20], or by using the Narrow-Groove Theory (NGT), first presented by Vohr and Pan [21] and later presented in more detail by Malanosky and Pan [22]. The NGT assumes an infinite number of grooves, which transforms the saw-toothed pressure profile of a bearing with a finite number of grooves into a smooth pressure distribution.

All bearing calculations for this thesis are performed as presented by Schiffmann [16], which applies a perturbation method and a separation of variables to solve the non-linear differential equation for the smooth pressure distribution resulting from the NGT to obtain the frequency dependent stiffness and damping matrices of the bearings.

A detailed overview on the modeling approaches of grooved bearings is offered by Gu et al. [23].

1.3 Problem statement

One of the disadvantages of gas lubricated bearings is their need for very small clearance to diameter ratios to allow stable rotor operation and to provide sufficient load capacity [23, 24]. The radial clearance is usually in the region of 5 to 10 μm for a shaft of 10 mm diameter.

The consequences of the required very small clearance ratios are listed below:

- High cost: To ensure high critical bending speeds, materials featuring a high ratio of elastic modulus to density are required. In combination with the requirement for low thermal expansion coefficients and sufficient hardness to achieve the tight tolerances, the list of eligible materials reduces to ceramics and tungsten-carbides and in some rare cases steel. Ceramic and tungsten-carbide raw materials are expensive due to the required sintering process. The machining process of high-precision rotors and bushings consists of multiple processes but the finishing is usually done by grinding and/or honing, which are manufacturing processes that are time consuming due to the low material removal rate. The manufacturing cost is further increased by the required machining tools and the

need for high-quality machines. Furthermore, parts that feature strict tolerances require a higher rate of inspection, performed in air-conditioned rooms with expensive measurement equipment that needs regular calibration. Companies that are able to offer these services are scarce and demand high prices to pay back for the substantial investment in the required high-tech equipment. Last but not least, it is evident that strict tolerances yield increased rejection rates and therefore a higher volume of parts that do not pass quality control, further increasing cost.

- Stringent misalignment tolerances: In addition to the strict manufacturing tolerances, the required small clearance ratios also require for a perfect alignment of the two bearing surfaces with respect to each other. In terms of alignment, the two bearing surfaces are ideally contained in one bearing sleeve and manufactured in the same setting. If the required bearing distance is large, however, the machining of both bearing surfaces in the same setting is not feasible due to tool depth restrictions and therefore requires the manufacturing of two separate bearing bushings. The concept of a bearing sleeve, which is a single part containing both bearing planes, as well as the concept of using two separate bearing bushings, are presented in Fig. 1.2.

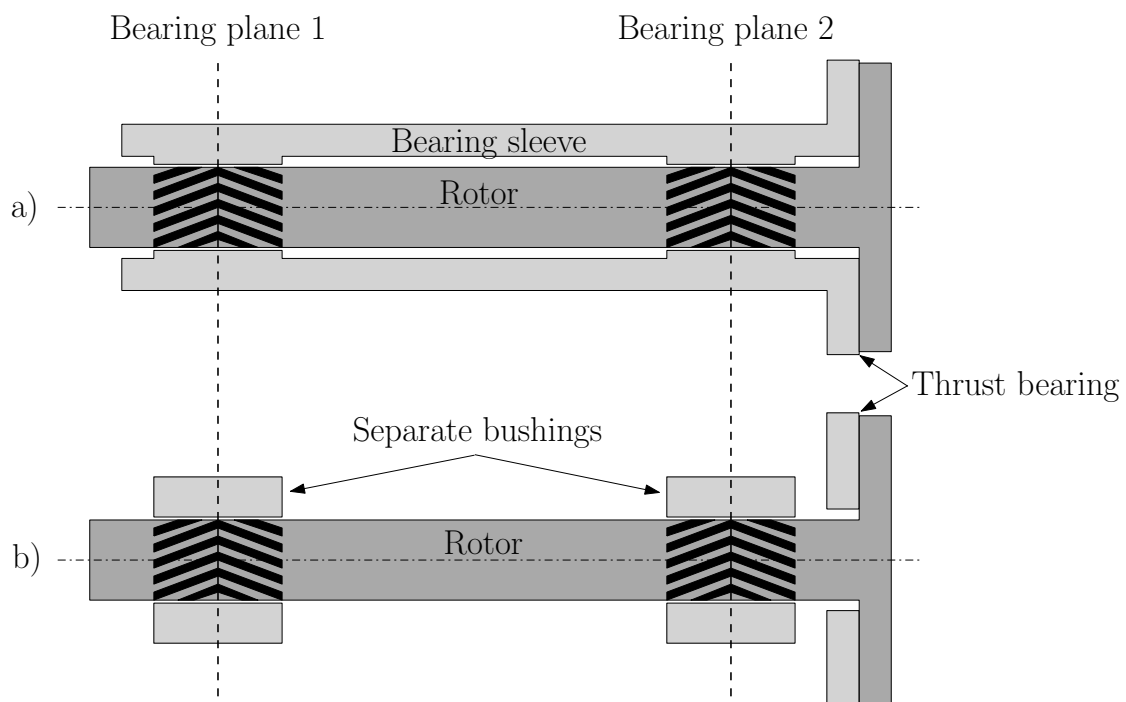


Figure 1.2 – a) Rotor supported on bearing sleeve containing both bearing planes in one part; b) Rotor supported by two separate bearing bushings

Obtaining concentric and angular alignment of two separate bearing bushings fitted in considerable distance within a structure of various sub-assemblies is

extremely challenging due to the concatenation of form and dimensional errors of each individual part. Manufacturing of two separate bearing bushings, however, is considerably cheaper compared to a bearing sleeve and offers further advantages, especially for electric motor driven rotors that incorporate a permanent magnet inside the rotor. Two separate bearing bushings allow for longer rotors, which can incorporate longer permanent magnets and therefore yield lower electrical losses. Furthermore, if a bearing sleeve is used, it has to be manufactured from non-conductive materials in order to avoid Eddy-currents in the bearing sleeve induced by the electrical windings of the surrounding stator, a restriction that does not exist for the concept of two separate bushings. Unfortunately, the small clearances of HGJBs are hindering the exploitation of the various advantages that are offered by using two separate bearing bushings.

- Low thermal stability: Small clearance to diameter ratios require the use of materials with a small thermal expansion coefficient and careful design in order to obtain thermal stability. Various heat sources affect the temperature of the rotor and the bearing bushings: Windage losses generated in the bearing itself and at the surface of the rotor, heat induced by turbine and/or compressor wheels mounted on the rotor, as well as potential electrical losses in the rotor. The resulting temperature distribution in rotor and bearing bushing governs the thermal expansion of rotor and bushing and can be the cause for thermal instability if the bearing clearance deviates too much from the designed clearance or even causes contact between rotor and bushing in extreme cases.
- Increased bearing losses: Assuming a laminar flow in the bearing, the losses in a HGJB are inversely proportional to the bearing clearance [16]. Hence, small clearance ratios increase the specific windage losses in the bearing, resulting in a mitigation of thermal stability and overall efficiency of the turbomachine.

To reiterate, increasing the bearing clearance yields a significant cost reduction, simplifies the manufacturing and assembly processes and allows to loosen the very stringent misalignment tolerances. In addition, increased clearances yield reduced bearing losses and improved thermal stability. Furthermore, some constraints in terms of rotor design can be relaxed due to the fact that enlarged clearances allow for larger rotor bending amplitudes, as well as larger tolerable centrifugal and thermal growth of the rotor.

The bearing clearance and the stability of a HGJB supported rotor are two competing design objectives [16, 23, 25, 26]. Measures that positively effect one of these objectives, cause a negative effect on the other and vice versa. However, if the stability threshold can be increased, this gain in stability can be compensated by an appropriate increase in bearing clearance, resulting in a rotor-bearing-system that offers the same stability threshold at larger bearing clearances.

For a given HGJB supported rotor design with a given bearing clearance, there are two possible approaches to increase the stability threshold:

1. Apply measures that directly influence the dynamic characteristics of the gas film itself → design of the groove pattern
2. Apply measures that induce external damping to the bearing bushing → flexible, damped support of the bearing bushing

Herringbone-Grooved Journal Bearings are traditionally designed using helical grooves with constant pitch and cross section. A recent study by Schiffmann [26] addresses approach 1 and has shown theoretically that by using enhanced groove geometries, an increase in bearing clearance by more than 50% is possible compared to state-of-the-art bearings, while maintaining the same rotordynamic stability. These findings, however, have not been tested experimentally.

Approach 2 is commonly used by supporting the bearing bushings on elastomeric O-Rings [27, 28, 29, 30, 31, 32]. The stiffness and damping of the O-Rings, which play an important role in the rotordynamic behavior and in the maximization of the nominal bearing clearance, are both difficult to tune and to measure accurately. In addition, O-Rings suffer from limited lifetime at high temperatures and their dynamic characteristics depend on many variables such as temperature, frequency, vibration amplitude, age, geometry, material and loading type, just to name a few. One of the most important downsides of using O-Rings to flexibly support HGJB bushings, however, are their geometrical manufacturing tolerances. The tolerances on O-Ring diameter and thickness are typically around 0.02 mm, which yields misalignment issues and make a reliable and reproducible implementation into products challenging.

Figure 1.3 presents measurements of the total frictional torque as a function of rotor speed obtained through coast-down tests of a HGJB supported rotor with flexibly mounted bushings on O-Rings obtained from a LAMD prototype. All measurement sets were obtained from the same prototype using the same shaft on identical O-Ring supported bearing bushings. The rotor speed with the lowest frictional torque can be associated to the bearing lift-off speed. The difference in the presented measurement results stems only from disassembly and reassembly of the shaft and/or bearing bushings. Since all the mechanical parts (rotor, bearing bushings, O-Rings) are identical, the results suggest that the difference in the measured frictional torque is caused solely by the quality of the bearing bushing alignment.

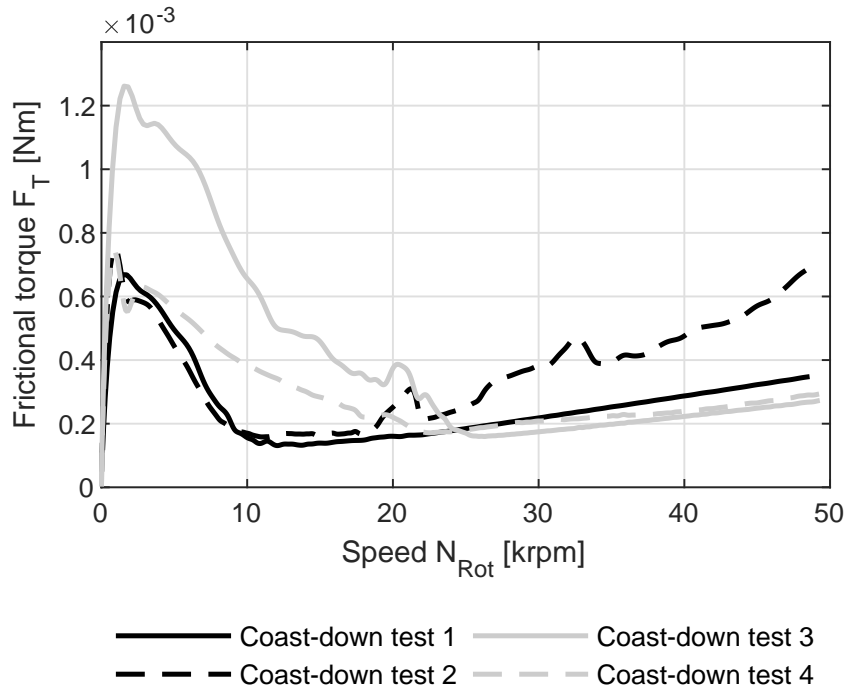


Figure 1.3 – Coast-down frictional torque measurement results of O-Ring supported HGJB bushings

These results clearly suggest that O-Rings do not offer a repeatable and reliable means to flexibly support gas bearing bushings.

1.4 Goal and objectives

One of the main challenges of HGJBs is the required small clearance ratio to ensure stable operation, which yields high manufacturing cost, stringent misalignment tolerances and increased specific bearing losses. These shortcomings can be overcome by an increase in bearing clearance, while maintaining the rotordynamic performance of the bearings, which is the main goal of this thesis.

In order to attain this goal, the following objectives are defined:

1. Identification of the potential of enhanced groove geometries and a flexible bearing bushing support to increase bearing clearance while keeping rotordynamic stability.
2. Identification of the dynamic characteristics of O-Rings currently used in LAMD prototype.
3. Identification of the variables governing the dynamic characteristics of O-Rings

in terms of stiffness and damping.

4. Development of a model for stiffness and damping of O-Rings that is based on the collected experimental data.
5. Development of a flexible, tunable support capable of supporting two separate HGJB bushings.
6. Development of an alignment concept to align the two separate bearing bushings to each other, as well as to the stator housing and the thrust bearing surface.
7. Integration of the new flexible support concept into the prototype.
8. Experimental performance assessment of the proposed flexible support by evaluating the stability of the rotor-bearing-system.
9. Identification of the improvements in terms of bushing alignment and wear by performing coast-down measurements and start-stop tests.
10. Experimental investigation of enhanced groove geometries and their potential to increase the bearing clearance.

1.5 Methodology

At the Laboratory for Applied Mechanical Design (LAMD), a radial compressor prototype to supply compressed air to a Proton-exchange Membrane (PEM) fuel cell has been designed and manufactured according to the specifications presented in Tab. 1.1.

Table 1.1 – Specifications of LAMD prototype for PEM fuel cell pressurization

Nominal rotor speed N_{Rot}	250 krpm
Nominal pressure ratio π	1.5
Nominal air mass flow \dot{m}	10 g/s
Inlet pressure p_{in}	70-105 kPa
Inlet temperature T_{in}	-20 \cdots + 40°C
Outlet condition	Oil-free air
Lifetime without maintenance	> 4000 hours
Start/Stop cycles without maintenance	> 15000

The rotor of this prototype is made from Silicone-Nitride (SiN) ceramic and runs in two separate O-Ring supported HGJB bushings made from SiN. The rotor is driven by an electric motor positioned between the bushings. The axial loads are compensated

by means of a Spiral-Grooved Thrust Bearing (SGTB). A conceptual sketch of the rotor-bearing-system is presented in Fig. 1.4.

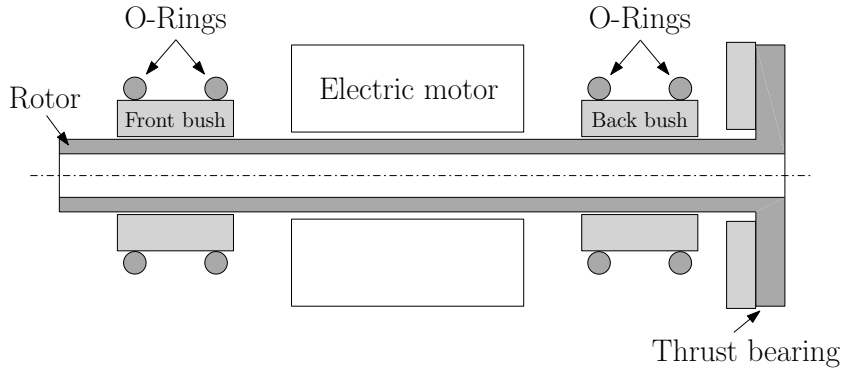


Figure 1.4 – Conceptual sketch of LAMD prototype with O-Ring supported HGJB bushings

After solving initial thermal instability problems of the prototype at the beginning of this thesis, coast-down tests were performed, which highlighted the various issues of O-Ring supported bearing bushings (refer to Fig. 1.3), namely misalignment, a low degree of repeatability and dynamic characteristics that are difficult to tune and to measure.

The current O-Ring supported prototype therefore serves as a base-line for the development of a novel flexible bearing bushing support and alignment concept, which will be implemented and experimentally tested in this prototype.

Each chapter of this thesis is devoted to attain a specific set of objectives. The detailed methodology applied to attain the objectives of each particular chapter is therefore individually described in the subsequent chapters.

1.6 Thesis outline

A short summary of each chapter presented in this thesis is given below:

Chapter 2 - Potential of flexible bearing bushing support and enhanced groove geometries This first chapter addresses the general potential of increasing the bearing clearance by means of a flexible bearing bushing support and enhanced groove geometries. In a first part, the effect of support stiffness, support damping and bearing bushing mass on the stability of a classically grooved rotor is investigated by performing Monte-Carlo simulations. In a second part, the stability and the bearing clearance

of classically and enhanced grooved rotors on both rigid and flexible supports is optimized using a multi-objective optimization approach and the effect of the support characteristics on the optimum groove geometry studied.

Chapter 3 - Data-driven model for stiffness and damping of O-Rings This chapter describes a method to measure the stiffness and damping of O-Rings, commonly used to flexibly support HGJB bushings. In a first part, the dynamic characteristics of the silicone O-Rings that are currently implemented in a LAMD prototype are identified. In a second part, the dynamic characteristics of 60 representative O-Ring sizes are measured and the major factors affecting stiffness and damping identified. In a third part, the measurement results are condensed into a data-driven, reduced-order model for stiffness and damping that allows the prediction of the dynamic characteristics of O-Rings in cyclic radial loading as a function of their geometry and operating conditions.

Chapter 4 - Flexible support for Herringbone-Grooved Journal Bearings This chapter presents a novel flexible support for HGJB bushings, which allows independent tuning of the radial and tilting support stiffness and that can be coupled to various damping concepts. In a first part, a parametric model is presented that allows to predict the stiffness of the membrane-shaped support structure in radial and tilting direction. In a second part, the dynamic characteristics of the flexible support are experimentally tested and compared to the predicted results from the developed parametric model. A third part addresses the alignment problem of separate HGJB bushings and presents a procedure based on a thermally expanding shaft to accurately align the bearing bushings relative to each other, to the stator housing and to the thrust disk surface. In a last part, the novel flexible bearing bushing support is implemented in the base-line prototype and its performance assessed by means of high-speed measurements and start-stop testing.

Chapter 5 - Enhanced groove geometries for Herringbone-Grooved Journal Bearings This chapter presents the results of a theoretical and experimental enhanced groove geometry exploration. In a first part, enhanced groove geometries are investigated by means of multi-objective optimizations for a rotor previously tested with classical grooves. In a second part, five rotors are manufactured and engraved with the identified optimized groove geometries of varying design complexity. In a third part, all five rotors are experimentally tested and their performance compared to the predicted results and the base-line rotor featuring classical grooves.

Chapter 6 - Conclusions Chapter 6 wraps up the thesis with a summary and conclusions and gives recommendations for future work.

1.7 Specific aspects of novelty

The work presented in this thesis contains several aspects of novelty, which are summarized in the following points:

- Identification of the variables governing stiffness and damping of O-Rings.
- Development of a data-driven model for the dynamic characteristics of O-Rings that distinguishes between geometrical and material effects.
- Embodiment of a flexible support for HGJB bushings that is tunable in radial and tilting stiffness and whose characteristics are largely independent of frequency, age and temperature.
- Presentation of an alignment concept based on thermal expansion, suitable to align HGJB bushings of considerable distance.
- Theoretical and experimental identification of a bearing bushing tilting instability.
- Experimental confirmation of the stabilizing effect of enhanced groove geometries and identification of groove parameters offering the best trade-off between performance enhancement and design/manufacturing cost.

2 Potential of flexible bearing bushing support and enhanced groove geometries

This chapter focuses on the potential of classical and enhanced Herringbone-Grooved Journal Bearing (HGJB) geometries in combination with rigidly and flexibly supported bearing bushings, to either increase bearing clearance or the stability threshold of the rotor-bearing-system. The potential is investigated by means of Monte-Carlo simulations and multi-objective optimizations of classical HGJB on rigid bearing bushing supports as well as on flexible supports. The combination of enhanced grooves, where groove angle, depth and width evolve in axial direction of the shaft, in combination with rigid and flexible supports is investigated in a second stage.

The Monte-Carlo simulation results suggest a gain of up to 100% in stability is achievable by reducing the reduced frequency and by increasing the relative damping of the flexible support.

The results obtained from multi-objective optimization suggest that a flexible support of the bearing bushings allows to increase bearing clearance by up to 50% above the threshold clearance of $7.5 \mu\text{m}$. Below this threshold, a rigid bearing support offers better performance. The use of enhanced groove geometries suggests a gain of up to 50% in bearing clearance, which can be extended to even larger bearing clearances when supporting the rotor on a flexible support with damping. Furthermore, combining enhanced groove geometries with a flexible, damped bearing bushing support structure allows to achieve higher load capacity (+50%) compared to flexibly supported classical grooves.

2.1 Introduction

As discussed in chapter 1, gas lubricated bearings generally require very small clearance to diameter ratios to allow stable rotor operation. On the one hand, one wants to maximize the stability threshold of the system in order to have a reliable system offering a high lifetime. On the other hand, one wants to maximize the radial bearing clearance in order to reduce manufacturing cost and slacken the stringent alignment tolerances.

Chapter 2. Potential of flexible bearing bushing support and enhanced groove geometries

As in many engineering problems, these two objectives are competing against each other, requiring the designer of such systems to find the best trade-off between stability and bearing clearance. Due to the competing nature of bearing clearance and stability, one can deduct that any applied measure to increase the stability threshold can be profited from by allowing an increase in bearing clearance.

Depending on the chosen bearing type, many approaches exist to reduce unwanted vibration and to increase the stability threshold of high-speed rotor systems. Most of them focus on increasing the damping of the bearing itself or by introducing a flexible bearing support with damping. The inherent very low damping of rolling-element bearings for example can be compensated by supporting the bearing on a flexible element that provides damping, on O-Rings for example [33, 34, 35], by the application of a squeeze film damper [36, 37, 38, 39], or a combination of both measures [40].

A fluid film bearing type often used in high-speed turbomachinery is the foil bearing [41, 42]. The advantage of this bearing type is its flexible support structure comprising of a top foil and a bump foil, which creates Coulomb damping and helps to stabilize the bearing. Various research has been conducted in order to further improve the stability of this bearing type, including approaches to directly alter the damping properties of the gas film by means of selective shimming [43, 44], where thin shims are introduced to preload the bump foil support structure, locally altering the film thickness in such a way so as to increase the damping of the fluid film. Another method to directly alter the damping of the gas film in foil bearings itself include the actively controlled injection of lubricant gas [45, 46]. Research focusing on the external damping of the support structure of foil bearings was performed amongst others by San Andrés et al. [47, 48] and Feng et al. [49], who found that metal-mesh structures successfully increase the damping coefficient of the support and therefore yield increased stability of the rotor-bearing-system, whereas Sim and Park [50] obtain similar results by introducing high damping polymer materials in the flexible foil bearing structure.

For the particular case of HGJBs, both active and passive approaches have been followed to increase the damping of the gas film and/or the support structure. Santos et al. [51, 52] present an active approach to directly control the damping of the gas film, which involves a controlled injection of lubricant into the gas film and has shown to considerably increase the direct damping coefficient of the gas film. Passive approaches to alter the gas film and increase damping have been presented in terms of enhanced groove geometries by Ikeda et al. [53] and Schiffmann [26], who showed enhanced groove geometries to have a large potential in increasing the stability threshold of the rotor-bearing-system.

Passive methods to increase the stability threshold of HGJBs have been presented by means of increasing the external damping of the bearing bushing through flexibly supporting it on elastomeric O-Rings [27, 28, 29, 30, 31, 32], or by using flexible structures that provide Coulomb damping [54, 55]. Both methods have shown promising results to increase the stability threshold of HGJBs.

A third method to ensure stable operation of a rotor running on HGJBs is to dampen the motion of the rotor itself by means of damper seals [56]. Damper seals are a non-contacting labyrinth type seal that reduce the circumferential flow within the seal by means of pockets. The reduction in circumferential flow allows to significantly increase the direct damping coefficient of the seal, hence increasing the rotordynamic stability.

2.2 Motivation and nature of the issue

As suggested by the results presented in the literature, both approaches, the one focusing on altering the gas film itself as well as supporting the bearing bushing in a flexible and damped manner, show a promising potential to increase the stability threshold of a HGJB supported rotor and therefore allow to increase the bearing clearance, which yields a reduction in bearing losses, manufacturing cost, as well as a relaxation of the assembly and alignment tolerances.

Even though active approaches to control the stability of HGJBs offer inherent advantages, they yield more complex systems that are not favorable due to constraints in complexity, price, weight, reliability and need for auxiliary systems, hence a passive approach is favored for the LAMD prototype investigated in this thesis.

The results obtained from the LAMD prototype featuring O-Ring supported bearing bushings have been promising in terms of rotordynamic stability thanks to the favorable stiffness and damping characteristics of the O-Rings, however, the sweet-spot of ideal support stiffness and damping characteristics has not yet been identified.

As previously mentioned, methods to increase the stability threshold of a given HGJB supported rotor are limited to measures that impact directly the gas film itself, enhanced groove geometries for example, or a flexible support structure that provides external damping to the bearing. Both methods have been treated separately in the current literature. It is evident that the combination of both approaches could yield an even larger potential to increase the stability threshold of a HGJB. Furthermore, Herringbone grooves are usually manufactured by laser etching, hence enhanced groove geometries are of particular interest since they offer a potential increase in performance of the rotor-bearing-system with no increase in manufacturing cost.

2.3 Goals and objectives

The objectives of this chapter are summarized below:

1. General investigation of the potential of a flexible bearing bushing support to increase bearing clearance while keeping rotordynamic stability, based on the rotor geometry of the LAMD prototype.

Chapter 2. Potential of flexible bearing bushing support and enhanced groove geometries

2. Identification of support characteristics suggested to offer the highest potential for classical and enhanced groove geometries.
3. Identification of the effect of the support characteristics and groove geometries on the load capacity of the bearings.

2.4 Methodology

2.4.1 Rotordynamic model

The rigid-body rotordynamic system that is used to predict whirl speed and stability maps is presented in Fig. 2.1. Each bearing bushing is flexibly supported, allowing a modification of the support properties to study the effect of support stiffness and damping on the stability of the rotor-bearing system. A rigid support is modeled by increasing the support stiffness k_S to a very high value.

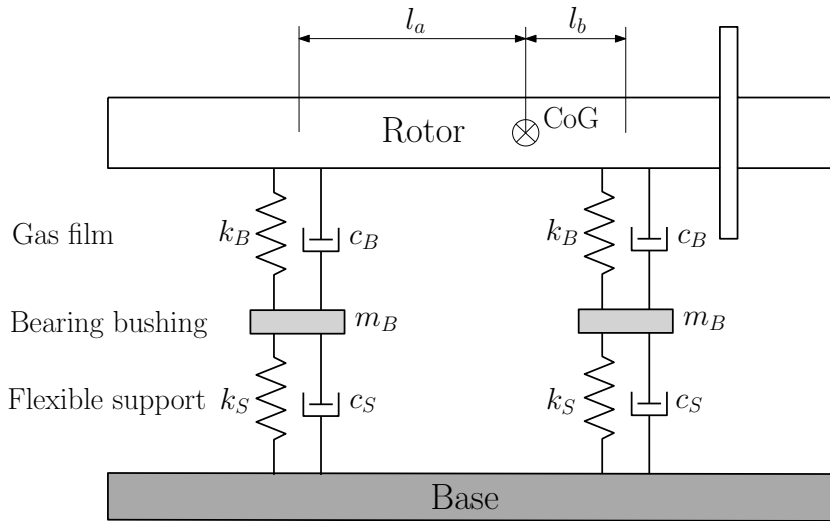


Figure 2.1 – Rotordynamic model used for multi-objective optimizations

The rotordynamic system in Fig. 2.1 can be described by Eqn. (2.1).

$$K\vec{q} + B\dot{\vec{q}} + M\ddot{\vec{q}} = \vec{F} \quad (2.1)$$

M is the inertia matrix of the system, K the matrix containing bearing and support stiffnesses and B is the damping matrix containing the bearing and support damping coefficients as well as the gyroscopic effects. The rotordynamic properties of the rotor-bearing-support system are described in terms of rotor mass m_{Rot} , polar and transverse rotor inertia J_P and J_T , the distance of bearing mid-planes relative to the rotor center of gravity l_a and l_b and the mass m_B of the flexibly supported bearing

Chapter 2. Potential of flexible bearing bushing support and enhanced groove geometries

In the case of enhanced grooves, the variables for groove width α , groove angle β and groove depth ratio H evolve along the axial position z described by a 3rd order polynomial expression using the interpolation points at Pos1 to Pos4, which are equally distributed within the grooved region. Pos1 refers to the position where the grooves start, in the bearing center $z=0$ for $\gamma=1$, while Pos4 is the position at the outer groove edge. The dimensionless variables for the groove depth ratio H , groove width ratio α and the bearing length ratio γ are defined in Eqn. (2.4).

$$H = \frac{h_g}{C}, \quad \alpha = \frac{w_g}{w_g + w_r}, \quad \gamma = \frac{L - L_{Land}}{L} \quad (2.4)$$

The bearing properties for classical and enhanced groove geometries have been modeled using the adapted Narrow-Groove-Theory as presented by Schiffmann [26].

2.4.2 Boundary conditions

Table 2.1 presents the rotor and bearing design parameters used to perform the multi-objective optimizations in this chapter. Note that these design parameters correspond to the rotor that is experimentally investigated with flexible bushing support, with the results presented in chapter 4.

Table 2.1 – Rotor design properties of LAMD prototype used to investigate the effect of flexible support characteristics

Bearing diameter D_{Brq}	10 mm
Bearing length-to-diameter ratio L_{Brq}/D_{Brq}	1
Rotor mass m_{Rot}	0.0289 kg
Polar rotor inertia J_P	4.3258e-07 kgm ²
Transverse rotor inertia J_T	1.8112e-05 kgm ²
Bearing distance l	58.5 mm
Distance front bearing mid-plane to rotor center of gravity l_a	30.7mm
Distance back bearing mid-plane to rotor center of gravity l_b	27.8mm
Nominal rotor speed N_{Rot}	250 krpm

The calculations and optimizations performed in this chapter are based on air as the bearing lubricant. The fluid properties are summarized in Tab. 2.2.

Table 2.2 – Fluid properties used to investigate the effect of flexible support characteristics

Viscosity μ	18 Pas
Temperature T	313 K

2.4.3 Monte-Carlo simulations

The effect of the flexible support characteristics in terms of support stiffness k_S , damping coefficient c_S and bearing bushing mass m_B compared to rigidly supported bushings, is assessed by performing Monte-Carlo simulations. The analysis is based on the rotor design according to Tab. 2.1, featuring classical grooves of constant groove angle β , groove width ratio α and groove depth ratio H . The assessment is based on the evaluation of relative stability change $\bar{\Gamma}$ of the flexibly supported rotor compared to a rigidly supported rotor. The relative stability change $\bar{\Gamma}$, used to evaluate the results of the Monte-Carlo simulations, is defined in Eqn. (2.5).

$$\bar{\Gamma} = \frac{\Gamma_{flex} - \Gamma_{rigid}}{\Gamma_{rigid}} \quad (2.5)$$

Γ_{rigid} represents the minimum logarithmic decrement in the rotational speed range from 0-250 krpm for the rotor presented in Tab. 2.1, supported on a rigid support. Γ_{flex} is the minimum logarithmic decrement for the same rotor, supported on a flexible support. A positive relative stability change $\bar{\Gamma}$ denotes an increase in stability compared to rigidly supported bearing bushings, while a negative $\bar{\Gamma}$ represents a stability decrease. The baseline values of the dynamic support characteristics correspond to the identified O-Ring support properties determined for the previously used pair of silicone O-Rings (see chapter 3) and are summarized in Tab. 2.3.

Table 2.3 – Baseline properties of flexible support for Monte-Carlo simulations

Base support stiffness k_{S0}	1.12e+06 N/m
Base support damping coefficient c_{S0}	4 Ns/m
Base bushing mass m_{B0}	2.5e-03 kg

The baseline properties in Tab. 2.3 are varied according to Tab. 2.4, resulting in a range of flexible support characteristics that cover two orders of magnitude.

Chapter 2. Potential of flexible bearing bushing support and enhanced groove geometries

Table 2.4 – Range of investigated support characteristics for Monte-Carlo simulations

Support stiffness $k_S \in$	$[0.1, 10] k_{S0}$
Support damping coefficient $c_S \in$	$[0.1, 10] c_{S0}$
Bushing mass $m_B \in$	$[0.1, 10] m_{B0}$

2.4.4 Design variables and optimization objectives

Table 2.5 presents the range of optimization variables for the multi-objective optimizations performed for the rotor with the properties summarized in Tab. 2.1. In the case of enhanced grooves, the parameters α , β and H evolve along the axial position z of the rotor described by a 3^{rd} order polynomial expression using the interpolation points at Pos1 to Pos4, which are equally distributed within the grooved region (see Fig. 2.2).

Table 2.5 – Range of design variables for the multi-objective optimization

Groove width ratio $\alpha \in$	$[0.35, 0.65]$
Groove angle $\beta \in$	$[110, 175] \text{ deg}$
Groove depth ratio $H \in$	$[0.1, 6.0]$
Groove length ratio $\gamma \in$	$[0.1, 1.0]$
Radial clearance $C \in$	$[4, 20] \mu\text{m}$
Support stiffness $k_S \in$	$[0.01, 50] 1\text{e}+06 \text{ N/m}$
Support damping coefficient $c_S \in$	$[0, 3] \text{ Ns/m}$

The optimizer will vary these variables within their defined ranges while trying to maximize or minimize the given objectives. In addition to the bearing properties, the support stiffness k_S and support damping coefficient c_S are also considered in the optimization problem.

The highest stiffness value for k_S approaches a stiff bushing support, while the lowest stiffness value represents a support of very high compliance. The upper limit of support damping coefficient c_S corresponds to the damping coefficient of a typically used O-Ring, while the lower bound represents a flexible support without damping.

In a rotor-bearing system featuring fluid-film bearings, the performance measures of high importance are the rotordynamic stability, the bearing clearance, the load capacity of the bearings, as well as the bearing losses. One wants to maximize the stability and bearing clearance, while minimizing the bearing losses. All of these objectives are competing, which is why they should be optimized simultaneously. Multi-objective optimizations, however, require large computational resources forcing designers to focus on only two to three objectives in order to save computational time and ensure convergence. The optimization objectives for all performed optimizations presented in this chapter are:

1. Maximize rotordynamic stability Γ
2. Maximize radial clearance C

All multi-objective optimizations performed for this thesis were done using the evolutionary algorithm *moo*, developed by two PhD students [57, 58] from EPFL, which has shown very good results in solving non-linear optimization problems, whose optimal solution space is often disjoint, discontinuous and yields multiple local optima. The optimization algorithm *moo* uses a population-based approach that starts from an initial population of solutions, while the generation of new and the removal of unfit solutions is based on a heuristic method. The advantages of such an approach are the exploration of the whole solution space and the insensitivity of the found solution with regards to the initial starting point of the optimization.

2.5 Results and discussion

2.5.1 Monte-Carlo simulation results - Classical grooves on flexible support

The Monte-Carlo simulation results are presented in Fig. 2.3 as a 3D data cloud. Red dots indicate cases for which the flexibly supported rotor yields lower rotordynamic stability compared to the baseline case. The color scale indicates the level of relative change in stability according to Eqn. (2.5).

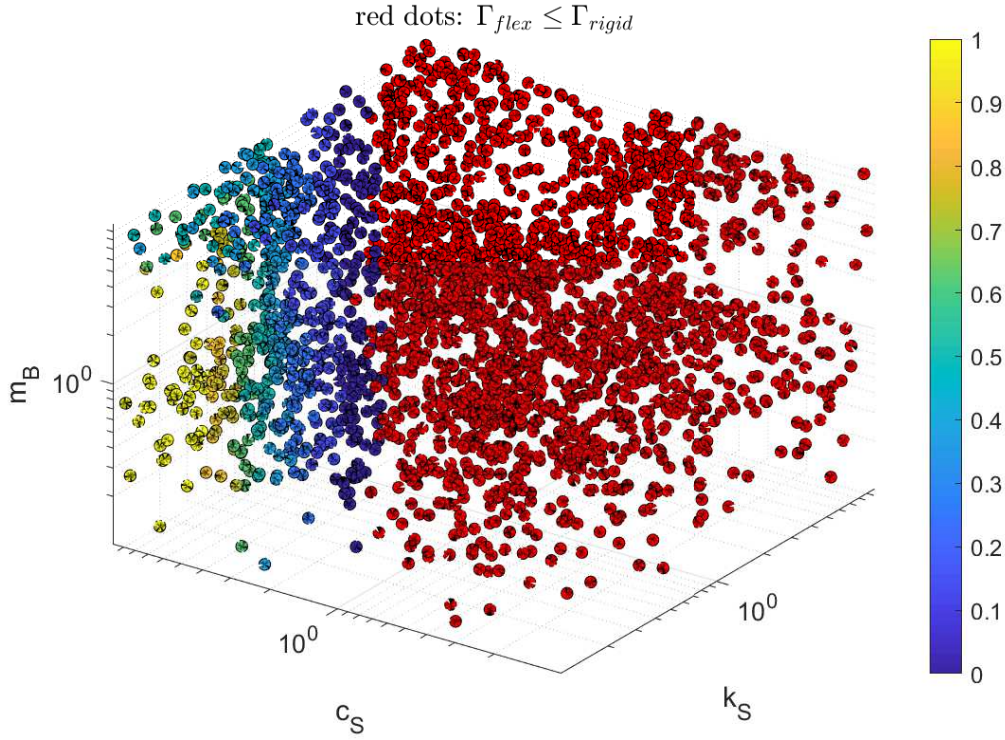


Figure 2.3 – Monte-Carlo simulation results present the effect of support stiffness k_S and damping coefficient c_S on the relative stability change of classical HGJB on a flexible support. Red dots represent lower rotordynamic stability compared to a rigid bushing support.

The results suggest that in some cases, the logarithmic decrement Γ can be increased by 100% compared to the baseline figure obtained for a rigid bushing support. The results suggest that the bushing mass has limited influence on the stability. Stability increase occurs at high support damping combined with low support stiffness. An alternative way to present the results is by expressing them in terms of reduced frequency $\bar{\Omega}$ and relative damping coefficient \bar{N} , as defined in Eqn. (2.6)

$$\bar{\Omega} = \frac{\omega}{\omega_0}, \quad \bar{N} = \frac{\eta}{\eta_0} \quad (2.6)$$

, where $\omega = (k_S/m_B)^{1/2}$ is the critical frequency and $\eta = c_S/(2m_B \cdot \omega)$ is the damping factor. ω_0 and η_0 represent the critical frequency and damping factor obtained with the base-line values presented in Tab. 2.3. The relative stability change $\bar{\Gamma}$ plotted against relative damping \bar{N} and reduced frequency $\bar{\Omega}$ is presented in Fig. 2.4. The 3D data cloud collapses to a surface when plotted against reduced frequency $\bar{\Omega}$ and relative damping \bar{N} .

Stability gains through using a flexible support can be achieved by reducing the reduced

frequency $\bar{\Omega}$ and by increasing the relative damping \bar{N} of the flexible support.

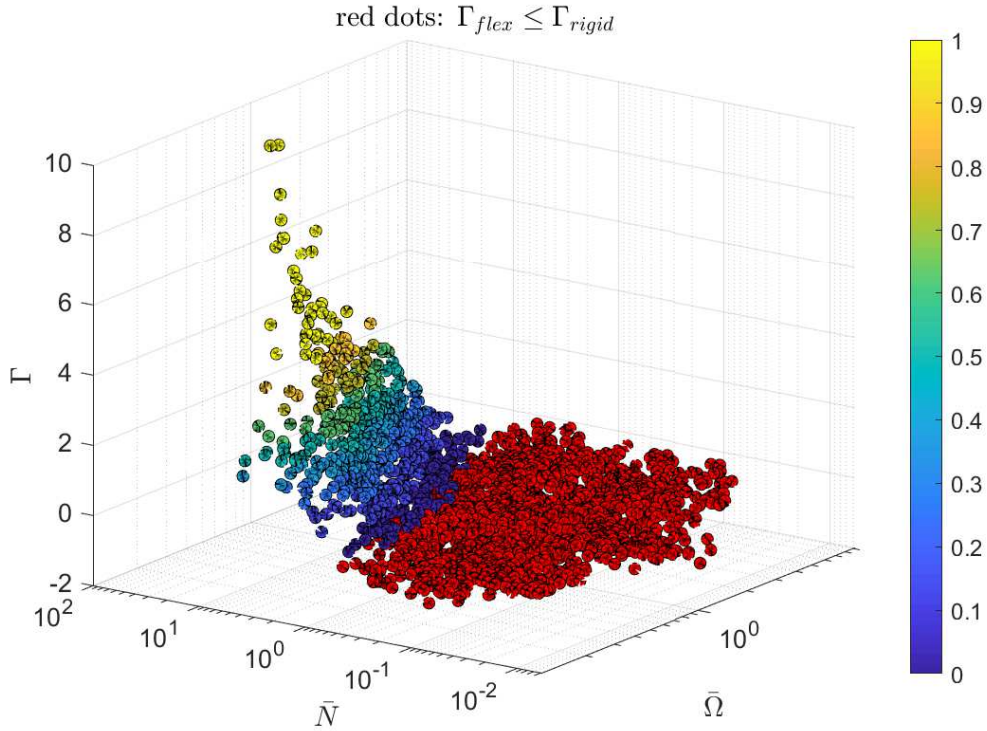


Figure 2.4 – Influence of the reduced frequency $\bar{\Omega}$ and the relative damping \bar{N} on the stability of a classical HGJB on a flexible support. Red dots represent lower rotordynamic stability compared to a rigid bushing support.

2.5.2 Optimization results - Classical grooves on rigid and flexible support

The results for the multi-objective optimization for maximizing both the logarithmic decrement Γ and the radial clearance C for soft and rigidly supported classical HGJB are presented in Fig. 2.5. For the flexible bushing support, the support stiffness and damping are part of the optimization variables. Their ranges are given in Tab. 2.5. Since the support damping coefficient saturates at the maximum value for all cases, a second optimization has been performed for which the maximum damping is limited to 0.01 Ns/m, representing a flexible support without damping.

Chapter 2. Potential of flexible bearing bushing support and enhanced groove geometries

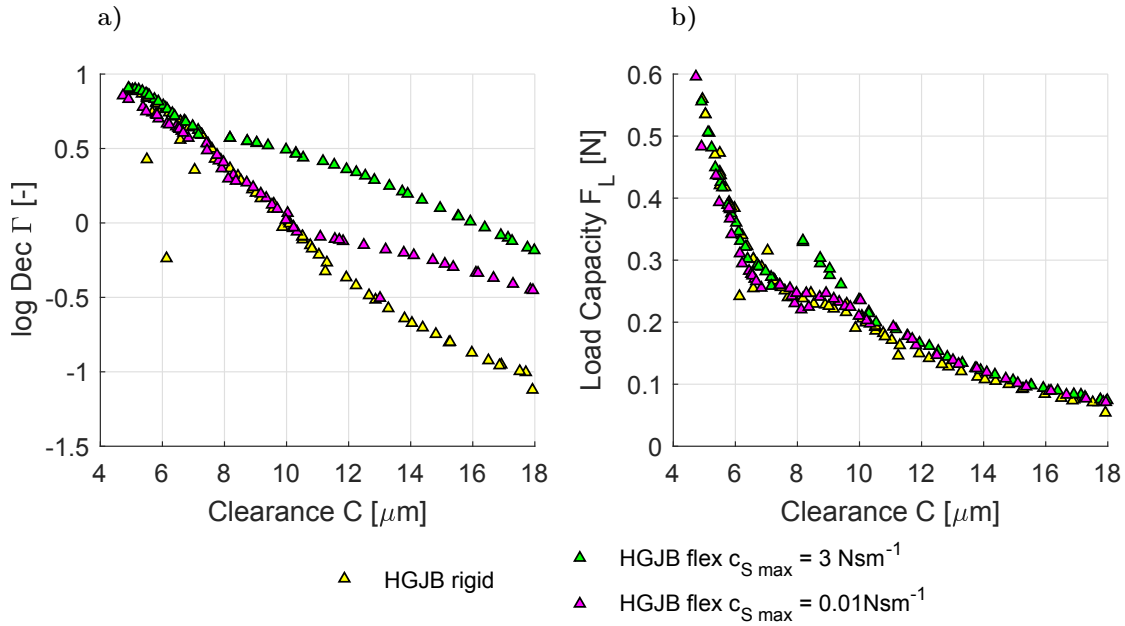


Figure 2.5 – a) Logarithmic decrement Γ against radial clearance C for classical grooves on flexible support; b) Load capacity against radial clearance C

As suggested by the results presented in Fig. 2.5 a), up to a radial clearance C of $7.5 \mu\text{m}$, classical grooves on rigid support offer the highest stability threshold. For clearances larger than $7.5 \mu\text{m}$, a flexible support with damping (green markers) offers increased stability. The results suggest that stable operation can be achieved with clearances up to $16 \mu\text{m}$, which corresponds to a $>50\%$ increase compared to the baseline case. In the absence of damping (magenta markers), stability is not improved by a flexible bearing bushing support at low clearances. At larger clearances ($>10 \mu\text{m}$) an improvement can be achieved, at negative logarithmic decrements, though. Figure 2.5 b) presents the results of load capacity versus radial clearance for the three investigated cases of rigid support, flexible support with damping and flexible support without damping. The load capacity is evaluated at 20 krpm and 50% eccentricity using a linear extrapolation approach. As suggested by the results, a flexible support with damping offers increased load capacity in certain clearance ranges.

Figure 2.6 a) and Fig. 2.6 b) present the optimization results for support stiffness and damping in the case of the classically grooved shaft on a flexible support. In general, the support stiffness k_S saturates towards its minimum value ($1\text{e}+04 \text{ N/m}$) while the support damping saturates towards its maximum value. In practice this would mean a very compliant support with high damping coefficient, which results in large support displacements and in combination with high support damping to a large amount of dissipated energy. These results are in agreement with the results obtained from the Monte-Carlo simulations. In the absence of damping, the optimization results suggest to use a support with high stiffness (rigid support) to maximize stability. Note that

the transition from high to low support stiffness occurs at the same clearance as the departure from the rigid HGJB Pareto curve (Fig. 2.5).

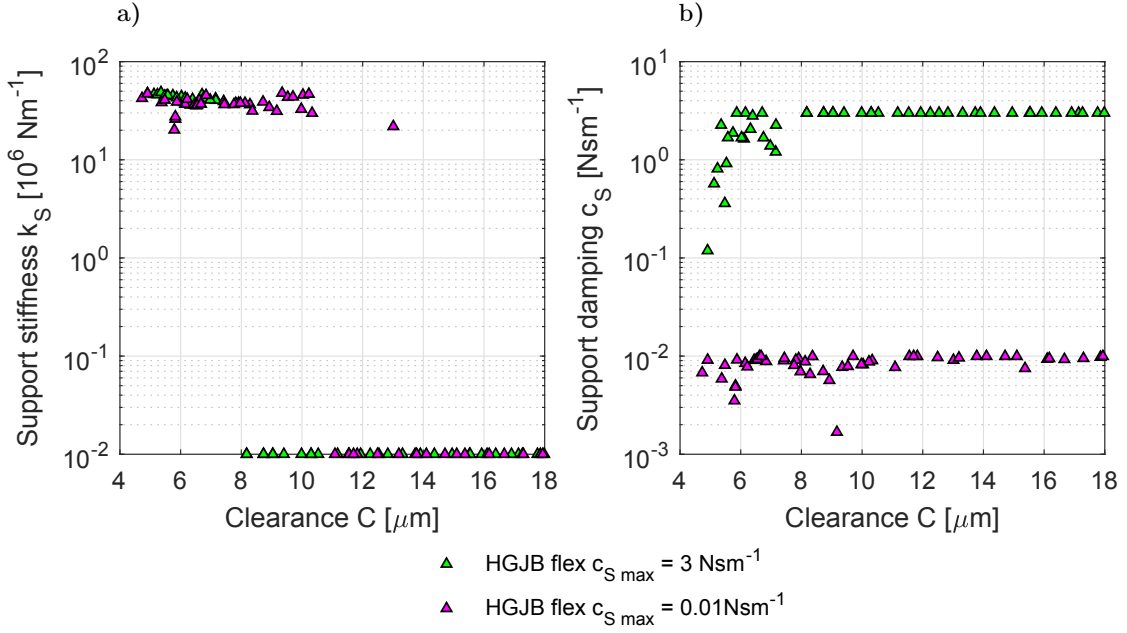


Figure 2.6 – a) Optimum support stiffness k_S against radial clearance C for classical grooves on flexible support; b) Optimum damping coefficient c_S against radial clearance C

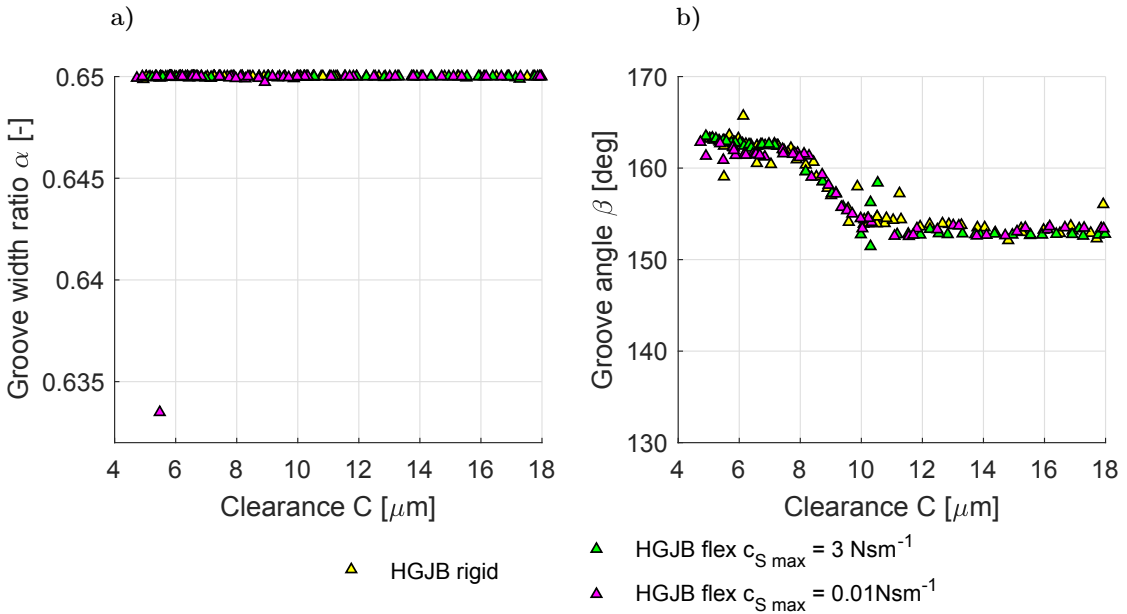


Figure 2.7 – a) Groove width ratio α against radial clearance C for classical grooves on flexible support; b) Groove angle β against radial clearance C

Chapter 2. Potential of flexible bearing bushing support and enhanced groove geometries

Figure 2.7 a) and Fig. 2.7 b) present the evolution of the groove width ratio α and groove angle β for classical grooves along the Pareto curve for a rigid support, a flexible support with damping and a flexible support without damping. The results suggest that the groove width ratio α and groove angle β are mostly independent of the support properties.

The evolution of the groove depth ratio H and the bearing length ratio γ along the Pareto front as a function of the radial clearance C is presented in Fig. 2.8 a) and Fig. 2.8 b) respectively. The groove depth for low support damping converges towards the solution for a rigid support. All solutions converge towards fully grooved bearing designs (no land region), independently of the bushing support properties.

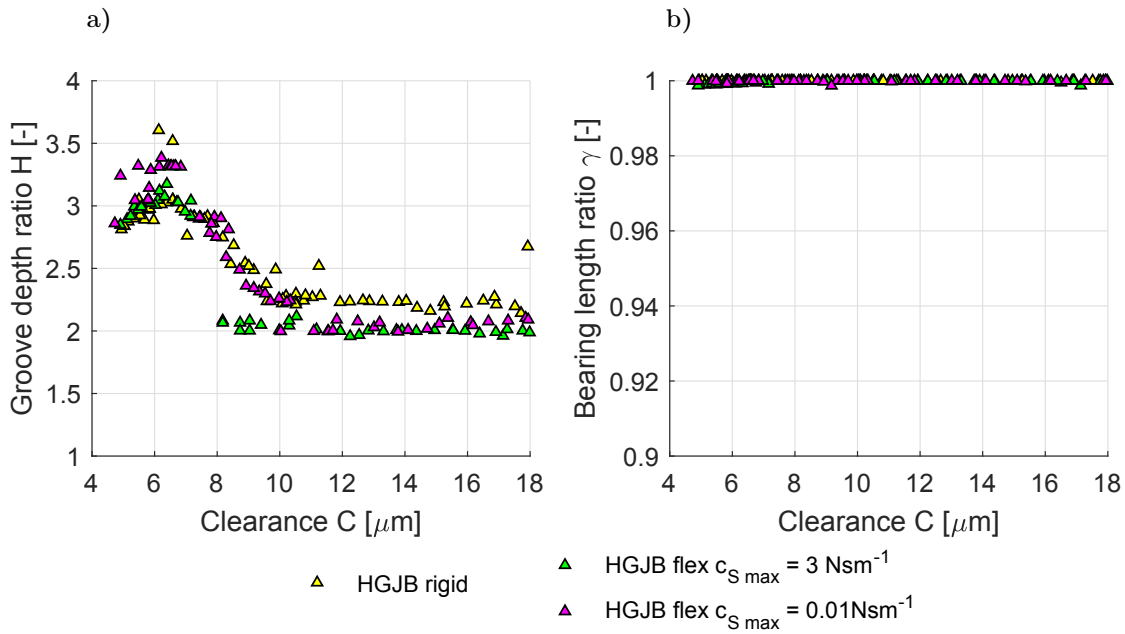


Figure 2.8 – a) Groove depth ratio H against radial clearance C for classical grooves on flexible support; b) Bearing length ratio γ against radial clearance C

2.5.3 Optimization results - Enhanced grooves on rigid support

Figure 2.9 a) presents the evolution of the logarithmic decrement, while Fig 2.9 b) presents the load capacity F_L against nominal radial bearing clearance C of two enhanced groove geometries on rigidly supported bearing bushings and compares the results to a shaft with classical grooves. For the optimizations with enhanced grooves, an additional constraint in terms of a minimum load capacity was added ($F_L \geq 0.15 \text{ N}$). This constraint is introduced due to the fact that deep grooves increase the average bearing clearance, which leads to lower load capacities F_L .

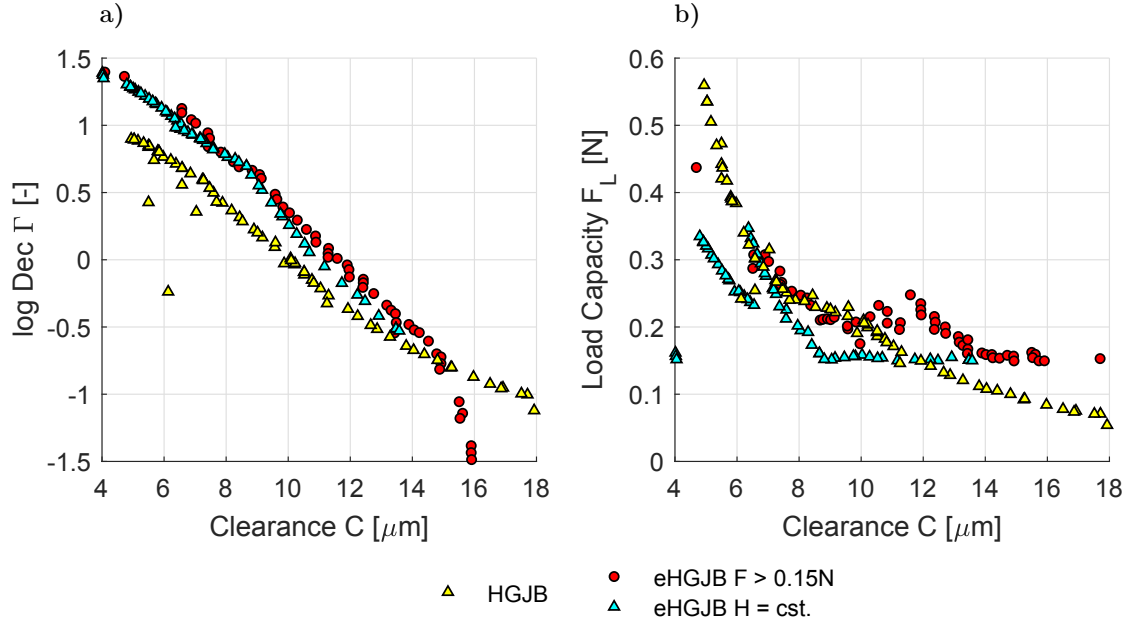


Figure 2.9 – a) Logarithmic decrement Γ for classical grooves (yellow), fully enhanced grooves (red) and enhanced grooves with constant groove depth H (cyan); b) Load capacity F_L versus radial clearance C

The results of the logarithmic decrement Γ presented in Fig. 2.9 a) suggest a possible increase in radial clearance C of 20-50% compared to classical grooves, while maintaining the same rotordynamic stability for this particular rotor geometry. At low clearances, the restriction to a constant groove depth ratio H only has a limited impact on the Pareto curve. For clearances above 9 μm , the variable groove depth has an increasingly positive effect with rising clearance. Figure 2.9 b) presents the results for load capacity F_L , against radial clearance C . Enhanced grooves and classical grooves yield similar load capacities at the same clearance, whereas a slight deficit is suggested by restricting the groove depth H to constant values.

The results in Fig. 2.10 a) present the evolution of groove width ratio α for enhanced groove geometries on a rigid support. In a similar manner as for the classical grooves, the groove width ratio α converges towards the maximum values for both enhanced groove designs. However, when restricting the groove depth H to a constant value, the optimal groove width ratio α sees a restriction around Pos3, in particular for low radial clearances C . The results for the groove angle distribution β are shown in Fig. 2.10 b), which reveal no clear trends.

Chapter 2. Potential of flexible bearing bushing support and enhanced groove geometries

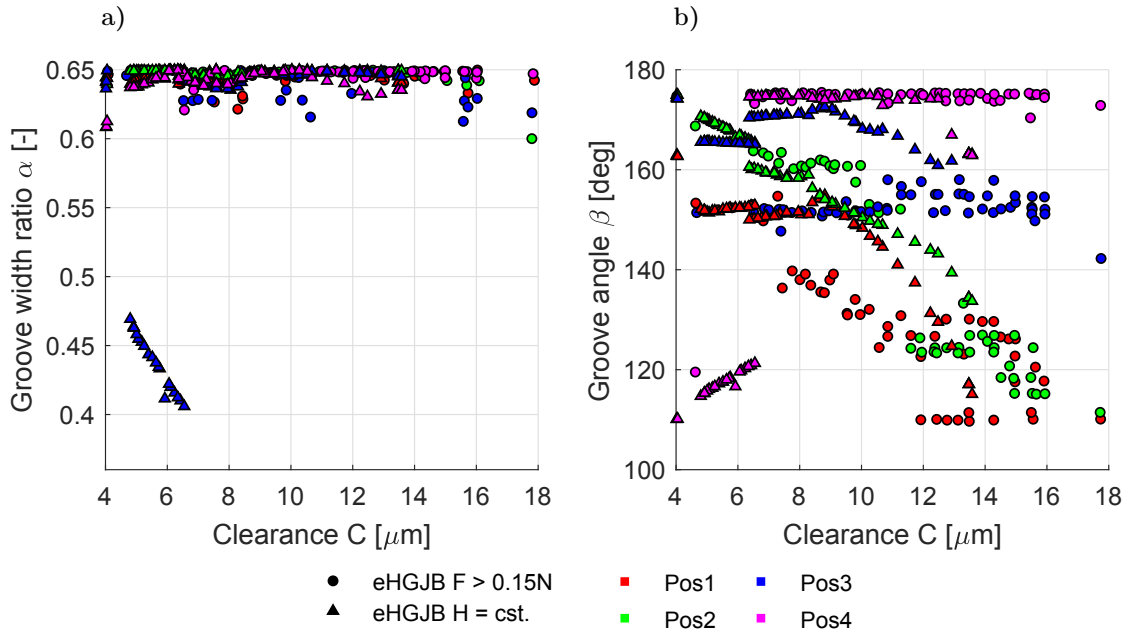


Figure 2.10 – a) Groove width ratio α versus radial clearance C for enhanced grooves with minimal load capacity constraint (dots) and enhanced grooves with constant groove depth ratio H (triangles); b) Groove angle β versus radial clearance C

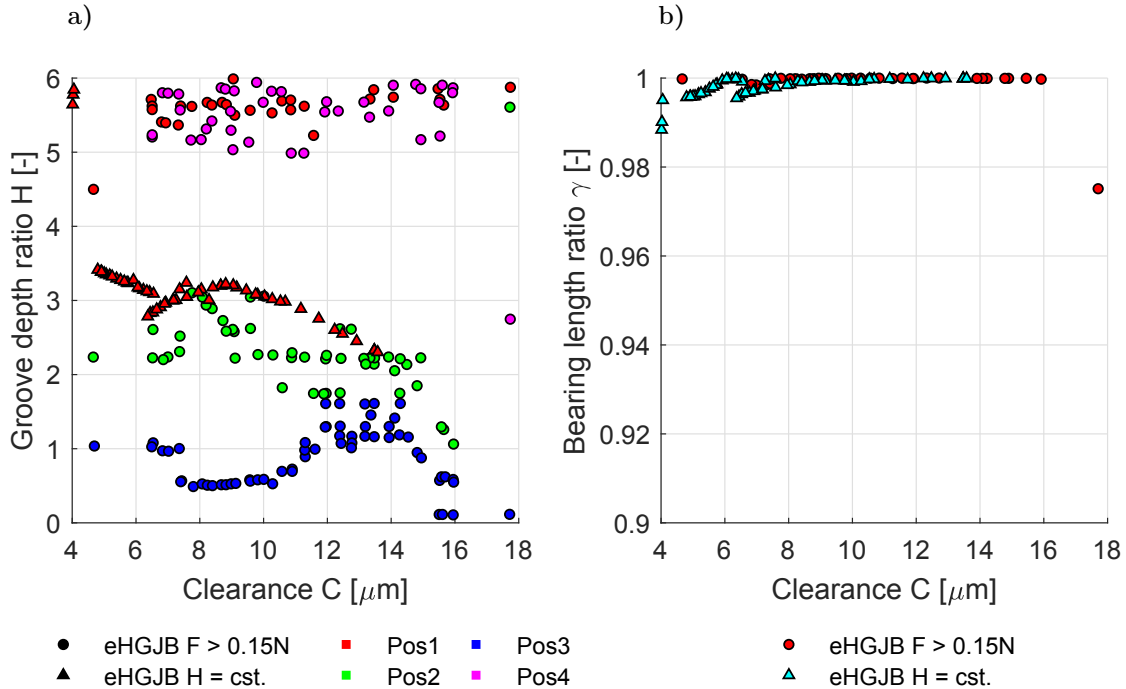


Figure 2.11 – a) Groove depth ratio H versus radial clearance C for enhanced grooves with minimal load capacity constraint (dots) and enhanced grooves with constant groove depth ratio H (triangles); b) Bearing length ratio γ versus radial clearance C

The optimization results for groove depth ratio H , presented in Fig. 2.11 a), suggest that the optimum groove depth evolves from deep grooved in the land and edge regions, towards shallow grooves in between. Note that for enhanced grooves with constant depth, the evolution with clearance follows the same trend as for classical grooves, yet at different values.

It is evident from Fig. 2.11 b) that all solutions converge towards a fully grooved bearing ($\gamma \geq 0.98$).

2.5.4 Optimization results - Enhanced grooves on flexible support

Figure 2.12 a) presents the logarithmic decrement Γ against the nominal bearing clearance C for a flexibly supported rotor featuring an enhanced groove geometry, while Fig. 2.12 b) presents the corresponding load capacity F_L as a function of the radial bearing clearance C . For the case of enhanced grooves, one optimization was again performed constraining the minimum load capacity to $F_L \geq 0.15$ N.

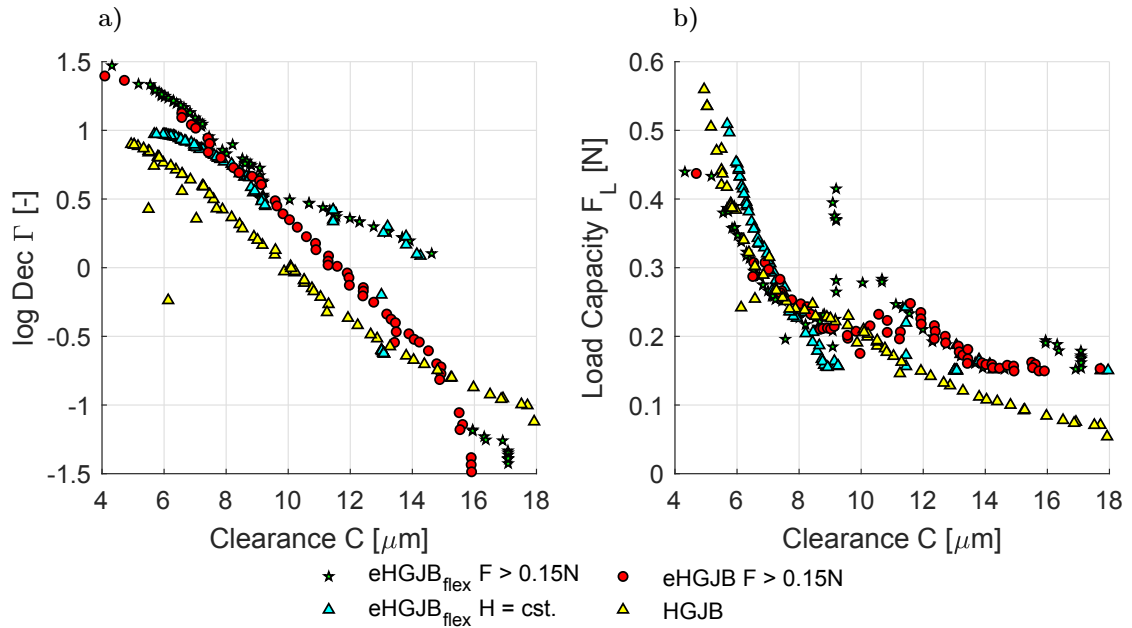


Figure 2.12 – a) Logarithmic decrement Γ versus radial clearance C for classical grooves on rigid support (yellow), enhanced grooves with load capacity constraint on rigid support (red) and enhanced grooves without and with constant groove depth on flexible support (green cyan); b) Load capacity F_L versus radial clearance C

The results for the logarithmic decrement presented in Fig. 2.12 a) suggest a possible increase in bearing clearance of 40-50% compared to a classically grooved rotor on a rigid support. Compared to enhanced grooves on rigid supports, the flexible support allows to increase the clearance significantly, in particular in the region of logarithmic

Chapter 2. Potential of flexible bearing bushing support and enhanced groove geometries

decrements between 0 and 0.5. At large clearances, the restriction to constant groove depth has nearly no impact on the Pareto curve. For clearances below $9\ \mu\text{m}$, the variable groove depth ratio H has an increasingly positive effect with decreasing clearance.

Figure 2.12 b) presents the results for the load capacity F_L evaluated at 20 krpm and 50% eccentricity. The compared cases yield very similar load capacities at low clearances. At large clearances, however, the enhanced grooves are suggested to achieve slightly higher load capacities compared to classical grooves.

The results in Fig. 2.13 a) suggest that for flexibly supported enhanced grooves, the evolution of the groove width ratio α along the axial rotor direction does not converge towards the maximum values, as is the case for classical groove geometries on either flexible and rigid support. Grooves with variable width are preferred, both for constant and variable groove depths. However, when restricting the groove depth, the optimal groove width sees a restriction around Pos3, in particular for low clearances. No clear trends can be observed from the results of the groove angle distribution β shown in Fig. 2.13 b). Note that this is also the case for a rotor with enhanced grooves supported in rigid bearing bushings (Fig. 2.10 b))

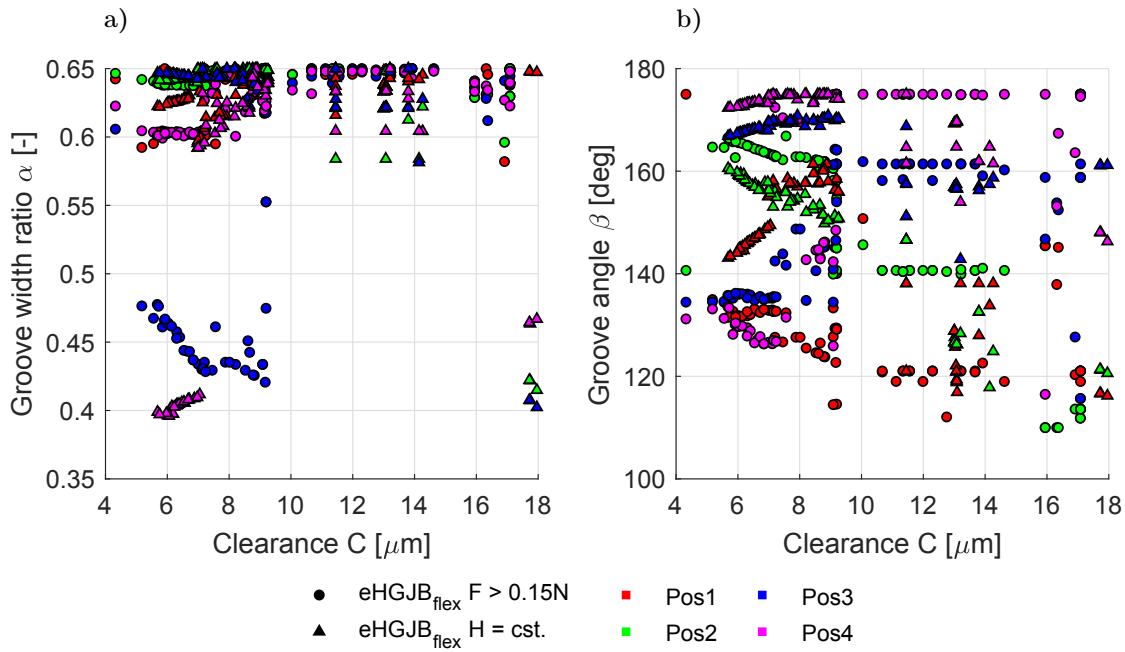


Figure 2.13 – a) Evolution of groove width ratio α versus radial clearance C for enhanced grooves with load capacity constraint on flexible support (dots) and enhanced grooves with constant groove depth on flexible support (triangles); b) Groove angle β versus radial clearance C

The optimization results for groove depth ratio H (Fig. 2.14 a)) suggest that the optimum groove depth evolves from deep grooved in the land and edge regions towards

shallow grooves in-between. Note that for enhanced grooves with constant depth, the evolution with clearance follows the same trend as for classical grooves, yet at different values. The results presented in Fig. 2.14 b) suggest that all solutions converge towards a fully grooved bearing ($\gamma \geq 0.98$), as is also the case for classical grooves on rigid/flexible support as well as for enhanced grooves on a rigid support.

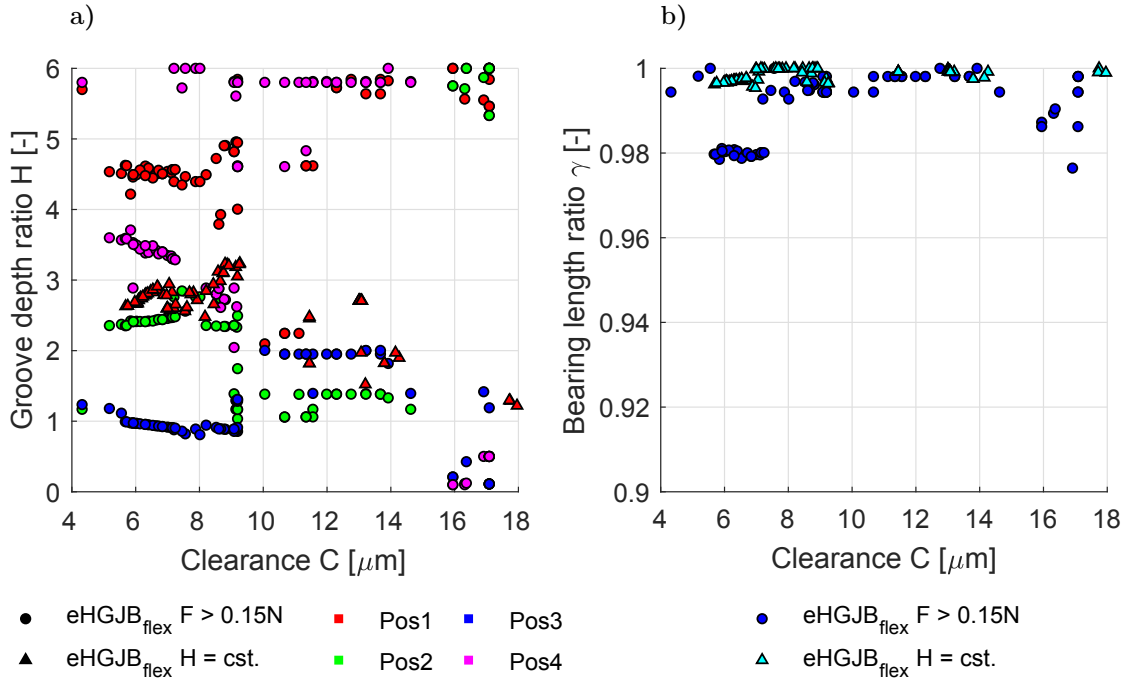


Figure 2.14 – a) Evolution of groove depth ratio H versus radial clearance C for enhanced grooves with load capacity constraint on flexible support (dots) and enhanced grooves with constant groove depth on flexible support (triangles); b) Bearing length ratio γ versus radial clearance C

2.6 Summary and chapter conclusions

This chapter presents the results of a theoretical investigation concerning the potential of flexible bearing bushing support and enhanced groove geometries to increase radial bearing clearance C and/or load capacity F_L , while retaining rotor-dynamic stability. The results obtained in this chapter cover 2-objective optimizations of classical grooves on a rigid and flexible support, as well as 2-objective optimizations of enhanced grooves on rigidly and flexibly mounted bearing bushings. The results obtained in this chapter suggest that supporting the bushing in a flexible manner allows to increase the radial bearing clearance C by more than 50%, while retaining the same rotordynamic stability. Enhanced grooves with constant groove depth H but varying groove angle β and groove width α offer almost the same performance as fully enhanced grooves with varying depth, width and angle. Manufacturing of such a groove type is not more expensive

Chapter 2. Potential of flexible bearing bushing support and enhanced groove geometries

than classical grooves with constant depth, width and angle, therefore offering the best compromise between design simplicity, manufacturing cost and performance. The key findings of this chapter are summarized below:

Classical grooves on flexible support

- An increase in bearing clearance up to 50% is achievable when flexibly supporting a classically grooved shaft.
- In presence of damping, a low support stiffness improves stability for clearances larger than the threshold clearance of $C=7.5 \mu\text{m}$.
- Below the threshold clearance ($C=7.5 \mu\text{m}$), a rigid bearing support offers better performance.
- Flexible bushing support is beneficial in terms of stability only if the damping coefficient of the support is sufficiently high. In absence of support damping, the optimization results tend to favor a rigid bearing support solution.
- A flexible bushing support with no damping yields no stability improvement for clearances lower than $C=10 \mu\text{m}$ and can even be detrimental for the bearing stability.
- Optimum relative groove width ratio α and bearing length ratio γ are unaffected by the support properties.
- Optimum groove angle β and groove depth ratio H are dependent on the support properties.

Enhanced grooves on rigid support

- Enhanced groove geometries improve stability compared to classical groove geometries.
- The bearing clearance (at low values) can be increased by up to 50% compared to classical HGJB while keeping the same rotor-dynamic stability.
- Although the enhanced grooves are deeper on average than the classical ones, the load capacity of enhanced groove bearings are in the same order of magnitude.
- Enhanced groove bearings with constant depth ratio H yield slightly lower stability and load capacity compared to classical grooves.
- Constant groove depth and minimum load capacity limitations yield a significant impact on the optimum groove geometry.

- All solutions tend to converge to a fully grooved bearing design ($\gamma = 1$).

Enhanced grooves on flexible support

- Enhanced groove geometries on flexible support improve stability compared to classical and enhanced groove geometries on a rigid support.
- The 50% gain in bearing clearance can be extended to even higher bearing clearances when supporting a rotor with enhanced groove geometry on a flexible support with damping. The results are very similar to a flexibly supported, classically grooved rotor, yet the enhanced groove geometry yields higher load capacity (+50%) compared to the classically grooved rotor.
- A clear trend in the enhanced groove geometry does not appear. However, the optimum groove depth, as suggested by the results, seems to evolve from deep grooved in the land and edge regions towards shallow grooves in-between.
- Analog to the results for classical grooves on rigid/flexible support and enhanced grooves on flexible support, all solutions tend to converge to a fully grooved bearing design ($\gamma = 1$).

The results suggest that both approaches, internal approaches modifying the gas film itself by means of enhanced groove geometries, as well as external approaches, by means of a flexible damped support, have a large potential to increase the stability threshold of the rotor-bearing-system and therefore allow an increase in bearing clearance. Furthermore, the combination of both approaches yields even more potential.

3 Data-driven model for stiffness and damping of O-Rings

This chapter presents the methodology to obtain stiffness and damping coefficients of the viscoelastic O-Rings currently used in the prototype at LAMD to flexibly support HGJB bushings. Furthermore, the measurement results of various Nitrile-Butadiene-Rubber (NBR) O-Ring sizes are presented and the variables governing stiffness and damping coefficient of the O-Rings are identified. Reduced order models are developed in order to predict the stiffness and damping coefficient as a function of O-Ring geometry, Shore hardness, squeeze and excitation frequency. The results show that the curvature ratio d/D , with D being the diameter and d being the cross-sectional diameter of the O-Ring, needs to be considered in the reduced order models. Assessment of the model suggests a maximum deviation of 30% in predicted stiffness compared to the measurement data. However, taking into account the typical Shore hardness tolerance given by O-Ring manufacturers and other measurement uncertainties, the proposed model enables the prediction of various O-Rings to a good accuracy in the frequency range of 1.5 to 3.75 kHz, which corresponds to typical gas bearing supported rotor applications.

Some of the results presented in this chapter have been published in:

P. Bättig and J. Schiffmann. Data-Driven Model for the Dynamic Characteristics of O-Rings for Gas Bearing Supported Rotors. *Journal of Applied Mechanics*, 86(8):081003, 2019.

3.1 Introduction

Gas lubricated bearings generally require very small clearances to allow stable rotor operation [16]. The consequences are high manufacturing costs, stringent misalignment tolerances and increased specific windage losses. Increased clearances are possible if the loss in rotordynamic performance is compensated by the addition of external damping [27]. External damping requires a flexible bushing support and can be intro-

duced either through squeeze film dampers [37, 38] or by other soft supports [54]. A commonly used procedure to stabilize gas lubricated bearings is to add external damping by supporting the bushings in a flexible manner, by supporting them on O-Rings for example [27, 28, 29, 30, 31, 32]. Figure 3.1 presents the evolution of synchronous motion amplitudes of O-Ring supported bearing bushings obtained from a gas bearing supported rotor accelerating from 20 krpm to 220 krpm, tested in the laboratory at LAMD. The measurements suggest motion amplitudes peaking at 1 μm .

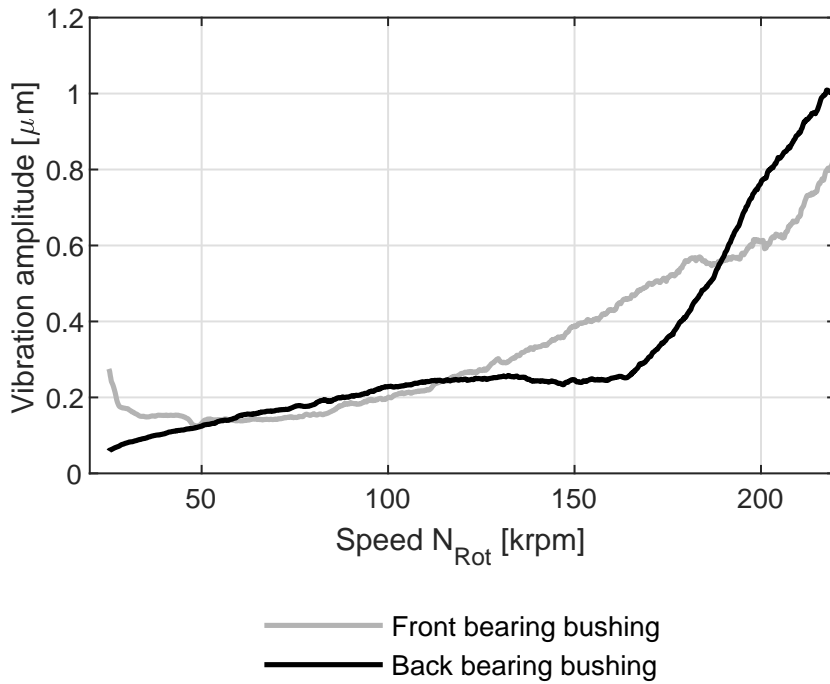


Figure 3.1 – Measurement of O-Ring supported bearing bushing amplitudes

The dynamic behavior of O-Rings is dependent on the pre-load (namely squeeze and stretch), the excitation frequency and amplitude, the O-Ring dimensions, the operating temperature and the manufacturing tolerances [59].

The nomenclature of all relevant O-Ring dimensions is presented in Fig. 3.2 with the definitions of squeeze δ and stretch ε given in Eqn. (3.1) and Eqn. (3.2). It is noted that the tested O-Rings are installed in an axially unconstrained setup.

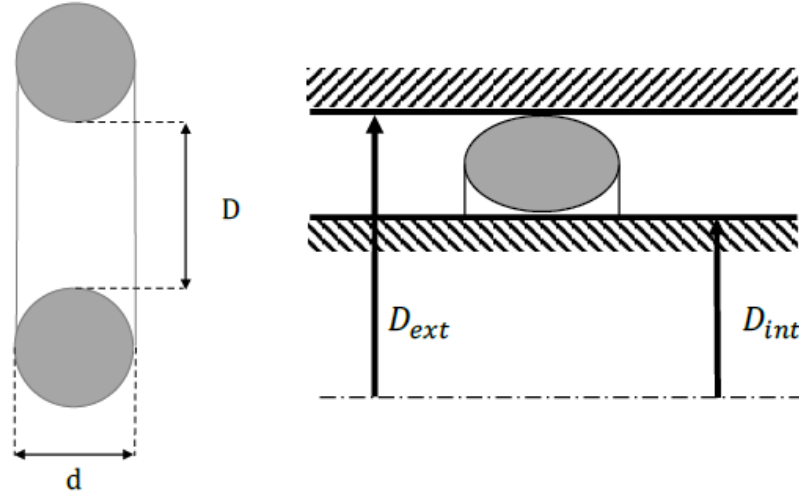


Figure 3.2 – O-Ring nomenclature

$$\text{Squeeze } \delta = \frac{d - \frac{1}{2}(D_{ext} - D_{int})}{d} \quad (3.1)$$

$$\text{Stretch } \varepsilon = \frac{D_{int} - D}{D} \quad (3.2)$$

The dynamic characteristics of O-Rings have been investigated by Smalley et al. [59], Tomioka et al. [31], Green et al. [60] and lately by Al-Bender et al. [61]. Most of these investigations have been performed focusing on the effects of excitation frequency, temperature, O-Ring diameter, cross-sectional diameter and squeeze on the stiffness and damping properties of various O-Ring materials. However, no reduced order model has been developed using the measurement data. Green and English [62] performed a finite element analysis of elastomeric O-Rings in axial and radial compression and present a correlation for a non-dimensional stiffness as a function of the squeeze δ . The influence of O-Ring curvature ratio d/D has been discarded after analyzing its effect by varying d/D . The authors investigated the effect of the curvature ratio d/D by varying the cross-sectional diameter d of the O-Ring, while keeping the O-Ring diameter D constant, which filters out the effect of the O-Ring diameter D on its stiffness.

Al-Bender et al. [61] have performed measurements of Viton and Kalrez O-Rings and provide expressions for the frequency dependence of stiffness and damping for specific O-Ring geometries in a frequency range of 0.1-0.8 kHz. Unfortunately, this range only covers the lower end of typical gas bearing supported rotors, which often rotate at speeds above 2 kHz [28, 63]. Shoyama and Fujimoto [64] measured the stiffness

and damping coefficients of three different NBR O-Ring diameters of constant cross-sectional diameter in the frequency range of 0.4-0.7 kHz and developed a material model that can be used in FEM analysis to predict the dynamic characteristics of NBR O-Rings.

3.2 Motivation and nature of the issue

The O-Rings currently implemented in the prototype at LAMD to flexibly support the bearing bushings have shown favorable stiffness and damping characteristics during testing. Stable operation of the prototype, even though the radial clearance C of rotor and bearing bushings was larger than designed, suggests that the damping coefficient of the O-Rings is higher than assumed. Furthermore, the stiffness of the fitted O-Rings enables stable rotor operation as well as the possibility to measure the motion of the bearing bushings. The latter enables to detect instabilities of the rotor-bearing system as well as balancing of the rotor due to the stiffness of the gas film transmitting the motion of the rotor to the bearing bushings.

In order to design an alternative flexible bearing bushing support, the O-Rings currently implemented in the prototype at LAMD need to be characterized in terms of stiffness and damping and will act as a base-line figure for the dynamic characteristics of the new flexible support.

The current literature very often presents the dependence of stiffness and damping results of O-Rings on variables such as excitation frequency, temperature only in graphical form (see for example [31, 59, 60, 61]), which makes it difficult to establish the governing variables on the stiffness and damping characteristics of the investigated O-Rings. A Design of Experiments (DOE) approach using a full factorial experimental design on the other hand enables to identify the governing variables on stiffness and damping by conducting only a limited amount of experiments [65] and thanks to a normalization of the variables, allows a direct comparison between the governing variables. Knowledge of the governing variables on stiffness and damping of O-Rings significantly simplifies the task of tuning the stiffness and/or damping coefficient of an O-Ring to flexibly support a bearing bushing for the engineer in charge of designing such a system.

The level of stiffness and damping of the flexible bearing bushing support determines the rotordynamic stability and/or the potential gain in bearing clearance. A reduced order model to predict the dynamic characteristics of O-Rings is therefore of great importance to assess and predict the rotordynamic performance of the rotor-bearing system.

A simple parametric model that is not depending on FEM analysis and that is able to predict the dynamic stiffness and damping characteristics of O-Rings as a function of their geometry, squeeze, frequency and Shore hardness is still missing in the current literature.

The effect of d/D on the dimensionless stiffness was discarded by Green and English [62] after varying d/D but keeping D constant. As previously mentioned, this approach does not reflect a real variation of d/D . To illustrate this, a random example of the dimensionless stiffness \underline{k} as a function of d and D is presented in Fig. 3.3. As suggested by Fig. 3.3, varying d/D while keeping the O-Ring diameter D constant corresponds to investigating only a slice of the surface but does not capture the real dependency of d/D .

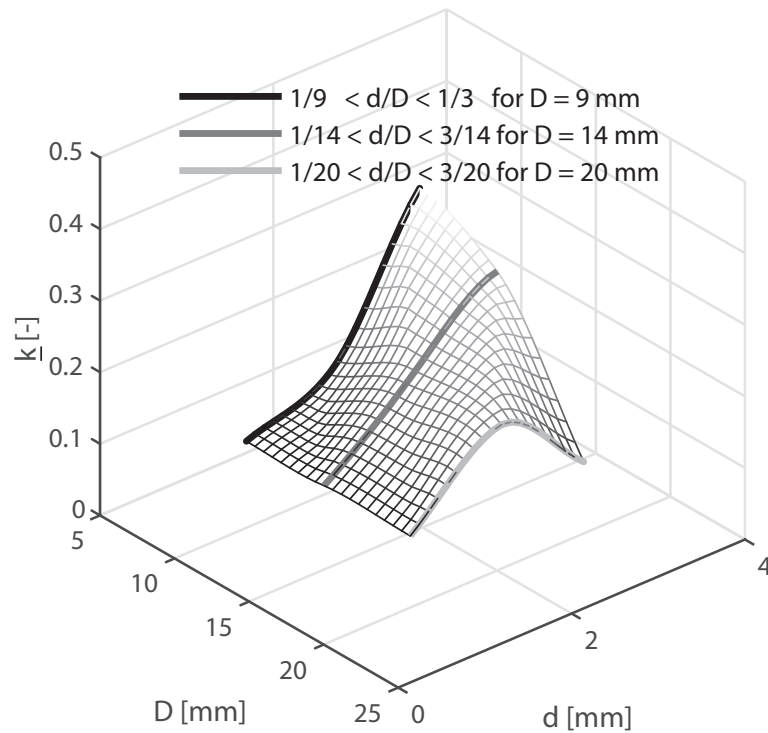


Figure 3.3 – Example of dimensionless stiffness \underline{k} as a function of d and D to illustrate the importance of varying d and D simultaneously for capturing the real dependency of d/D

The effect of d/D therefore requires to be further investigated and considered to be taken into account in a reduced-order model for stiffness and damping of O-Rings.

3.3 Goals and objectives

The objectives of this chapter are summarized as follows:

1. Design and manufacturing of a test rig enabling the identification of stiffness and damping of O-Rings and other flexible structures used to support HGJB bushings.
2. Measurement campaign 1 - Identification of the dynamic characteristics of the O-Rings currently implemented in the LAMD prototype, which will act as a baseline for the new flexible bushing support and are required to validate the bearing tools at LAMD.
3. Measurement campaign 2 - Identification of the governing variables on stiffness and damping of O-Rings.
4. Development of a data-driven model for stiffness and damping of O-Rings from the results obtained in measurement campaign 2.
5. Assessment of the restrictions of the developed O-Ring model.

3.4 Methodology

3.4.1 Experimental setup

In order to characterize the dynamic properties of O-rings, two test sections have been designed, referred to as *ORI1* and *ORI2*. Both test rigs make use of the same measurement procedure, which is based on the Base Excitation - Resonant Mass Method (BERM) [59], where a mass is supported by flexible elements, which are held in a housing. The housing is mounted on a base plate which is excited by an electromagnetic shaker. Displacement measurements taken on the housing and the suspended mass enable the evaluation of stiffness and damping coefficient of the O-Rings. *ORI1* is the test section designed to measure the dynamic characteristics of the O-Rings with the same dimensions and installation specifications as fitted to the existing prototype at LAMD, whereas *ORI2* was designed to measure O-Rings of various dimensions and squeeze δ levels in order to develop reduced-order models for stiffness and damping of O-Rings. Schematic diagrams of the *ORI1* and *ORI2* test sections are presented in Fig. 3.4 a) and Fig. 3.4 b) respectively.

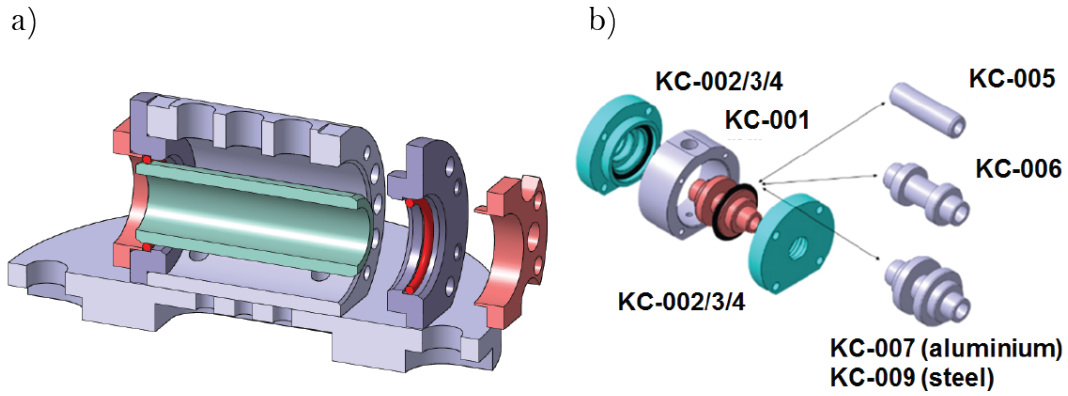


Figure 3.4 – a) Cut view of ORI1 test section; b) ORI2 test section

The test section of *ORI1*, as pictured in Fig. 3.4 a), is designed to replicate the installation specifications in terms of O-Ring diameter D , cross-sectional diameter d , squeeze δ and stretch ε of the silicone O-Rings previously fitted to flexibly support the HGJB bushings of the LAMD prototype. The O-Ring geometry and installation specifications for this first measurement campaign are summarized in Tab. 3.1. The first measurement campaign additionally included to investigate the effect of amplitude A_{O-Ring} on the stiffness and damping characteristics of the tested silicone O-Rings. The obtained results suggested the O-Ring amplitude A_{O-Ring} to have a negligible effect on the stiffness and damping in the investigated range of $1/2/3 \mu\text{m}$, which is a typical range of motion amplitude of well balanced rotors supported on O-Rings, as has been shown in Fig. 3.1, hence the amplitude A_{O-Ring} was held constant for measurement campaign 2.

The test section of *ORI2* is shown in Fig. 3.4 b) and enables to investigate O-Rings of various diameters D , cross-sectional diameters d and squeeze levels δ , by exchanging the supported mass (see KC-005/6/7/9 in Fig. 3.4 b)) and the covers (see KC-002/3/4 in Fig. 3.4 b)) on each side of the housing. The O-Ring material for the second measurement campaign, aiming at the investigation of the variables that govern the stiffness and damping of O-Rings and the development of a reduced-order model for stiffness and damping, is Nitrile-Butadiene-Rubber (NBR). The measurements have been performed with NBR O-Rings of Shore A hardness 70 and 90. The investigated O-Ring dimensions and squeeze δ levels for measurement campaign 2 are also summarized in Tab. 3.1. According to Smalley et al. [59], the stretch ε does not have a significant effect on stiffness and damping, hence it was held constant during all experiments. Note that the tested O-Rings are installed in an axially unconstrained setup during all experiments. The vibration amplitude A_{ORing} across the O-Rings was monitored during the tests and adjusted to $0.5 \mu\text{m}$ over the whole frequency range for measurement campaign 2, which corresponds to typical operation of well balanced gas bearing supported high-speed rotors.

Chapter 3. Data-driven model for stiffness and damping of O-Rings

Table 3.1 – Investigated O-Ring materials, dimensions and installation specifications in measurement campaign 1&2

	Campaign 1	Campaign 2
O-Ring material	Silicone HITEC VMQ 80.5	NBR
Shore A hardness	70	70/90
Diameter D	14 mm	9/14/20 mm
Cross-sect. diam. d	1.5 mm	1/2/3 mm
Squeeze δ	6.67%	5/10/20%
Stretch ε	1.43%	1.43%
Amplitude A_{O-Ring}	1/2/3 μm	0.5 μm

A more detailed schematic diagram of the modular experimental setup, which is based on the BERM method, is presented in Fig. 3.5, featuring the test section *ORI2*, as well as the displacement probes used to capture the motion of the supported mass and the housing, in order to evaluate the stiffness and damping of the O-Rings.

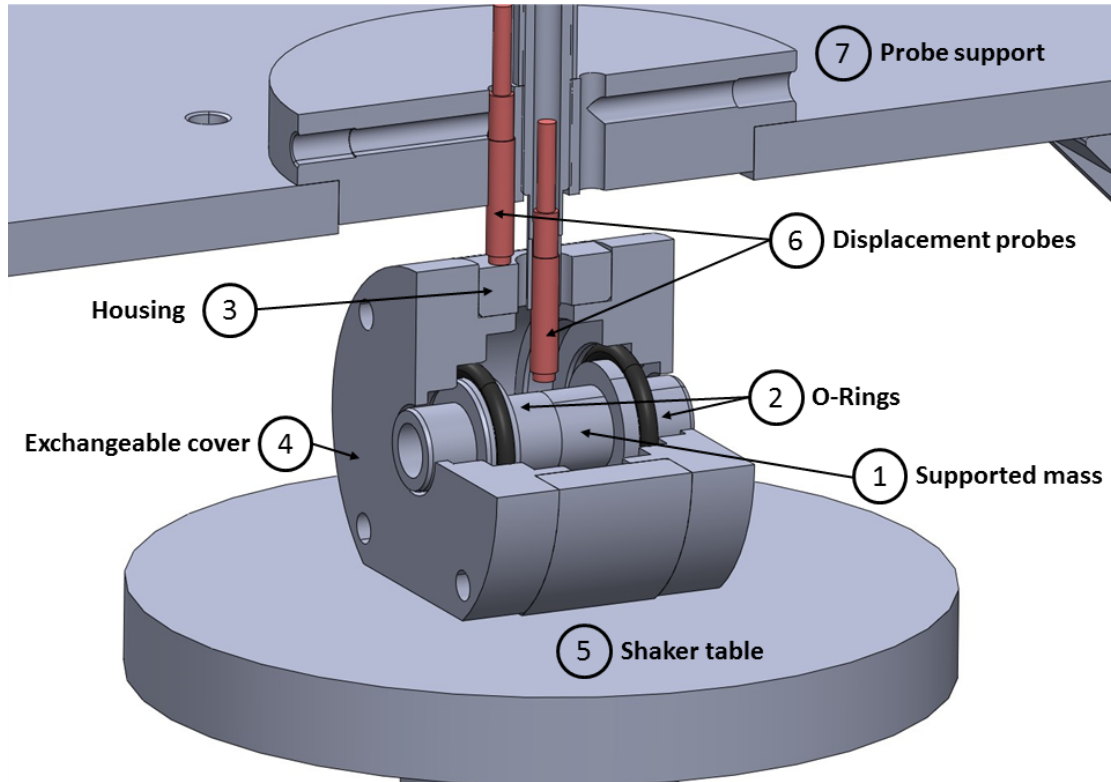


Figure 3.5 – *ORI2* test section with displacement probes on shaker table

In this test method, a non-rotating mass (1) is supported on a pair of O-Rings (2), which are held in place in a housing (3) by means of exchangeable covers (4). The housing is mounted on an electromagnetic shaker (5). The mass and O-Rings therefore form a 2-DOF damped resonant system which is excited by the vertical motion of the shaker. Measurement of the displacement of both the housing and the supported mass using capacitance displacement probes (6) enables the determination of stiffness and damping coefficients.

Exchangeable covers (element (4) in Fig. 3.5) were used to vary the O-Ring squeeze δ (5, 10 and 20%), while the stretch was held constant at $\varepsilon = 1.43\%$. The desired vibration frequency and amplitude is set using a waveform generator whose signals are fed to the shaker via an analog amplifier. The sensor signals of the capacitance displacement probes are amplified by means of a signal amplifier and then processed using LabVIEW. Table 3.2 summarizes the list of instruments used to perform the experiments.

Table 3.2 – List of instrumentation for O-Ring test rig

Device	Model
Displacement probes	Lion precision C3S
Signal amplifier	Lion Precision CPL290
DAQ system	NI PXIe-1078/6356
Electrodynamic Shaker	Labworks INC. ET-139
Analog amplifier	Labworks INC. PA-138-1
Waveform generator	Agilent 33500B-Series

3.4.2 Experimental procedure

The experimental setup presented in Fig. 3.5 consists of a mass supported on two flexible elements which represents a 2-DOF system with a translational and a tilting vibration mode. Measurements using two proximity probes at each end of the supported mass were performed to ensure that the motion of the shaft is purely translational, hence the system can be treated as a 1-DOF system in the investigated frequency range. The response of a 1-DOF system shows a natural frequency, which depends predominantly on the stiffness of the flexible elements and the supported mass. As described by Smalley et al. [59], accurate measurement data for stiffness and damping is restricted to the frequency range, where the phase angle difference between housing and supported mass is in the range of 15-165 deg. Taking this criteria into account, the natural frequency of the spring-mass oscillator has to be tuned such that it is located within the frequency range of interest. The supported mass (element (1) in Fig. 3.5) has been designed to tune the resonance frequency within 1500-4000 Hz, which is the typical range of the synchronous frequency for gas lubricated bearings.

The vibration amplitude across the O-Rings A_{O-Ring} was monitored over the whole frequency range during the tests and adjusted to the required level by evaluating Eqn. (3.3), which is valid for two sinusoidal signals of different amplitude but of identical frequency.

$$A_{O-Ring} = 2\sqrt{A_1^2 + A_2^2 - 2A_1A_2\cos(\Delta\varphi)} \quad (3.3)$$

where A_{O-Ring} is the amplitude across the O-Ring, A_1 is the measured amplitude of the housing, A_2 is the amplitude of the supported mass and $\Delta\varphi$ is the phase angle difference between housing and supported mass.

The calculation of stiffness and damping for a 1-DOF model has been performed using Eqn. (3.4) and Eqn. (3.5), as presented by Gupta et al. [66]:

$$\frac{k_1}{m\omega^2} = \frac{\alpha(\alpha - \cos(\Delta\varphi))}{1 + \alpha(\alpha - 2\cos(\Delta\varphi))} \quad (3.4)$$

and

$$\frac{c}{m\omega} = \frac{\alpha\sin(\Delta\varphi)}{1 + \alpha(\alpha - 2\cos(\Delta\varphi))} \quad (3.5)$$

where k_1 is the stiffness and c is the damping coefficient of the tested O-Ring pair, m the supported mass, ω the angular excitation frequency and α the amplitude ratio of supported mass and housing A_2/A_1 .

Measurements were performed in the frequency range of 1.5 to 3.75 kHz for every combination of O-Ring geometry, support and material configuration, as presented in Tab. 3.1.

3.5 Results and discussion

3.5.1 Measurement campaign 1 - Silicone O-Rings

Base-line values for stiffness and damping of the new flexible bearing bushing support are obtained by measurements performed on the silicone O-Rings currently used in the prototype with a diameter D of 14 mm, a cross-sectional diameter d of 1.5 mm, stretch δ of 1.43% and squeeze level ε of 6.67%, as presented in Tab. 3.1 for three different amplitude levels A_{O-Ring} of 1/2/3 μm . Fig. 3.6 presents the measurement results for radial stiffness k_1 and damping coefficient c of a single silicone O-Ring, obtained by applying the BERM method and using the experimental setup *ORII*, as shown in Fig. 3.4 a).

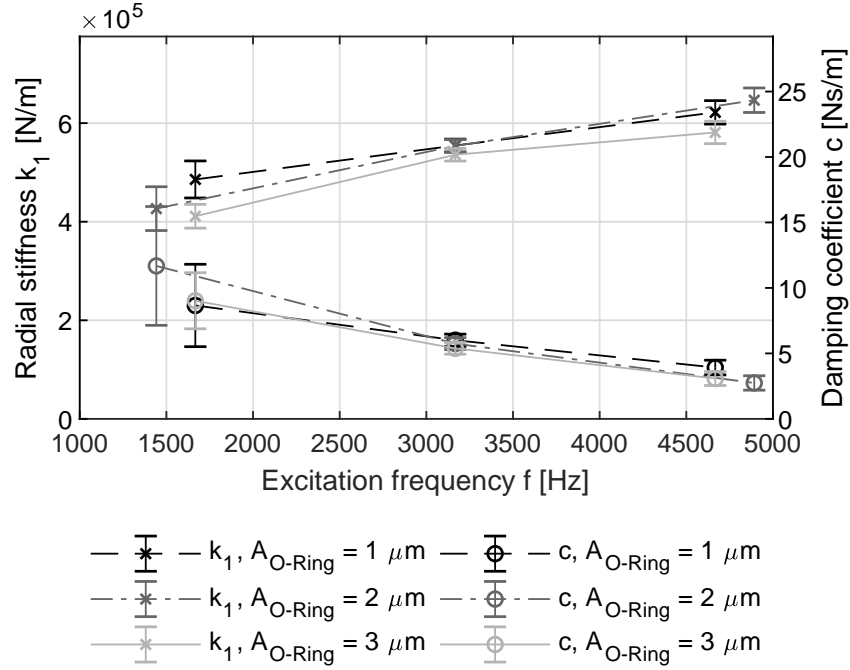


Figure 3.6 – Results of stiffness and damping measurements of a single silicone O-Ring using the measurement setup presented in Fig. 3.4 a)

The results suggest that the stiffness of the investigated O-Rings increases with frequency, while the damping coefficient decreases with increasing frequency. This corroborates results obtained by Smalley et al. [59], Tomioka et al. [31] and by Green et al. [60]. Furthermore, the measurement results suggest that the amplitude across the O-Rings A_{O-Ring} does not have a significant effect on the stiffness and damping of the investigated silicone O-Rings. In general, the results show a slight decrease in stiffness and damping with increasing vibration amplitude, which can be related to the Payne effect [67, 68, 69], describing a decrease in the storage modulus E' and the loss modulus E'' with increasing amplitude [70]. However, due to its negligible effect and the fact that no clear trends can be deduced from the data, it was decided for the vibration amplitude to be held constant at $A_{O-Ring} = 0.5 \mu\text{m}$ for measurement campaign 2. According to Smalley et al. [59], the stretch ε does not have a significant effect on stiffness and damping either, hence the stretch ε was also held constant for measurement campaign 2.

In the investigated frequency range of 1500-4500 Hz, the average radial stiffness for a single O-Ring is 5.5×10^5 N/m, while the average damping coefficient is 6.16 Ns/m. Since each bearing bushing is supported on a pair of O-Rings, this leads to a base-line figure of $k_1 = 1.1 \times 10^6$ N/m and $c = 12.32$ Ns/m for the stiffness and damping coefficient of each bearing bushing supported on silicone O-Rings.

3.5.2 Measurement campaign 2 - Pre-assessment of effects with a Design of Experiments (DOE) approach

In order to obtain initial insights with regards to the variables governing the stiffness and damping of O-Rings, the main relative effects have been determined using a full factorial design that allows to fit a linear model with interactions [65].

The dynamic factors investigated in this study are the Shore A hardness, O-Ring diameter D , cross-sectional diameter d , squeeze δ and excitation frequency f . These five factors were varied according to Tab. 3.3 and the response in terms of stiffness and damping analyzed, which results in a total of $N = 2^5 = 32$ measurement points for the full-factorial experimental design.

Table 3.3 – Measurement points for full factorial design

Factor	-	+
Squeeze δ	5%	10%
Shore A hardness	70	90
Diameter D	9 mm	14 mm
Cross-sect. diam. d	1 mm	2 mm
Frequency f	2500 Hz	3000 Hz

The frequency corner points for the full factorial design of NBR O-Rings were selected to be 2500 Hz and 3000 Hz whereas the squeeze δ was varied between 5% and 10%, the Shore A hardness from 70 to 90, inner diameter D from 9 mm to 14 mm and the cross-sectional diameter d from 1 mm to 2 mm. The 32x5 model matrix X is built according to Hunter et al. [65] with the variables from Tab. 3.3 normalized from "-1" to "+1" as follows:

$$\bar{X} = -1 + 2 \frac{X - X_{min}}{X_{max} - X_{min}} \quad (3.6)$$

This normalization enables the comparison of variables that have different metrics and orders of magnitude. The stiffness and damping coefficients can be expressed using a linear model as presented in Eqn. (3.7) with $a_{k_1 d}$, $a_{k_1 D}$, $a_{k_1 Sh_A}$, $a_{k_1 \delta}$ and $a_{k_1 f}$ being the main effects to be investigated, here in the example of the stiffness k_1 .

$$k_1 = a_{k_1 d} \cdot d + a_{k_1 D} \cdot D + a_{k_1 Sh_A} \cdot Sh_A + a_{k_1 \delta} \cdot \delta + a_{k_1 f} \cdot f \quad (3.7)$$

Equation (3.7) represents a linear system of equations $Y = A \cdot X$, where A represents the matrix containing the main effects on stiffness $a_{k_1 i}$ or damping a_{c_i} , Y is the response vector with the measurement results of stiffness/damping coefficients and X being the previously discussed model matrix. The main effect matrix A , containing the main

effects on stiffness $a_{k_1 i}$ and damping a_{ci} , is then determined as follows:

$$A = \frac{1}{N} X^T Y \quad (3.8)$$

where N is the number of performed experiments. The Pareto chart of the main effects, normalized by the average measured stiffness k_1 and damping coefficient c of all $N = 32$ experiments, is presented in Fig. 3.7. The plot allows to identify the dominant effects on stiffness and damping.

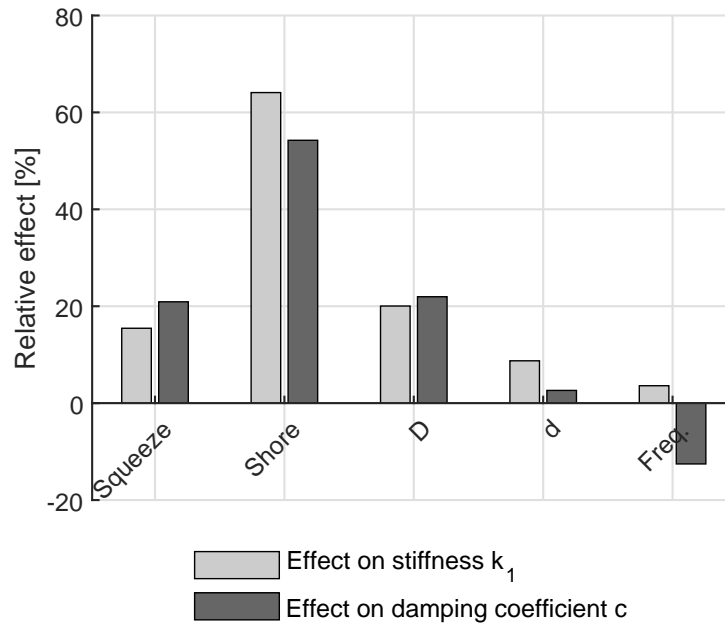


Figure 3.7 – Pareto chart of relative effects on stiffness and damping for the tested NBR O-Rings

The Shore hardness is suggested to be the factor with the largest effect on both stiffness and damping. The second most influential effect is the O-Ring diameter D , followed by the squeeze δ . The factors with the lowest effect on stiffness and damping are the cross-sectional diameter d , followed by the excitation frequency f . Note that the only factor that has a reducing effect on damping is the excitation frequency f , while all other factors cause an increase in both stiffness and damping. Since all factors show non-negligible effects on the dynamic characteristics of the tested O-Rings, it was decided to include all of them in the extended experimental campaign 2, in order to obtain a meaningful reduced-order model for predicting the dynamic O-Ring properties.

3.5.3 Measurement campaign 2 - Results of extended measurement campaign

Selected stiffness measurement results are presented in a log-log scale as a function of the excitation frequency in Fig. 3.8.

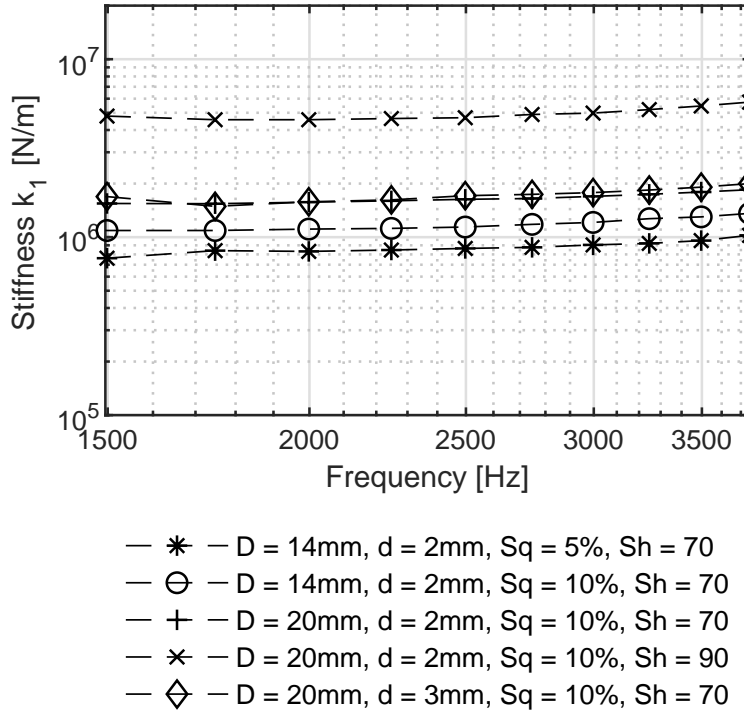


Figure 3.8 – Evolution of the measured stiffness k_1 as a function of excitation frequency for selected Shore 70 and 90 NBR O-Rings

The results suggest that the stiffness of Shore 90 O-Rings is approximately three times higher than the stiffness of the Shore 70 O-Rings within the tested frequency range. In addition, the stiffness of the investigated O-Rings seems to increase linearly with frequency in a log-log scale. This corroborates the results obtained by Smalley et al. [59], Tomioka et al. [31] and Green et al. [60]. Furthermore, the slope with which stiffness increases seems to be independent of the O-Ring diameter D , squeeze δ or the cross-sectional diameter d , which suggests that the frequency dependency is governed primarily by the material properties and is largely independent of the O-Ring geometry. General observation leads to the conclusion that the stiffness increases with increasing squeeze δ and increasing O-Ring diameter D , while the cross-sectional diameter d has little effect on the stiffness and shows no clear trends. This effect has also been noticed

by Green [60]. The complete set of stiffness measurement results is summarized in appendix A (Fig. A.1 - A.6).

Selected damping results are presented in Fig. 3.9.

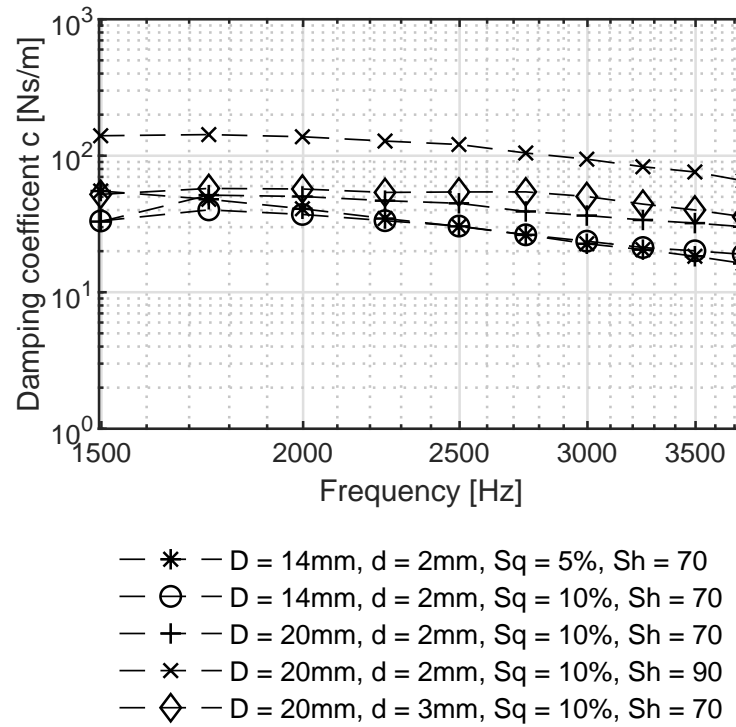


Figure 3.9 – Evolution of the measured damping coefficient c as a function of excitation frequency for selected Shore 70 and 90 NBR O-Rings

The average damping coefficient for the 70 Shore O-Ring is 50 Ns/m and 100 Ns/m for the Shore 90 O-Ring respectively. The results suggest a linear decrease in damping with frequency in a log-log scale for both Shore hardnesses, which is in agreement with the previous findings from the full factorial DOE analysis. The decline in damping coefficient with increasing frequency has also been observed by Tomioka et al. [31], while the measurements of Green and Etsion [60] show an increase in damping coefficient with frequency for Buna-N, but a decrease for Viton 75 O-Rings. The complete set of damping measurement results is attached in appendix A (Fig. A.7 - A.12).

3.5.4 Development of reduced-order models

Stiffness model

For the characterization of viscoelastic materials a complex modulus E^* is defined. The real part corresponds to the storage modulus E' and the imaginary one to the loss modulus E'' :

$$E^* = E' + iE'' \quad (3.9)$$

As suggested by Kareaga [70], the storage modulus E' is strongly dependent on excitation frequency, temperature, vibration amplitude and other factors, which leads to the conclusion that these effects can be contained in an isolated model for the storage modulus E' . The objective is to obtain a dimensionless reduced-order model for predicting the stiffness and damping properties of O-Rings as a function of their geometry and operating conditions, based on the experimental data. In order to condense the large amount of measured data and to enable the prediction of the dynamic characteristics for different O-Rings, a dimensionless group analysis was performed. The analysis is based on the Buckingham-Pi theorem [71], which enables the identification of the following dimensionless groups π_i :

$$\pi_0 = \frac{k_1}{E'D} \quad (3.10)$$

$$\pi_1 = \frac{d}{D} \quad (3.11)$$

$$\pi_2 = \frac{D_{int}}{D} \quad (3.12)$$

$$\pi_3 = \frac{D_{ext}}{D} \quad (3.13)$$

These dimensionless groups π_i can be reorganized into the following form:

$$\pi_0 = f(\pi_1, \pi_2, \pi_3) \quad (3.14)$$

Combining π_1 , π_2 and π_3 allows the expression of the squeeze δ and the stretch ε as shown in Eqn. (3.15) and Eqn. (3.16).

$$1 - \frac{1}{2} \frac{\pi_3 - \pi_2}{\pi_1} = \delta \quad (3.15)$$

$$\pi_2 - 1 = \varepsilon \quad (3.16)$$

π_1 represents the O-Ring curvature ratio d/D . Since the stretch ε was held constant in all experiments, the following relationship is obtained for the dimensionless stiffness \underline{k} , where g is an unknown function.

$$\underline{k} = \frac{k_1}{E'D} = g\left(\frac{d}{D}, \delta\right) \quad (3.17)$$

In order to evaluate \underline{k} based on the measured stiffness k_1 , knowledge of the storage modulus E' is necessary. Since both temperature and excitation amplitude have been kept constant throughout the experimental campaign, the storage modulus E' can be expressed by a frequency dependent component and by a second one, which is governed primarily by the Shore A hardness of the material.

Various models exist for the relationship between static storage modulus E'_0 (at $\omega = 0$) and Shore A hardness, such as proposed by Qi [72], Gent [73], Boussinesq [74] and Kunz and Studer [75]. However, the model that offers the best match to the values of static storage modulus E'_0 provided by the O-Ring manufacturer is Boussinesq's, as represented in Eqn. (3.18)

$$E'_0 = \frac{1 - \mu^2}{2RC_3} \cdot \frac{C_1 + C_2Sh_A}{100 - Sh_A} \quad (3.18)$$

where μ represents the Poisson ratio and the constants $R = 0.395$ mm, $C_1 = 0.549$ N, $C_2 = 0.07516$ N and $C_3 = 0.025$ mm are used as presented by Kunz and Studer [75]. The frequency dependence for storage modulus E' has been obtained by averaging the slopes of all stiffness measurements for Shore 70 and 90 hardness. As a consequence, the combination of Boussinesq's theory for the static storage modulus E'_0 with the frequency dependence obtained from the experimental data allows to express the frequency dependent storage modulus E' as follows:

$$\log(E') = a \cdot \log(f) + \log(E'_0) \quad (3.19)$$

where the coefficient a is the slope of the stiffness curves when plotted against the excitation frequency f in a log-log scale. The coefficient a was found to be $a = 0.259$ for Shore 70 and $a = 0.263$ for Shore 90 respectively. Figure 3.10 shows the resulting evolution of the storage modulus E' according Eqn. (3.19) for Shore 70 and Shore 90. The dashed lines represent the standard deviation of the averaged slope of all measured stiffness curves for Shore 70 and Shore 90 respectively.

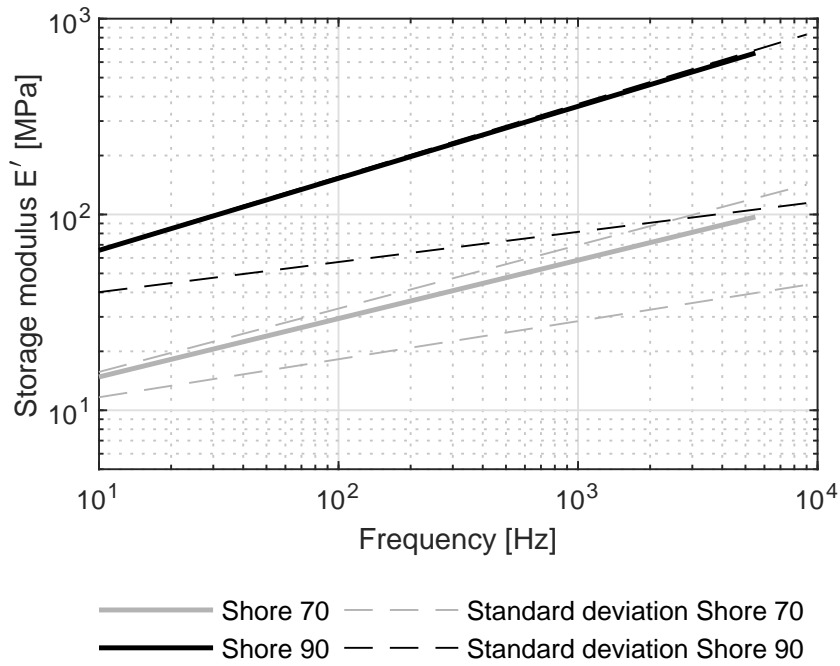


Figure 3.10 – Identified storage modulus E' as a function of frequency and Shore hardness

Evaluating Eqn. (4.12), using the frequency dependent model of E' (see Eqn. (3.19)), returns the dimensionless stiffness \underline{k} , which is frequency independent and therefore a purely geometrical function based on the dimensionless O-Ring curvature ratio d/D and the squeeze δ . As suggested by Fig. 3.11 for Shore 70 and by Fig. 3.12 for Shore 90 all the non-dimensional experimental data collapses onto a single surface. A model as in Eqn. (3.20), which is similar to the one used by Green [60], but including a linear term to account for the effect of the curvature ratio d/D , has been fitted separately to the data for Shore 70 and 90:

$$\underline{k} = a_0 + a_1 \delta^{a_2} + a_3 \left(\frac{d}{D} \right) \quad (3.20)$$

The resulting coefficients for Shore 70 and Shore 90 NBR O-Rings to be used with Eqn. (3.20) are detailed in Tab. 3.4, as well as the coefficient of determination R^2 for both fits.

Table 3.4 – Coefficients and R^2 for dimensionless stiffness model of Shore 70 and Shore 90 NBR O-Rings

	Shore 70	Shore 90
a_0	0.9198	0.09614
a_1	0.0624	0.07656
a_2	1.123	1.033
a_3	-1.328	3.98
R^2	0.9143	0.8604

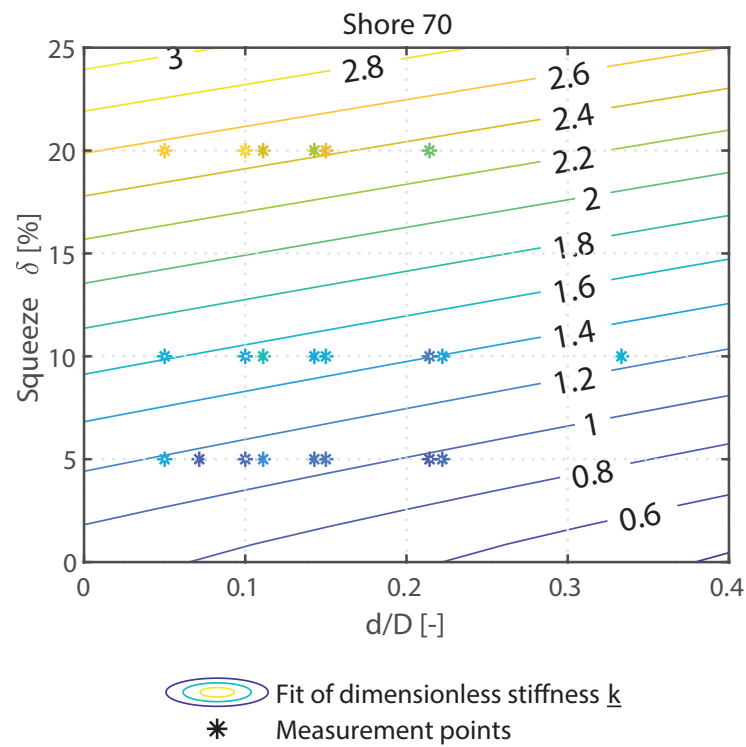


Figure 3.11 – Dimensionless stiffness \underline{k} as a function of d/D and squeeze δ for Shore 70

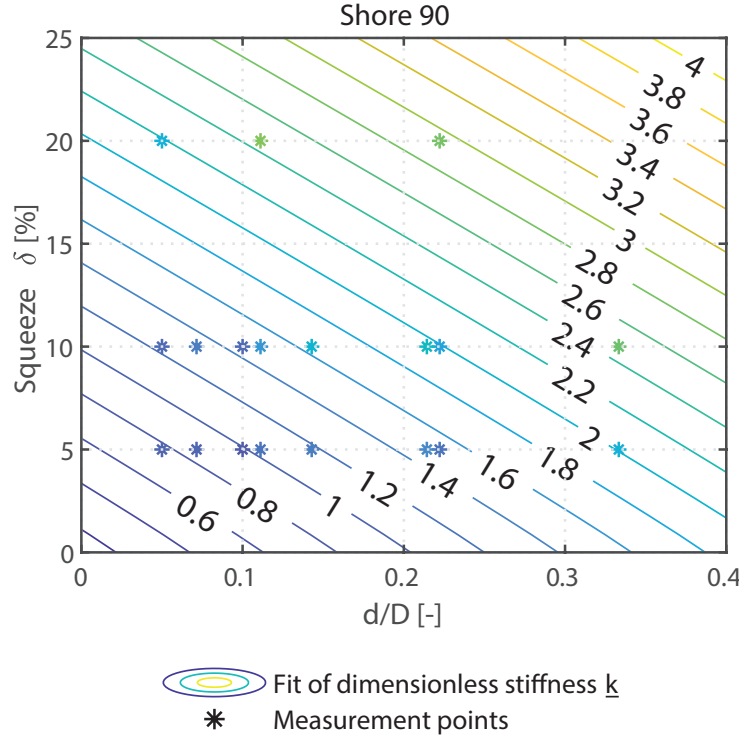


Figure 3.12 – Dimensionless stiffness \underline{k} as a function of d/D and squeeze δ for Shore 90

The dimensionless stiffness \underline{k} for Shore 70 is less dependent on the curvature ratio d/D than for Shore 90 O-Rings (see Fig. 3.12). In addition, the comparison between the two Shore A data sets suggests an inversion of trend with regards to the effect of the curvature ratio d/D on the dimensionless stiffness \underline{k} . Note that Green et al. [62] suggested that the curvature ratio d/D can be neglected. They investigated the effect of the curvature ratio d/D by varying the cross-sectional diameter d while keeping the O-Ring diameter D constant, which filters out the effect of the O-Ring diameter D on its stiffness and does not capture the real dependency of d/D , as presented in this thesis.

Damping model

The loss factor η , commonly used to measure mechanical damping, is defined as the ratio of damping energy to strain energy [76].

$$\eta = \frac{k_2}{k_1} \quad (3.21)$$

where k_1 and k_2 form the complex stiffness k^* [77] of an elastomer element in the form of a mechanical impedance:

$$k^* = k_1 + ik_2 = k_1(1 + i\eta) \quad (3.22)$$

The relationship between k_2 and the viscous damping coefficient c is defined as follows:

$$k_2 = c\omega \quad (3.23)$$

where ω is the excitation frequency. Inserting Eqn. (3.23) into Eqn. (3.21) leads to a relationship between the loss factor η , k_1 and the viscous damping coefficient c , as follows:

$$\eta = \frac{c\omega}{k_1} \quad (3.24)$$

Evaluating the loss factor η for each O-Ring as defined in Eqn. (3.24) and averaging for Shore 70 and Shore 90 separately along the frequency f leads to the two curves for NBR O-Rings presented in Fig. 3.13, including the respective standard deviations for both Shore hardnesses separately. Averaging for a given Shore hardness is permitted due to the fact that the loss factor η is indicative of the visco-elastic characteristics of the measured material and is commonly used as a measure of the damping in a visco-elastic system according to the ISO 6721-1:2011 standard [78]. The results suggest that the loss factor η can therefore be assumed to be identical for all tested O-Rings of the same Shore hardness. The averaged loss factor η has been fitted by a 2nd order polynomial for both Shore hardnesses:

$$\eta = a_0 + a_1f + a_2f^2 \quad (3.25)$$

with f being the excitation frequency. The averaged loss factor η for Shore 70 and Shore 90 NBR O-Rings including standard deviations and 2nd order polynomial fit are presented in Fig. 3.13 with the coefficients summarized in Tab. 3.5.

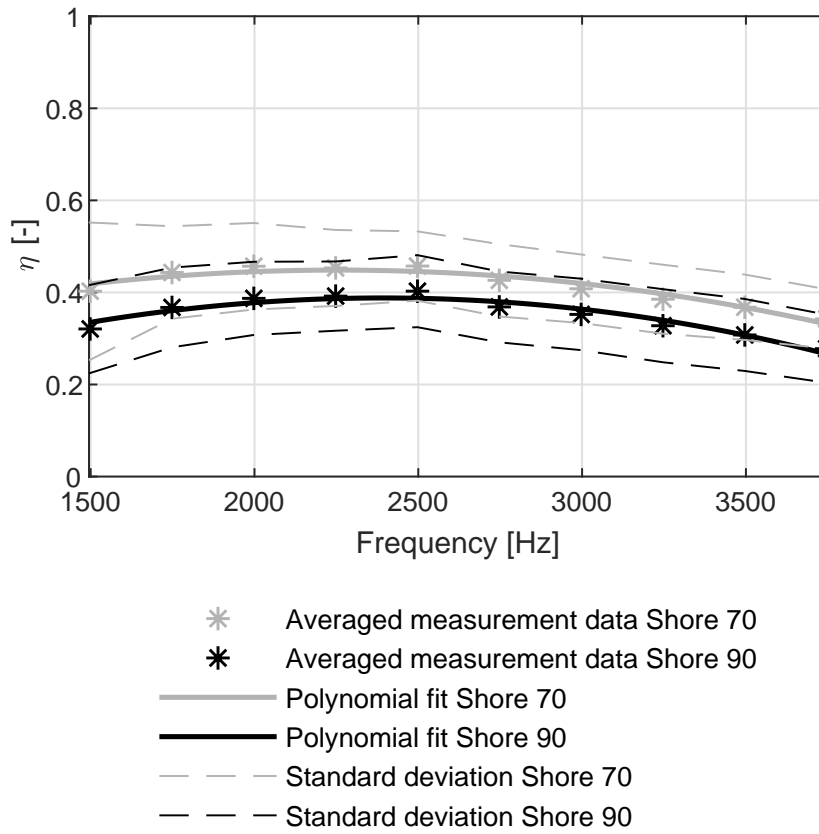


Figure 3.13 – Averaged loss factor η for Shore 70 and Shore 90 NBR O-Rings including standard deviations and 2nd order polynomial fit for Shore 70 and Shore 90 NBR O-Rings

Table 3.5 – Coefficients and R^2 for 2nd order polynomial fit of loss factor η for Shore 70 and Shore 90 NBR O-Rings

	Shore 70	Shore 90
a_0	0.1811	0.008309
a_1	2.372e-04	3.174e-04
a_2	-5.261e-08	-6.632e-08
R^2	0.924	0.923

Knowledge of the dimensionless stiffness \underline{k} and loss coefficient η therefore allows to predict the damping coefficient c using Eqn. (3.24) as follows:

$$c = \frac{\eta k_1}{\omega} = \frac{\eta \underline{k} D E'}{\omega} \quad (3.26)$$

3.6 Reduced-order model performance and limitations

Figure 3.14 a) and Fig. 3.14 b) compare the measured and the predicted stiffness k_1 and damping coefficient c using the models developed in this chapter. The dashed lines represent an error band of $\pm 30\%$.

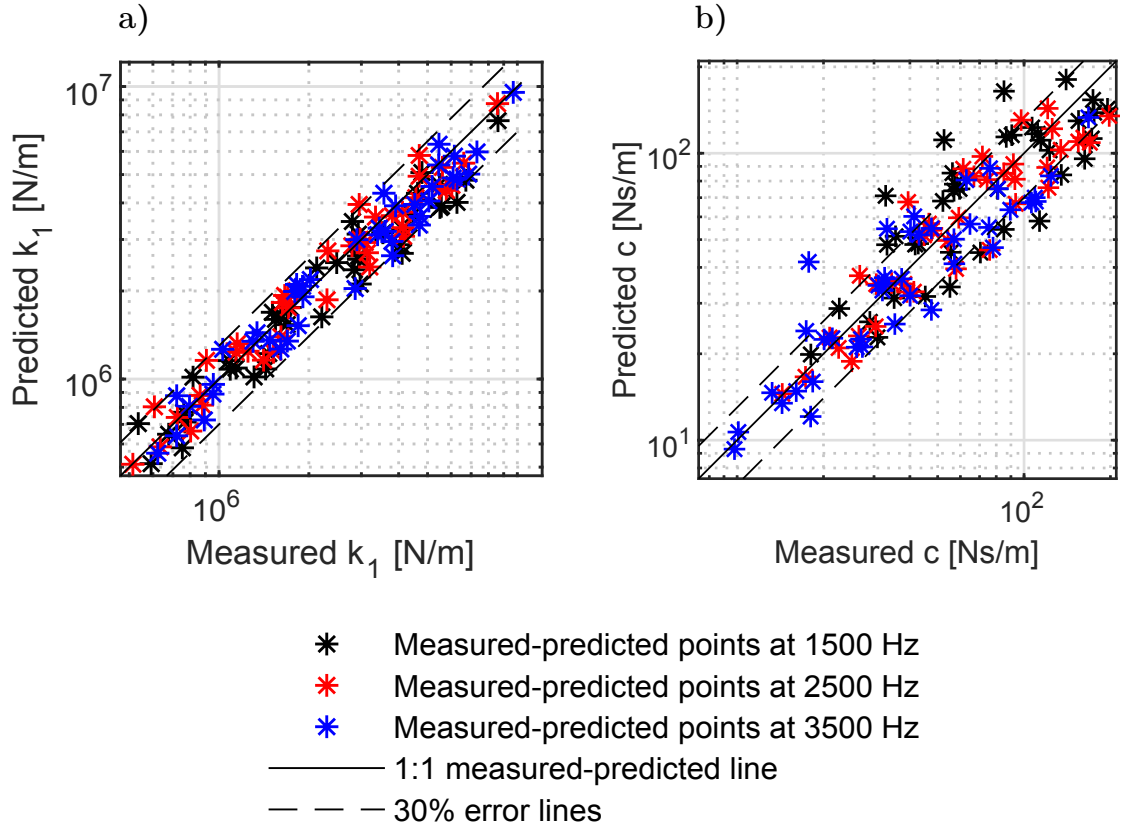


Figure 3.14 – Comparison of model prediction and measurement: a) Stiffness k_1 ; b) Damping coefficient c

Figure 3.14 a) suggests that the error between predicted and measured stiffness is less than 30% for almost the complete data set. Only 5% of the predicted values yield errors above 30%. The prediction of the damping coefficient yields larger errors as suggested by Fig. 3.14 b), with 33% of the predicted values exhibiting an error above 30%. The differences between measurement and prediction originate from various contributions, as listed below:

Measurement errors. The expected effect from measurement errors of phase angle, housing and supported mass amplitudes, excitation frequency as well as the weight of the supported mass on the calculated stiffness k_1 and damping coefficient c when evaluating Eqn. (3.4) and Eqn. (3.5) were estimated using the approach of Gaussian error propagation and sum up to a maximum of $\pm 8.1\%$.

Model of storage modulus E' . The error from the proposed frequency dependent storage modulus E' model (see Fig. 3.10) has been analyzed by evaluating the standard deviation of the identified E' slopes that were derived from the frequency dependent stiffness measurements.

Dimensionless stiffness model. The uncertainty introduced by the reduced order model for the dimensionless stiffness \underline{k} as a function of curvature ratio d/D and squeeze δ has been assessed by analyzing the fitted surface in Fig. 3.11 and Fig. 3.12. The residuals represent the differences between the measured data and the fitted surface and are plotted in Fig. 3.15.

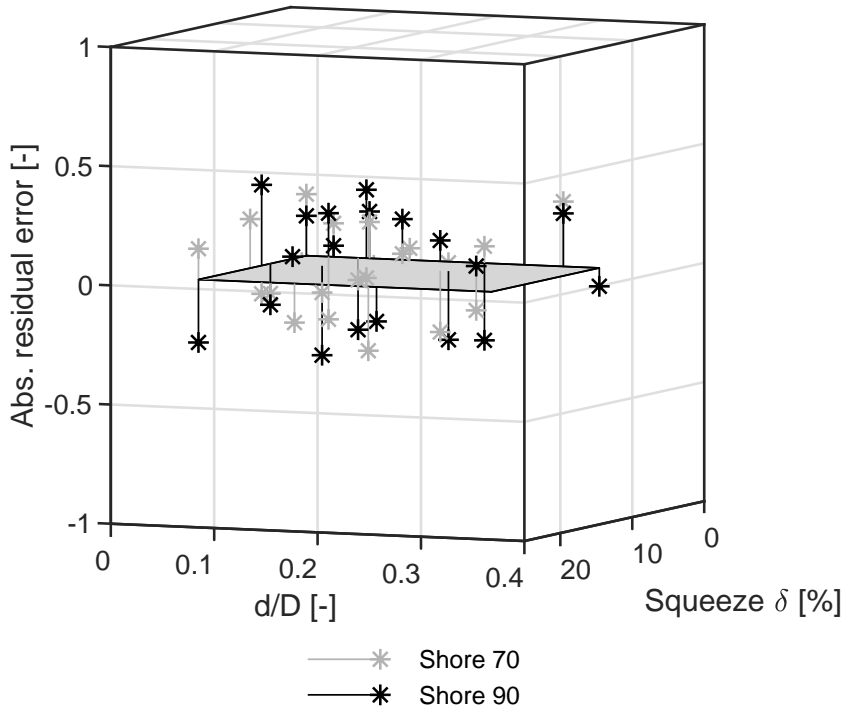


Figure 3.15 – Residual error of fitted surface of dimensionless stiffness vs d/D and squeeze δ

The largest relative residual is -34.8%, which corresponds to the measured 90 Shore O-Ring of $D = 20$ mm, $d = 2$ mm ($d/D = 0.1$) and a squeeze δ of 10%. The measurement results suggest a dimensionless stiffness $\underline{k}=0.9801$ while the model according to Eqn. (3.20) suggests $\underline{k}=1.3202$.

Shore hardness tolerance. The tolerance for Shore A hardness indicated by the manufacturer for the O-Ring measurements performed in this chapter is ± 5 Shore A, which is typical for mass-produced O-Rings. As previously presented in Eqn. (3.18), the static storage modulus E'_0 is a function of the Shore hardness and strongly affects the measured dynamic characteristics (see Eqn. (3.18)). In order to visualize the effect of

3.6. Reduced-order model performance and limitations

Shore hardness deviation on the static storage modulus E'_0 , Boussinesq's relation (refer to Eqn. (3.18)) is represented in Fig. 3.16. The gray areas represent the typical hardness tolerance of ± 5 Shore A as given by the O-Ring manufacturer.

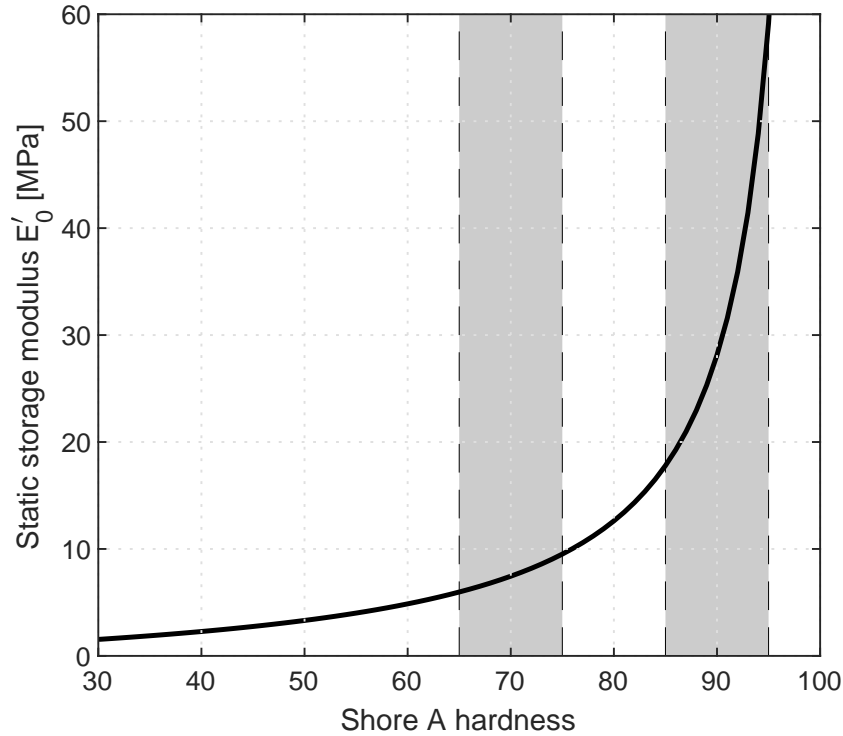


Figure 3.16 – Plot of static storage modulus E'_0 as a function of Shore hardness according to Eqn. (3.18) and Shore hardness tolerance band as given by O-Ring manufacturer

For a Shore 70 material the deviation of ± 5 Shore A yields a variation of +28% and -20%, whereas for a Shore 90 material, the variations are +110% and -37% in static storage modulus E'_0 respectively.

Handling inconsistencies. In agreement with the findings of Green and English [62], the experiments showed that sliding the mass into the O-Rings may introduce some uncertainty to the measurements due to twisted or nonplanarly fitted O-Rings. Measurements of O-Rings featuring a small cross-sectional diameter d suffer the most from this uncertainty since they are prone to twist during assembly.

Geometrical tolerances. Geometrical deviations of the O-Ring size compared to its specification as well as manufacturing tolerances of the test section parts can lead to further measurement errors.

In order to assess the impact of the different error components, Fig. 3.17 presents the measured stiffness evolution of the O-Ring with the highest residual error as discussed before (Shore 90, $D = 20$ mm, $d = 2$ mm, $\delta = 10\%$) and compares it to the prediction

from the model developed in this chapter. The dashed lines represent the expected measurement uncertainty, while the dash-dotted lines include both measurement and Shore 90 hardness uncertainty.

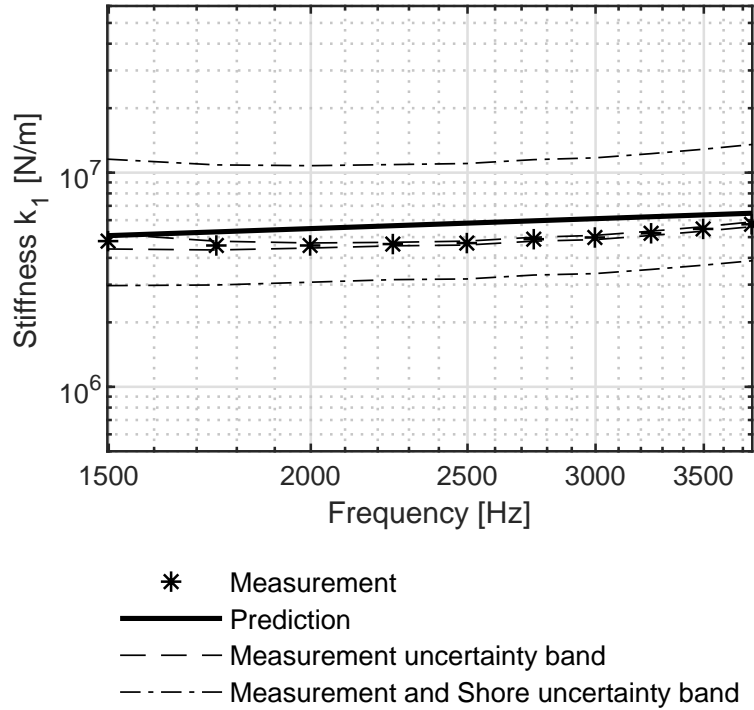


Figure 3.17 – Measured O-Ring stiffness compared to predicted stiffness for Shore 90, $D = 20$ mm, $d = 2$ mm, $\delta = 10\%$. Dashed lines represent measurement uncertainty while dash-dotted lines include measurement and Shore hardness uncertainty.

As suggested by the dashed lines in Fig. 3.17 the estimated measurement uncertainty increases when moving away from the resonance frequency (≈ 2500 Hz) of the 1-DOF system. This corroborates the recommendation by Smalley et al. [59], that accurate measurement data should be obtained in a frequency range where the phase angle difference between housing and supported mass falls within the range of 15-165 deg. Furthermore, Fig. 3.17 suggests that the proposed model overestimates the stiffness of the worst case O-Ring by 35%. However, compared to the uncertainty caused by the typical hardness tolerance of ± 5 Shore A given by the O-Ring manufacturer, which can lead to a variation in stiffness of up to 110% in the case of Shore 90 O-Rings, puts the relatively high errors of the proposed model into perspective.

3.7 Summary and chapter conclusions

In this chapter, a test procedure is described to determine the dynamic properties, namely stiffness and damping coefficient, of elastomeric O-Rings in cyclic radial compression. The effects of O-Ring diameter D , cross-sectional diameter d , squeeze δ , Shore A hardness and excitation frequency f have been investigated experimentally and identified as the main governing effects on the dynamic characteristics using a full factorial experimental design. Measurements of a wide range of O-Ring geometries and assembly combinations enabled the determination of a novel reduced order model for O-Ring stiffness and damping based on actual measurements.

The following conclusions have been drawn from the results obtained in this chapter:

- A stiffness of $k_1=1.1\text{e}+06$ N/m and a damping coefficient of $c=12.32$ Ns/m has been determined for the silicone O-Rings that are currently used to flexibly support the bearing bushings in the LAMD prototype. These measurements act as a base-line for the new flexible bearing bushing support to be developed.
- Contrary to the presented model by Green and English [62], it was found that the O-Ring cross-sectional diameter d does have an effect on the stiffness and damping coefficients of the O-Rings investigated in this thesis. It was found that the curvature ratio d/D does affect the stiffness and damping of Shore 70 and Shore 90 O-Rings in a different way. At a constant squeeze, increasing d/D yields a reduction in stiffness for a Shore 70 O-Ring whereas it increases stiffness for a Shore 90 O-Ring. Additional measurements with O-Rings of an intermediate Shore hardness would be needed to investigate the transition from Shore 70 to Shore 90 in more detail.
- Considering the hardness uncertainty of ± 5 Shore A given by the O-Ring manufacturer, the proposed models show a good agreement with the measurement results.
- The reduced-order O-Ring model presented in this chapter distinguishes between geometrical effects and effects that have an impact on the storage modulus E' and loss coefficient η , namely excitation frequency and Shore hardness as investigated in this thesis. This approach allows the extension of the presented model to accommodate additional effects such as temperature and excitation amplitude by including them in the models for the storage modulus E' and the loss factor η . Furthermore, the modular approach of the presented model allows its modification and use for various other applications, such as tuned mass dampers or centering springs in squeeze film dampers.

4 Flexible support for Herringbone-Grooved Journal Bearings

A parametric model has been developed with the aim to design a flexible membrane bushing support that offers tunable tilting and radial stiffness and can be coupled to various concepts to provide suitable damping levels to support a gas lubricated bearing bushing. Three damping concepts have been investigated that offer independent tuning of the support damping coefficient and can be coupled to the novel modular flexible bearing bushing support.

The new flexible membrane support was manufactured and its stiffness in radial and tilting direction measured before it was successfully implemented into a prototype by applying an alignment method that ensures alignment of the bushings relative to each other, to the machine housing, as well as to the thrust bearing surface.

Test results obtained from the new prototype with membrane support show a significant improvement in bushing alignment quality compared to O-Rings, as well as stable operation up to the design rotor speed of 250 krpm. Furthermore, an unstable bearing bushing tilting mode was observed and its governing variables in terms of bearing bushing transverse moment of inertia and support tilting stiffness identified. The effectiveness of one of the proposed damping concepts was successfully demonstrated by its ability to increase the onset speed of instability of the observed unstable bush tilting mode.

The results of coast-down tests and start-stop testing suggest the novel flexible bearing bushing support to offer better alignment, significantly improved repeatability and reduced wear of rotor and bushings compared to the previously used O-Rings to flexibly support the bearing bushings.

The presented flexible bearing bushing support is cheap and easy to manufacture, provides tunable characteristics and is suggested to have unlimited lifetime, which makes it an easy to implement solution to introduce flexible and tunable support for fluid film bearings.

Some of the results presented in this chapter have been published in:

P. Bättig and J. Schiffmann. Flexible Support for Gas Lubricated Bearing Bushings. *Tribology Transactions*, 2019. (under review)

4.1 Introduction

As suggested by the results obtained in chapter 2, the radial clearance of a Herringbone-Grooved Journal Bearing (HGJB) supported rotor can be increased by up to 80%, while retaining the same rotordynamic performance, if the bearing bushings are supported in a flexible manner. These findings corroborate recent publications by Belforte et al. [27], Waumans et al. [28, 29] and Tomioka and Miyanaga [30, 31, 32], who propose the use of rubber O-Rings to flexibly support the bearing bushings.

Belforte et al. [27] investigate the unbalance response and rotordynamic stability of an ungrooved rotor rotating in an externally pressurized rigid bearing sleeve that is flexibly supported on O-Rings. Three different O-Ring materials (NBR, Viton and Silicone) are investigated that provide different stiffness and damping characteristics for the flexible support. The different stiffness and damping characteristics of the O-Rings are investigated by the authors by reducing the pressure of the external air supply until instability occurs. As suggested by the results obtained by Belforte et al. [27], the minimum supply pressure needed for stable rotor operation depends on the O-Ring material used to support the bearing bushings, more specifically on the stiffness and damping of the O-Rings.

Waumans et al. [28, 29] have achieved a DN value of 7.2 million by flexibly supporting a wave-shaped bearing bushing on O-Rings, which at the same time act as seals for a squeeze-film damper. Stiffness is provided by the O-Rings, while external damping is provided by both, the O-Rings and the squeeze-film damper, whose oil viscosity can be varied to tune the level of damping. The experimental results suggest the maximum obtainable speed before instability onset to be dependent on the chosen O-Ring stiffness and external damping. Furthermore, the authors concluded that the bearing bushing support stiffness has to be lower (<50%) than the gas film stiffness in order for the rotor-bearing system to operate in a stable manner.

Tomioka and Miyanaga [30, 31, 32, 79] provide theoretical and experimental results for a smooth rotor running in a grooved, rigid bearing sleeve, which is flexibly supported on O-Rings. Experimental results are provided for the speed of instability onset as a function of the O-Ring squeeze δ , which was varied from 22% to 30%. The results suggest an increase in maximum obtainable speed with increasing O-Ring squeeze δ . This corroborates results obtained by Shoyama et al. [64], Yan et al. [80], Green and Etsion [60], as well as Bättig and Schiffmann [81]. All show that an increase in O-Ring squeeze δ results in an increase in damping coefficient c , hence increasing the stability threshold of the bearing.

The only practical implementation of flexible elements to support Herringbone-Grooved Journal Bearings, other than O-Rings, have been presented by Somaya et al. [54] and Yoshimoto et al. [55]. The solution presented by Somaya et al. [54] consists of a rigid bearing sleeve supported on straight spring wires assembled in a hexagonal shape to provide elasticity as well as Coulomb damping due to friction at the contact points of the spring wires. Yoshimoto et al. [55] support the bearing sleeve by three- or four-layered foils containing hemispherical bumps, similar to bump foils used in foil bearings [41, 42]. Both solutions consist of a rigid, Herringbone-Grooved rotor that is rotating in a rigid bearing sleeve containing both bearing planes and that is flexibly mounted within the machine housing. An aerostatic thrust bearing to constrain the axial movement of the rotor is used in both prototypes.

4.2 Motivation and nature of the issue

The use of O-Rings as a means to flexibly support bearing bushings of HGJBs offers various advantages such as low cost, ease of availability, compactness and favorable damping properties. Limited lifetime at high temperatures [77], insufficient assembly repeatability [62] and dynamic characteristics that are difficult to measure and to tune due to their dependency on many variables such as geometry, squeeze, material, loading type, temperature, frequency, vibration amplitude and age, make a reliable and reproducible implementation into products challenging. The unfavorable repeatability of alignment is caused by twisted or nonplanarly fitted O-Rings during assembly and due to the typical O-Ring tolerance of 0.02 mm, which corresponds to about twice the radial clearance of a typical HGJB.

As presented in Fig. 1.3, chapter 1, O-Ring supported bearing bushings can yield alignment issues. Misaligned bearing bushings cause increased low-speed frictional torque and non-repeatable lift-off speeds, which can lead to increased losses and wear on bushings and rotor. A typical wear mark (wear dust accumulation in the bearing grooves) caused by O-Ring induced bushing misalignment is presented in Fig. 4.1. These results clearly suggest that O-Rings do not offer a repeatable and reliable means to flexibly support gas bearing bushings.

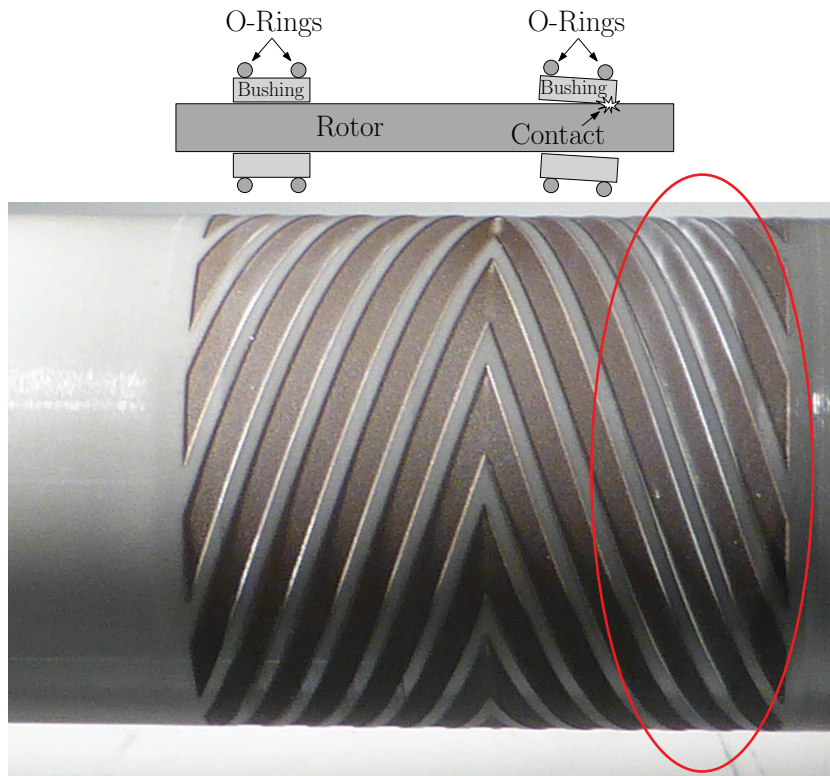


Figure 4.1 – Wear on HGJB due to misalignment, visible by the accumulation of white dust in the bearing grooves of a silicone-nitride rotor shaft

The two flexible support solutions, other than O-Rings, provided by Somaya et al. [54] and Yoshimoto et al. [55], seem to be challenging in terms of bearing bushing alignment, tuning of the stiffness and damping characteristics and appear to be prone to a variation in stiffness and damping with age. The stiffness and damping of a bump foil structure, as proposed to be used to support the bearing bushing by Yoshimoto et al. [55], is difficult to predict and large deviations between prediction and reality are to be expected due to their challenging manufacturing process, as recently shown by Shalash and Schiffmann [82].

Both practical implementations performed by Yoshimoto et al. [55] and Somaya et al. [54] consist of a rigid bearing sleeve (please refer to Fig. 1.2), which contains both bearing planes, therefore not causing an alignment problem of one bearing surface respective to the other, since both bearing planes are manufactured in the same setting. Furthermore, both examples are lab prototypes focusing on the stability of the rotor-bearing system and use an aerostatic thrust bearing to constrain the axial movement of the rotor. In real turbomachinery applications, where the rotor supports one or several impellers, such as a turbine or compressor wheel, the resulting axial forces require the implementation of a thrust bearing, often a spiral grooved thrust bearing [83, 84, 85] in the case of high speed oil-free turbomachinery. Due to the relatively large thrust disk

diameter and low axial clearance of spiral grooved thrust bearings, the rotor axis has to be perfectly aligned with regards to the thrust bearing surface. In addition, perfect concentric alignment of the rotor to the stator axis is essential in reducing tip clearance losses that can lead to a performance deterioration [86, 87]. Both presented solutions by Yoshimoto et al. [55] and Somaya et al. [54] mitigate the alignment problem of the bearing bushings relative to another by using a bearing sleeve, however, the authors do not provide a solution for aligning the bearing sleeve with respect to the stator or a possible thrust bearing surface.

Depending on the required bearing plane distance, the manufacturing of a rigid bearing sleeve that contains both bearing planes in one part is often not possible in one manufacturing step due to tooling depth restrictions. Manufacturing of the part in two steps is not possible since the required tolerances for bearing plane concentricity can not be fulfilled after the part has been removed from the chuck. Hence, the bearing bushings are manufactured separately and need to be aligned relative to each other, to the machine housing, as well as to the thrust bearing surface. An accurate and reliable solution to guarantee the alignment of two separate bearing bushings in high-speed turbomachinery therefore still remains a challenging problem.

4.3 Goals and objectives

The objectives to be treated in this chapter are:

1. Ideation, design and embodiment of a flexible support for Herringbone-Grooved Journal Bearing bushings that offers independently tunable radial and tilting stiffness and that can be coupled to various means to introduce damping. The novel flexible bearing bushing support shall be largely independent of temperature, vibration amplitude, frequency and age.
2. Development of a parametric model to predict the radial and tilting stiffness of the new membrane shaped flexible support.
3. Development of an alignment procedure that enables the alignment of two separate bearing bushings relative to each other and ensures concentricity of the rotor axis within the machine housing and perpendicularity to the thrust bearing surface.
4. Investigation of various damping concepts that can be coupled to the new flexible support.
5. Experimental validation of LAMD simulation codes for gas bearings and rotordynamics.
6. Performance evaluation of the novel flexible support and damping concepts in a prototype rotor running on HGJBs.

7. Evaluation of long-term flexible support performance by means of start-stop testing.

4.4 Methodology

4.4.1 Experimental methodology to determine stiffness and damping of flexible support

In order to characterize the dynamic properties of the flexible membrane support described in this chapter, an adapted test section has been designed that can be mounted on the modular experimental setup presented in Fig. 3.5. The applied BERM measurement method used to determine the radial stiffness of the membrane support is identical to the one used for O-Rings and has been detailed in chapter 3. The same setup is also used to investigate various damping concepts presented in the course of this chapter.

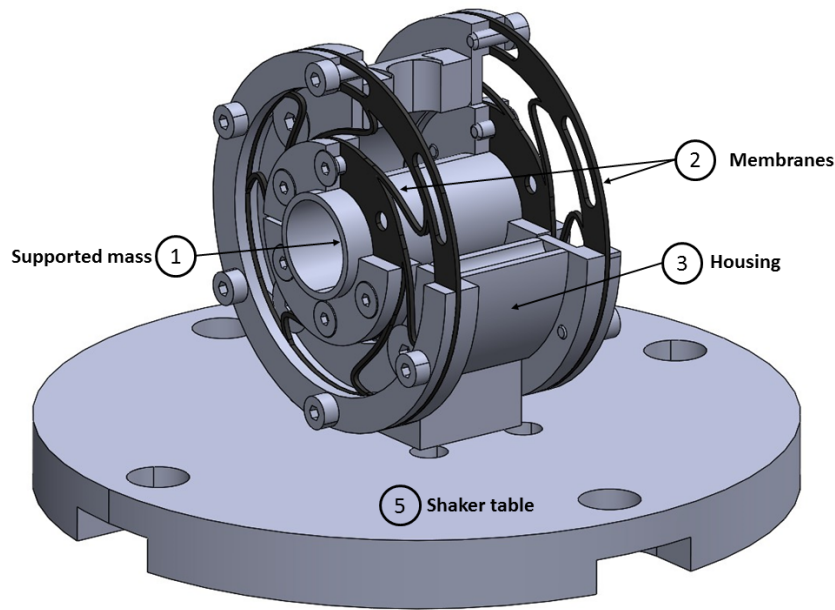


Figure 4.2 – 3/4 cut view of membrane test section

The modular test section presented in Fig. 4.2 furthermore allows the characterization of the tilting stiffness k_t for various membrane geometries. A capacitive displacement probe, calibrated to the cylindrical target, is used to determine the relationship between torque T applied to the center of the membrane and the resulting angular displacement ϕ . Figure 4.3 a) presents the measurement setup used to determine the tilting stiffness k_t of a membrane. The OD of the membrane is clamped to the housing, which is fitted to a base plate and fixed to a solid ground. A threaded rod is inserted in the center of the membrane that contains a cylindrical body, whose displacement is

captured by a capacitance probe. Varying the weight added at the end of the rod, as shown in Fig. 4.3 a), while measuring the displacements of the cylindrical body, allows the determination of the tilting stiffness k_t of a membrane. The added weight at the

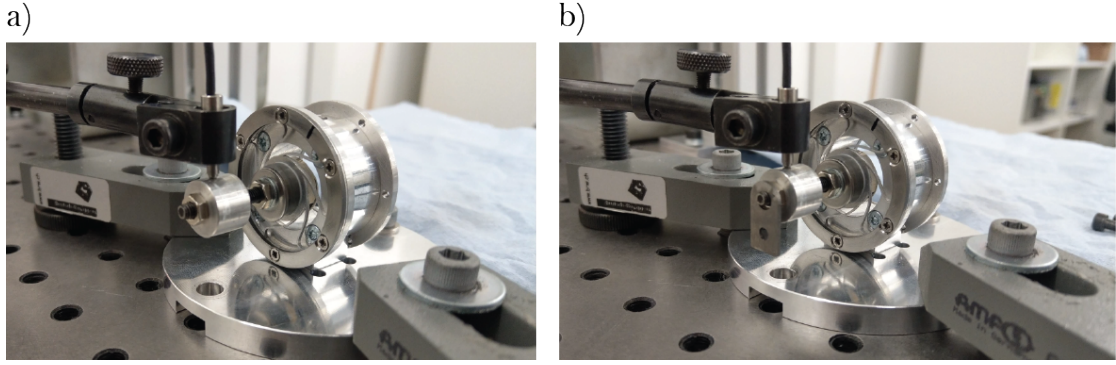


Figure 4.3 – Experimental setup for the determination of the membrane tilting stiffness k_t . a) Initial state b) Additional weight added at end of rod

end of the threaded bar allows to determine the torque T applied on the membrane and the measured displacement of the cylindrical body is transformed into an angular displacement ϕ after subtracting the radial displacement resulting from the added weight.

The relationship between angular displacement ϕ and applied torque T is characterized by a load-displacement curve that allows the determination of the tilting stiffness k_t as described in Eqn. (4.1).

$$k_t = \frac{\partial T}{\partial \phi} \quad (4.1)$$

4.4.2 Experimental methodology for performance evaluation of flexible support in prototype

Due to the stiffness of the gas film, the orbital movement of the rotating shaft is transmitted to the flexibly supported bearing bushings. Any potential instability of the rotor-bearing-system can therefore be detected by measuring the motion of the bearing bushings. Furthermore, measurement of the bearing bushing motion allows to balance the rotor shaft in-situ using the influence coefficient method [88], where an unbalance mass is first placed on the front and then the back balancing plane in consecutive order. Measurement of the bushing motion response on the front and back bearing bushing due to the added unbalance allows to identify the influence coefficients of front and back balancing planes, which provide information about the amount and the phase of where the correction masses have to be added on the two balancing planes.

As described in chapter 1, the signature of an unstable rotor or flexibly supported

bearing bushing due to self-excited whirl is the presence of sub-synchronous vibrations [25, 89]. The measurement data captured of the bearing bushing motion is analyzed by means of Fast-Fourier-Transformation (FFT) and the resulting frequency spectrum scanned for the presence of any sub-synchronous traces, which would indicate an instability of the rotor-bearing-system.

The introduction of a flexible bearing bushing support can potentially induce an unstable motion of the bushing. In order to capture such a phenomena, two additional optical displacement probes are placed on each bushing on the prototype. The motion of each bearing bushing is therefore captured by measuring its displacement in four different locations. The probe locations are shown in Fig. 4.4, where the motion in x- and y-direction is monitored using two LionPrecision capacitance displacement probes on one side of the flexible membrane support and two Philtec D20 optical displacement probes on the other side of the flexible membrane support, shifted by 30° relative to the x- and y-direction. l_a represents the distance of the LionPrecision

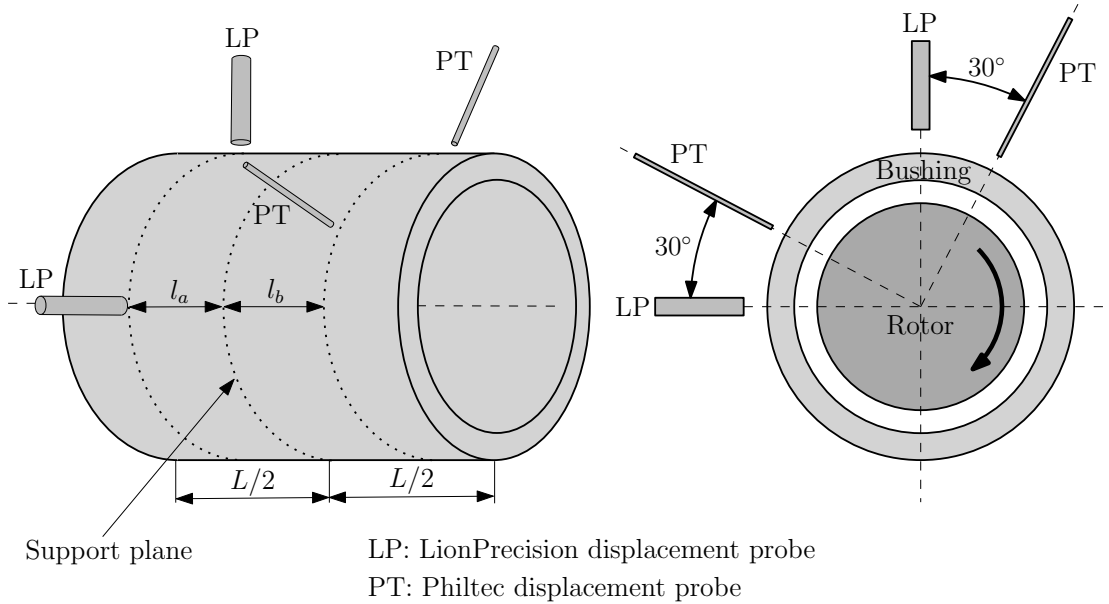


Figure 4.4 – Location of LionPrecision and Philtec displacement probes on bearing bushing

measurement plane to the center plane of the bearing bushing, whereas l_b is the distance of the Philtec measurement plane to the bushing center plane. The distances l_a and l_b measure 3.25 mm and 2.75 mm respectively.

The motion of a rigid body in the x- and y-plane can be described completely if two translational and two rotational degrees of freedom (DOF) of any point of the rigid body are known. By defining a master node, the motion of any slave node can therefore be predicted using a rigid-body-transformation matrix T_{ms} [90]. The transformation matrix T_{ms} transforms the degrees of freedom of the master node q_m into the degrees

of freedom of the slave nodes q_s , as presented in Eqn. (4.2).

$$q_s = T_{ms} \cdot q_m \quad (4.2)$$

By defining the center of the bearing bushing as the master node, with four degrees of freedom q_{ex} , q_{ey} , ϕ and θ , the displacement in x- and y-direction at each measurement location can be predicted. Reversing this procedure allows to reduce the measurement data at the four measurement points presented in Fig. 4.4, to a cylindrical motion of the bearing bushing center q_{ex} and q_{ey} , as well as two tilting motions ϕ and θ around the x- and y-axis respectively, as shown in Fig. 4.5, using Eqn. (4.3).

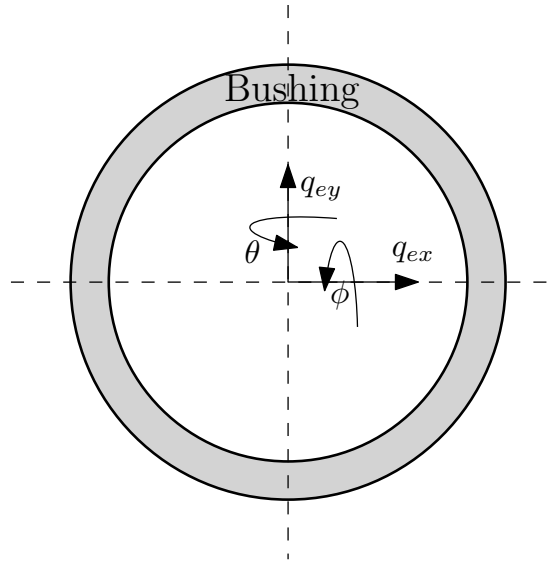


Figure 4.5 – Transformation of measurement data to a cylindrical and a tilting movement in the center of the bearing bushing

$$q_m = T_{ms}^{-1} \cdot q_s \quad (4.3)$$

During post-processing, the complete set of measurement data in the time-domain is transformed according Eqn. (4.3), followed by a separate FFT performed on the translational degrees of freedom q_{ex} and q_{ey} , as well as the two tilting degrees of freedom ϕ and θ of the bearing bushing center. This procedure allows to determine the origin of the instability to be a cylindrical or conical rotor instability, which is transmitted to the bearing bushings through the stiffness of the gas film, or a tilting instability of the bearing bushing.

The modified prototype used to investigate the flexible bearing bushing support developed in this chapter is shown in Fig. 4.6. The motion of each bearing bushing is constantly monitored using two LionPrecision capacitance displacement probes per

Chapter 4. Flexible support for Herringbone-Grooved Journal Bearings

bushing and can be extended to include two Philtec D20 optical displacement probes on each bushing in case the bushing tilting motion is investigated.

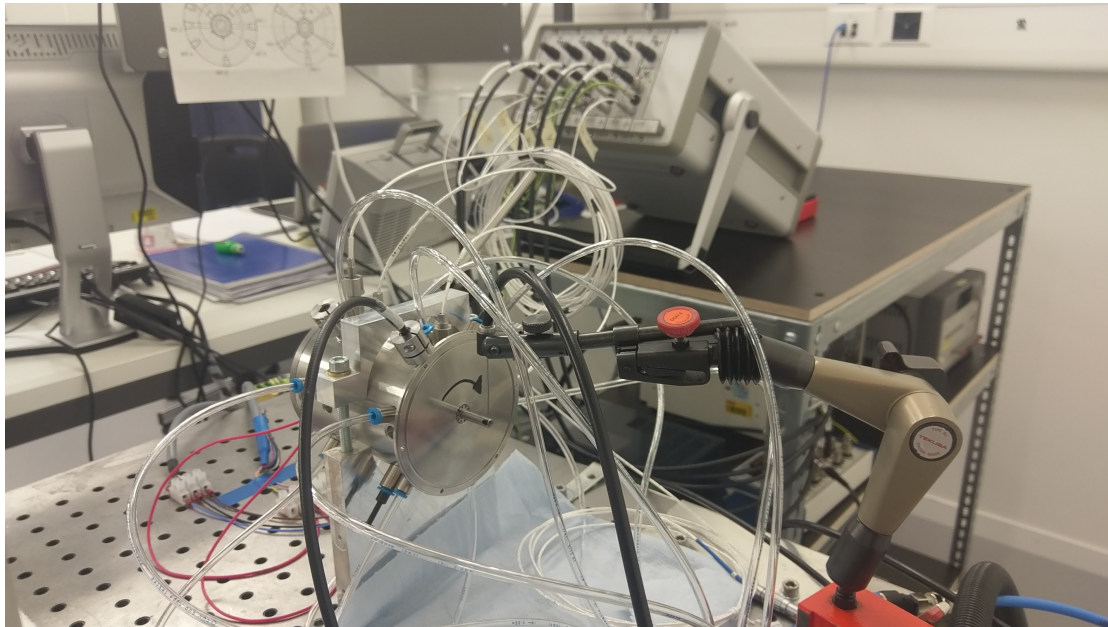


Figure 4.6 – Prototype with implemented flexible membrane bushing support and instrumentation

Table 4.1 lists all devices used to perform the radial and tilting stiffness measurements, as well as the performance verification of the new flexible bearing bushing support in the modified prototype.

Table 4.1 – List of instrumentation for membrane characterization and performance assessment of the new flexible support

Device	Model
Capacitive displacement probes	Lion precision C3S
Optical displacement probe	Philtec D20
Signal amplifier	Lion Precision CPL290
DAQ system	NI PXIe-1078/6356
Electrodynamic Shaker	Labworks INC. ET-139
Analog amplifier	Labworks INC. PA-138-1
Waveform generator	Agilent 33500B-Series

4.5 An alternative flexible bearing bushing support

4.5.1 Design requirements

The main requirements of the new flexible bearing bushing support are independently tunable radial and tilting stiffness and the option to add damping. Ideally, the dynamic characteristics of a flexible support should be independent of excitation frequency, amplitude, temperature, age and other effects. Further prerequisites are a long lifetime (≥ 4000 hours), minimal maintenance, low cost, as well as ease of manufacturing and implementation into existing prototypes and products. Additionally, the flexible bushing support needs to offer the possibility to perfectly align the bearing bushings. Theoretical investigations have shown the ideal support characteristics to be low radial stiffness, coupled with a high damping coefficient. However, too compliant supports potentially lead to large rotor orbits, which may cause a drop in turbomachinery performance due to the requirement of larger tip clearances [86, 87].

Table 4.2 summarizes the rotor and bearing configuration of the existing prototype, previously used with O-Rings to flexibly support the bearing bushings. Note that compared to the rotor diameter, the bearing bushings are far apart, which makes the manufacturing of rigidly supported bushings challenging and expensive. Hence, a solution with flexibly supported and well-aligned bushings offers competitive advantages. This prototype serves as a base-line and is used to develop and test the new flexible bearing bushing support.

Table 4.2 – Rotor design parameters

Bearing diameter D_{Brq}	10 mm
Bearing length-to-diameter ratio L_{Brq}/D_{Brq}	1
Rotor mass m_{Rot}	0.0289 kg
Polar rotor inertia J_P	4.3258e-07 kgm ²
Transverse rotor inertia J_T	1.8112e-05 kgm ²
Bearing distance l	58.5 mm
Nominal rotor speed N_{Rot}	250 krpm

4.5.2 Development of parametric membrane model

Various concepts were evaluated with regards to the requirements presented above, which led to the selected solution being a membrane with cut-outs that can be easily manufactured by means of laser or water jet from a flat sheet of metal. The solid inner and outer ring sections are connected via flexible arms whose shapes are obtained by the specifically shaped cut-outs. The inner ring is connected to the bearing bushing, while the outer ring is connected to the machine housing. In order to predict the radial

and tilting stiffness of such a flexible structure, a parametric model was developed. A sketch that illustrates the design variables of the flexible membrane model is presented in Fig. 4.7. The design variables of the model include inner radius R_i , outer radius R_o ,

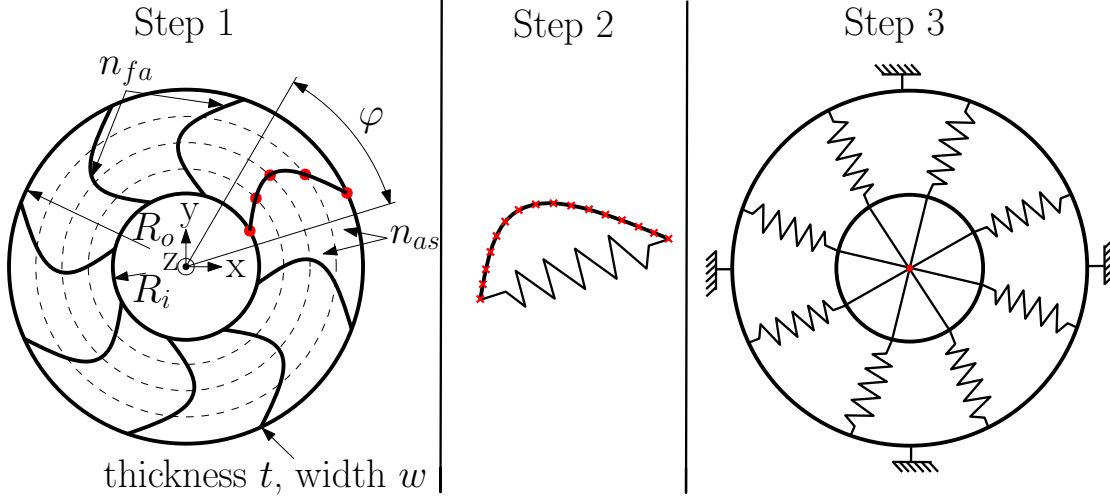


Figure 4.7 – Available parameters of membrane model for calculating radial and tilting stiffness

sector angle of one flexible element φ , the number of equally spaced annular sections n_{as} , the thickness t and width w of the flexible elements, the total number of flexible arms n_{fa} that form the complete flexible membrane structure, as well as the material to be used. In a first step, the shape of the flexible arm is determined by defining the angular location of a point on each of the equidistant annular sections. The points are then connected with a spline, which connects the inner and the outer ring. In order to predict the stiffness of such a structure, the flexible arms are modeled with finite elements along the spline. The shape of the spline and the desired number of finite elements per spline n_{FE} , define the locations of the FE-nodes along the flexible arm, as represented by the red markers in step 2 of Fig. 4.7. The 12x12 element stiffness matrices, offering three translational and three rotational degrees of freedom at each node, are defined between each pair of FE-nodes using Timoshenko's [91] beam theory (refer to appendix B), which includes both bending as well as shear effects and is based on the following assumptions:

- Linear-elastic behavior
- Center of cross-section only deforms in z-direction
- Small deformations
- Cross-section stays flat, no distortion
- The normal to the cross-section does not have to stay parallel to the tangent of

4.5. An alternative flexible bearing bushing support

the bending line, contrary to Bernoulli's beam theory, where shear strains are not considered

- 1D stress condition ($\sigma_{22} = \sigma_{33} = 0$)

Each element stiffness matrix is first defined in global coordinates and then transformed in order to respect its local orientation along the spline, as presented in Eqn. (4.4). K'_{el} represents the 12x12 stiffness matrix of the finite element in local coordinates, K_{el} the 12x12 stiffness matrix transformed into global coordinates, while T presents the direction transformation matrix. The direction transformation matrix T for a rotation φ around the z-axis is given in Eqn. (4.5), with φ being the angle of the finite beam element with respect to the x-axis of the global coordinate system.

$$K_{el} = T^T \cdot K'_{el} \cdot T \quad (4.4)$$

$$T_{sub} = \begin{bmatrix} \cos(\varphi) & \sin(\varphi) & 0 \\ \sin(\varphi) & -\cos(\varphi) & 0 \\ 0 & 0 & 1 \end{bmatrix} \quad T = \begin{bmatrix} T_{sub} & 0 & 0 & 0 \\ 0 & T_{sub} & 0 & 0 \\ 0 & 0 & T_{sub} & 0 \\ 0 & 0 & 0 & T_{sub} \end{bmatrix} \quad (4.5)$$

The direction transformation as presented in Eqn. (4.4) is performed for all n_{FE} element stiffness matrices before they are assembled according to the classical Finite-Element theory to form the $12n_{FE} \times 12n_{FE}$ stiffness matrix of one flexible arm K_{aba} , as shown in Eq.(4.6), where A represents the matrix assembly operator [92].

$$K_{aba} = A_{i=1}^{n_{FE}} K_{el_i} \quad (4.6)$$

In order to reduce the calculation time, the $12n_{FE} \times 12n_{FE}$ stiffness matrix of the complete flexible arm K_{aba} is reduced to a 12x12 matrix offering six degrees of freedom at the inner node as well as six degrees of freedom at the outer node by means of the Guyan transformation [93]. The inner node connects the flexible arm to the inner ring of the bushing support, while the outer node connects it to the outer ring of the bushing support. This procedure leads to the flexible arm being represented by an equivalent spring, as shown in step 2 of Fig. 4.7, with six degrees of freedom at each end node. The definition of the Guyan transformation matrix T_{aba} , which is used to express all degrees of freedom, q_a and q_b , by only the preferential degrees of freedom q_a , is presented in Eqn. (4.7):

$$\begin{pmatrix} q_a \\ q_b \end{pmatrix} = T_{aba} \cdot q_a \quad (4.7)$$

Chapter 4. Flexible support for Herringbone-Grooved Journal Bearings

The definition of matrix T_{aba} is given in Eqn. (4.8), where T_{aa} is an identity matrix of dimension 12x12, that is used to transform the 12 preferential degrees of freedom into itself, while T_{ba} is used to transform the preferential degrees of freedom q_a into the non-preferential ones q_b .

$$T_{aba} = \begin{pmatrix} T_{aa} \\ T_{ba} \end{pmatrix} \quad (4.8)$$

The matrix T_{ba} is defined according Eqn. (4.9), where K_{bb} and K_{ba} are sub-matrices of the original stiffness matrix K_{aba} with respect to the preferential and non-preferential degrees of freedom, as shown in Eqn. (4.10).

$$T_{ba} = -K_{bb}^{-1} \cdot K_{ba} \quad (4.9)$$

$$K_{aba} = \begin{bmatrix} K_{aa} & K_{ab} \\ K_{ba} & K_{bb} \end{bmatrix} \quad (4.10)$$

The reduced 12x12 stiffness matrix of the whole flexible arm K_a is then:

$$K_a = T_{aba}^T \cdot K_{aba} \cdot T_{aba} \quad (4.11)$$

As shown in step 3 of Fig. 4.7, the whole flexible membrane with n_{fa} flexible arms is constructed by assembling the n_{fa} 12x12 stiffness matrices K_a after transforming each of them with respect to their orientation in the global coordinate system, using the direction transformation as presented in Eqn. (4.4). Note that the sector angle φ only serves to define the spline shape of the flexible arm and is not linked to the selected number of flexible arms n_{fa} of the whole flexible membrane, which can be freely chosen. The center points of inner and outer rings act as the master nodes, which are rigidly connected to the nodes where the flexible arms are attached, modeled by means of rigid body transformation [90]. After Master-Slave transformation, the master node of the outer ring is constrained as presented in Eqn. (4.12), where T_c represents the transformation matrix to constrain the degrees of freedom of the master node that is rigidly connected to the outer ring.

$$K_{ac} = T_c^T \cdot K_a \cdot T_c \quad (4.12)$$

The transformation according Eqn. (4.12) results in a 6x6 diagonal stiffness matrix K_{ac} whose values on the diagonal represent the translational stiffness in x-, y- and z-direction as well as the rotational stiffness around the x-, y- and z-axis respectively. The translational stiffness in x- and y-direction represent the radial stiffness k_r , while the rotational stiffness around the x- and y-axis represent the tilting stiffness k_t of the flexible membrane support. Due to symmetry reasons, the radial stiffness in x- and

y-direction are identical, which is also the case for the tilting stiffness around the x- and y-axis.

Stresses in the flexible membrane For a given load, shown in Eqn. (4.13) for the example of a radial force F_r of 1 N, the global displacement vector of the six preferred, unconstrained degrees of freedom q_c is determined according to Eqn. (4.13).

$$q_c = K_{ac}^{-1} \cdot \begin{pmatrix} F_r = 1 \\ 0 \\ 0 \\ 0 \\ 0 \\ 0 \end{pmatrix} \quad (4.13)$$

The displacements of all degrees of freedom q_{ab} is obtained by an inverted Guyan transformation as presented in Eqn. (4.14) and Eqn. (4.15)

$$q_a = T_c \cdot q_c \quad (4.14)$$

$$q_{ab} = T_{aba} \cdot q_a \quad (4.15)$$

The displacement vector for each finite element q_{el} in global coordinates, a 1x12 subvector of the vector q_{ab} , is transformed into local coordinates as shown in Eqn. (4.16). T is the direction transformation matrix as presented in Eqn. (4.4).

$$q'_{el} = T \cdot q_{el} \quad (4.16)$$

Multiplying the element displacement vector in local coordinates q'_{el} with the corresponding element stiffness matrix K'_{el} in local coordinates results in the element forces F_{el} , as shown in Eqn. (4.17). F_{el} is a 1x12 vector that is determined individually for each finite element along the flexible arm and contains the forces and moments at the start node F_{el1} and end node F_{el2} of the finite element.

$$F_{el} = \begin{pmatrix} F_{el1} \\ F_{el2} \end{pmatrix} = K'_{el} \cdot q'_{el} \quad (4.17)$$

The inverse section modulus AW of a rectangular beam section is defined in Eqn. (4.18). The first entry in the AW vector represents the section modulus for axial loads parallel to the beam axis, entries two and three are the section modulus for shear loads, entry four the section modulus for a torsional load and entries five and six the section

modulus for bending loads.

$$AW = \begin{pmatrix} \frac{1}{wt} \\ \frac{6}{5wt} \\ \frac{6}{5wt} \\ \frac{2wt^2}{6} \\ \frac{wt^2}{6} \\ \frac{6}{w^2t} \end{pmatrix} \quad (4.18)$$

By multiplying the inverse section modulus AW with the corresponding 1x6 sub-vectors F_{el1} and F_{el2} for the element forces at the start and the end node of the finite element respectively, one obtains the stress vectors σ_{el1} and σ_{el2} , as shown in Eqn. (4.19).

$$\sigma_{el1} = AW \cdot F_{el1} \quad \sigma_{el2} = AW \cdot F_{el2} \quad (4.19)$$

From the stresses determined according to Eqn. (4.19) at the start node and end node of each finite element, the equivalent von-Mises stresses σ_{eq1} and σ_{eq2} are calculated as presented in Eqn. (4.20) and Eqn. (4.21) [94], where σ_{11} , σ_{12} and σ_{13} are the principal stresses at the start node and σ_{21} , σ_{22} and σ_{23} are the principal stresses at the end node of the finite element. Averaging the equivalent von-Mises stresses σ_{eq1} and σ_{eq2} allows to calculate the average von-Mises stress over one finite element.

$$\sigma_{eq1} = \frac{1}{\sqrt{2}} \sqrt{(\sigma_{11} - \sigma_{12})^2 + (\sigma_{12} - \sigma_{13})^2 + (\sigma_{13} - \sigma_{11})^2} \quad (4.20)$$

$$\sigma_{eq2} = \frac{1}{\sqrt{2}} \sqrt{(\sigma_{21} - \sigma_{22})^2 + (\sigma_{22} - \sigma_{23})^2 + (\sigma_{23} - \sigma_{21})^2} \quad (4.21)$$

4.5.3 Verification of parametric membrane model

The results of the parametric membrane model were verified for various geometries using the commercial software ABAQUS. A model using 1D beam elements as well as a 3D model using tetrahedral elements has been set up to determine the radial and tilting stiffnesses k_r and k_t . Figure 4.8 compares the displacements of the parametric membrane model presented in this paper with the results from 1D and 3D models obtained with the commercial software ABAQUS for a radial force F_r of 1 N applied in the center of the membrane, corresponding to the maximum expected force acting on the membranes during operation.

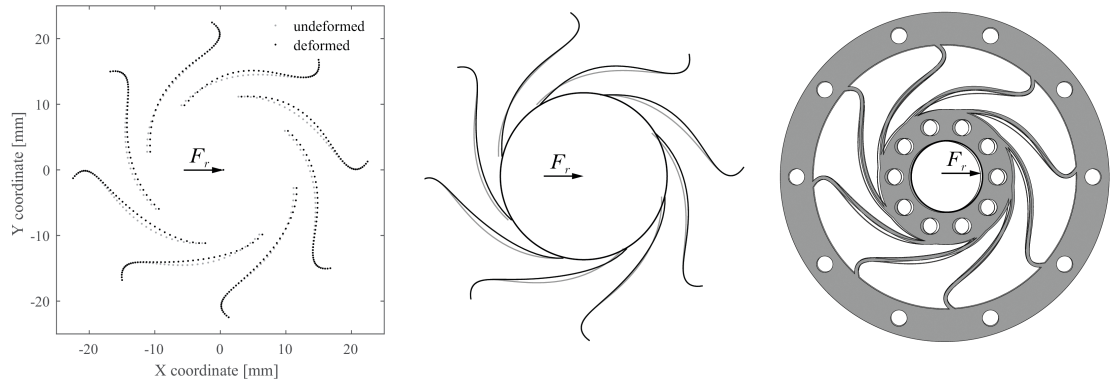


Figure 4.8 – Comparison of displacement due to a radial force F_r of 1 N in x-direction from parametric membrane model (left) with 1D ABAQUS (middle) and 3D ABAQUS results (right) (displacements scaled x500).

Evaluating the radial displacement for a given force applied to the center node of the membrane allows the determination of the radial stiffness k_r . The same procedure was followed to calculate the tilting stiffness k_t , where the angular displacement ϕ for a given torque T in the center of the membrane was evaluated. Table 4.3 presents the radial and tilting stiffnesses k_r and k_t , obtained with the parametric membrane model and compares them to the results from ABAQUS 1D and 3D FEM simulations.

Table 4.3 – Radial stiffness k_r and tilting stiffness k_t obtained with the parametric membrane model compared to results from 1D ABAQUS and 3D ABAQUS models

Method	k_r and deviation from (2)	k_t and deviation from (2)
(1) Membrane model	1.067e+06 N/m (-0.19%)	9.641 Nm/rad (+0.12%)
(2) ABAQUS 1D	1.069e+06 N/m	9.629 Nm/rad
(3) ABAQUS 3D	1.167e+06 N/m (+9.17%)	9.999 Nm/rad (+3.84%)

As suggested by Tab. 4.3, the stiffness results obtained with the membrane model match the 1D ABAQUS results very well with a deviation of only 0.19% and 0.12% for radial stiffness k_r and tilting stiffness k_t respectively. Stiffness values obtained with the 3D ABAQUS model are 9.17% and 3.84% higher for radial and tilting stiffness compared to the 1D model, which is most likely caused by the different boundary conditions at the end of the flexible arms at the inner and at the outer radius. The comparison of the parametric reduced-order model and more sophisticated modeling approaches clearly show a good agreement.

4.6 Results and discussion

4.6.1 Monte-Carlo simulations

In order to assess the design space of the parametric membrane support, three Monte-Carlo simulations have been performed for 500'000 membrane geometries made of PEEK, AL6082-T6 aluminum and 1.4310 stainless steel. The range of design variables used to perform the Monte-Carlo simulations is presented in Tab. 4.4.

Table 4.4 – Range of design variables for the performed Monte-Carlo simulations

Material: Steel/aluminum/PEEK
Thickness t , width $w \in [0.3, 2]$ mm
Inner radius $R_i \in [8, 30]$ mm
Outer radius $R_o \in [8, 30]$ mm
Sector angle $\varphi \in [\pi/30, \pi/2]$
Number of annular sections $n_{as} \in [2, 6]$
Number of flexible arms $n_{fa} \in [4, 12]$
Number of finite elements per arm $n_{FE} = 20$

Figure 4.9 presents the corresponding results of radial stiffness k_r against tilting stiffness k_t . The three points in the design space represent selected solutions of low, intermediate and high radial stiffness, whose shapes are shown in Fig. 4.10. The results presented in Fig. 4.9 suggest a possible design space ranging from $7e+00$ N/m to $7e+09$ N/m for the radial stiffness k_r , while the obtainable tilting stiffness k_t ranges from $6e-04$ Nm/rad to $2e+06$ Nm/rad, depending on the selected material. Even though the investigated range of design variables is comparatively small, the results cover 9 orders of magnitude in radial and tilting stiffness, which offers a vast domain to select appropriate stiffness values.

As suggested by Fig. 4.10, the membrane design with the lowest stiffness (point 1) features four very long flexible arms. The stiffest solution (point 3) on the other hand, features the maximum amount of 12 straight radial elements. As can be observed in Fig. 4.9, the upper and lower boundaries of the design space converge at its extremities of low and high radial stiffness, causing a reduction in the range of tunable tilting stiffness, while the center region of the design space (point 2) offers the largest range of selectable tilting stiffness for a given radial stiffness.

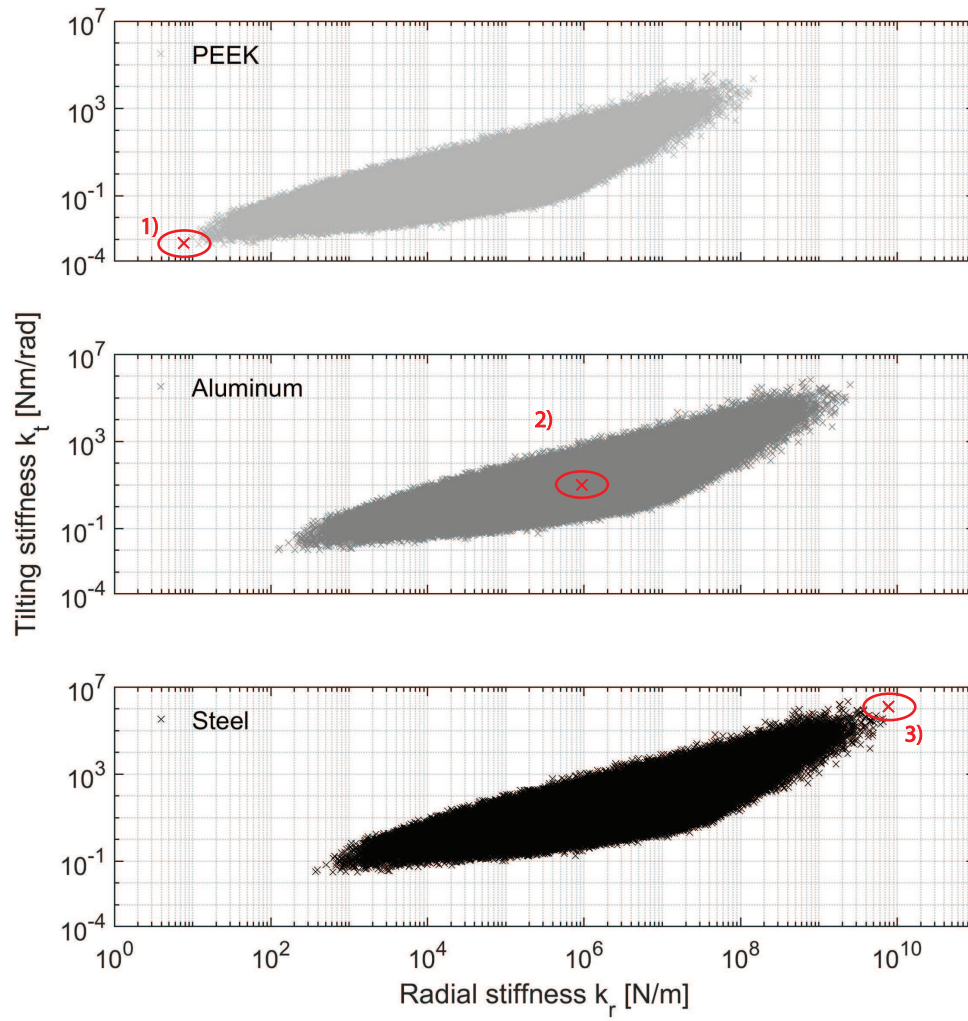


Figure 4.9 – Results of 500000 Monte-Carlo simulations for PEEK, aluminum and steel membranes according the design variables in Tab. 4.4

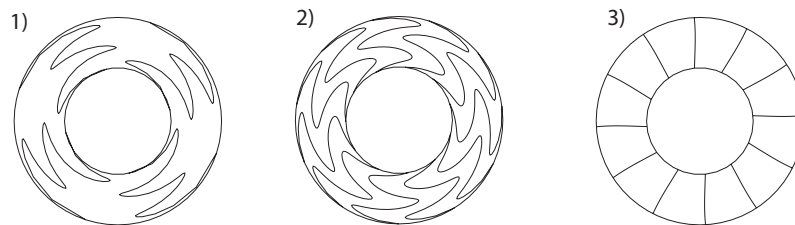


Figure 4.10 – Three selected results in design space for low, intermediate and high stiffness

Chapter 4. Flexible support for Herringbone-Grooved Journal Bearings

For a given thickness t and width w , the stiffness of a flexible arm is predominantly governed by its length and shape. In theory, the softest possible solution features flexible arms that weave n_{as} times in alternating direction within the defined sector angle φ , whereas the theoretically stiffest solution is obtained by connecting the outer and inner radii covering the shortest possible distance, resulting in straight radial elements. For both of these two extreme cases, only one geometrical solution exists, which explains the convergence of the design space to a tip at both extremities. In the center section of the design space, however, an infinite amount of geometrical solutions exists, meaning that the flexible arms can take any shape or length, resulting in a wide domain of results for the designer to choose from. Narrowing of the design variables presented in Tab. 4.4 leads to a reduction in design space size.

The tip at the lower stiffness end of the design space is less densely populated than the tip at the upper end. In order to obtain the solution with the lowest stiffness, the randomly chosen design parameters have to converge either at the upper or lower bound, whereas the stiffest solution, featuring straight radial elements, can be obtained within any sector angle φ , making it statistically more likely to find the stiffest solution.

Figure 4.11 presents the maximum von-Mises stresses σ_{eq_max} obtained with the developed membrane tool in this thesis for a radial force of 1 N for aluminum membranes with a thickness t of 1 mm, inner radius R_i of 9 mm and outer radius R_o of 17.5 mm. The maximum von-Mises stress σ_{eq_max} represents the highest value in the flexible membrane for the subjected radial force of 1 N.

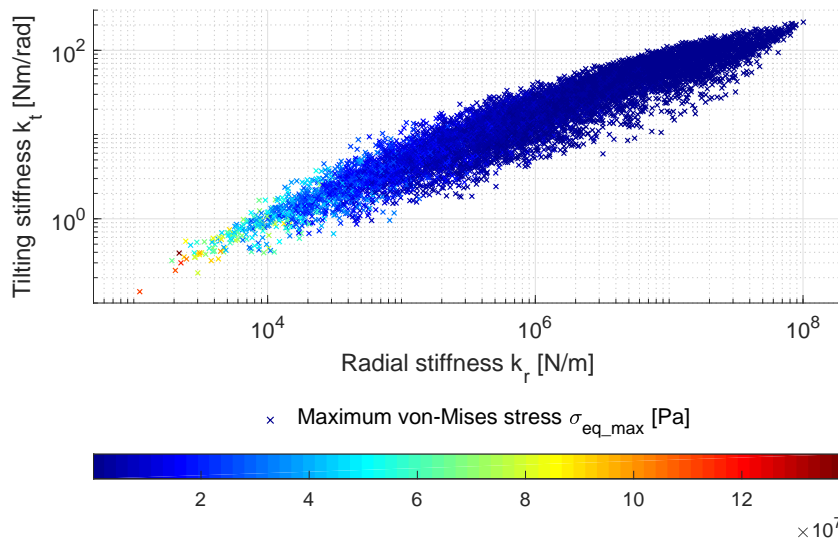


Figure 4.11 – Maximum von-Mises stresses obtained with the membrane tool for a radial force of 1 N for aluminum membranes with a thickness t of 1 mm, inner radius R_i of 9 mm and outer radius R_o of 17.5 mm

As suggested by the results presented in Fig. 4.11, the maximum equivalent von-Mises stress σ_{eq_max} decreases with increasing stiffness of the flexible membrane support for a constant radial force, whereas the opposite were the case if the presented membrane solutions were subjected to a constant radial displacement. A maximum von-Mises stress of 140 MPa is observed for some membrane geometries of very low stiffness, the vast majority of membrane designs, however, suggest the expected stress level to be between 20 and 40 MPa, a very low value that suggests unlimited lifetime of the novel flexible membrane support.

4.6.2 Manufacturing of flexible membranes

All membrane geometries manufactured and tested during this thesis are presented in Fig. 4.12 with their geometrical properties detailed in Tab. 4.5.

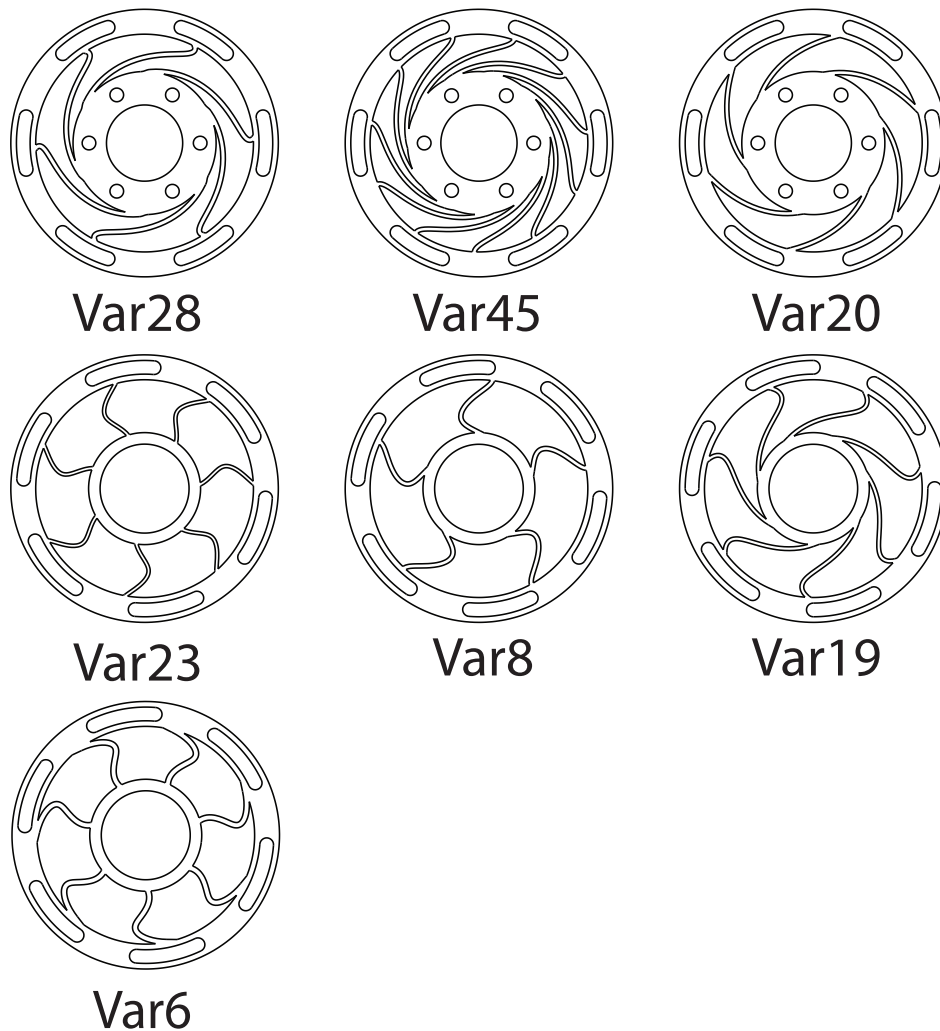


Figure 4.12 – Overview of investigated membrane designs

Table 4.5 – Geometrical properties of investigated flexible membrane designs

	Var28	Var45	Var20	Var23	Var8	Var19	Var6
Material	1.4310	AL6082	AL6082	1.4310	1.4310	AL6082	AL6082
t [mm]	0.9	1.0	1.0	0.9	0.9	0.9	1.5
w [mm]	0.74	0.65	0.67	0.524	0.68	0.6	0.86
R_i [mm]	11.5	11.5	11.5	9.0	9.0	9.0	9.0
R_o [mm]	17.5	17.5	17.5	17.5	17.5	17.5	17.5
n_{fa} [-]	6	11	6	7	5	7	7

After selecting a membrane geometry featuring the desired stiffness in radial and tilting direction, the node coordinates of the flexible arms are exported into a CAD software, where a file suitable for laser cutting is produced. The membrane geometries are then laser cut from a precision metal sheet of the required thickness t .

Other manufacturing methods for membranes include water jet cutting, wire electric discharge machining (EDM) or 3D printing. Water jet cutting would lead to less thermal distortion due to the absence of a heat-affected zone causing internal stresses. EDM wire cutting could be used for mass manufacturing, where a whole stack of metal sheets are cut simultaneously, enabling high geometrical accuracy and a high production rate.

4.6.3 Experimental validation of the parametric membrane model

Radial stiffness measurements of three selected membrane geometries were performed using the test rig shown in Fig. 4.2. Two of the tested membranes were manufactured in aluminum AL6082-T6 and one in steel 1.4310, all laser cut starting from a precision metal sheet. Figure 4.13 presents the measured radial stiffness k_r for aluminum membrane Var20 and Var45 and steel membrane Var28 using the BERM method. The designed radial stiffness k_r for membrane Var20, Var45 and Var28 is 1.00e+06 N/m, 1.04e+06 N/m and 1.04e+06 N/m respectively.

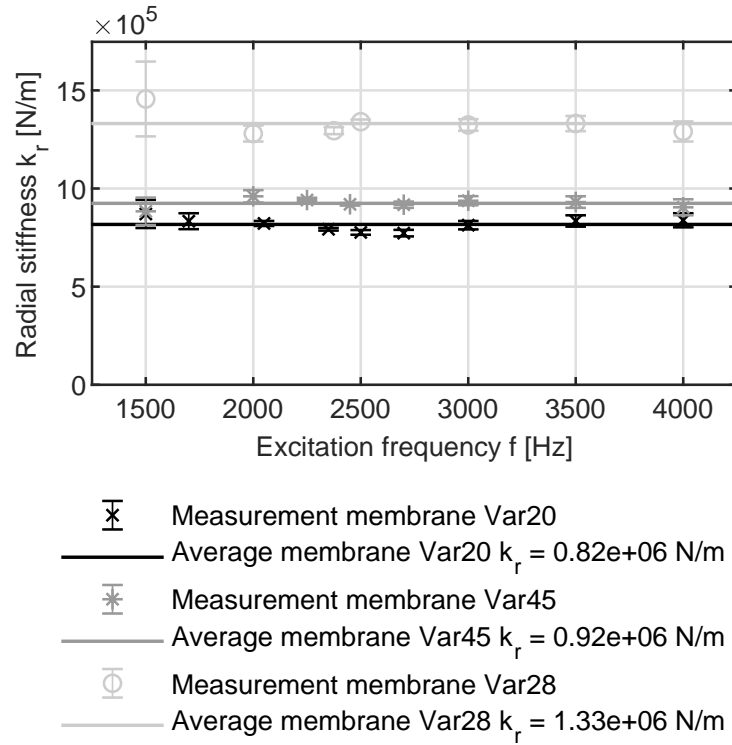


Figure 4.13 – Measurement of radial stiffness k_r for aluminum membrane Var20 and Var45 and steel membrane Var28 using the base excitation-resonant mass method

Averaging the measured radial stiffness k_r over the investigated frequency range results in $0.82e+06$ N/m for membrane Var20, $0.92e+06$ N/m for membrane Var45 and $1.33e+06$ N/m for membrane Var28. This corresponds to -18%, -11.5% and +27.9% for membranes Var20, Var45 and Var28 compared to the design values obtained by the parametric membrane model. Compared to O-Rings, whose dynamic characteristics are highly dependent on the excitation frequency [59, 60, 64, 80, 81], the membrane measurement results suggest that the radial stiffness k_r is independent of the excitation frequency f , which makes their use as a flexible support for HGJB bushings significantly easier and more predictable.

Smalley et al. [59] have investigated the effect of temperature on the stiffness and damping of O-Rings. They found the stiffness to decrease by a factor of 2 and the damping coefficient by a factor of 4 when increasing the temperature from 25 °C to 66 °C. In contrast, the elastic modulus for 1.4310 stainless steel and AL6082-T6 aluminum, which is the governing variable for the stiffness of the presented flexible membrane support, decreases by only 7% [95] and 0.8% [96] respectively in the temperature range up to 66 °C and by 17% and 8.5% respectively for a temperature increase up to 200 °C. Measurements of the tilting stiffness k_t were performed on three different membranes.

The designed tilting stiffness k_t is 5.1 Nm/rad, 35.2 Nm/rad and 64.8 Nm/rad for aluminum membrane Var19, steel membrane Var8 and Var23 respectively. Figure 4.14 presents the measured angular displacement ϕ of the membrane center when a torque T is applied. The slope of a line fitted to the measurement results represents the tilting stiffness k_t for each membrane.

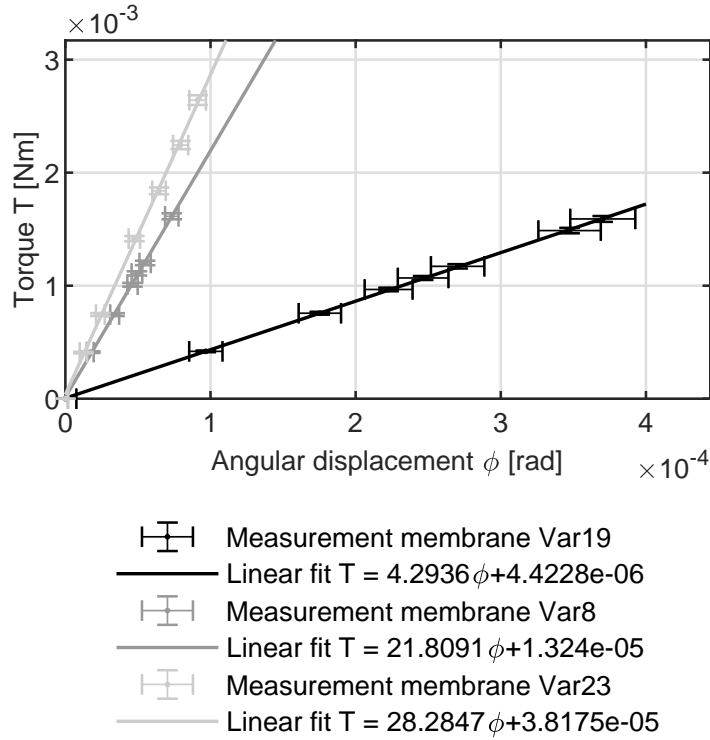


Figure 4.14 – Measurement of tilting stiffness k_t for aluminum membrane Var19 and steel membranes Var8 and Var23

As suggested by Fig. 4.14, the measured tilting stiffness k_t is 4.3 Nm/rad, 21.8 Nm/rad and 28.3 Nm/rad for membranes Var19, Var8 and Var23 respectively. This corresponds to a difference of -16% for Var19, -38% for Var8 and -56% for Var23 compared to the predicted tilting stiffness k_t by the parametric membrane model.

The difference in predicted and measured radial and tilting stiffness has been identified to be caused by manufacturing errors during the laser-cutting process, which caused some membranes to have flexible arms of significantly different width w than designed. Figure 4.15 presents an overlay of the designed geometry and the real geometry achieved by laser cutting for membrane Var23, which presented the largest deviation of predicted and measured stiffness.



Figure 4.15 – Overlay of designed geometry in CAD and real geometry of membrane Var23 achieved by laser cutting

The geometry of this membrane was scanned in high-resolution and imported into a CAD software which allowed geometrical measurements to be performed. The measurement results suggest some flexible arms to be of only 0.3 mm in width w instead of the designed 0.524 mm. Using the parametric membrane model presented in this paper, the predicted tilting stiffness k_t for this membrane with flexible arms of 0.3 mm width w is 33.0 Nm/rad, resulting in a deviation of only 14.2% between measurement and calculation. The radial stiffness k_r decreases to 0.21e+06 N/m, which represents a drop of 81%. The difference in designed and real geometry stems from incorrect compensation of the laser beam radius as well as thermal deflection due to the heat input during the laser cutting process. The results suggest that aluminum membranes suffer less from this effect, most probably due to the significantly higher thermal conductivity of aluminum compared to stainless steel. The manufacturing errors caused by thermal distortion during the cutting process could be further reduced by using water-jet or wire-erosion technology.

4.6.4 Damping concepts

Three damping concepts have been studied that can be combined with the presented flexible membrane support due to its modular design. The three investigated concepts are presented in Fig. 4.16 and consist of a silicon coating, a friction disk and a membrane stack.

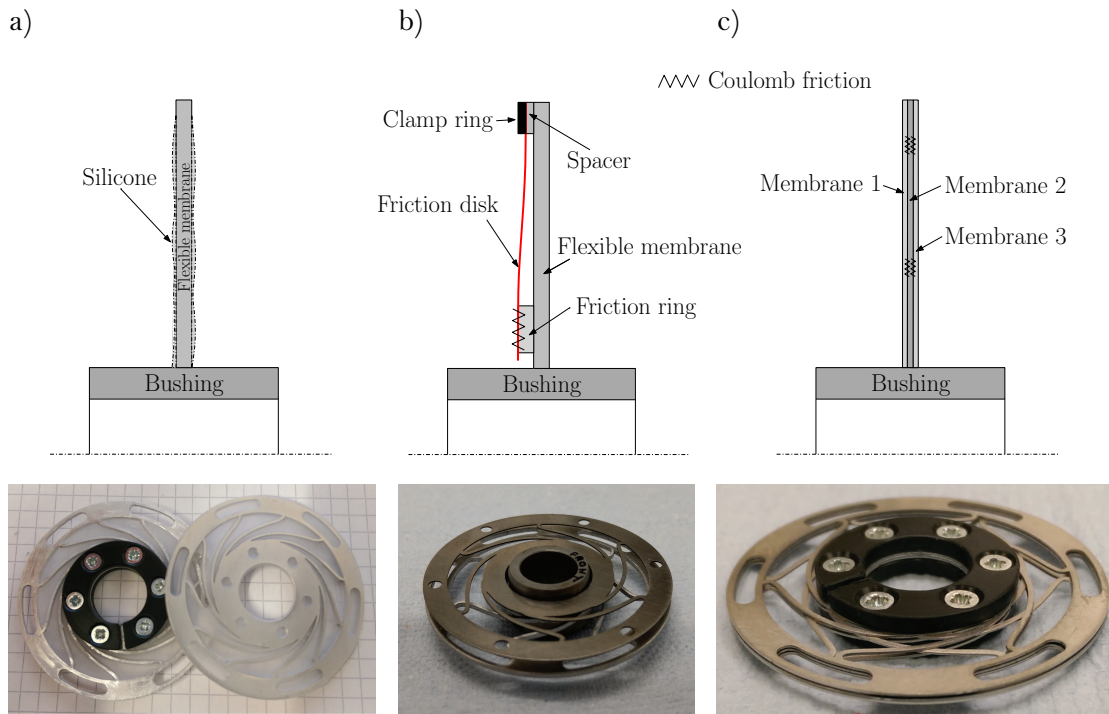


Figure 4.16 – Investigated damping concepts: a) Silicone coating (Sil); b) Friction disk (FD); c) Membrane stack (MS)

Subfigure a) in Fig. 4.16 presents the silicone coating concept (Sil), where a membrane is dipped into liquid SS-101 silicone and then left to rest for the silicone to solidify. b) presents the friction disk concept (FD), which consists of an axially preloaded flexible friction disk rubbing on a friction ring that is fixed to the flexible membrane support. The relative motion between friction disk and friction ring causes a radial friction force, which induces Coulomb damping, that can be tuned either by a variation of the axial preload between the friction disk and the flexible membrane using a spacer, or by modifying the friction coefficient between friction disk and friction ring. The third damping concept presented in c) consists of a stack of three membranes, each one $1/3$ of the thickness t of the regular membrane, resulting in an identical radial stiffness as the regular membrane. The membrane stack (MS) is constructed by stacking three membranes in alternating direction in order to generate friction between the flexible arms, which leads to Coulomb damping. The damping concepts silicone coating (Sil) and membrane stack (MS) present a coupling effect between the membrane design

and the resulting damping, since the damping is a result of the motion of the flexible arms. In the case of the friction disk concept (FD), the damping is governed primarily by the friction between the friction disk and the bushing. Hence, the stiffness and the damping can be considered as coupled in parallel with a minimal coupling effect between the membrane design and the resulting damping.

The effectiveness of the three presented damping concepts was investigated using the same measurement methodology as presented in section 4.4.1. Fitting the response of a 1-DOF spring-damper system to the measurement data allows the identification of an equivalent damping coefficient c for the presented damping concepts. The bar plot in Fig. 4.17 presents the determined equivalent damping coefficient c for membranes Var45 with/without silicone coating (Sil), Var20 with/without friction disk (FD), as well as for membrane Var28 as a single membrane compared to a membrane stack (MS). The dashed line represents the average damping coefficient of the previously used pair of silicone O-Rings, as presented in Fig. 3.6.

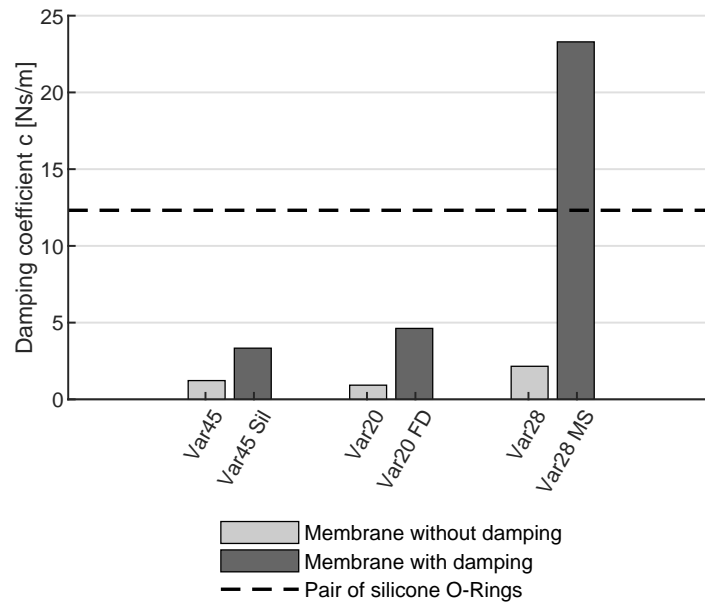


Figure 4.17 – Comparison of damping coefficient c for aluminum membrane Var45 and Var20 and steel membrane Var28 in combination with the investigated damping concepts silicone coating (Sil), friction disk (FD) and membrane stack (MS)

As suggested by Fig. 4.17, the silicone coating (Sil) increases the damping coefficient c of membrane Var45 by 125%, while the friction disk concept (FD) increases the damping coefficient c of membrane Var20 by 400%. The results suggest that the membrane stack damping concept (MS) offers the highest potential to increase damping. Replacing

membrane Var28 by a membrane stack of three identical membranes with 1/3 of the thickness increases the damping coefficient c by 860%. Furthermore, the results suggest that all three investigated damping concepts offer damping coefficients in the same order of magnitude as the previously measured pair of O-Rings, which makes them viable candidates to be coupled with the flexible membrane support.

4.6.5 Fatigue failure investigation

One of the membrane version to be implemented in the prototype is the aluminum membrane Var6 (for details refer to Fig. 4.12 and Tab. 4.5). The fatigue strength of this flexible membrane geometry has been evaluated by comparing the maximum von-Mises stress, caused by a radial vibration amplitude of $5 \mu\text{m}$, with measured fatigue data of AL6082-T6. The FEM predicted maximum von-Mises stress is $\sigma_{nom}=17.85 \text{ MPa}$ for a radial displacement of $5 \mu\text{m}$. Figure 4.18 presents the results of the FEM analysis and shows the location of where the maximum stress appears. The gray line represents the undeformed shape of the flexible arms.

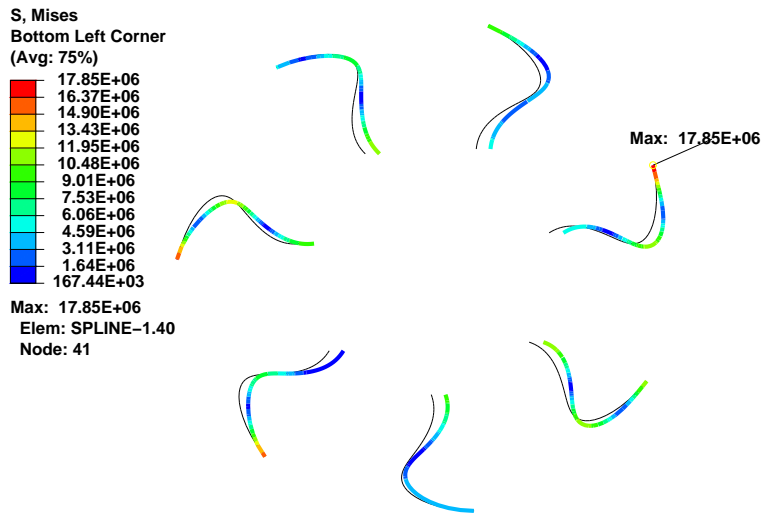


Figure 4.18 – Maximum von-Mises stress of $\sigma_{nom}=17.85 \text{ MPa}$ as a result of a radial displacement of $5 \mu\text{m}$ on membrane Var6. Displacements are scaled x200

Karolczuk et al. [97] present experimental fatigue failure data for AL6082-T6 in pure cyclic bending, which allows to predict the expected cycles to failure according to Eqn. (4.22).

$$\log_{10}(N_f) = 23.8 - 8\log_{10}(\sigma_a) \quad (4.22)$$

The number of cycles to failure N_f as a function of the applied stress amplitude σ_a , described by Eqn. (4.22), is plotted in Fig. 4.19.

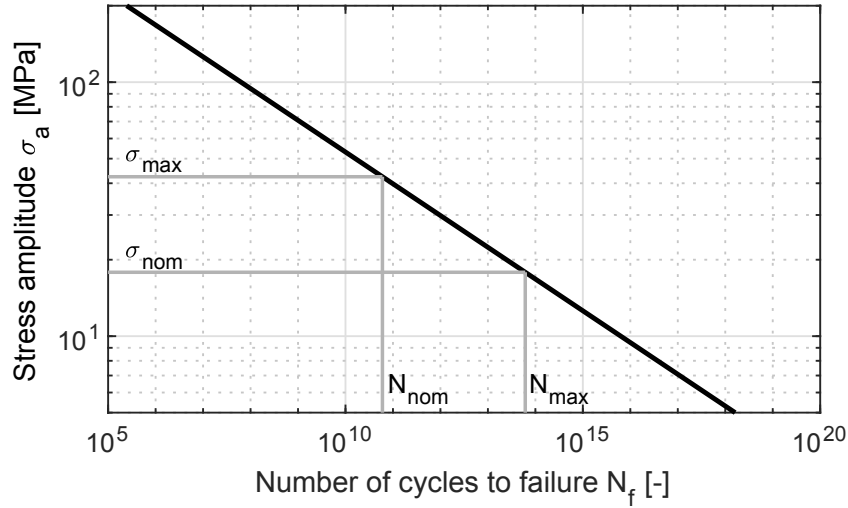


Figure 4.19 – Stress-cycle curve for aluminum AL6082T-6, according to the measured fatigue data by Karolczuk et al. [97]

For a predicted stress amplitude of $\sigma_{nom}=17.85$ MPa, the results suggest an expected number of cycles to failure of $N_{max}=6.12e+13$, according to Eqn. (4.22). Assuming a 4000 hour service life at a nominal speed of 250 krpm, resulting in $N_{nom}=6e+10$ cycles before failure, the safety factor for life is therefore $s_l=1.02e+03$. Evaluation of Eqn. (4.22) for the required $6e+10$ cycles allows to calculate the maximum allowed stress amplitude for the structure to not fail before the required number of cycles and results in $\sigma_{max}=42.44$ MPa. The ratio of maximum allowed stress amplitude σ_{max} and predicted stress amplitude σ_{nom} represents a safety factor for stress of $s_\sigma=2.4$. Both safety factors show a sufficiently high margin against fatigue failure, suggesting unlimited endurance for the introduced flexible bearing support concept.

4.6.6 Bearing bushing alignment

In order to ensure perfect alignment of the two flexibly supported bearing bushings relative to each other, as well as concentricity to the stator axis and perpendicularity of the bearing bushing axes to the thrust bearing surface, a special procedure is used to align the front and back bearing bushings in their respective flexible membranes.

The procedure consists in aligning the bushings on a high precision assembly shaft that is mounted on the prototype and serves to position the bushings within the stator. The membranes are fixed on their OD to the stator body. The membrane ID is designed such that an assembly gap forms between the OD of the bearing bushing and the membrane ID, allowing the bushings to have a certain degree of freedom in radial

Chapter 4. Flexible support for Herringbone-Grooved Journal Bearings

and tilting direction, which is required for the alignment. After glue is applied to the interface of bearing bushing and flexible membrane, the alignment shaft is radially expanded in order to remove the clearance between alignment shaft and bearing bushings, allowing a perfect alignment of said bushings. The glue is then left to cure with the alignment shaft still in its expanded state. After hardening of the glue, the alignment shaft is contracted and removed, resulting in a perfectly aligned stator-membrane-bushing package.

Figure 4.20 presents the alignment concept to align and glue the bushings to their respective membranes. The electric stator is represented in orange, the alignment shaft in gray, the rear thrust bearing disk in blue and the front centering flange in green. The glue applied between membrane and bearing bushings is shown in yellow.

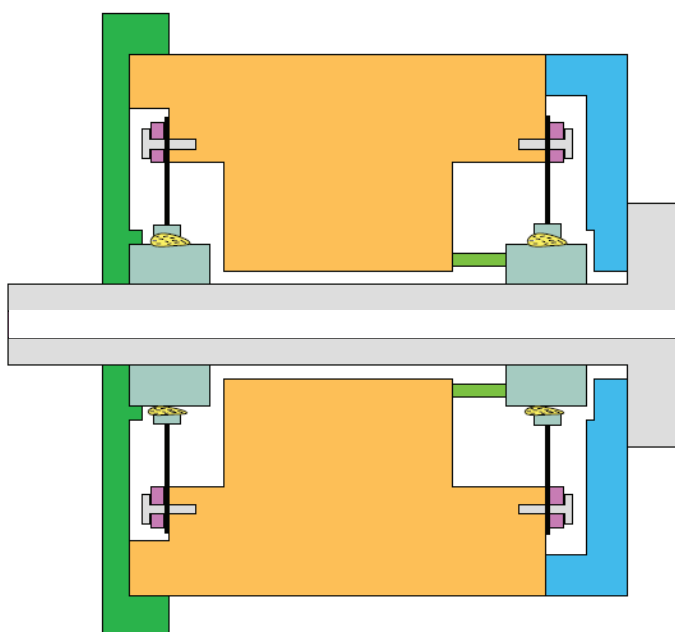


Figure 4.20 – Alignment concept consisting of electric stator (orange), alignment shaft (gray), thrust bearing disk (blue) and front centering flange (green)

The membranes are fixed to the electric stator (orange) by a clamp ring (purple) and screws. The concentric alignment of front and back bearing bushing is achieved by expanding the high-precision alignment shaft, while concentric alignment of the bushing axes with the stator axis is accomplished by the front centering flange (green), that offers a low-clearance fit between stator OD and alignment shaft OD. The third important alignment requirement, perpendicularity between bushing axes and thrust disk surface, is guaranteed by contact of the rear alignment shaft flange with the thrust bearing disk (blue).

Various concepts have been investigated that allow a controlled, reversible, radial

expansion of the alignment shaft and are presented and evaluated in the following paragraphs.

Selection of alignment shaft expansion concept

Various concepts that enable the radial expansion of a shaft in a controlled, reversible manner are presented in the following paragraphs. The investigated concepts consist of two mechanical expansion concepts (hydraulic pressure and cone), as well as two thermal expansion concepts (hot fluid and heating cartridge)

Hydraulic expansion. One possible solution to expand a shaft radially in a controlled manner is by subjecting the inner bore of a hollow shaft to hydraulic pressure. The required pressure to expand the shaft has been calculated using Eqn. (4.23) [98], where q_r is the radial displacement, R_i and R_o are the inner and outer radii of the cylinder, E the Young's modulus, G the shear modulus and p_0 is the pressure applied on the inside of the cylinder. Equation (4.24) presents the tangential stresses $\sigma_{\theta\theta}$ in the cylinder as a result of the applied pressure p_0 . The radial displacement at the outer radius of the shaft is calculated by evaluating $q_r(R_o)$. The tangential stresses however reach a maximum at the inner bore of the hollow shaft, which is why $\sigma_{\theta\theta}$ is evaluated at R_i .

$$q_r(r) = \frac{R_i^2}{R_o^2 - R_i^2} r \left[\frac{3}{E} + \left(\frac{1}{2} \left(\frac{R_o}{r} \right)^2 - 1 \right) \frac{1}{G} \right] p_0 \quad (4.23)$$

$$\sigma_{\theta\theta}(r) = \frac{R_i^2}{R_o^2 - R_i^2} \left[1 + \left(\frac{R_o}{r} \right)^2 \right] p_0 \quad (4.24)$$

Figure 4.21 presents the outer diameter D_o as a function of the internal pressure p_o applied to a steel cylinder ($E=210$ GPa) of outer diameter $D_o=10$ mm, inner diameter $D_i=7$ mm. The outer diameter D_o equals to the nominal bearing diameter, while an inner diameter of $D_i=7$ mm is chosen as a compromise between minimizing the required pressure for expansion, as well as to ensure high enough rigidity for the required high precision manufacturing.

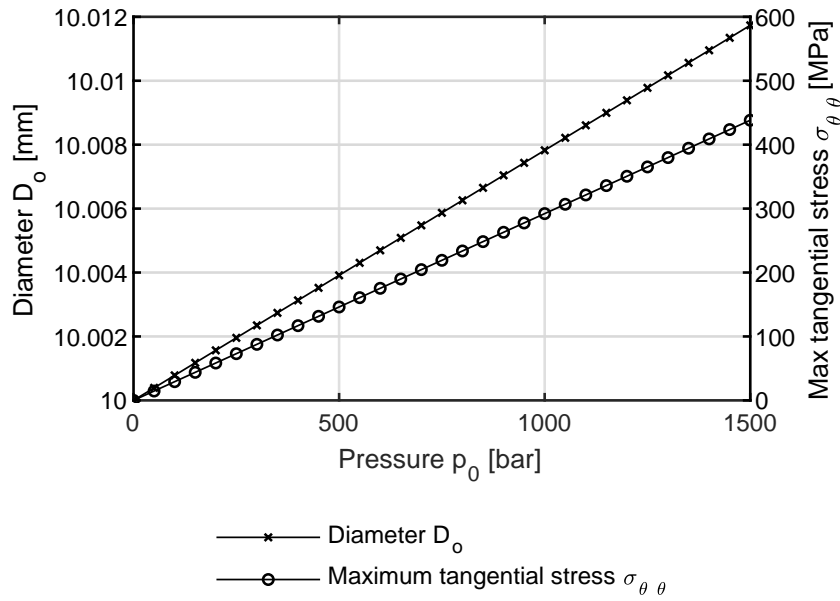


Figure 4.21 – Outer diameter D_o and maximum tangential stress $\sigma_{\theta\theta}$ of a steel shaft with internal diameter $D_i = 7\text{mm}$ as a function of internal pressure p_0

As suggested by the results presented in Fig. 4.21, a steel shaft of $D_o=10\text{ mm}$ and $D_i=7\text{ mm}$ requires a hydraulic pressure p_o of 1279 bar to expand it by $10\text{ }\mu\text{m}$, which is the required clearance to easily slide the shaft into the bearing bushings. The maximum tangential stresses $\sigma_{\theta\theta}$ caused by the internal pressure p_o of 1279 bar equates to 374 MPa. Even though a pressure of 1279 bar could be reached quite easily and the resulting material stress is within acceptable limits, the fact remains that such high pressure levels cause a safety risk. Furthermore, an individual expansion of the shaft at the front and back bearing location is challenging to achieve and further increases the required infrastructure. In addition, the weight of the hydraulic pipes could cause the alignment of the shaft to be disturbed. The advantages and disadvantages of using hydraulic pressure for the alignment concept are summarized in Tab. 4.6.

Mechanical expansion with cone. Figure 4.22 presents the FE analysis results of a cone that is axially inserted into a hollow, slotted shaft. The required axial force could be applied by means of a fine pitch thread. The presented results are transformed into a cylindrical coordinate system. As suggested by the results, the radial expansion is non-uniform in axial and tangential direction on the surface of the shaft, causing only four points of contact between alignment shaft and bearing bushing rather than the desired surface contact.

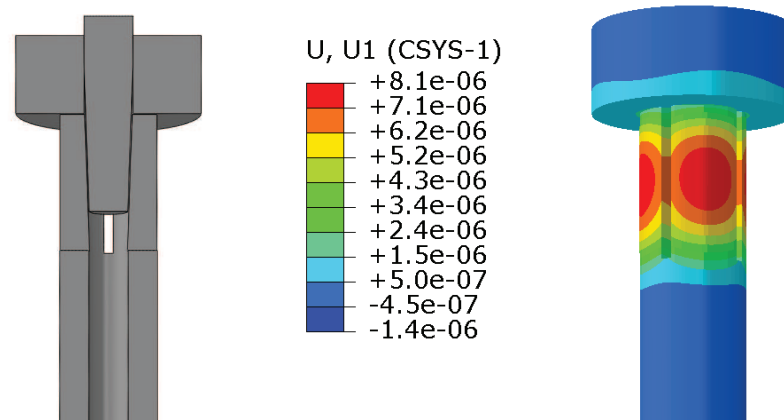


Figure 4.22 – Results of FEM simulation using a cone to radially expand a slotted shaft. Left figure shows the half-model of the slotted shaft and the cone to be inserted. Right figure presents the radial expansion after inserting the cone.

Further advantages and disadvantages of using a cone shaped pin to mechanically expand a shaft in radial direction are listed in Tab. 4.6.

Thermal expansion with thermal fluid. A uniform radial expansion can be realized by thermally dilating the alignment shaft, which could be achieved by flowing hot liquid through the internal bore of a hollow shaft. This requires a closed system with potentially thermal oil as the liquid if temperatures in excess of 100 °C are needed. Individual control of front and back alignment shaft diameter is, similar to hydraulic expansion, difficult to realize. Furthermore, the introduction of liquid into the electrical components of the stator could cause damage. Positive and negative aspects of using hot fluid as a means to dilate a shaft are summarized in Tab. 4.6.

Thermal expansion with heating cartridges. Individual control of front and back alignment shaft diameter can be realized by inserting two heating cartridges on both front and back side of a hollow shaft. The temperature control is performed using relays that switch electrical power to the heating cartridges on and off, dependent on the feedback given by a temperature probe within the heating cartridges. Advantages and disadvantages of the heating cartridge concept as well as the other investigated concepts that allow a controlled, reversible, radial expansion of the alignment shaft are listed in Tab. 4.6.

Chapter 4. Flexible support for Herringbone-Grooved Journal Bearings

Table 4.6 – Overview of advantages and disadvantages of bearing bushing alignment concepts

Hydraulic pressure	
+ No complicated control systems needed	- High hydraulic pressure needed → safety risk - Individual expansion front/back bearing location challenging - Weight of hydraulic pipes may disturb alignment - Pressure loss during curing of glue could potentially lead to misalignment
Mechanical expansion with cone	
+ No need for a control system	- Non-uniform radial expansion
+ No pipes or cables needed	- Precise radial expansion difficult to achieve
+ Individual expansion front/back easy to realize	- Price of shaft more expensive than plain shaft
Thermal fluid	
+ Temperature control easy by using available thermostat controlled through-flow heater at LAMD	- Potentially time consuming to reach desired temperature due to low heat transfer coefficient of liquid flow
+ Alignment shaft cheap to manufacture	- Individual expansion front/back bearing location challenging - Weight of hydraulic pipes may disturb alignment - Leakage could damage electrical stator
Heating cartridges	
+ Individual expansion front/back bearing location easy	- Temperature control system to be developed
+ Alignment shaft cheap to manufacture	
+ Quick to reach desired temperature due to high heat transfer coefficient	
+ Low weight of cables advantageous for alignment	

The heating cartridge concept was selected to be implemented due to the exceeding number of advantages compared to the other concepts. Furthermore, the use of two separate heating cartridges allows to independently control the diameter of the front and the back of the alignment shaft, which is of great importance to compensate for

different clearances between alignment shaft and front/back bearing bushings.

Thermo-mechanical analysis of heating cartridge concept

High precision machining is facilitated by the use of hard materials, which is why the material for the alignment shaft was selected to be 1.4034, a stainless steel that can be heat treated to reach a hardness of 60 HRC. The thermal expansion coefficient of steel 1.4034 is $\alpha=11\text{e-}06$ 1/K, about three times higher than the thermal expansion coefficient of the SiN bearing bushings to be aligned ($\alpha=3.4\text{e-}06$ 1/K). The ID of the bearing bushing was measured to be 10.016 mm at 20 °C.

Figure 4.23 a) presents the results of expected outer diameter D_o of the alignment shaft and inner diameter D_i of the SiN bearing bushings for an initial clearance of 5 μm at 20 °C.

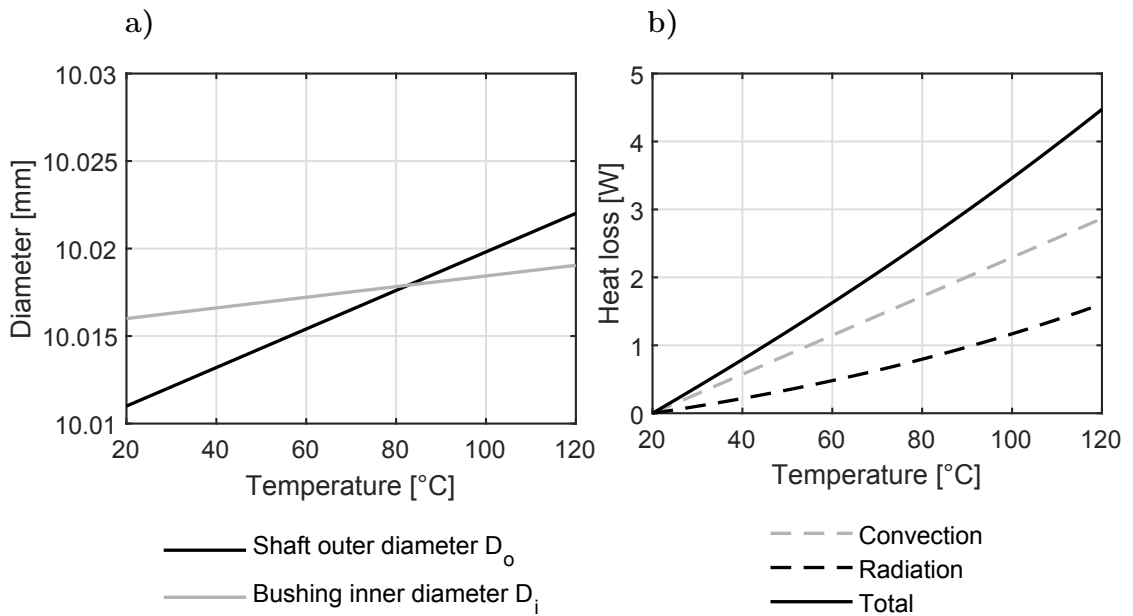


Figure 4.23 – a) Diameter of alignment shaft and bushing as a function of temperature; b) Heat loss of alignment shaft and bearing bushing as a function of uniform temperature

As suggested by the results, a temperature of 83 °C is needed to reach an identical diameter of 10.0179 mm for both alignment shaft and bearing bushings. This temperature, representing a state of zero clearance, is desired for optimum alignment of the bushings and should not be exceeded due to the risk of cracking the bearing bushings. The estimated heat losses due to convection and radiation of the alignment shaft and bearing bushings, as well as the total required heating power are presented in Fig. 4.23 b). As suggested by the results, a total heating power of 2.7 W is required to achieve the desired uniform temperature of 83 °C for the alignment shaft.

Chapter 4. Flexible support for Herringbone-Grooved Journal Bearings

A FE model was set up to verify the results from the 0-D model presented in Fig. 4.23. The model consists of the alignment shaft and both bearing bushings, whose contact interaction has been modeled by a friction coefficient, as well as a thermal contact interaction. The thermal contact interaction represents the heat transfer between alignment shaft and bearing bushings and is modeled as defined in Eqn. (4.25), where \dot{q} is the heat flux from one surface to the other, λ is the thermal conductivity of air, T_{S0} and T_{B0} are the surface temperatures of alignment shaft and bushing respectively and l is the distance between alignment shaft and bearing bushing surface. The contact gap between alignment shaft and bushings is therefore modeled as a layer of air, whose thermal resistance decreases with decreasing thickness of the layer.

$$\dot{q} = -\lambda \frac{T_{S0} - T_{B0}}{l} \quad (4.25)$$

The boundary conditions with regards to the heat transfer to the environment have been set by specifying a convective heat transfer coefficient of $\alpha = 5 \text{ W/m}^2\text{K}$ and an emissivity $\epsilon = 0.3$ to account for convective and radiative heat transfer. Separate regions on the front and back alignment shaft ID were defined according to the location of the heating cartridges. Each region was then subjected iteratively to a separate heat flux until the contact between alignment shaft and bearing bushings was closed.

The resulting steady-state temperature distribution with a heat flow of 1.1 W and 1.45 W on the front and back heating cartridge location respectively is presented in Fig. 4.24 a), where NT11 presents the nodal temperatures in °C.

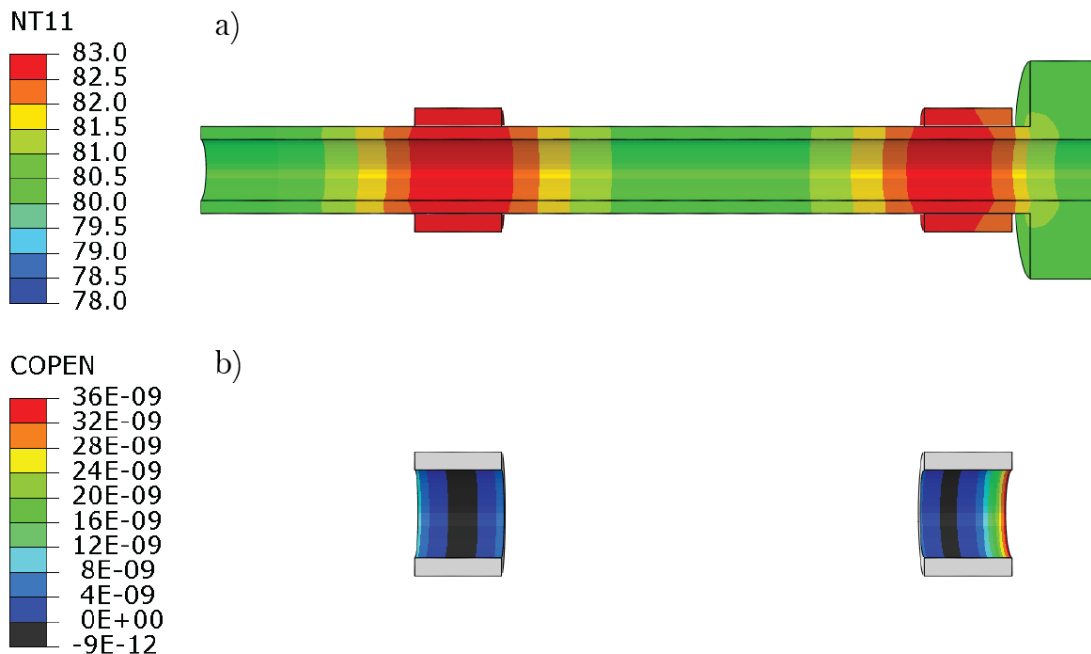


Figure 4.24 – a) FEM results for steady-state temperature distribution of alignment shaft and bushings; b) Simulated distance of defined contact surfaces

As suggested by the results, the resulting temperature distribution is largely uniform with a maximum temperature of 83 °C at both bearing bushing locations and 80 °C on the front and back of the alignment shaft. The total heat flow of 2.55 W matches well with the predicted 2.7 W of the 0-D model. Furthermore, the resulting temperature level corroborates the results of the 0-D calculation, which predicted a uniform temperature of 83 °C. The reason for the higher heat flow at the back location of the alignment shaft required to reach the same temperature as at the front bearing location is due to the thrust disk alignment flange, which acts as a cooling fin.

Figure 4.24 b) shows the results for the distance between the defined contact surfaces of alignment shaft and bearing bushings, where a COPEN value of 0 represents contact between the two bodies. As suggested by the results, both bearing bushings are touching the alignment shaft in a largely uniform manner. The largest remaining distance on the front bearing bushing is less than $8\text{e-}03 \mu\text{m}$, while the largest distance on the back bearing bushing is below $36\text{e-}03 \mu\text{m}$. At a nominal radial clearance C of $7.6 \mu\text{m}$ between real rotor and bearing bushings, this corresponds to 0.11% and 0.47%, suggesting a very good alignment of the bearing bushings.

To conclude, two heating cartridges, each providing a minimum of 2 W, are required to get contact between alignment shaft and bearing bushings for an initial clearance of $5 \mu\text{m}$ in diameter. The resulting temperature of the alignment shaft and the bearing bushings in average will be about 82 °C. As a result of this feasibility investigation, two heating cartridges of OD 6.5 mm, length 40 mm and 100 W heating power have been selected that feature internal Fe/CuNi thermocouples of the type L, which will be used for the closed-loop temperature control system. Furthermore, an alignment shaft of ID 6.5 mm and OD 10.011 mm was designed and manufactured in 1.4034 heat-treated stainless steel.

Development of temperature control system and testing

The selected heating cartridges to be used with the thermal alignment shaft are shown in Fig. 4.25 a), while Fig. 4.25 b) presents the alignment shaft with PT100 temperature probes applied on its surface in the location of the bearing planes. The PT100 temperature probes are used to monitor the surface temperature T_{S0} of the alignment shaft, while the set temperature of the heating cartridges T_{set} is varied.

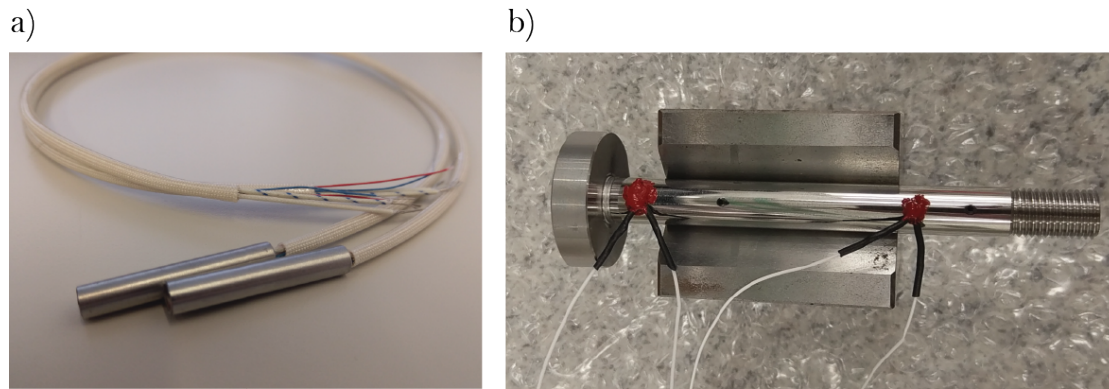


Figure 4.25 – a) Selected heating cartridges of ID = 6.5 mm and $P=100$ W; b) Alignment shaft with PT100 temperature probes applied at bearing bushing locations

The developed temperature control system for independent closed-loop control of both heating cartridges consists of two Philips digital 380 temperature control modules, two solid-state relays and a transformer, required to reduce the power of the heating cartridges. The alarm relay output of the two Philips modules is used to switch the two solid-state relays who individually supply electrical power to both heating cartridges, after being reduced in voltage by the transformer. As soon as the measured temperature inside the heating cartridges exceeds the set temperature of the control unit, the relay is opened and the power to the heating cartridges interrupted. For more information on the temperature control system, please refer to appendix C for the electrical wiring diagram.

As suggested by the results presented in Fig. 4.23 b), the required total heating power is 2.7 W, while the selected heating cartridges are delivering 100 W each at their nominal voltage of 230 V, yielding to a duty cycle of only about 1.35% for each relay and therefore high oscillations in temperature. Transforming the voltage to 70 V reduces the power of each heating cartridge to 10 W, resulting in a much more manageable duty cycle of 13.5% and therefore a stable system with low temperature oscillations.

The temperatures were monitored using PT100 elements (see Fig. 4.25 b)) on the surface of the alignment shaft T_{S0} on both the front and back bearing locations, while varying the set temperature T_{set} using the temperature control system described above. Figure 4.26 a) presents the evolution of measured surface temperature T_{S0} with set temperature T_{S0} on the control unit after steady-state conditions are reached. Furthermore, the diameter of the alignment shaft was measured using a Tesa digital gauge after each temperature increment, again in steady-state conditions. The evolution of alignment shaft diameter D_S with alignment shaft surface temperature T_{S0} is presented in Fig. 4.26 a) for both front and back bearing bushing locations.

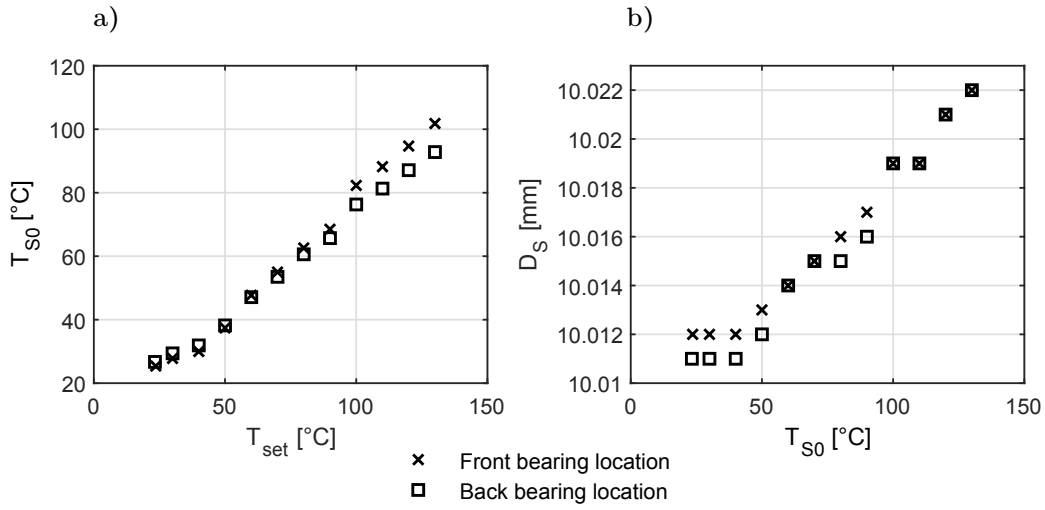


Figure 4.26 – a) Set temperature at heating cartridge T_{set} versus measured temperature on alignment shaft surface T_{S0} ; b) Measured temperature on alignment shaft surface T_{S0} plotted against measured diameter of alignment shaft

The evolution of the surface temperature T_{S0} presented in Fig. 4.26 a) rises in a linear fashion with the set heating cartridge temperature T_{set} on both front and back locations. As expected, the relationship between T_{S0} and T_{set} is not directly proportional due to the thermal resistance between heating cartridge and alignment shaft surface. For the same set temperature T_{set} , the temperature on the front bearing bushing location is slightly higher than the back bearing location. This is caused by the rear thrust disk alignment flange of the alignment shaft, which yields a large heat loss to the environment due to its large surface area.

In order to precisely determine the required temperature T_{set} , resulting in a state of zero clearance between bushings and alignment shaft, both bearing bushings have been fitted to the alignment shaft and the temperatures of both front and back heating cartridges T_{set} successively increased until the bearing bushings were sticking on the shaft. The required set temperature T_{set} for both bearing bushings to stick was measured at 80 °C and 83 °C for the front and back bearing locations respectively.

Integration into prototype and alignment procedure

The membranes are fixed on their OD to the stator body using a clamp ring and screws. The clamp ring features threads that can be utilized to fix the modular friction disk damping concept if required. As mentioned before, the bearing bushings are aligned within their respective membranes by means of a radially expanding alignment shaft and fixed with high temperature glue. The selected glue is Loctite EA 9497, a high temperature glue featuring high mechanical strength and high thermal conductivity.

Figure 4.27 presents a cut-view of the realized alignment setup. The electric stator is represented in white, the alignment shaft in brown, front and back heating cartridges in gray, the front centering cover in orange and the thrust bearing disk in yellow.

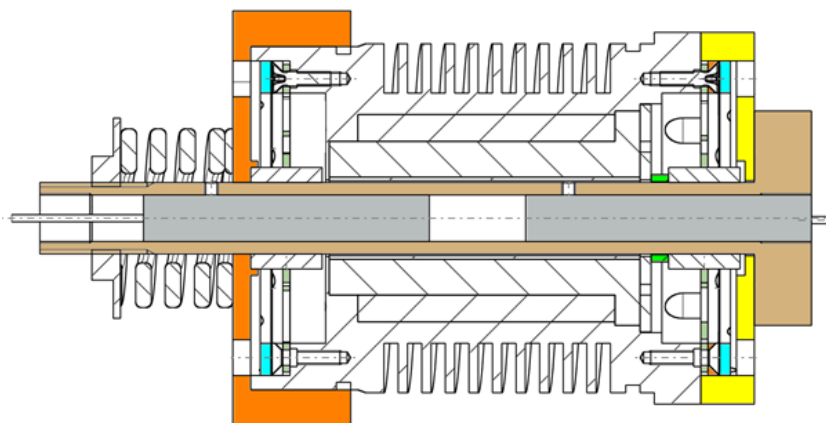


Figure 4.27 – Cut-view of alignment setup featuring electric stator (white), alignment shaft (brown), heating cartridges (gray), front centering cover (orange) and thrust bearing disk (yellow)

The procedure to align and glue the bearing bushings is detailed below:

1. Fix OD of front and back membranes to stator by means of clamp ring and screws, without tightening the bolts.
2. Apply glue Loctite EA 9497 to the front bearing bushing OD.
3. Place front bearing bushing in the front centering cover (orange).
4. Slide the electric stator into the front centering cover, allowing the front bushing to slide into the front membrane.
5. Apply glue to the back bearing bushing, insert axial spacer on the back of the electric stator (green) and slide bushing into back membrane.
6. Place thrust bearing disk (yellow) on the back of the electric stator.
7. Insert alignment shaft with back heating cartridge inserted. The heating cartridge is fixed inside the alignment shaft beforehand by means of a grub-screw.
8. Insert front heating cartridge and fix with grub-screw.
9. Fit spring and tighten nut on the alignment shaft in order to axially preload the system. This ensures good alignment to the thrust bearing disk (yellow).

10. Switch on heating cartridge system, regulated to the required temperature on front and back.
11. After the desired temperature on front and back is reached, tighten the screws of the membrane clamp ring on front and back.
12. Let the glue cure for at least 8 hours with the heating cartridges switched on.

After curing of the glue, the heating cartridges are switched off, the spring and nut on the front of the alignment shaft removed and the front heating cartridge retracted, which enables the alignment shaft to be removed.

According to the data sheet of the utilized Loctite EA 9497, its high temperature mechanical strength depends on the curing temperature of the glue. As suggested by the measurement data presented in the data sheet, the high temperature strength of the glue is at its maximum when cured at 80 °C. The required temperature of around 83 °C to ensure a state of zero clearance between bearing bushings and alignment shaft is therefore ideal to achieve the maximum high temperature strength of the selected glue.

Figure 4.28 a) shows the alignment system in use, while Fig. 4.28 b) presents the electric stator with aligned and glued front bearing bushing.

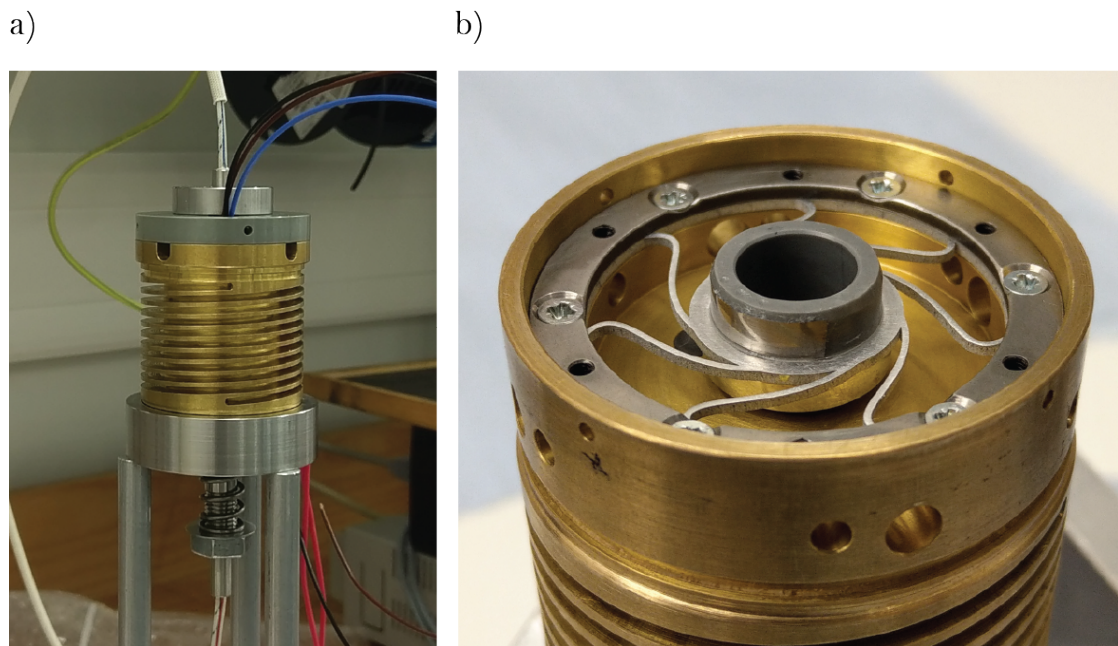


Figure 4.28 – a) Alignment station to glue and align bushings to flexible support; b) Aligned and glued bearing bushing supported on flexible membrane and fitted to electric stator

In case a very high radial stiffness of the bearing bushing support is required, the

flexible membranes can be replaced by solid disks. In combination with the alignment procedure described before, a rigid bearing bushing support can be realized, while still guaranteeing perfect alignment of the bearing bushings in the electric stator.

4.6.7 Assessment of bearing bushing alignment quality

In order to evaluate the alignment quality and repeatability of the developed flexible membrane support, the frictional torque of the rotor shaft during coast-down is measured and compared to the data previously obtained for O-Ring supported bearing bushings (see Fig. 1.3, chapter 1). The frictional torque T_F during coast-down is determined according to Eqn. (4.26), where ω is the angular velocity of the rotor, measured during coast-down, and J_P is the polar mass moment of inertia of the rotor. The determined total frictional torque T_F during coast-down consists of the frictional torque of the radial bearings, the thrust bearing, as well as the winding losses of the rotor.

$$T_F = -\frac{\partial \omega}{\partial t} \cdot J_P \quad (4.26)$$

Figure 4.29 presents four coast-down measurements from 50 krpm to 0 krpm obtained from the new prototype with bearing bushings supported on flexible membranes. The presented measurement results stem from an identical prototype using the same rotor on identical membrane supported bearing bushings and were obtained after dis-assembly and re-assembly of the rotor and/or bearing bushings for inspection as well as after varying length of operational time.

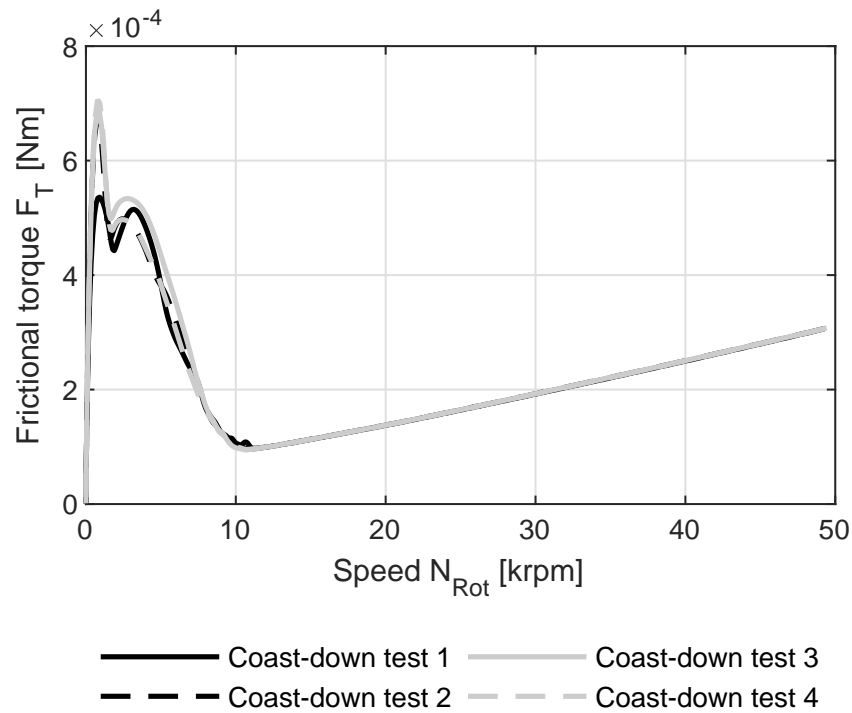


Figure 4.29 – Coast-down measurement results of HGJB bushings supported on flexible membrane

The results in Fig. 4.29 suggest that the coast-down torque and therefore the alignment of the bushings to be unaffected by operational time and to be reproducible after disassembly and re-assembly of the prototype. Compared to the situation with the O-Ring supported bushings (see Fig. 1.3, chapter 1), the membrane solution together with the assembly procedure allows to improve the repeatability of the assembly significantly.

4.6.8 Analysis of the bearing bushing motion

Presented in Fig. 4.30 are the synchronous and sub-synchronous motion amplitudes recorded on the front bearing bushing supported on the flexible membrane Var19 during a speed ramp up to 116 krpm. For geometrical details on the mounted membrane Var19, please refer to Fig. 4.12 and Tab. 4.5. The presented measurement results are taken by means of two LionPrecision displacement probes located on the back measurement plane of the front bearing bushing according to Fig. 4.4.

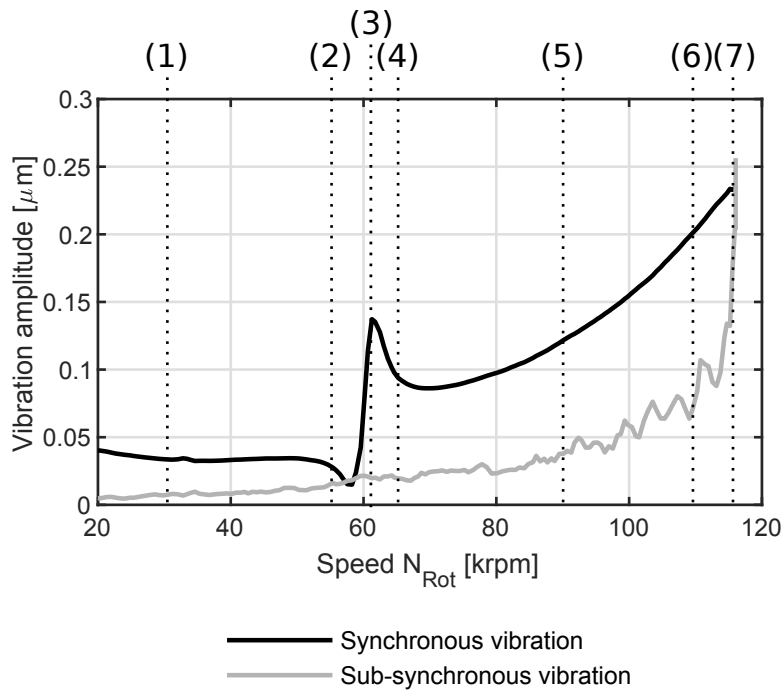


Figure 4.30 – Recorded synchronous and sub-synchronous motion amplitudes of front bearing bushing supported on membrane Var19

As suggested by the evolution of the recorded synchronous motion amplitude, the bearing bushing does not exhibit a motion that can be easily explained. If the motion of the bearing bushing were purely cylindrical, due to the imbalance of the rotor, one would expect to see a steady rise in motion amplitude, roughly proportional to N_{Rot}^2 , up to the critical speed. After crossing the critical speed, the rotor rotates around its center of mass and the measured amplitudes should not evolve anymore with rotor speed. The recorded data, however, presents local minima and maxima, which leads to the conclusion that the bushing motion consists of the super-positioning of a vibration of cylindrical nature as well as a tilting vibration.

The evolution of the sub-synchronous motion amplitude (Fig. 4.30) presents a steady increase until 110 krpm, after which the rise progresses much more quickly until at 116 krpm, at which point the sub-synchronous vibration amplitude exceeds the synchronous amplitude. This phenomena suggests the onset of an instability in the bearing bushing or rotor motion and the prototype was stopped in order to avoid a failure.

Due to the fact that the measurement plane of the two LionPrecision displacement probes is offset to the center plane of the bushing (offset $l_a = 3.25$ mm), any instability in the rotor-bushing-system can be detected, however, the mode of instability can not be identified by this measurement method. The nature of instability of the studied flexible bushing system can either be of cylindrical nature, caused (1) by an unstable radial bushing mode, (2) by a rotor instability transferred to the bushing through

the stiffness of the gas film, or (3) of a tilting nature, caused by a bush tilting mode becoming unstable.

Equipping the measurement setup with two additional Philtec optical displacement probes according to Fig. 4.4, with an offset $l_b = 2.75$ mm to the bushing center plane, and transforming the measurement data into a cylindrical motion and a tilting motion of the bushings, allows to determine the source of the recorded instability presented in Fig. 4.30. The recorded measurement data of the four displacement probes is therefore transformed according to Eqn. (4.3) into the cylindrical motion q_{ex} and q_{ey} , as well as the tilting angles ϕ and θ around the x- and y-axis of the bushing respectively. Performing a Fast-Fourier-Transformation (FFT) on each of the four bushing degrees of freedom q_{ex} , q_{ey} , ϕ and θ then allows to determine whether the origin of the instability is of cylindrical or tilting nature.

Presented in Fig. 4.31 are the resulting frequency spectrums of the cylindrical degrees of freedom q_{ex} and q_{ey} at the center of the front bearing bushing, while Fig. 4.32 presents the spectrums of the two tilting degrees of freedom ϕ and θ .

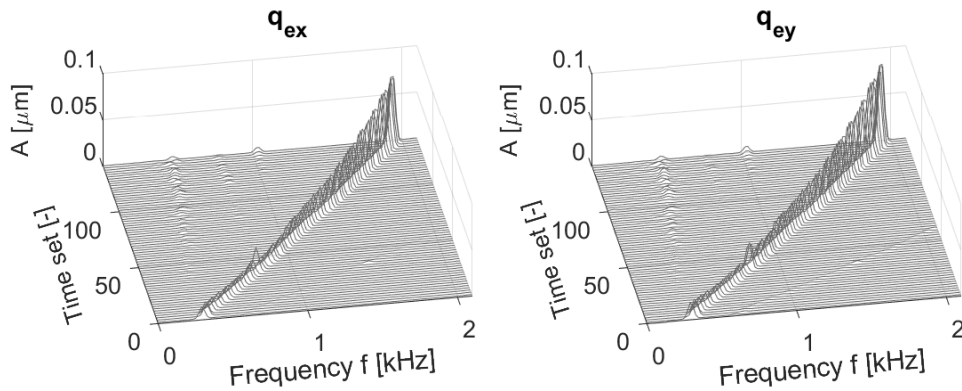


Figure 4.31 – Frequency spectrum of cylindrical bushing motion q_{ex} and q_{ey}

The dominant trace in Fig. 4.31, present in both frequency spectrums of q_{ex} and q_{ey} , whose frequency increases proportional with time, is the synchronous vibration amplitude, which is excited by the imbalance of the rotor. In both frequency spectrums, the synchronous amplitude suggests to increase roughly proportional to N_{Rot}^2 . The maximum value of 1933 Hz for the synchronous frequency corresponds to the maximum rotor speed of 116 krpm obtained in this experiment. As suggested by the presented frequency spectrums in Fig. 4.31, no relevant sub-synchronous vibrations appear, leading to the conclusion that the observed instability does not stem from an unstable cylindrical bearing bushing motion or from a rotor instability.

The frequency spectrums of the two tilting angles ϕ and θ , however, clearly show the presence of sub-synchronous vibrations at around 1000 Hz (60 krpm) for a synchronous frequency of 1933 Hz. To conclude, the results clearly suggest that the origin of the observed instability is caused by an instability in the bearing bushing tilting motion.

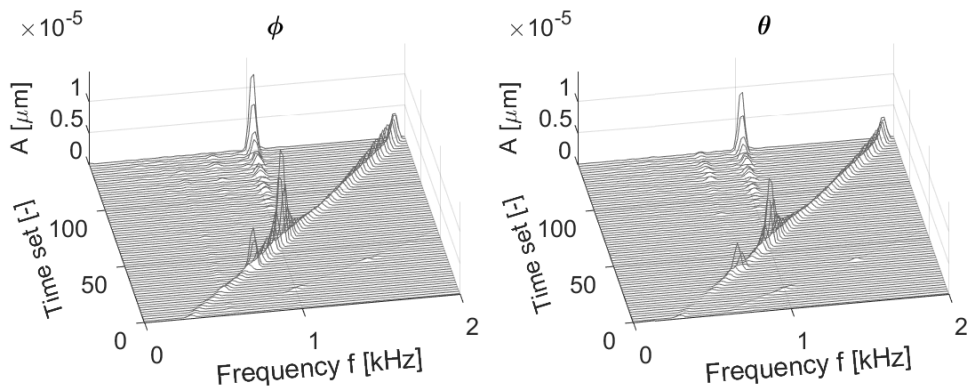


Figure 4.32 – Frequency spectrum of bushing tilting angles ϕ and θ

As previously mentioned, the bearing bushing motion is a superposed cylindrical and tilting motion, depending on the rotational speed of the rotor. In order to better understand the evolution of the bearing bushing motion with speed, its motion has been analyzed by visualizing the bearing bushing axis at distinctive selected speeds from 20 krpm up to 116 krpm, where the onset of bush tilting instability is located.

Figure 4.33 presents the orbits of the back plane (top), center plane (middle) and front plane (bottom), as well as the bearing bushing axis (gray) of the bearing bushing at the selected speeds marked in Fig. 4.30. The front, center and back planes of the bearing bushing are located at $z = +L/2$, $z = 0$ and $z = -L/2$ respectively, where L denotes the length of the bearing bushing.

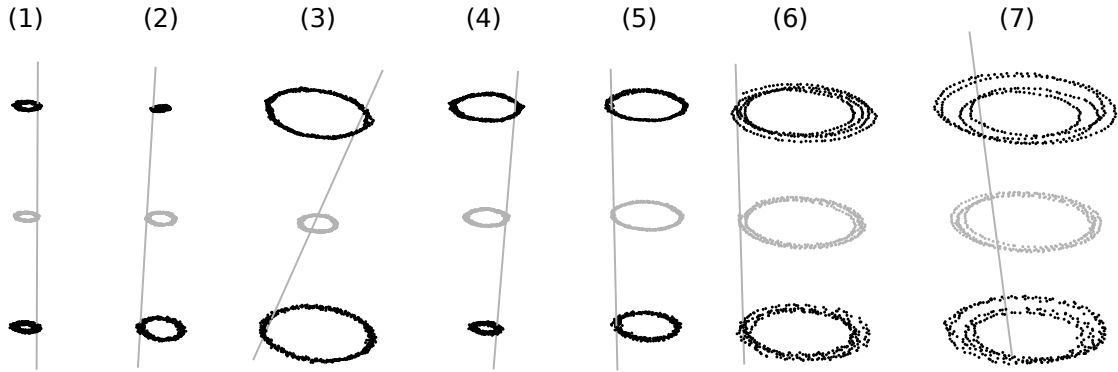


Figure 4.33 – Evolution of measured front bearing bushing motion during a speed ramp from 20 krpm to 116 krpm. The selected speeds for the visualization are marked in Fig. 4.30

At 30 krpm (1), the front, center and back orbits of the bearing bushing are of identical diameter, suggesting a purely cylindrical motion of the bushing due to the imbalance of the rotor shaft. With increasing speed, a tilting motion of the bearing bushing starts appearing (2), which reaches its maximum at 61 krpm (3) to decrease again in amplitude (4) at speeds above 61 krpm, suggesting a bearing bushing tilting mode to be located at 61 krpm, further confirmed by the the prominent peak at 1000 Hz in the frequency spectrum of the tilting angles ϕ and θ (see Fig. 4.32).

In order to confirm the hypothesis of the critical speed of the bush tilting mode to be located at 61 krpm, the critical angular frequency ω_{crit} of the bearing bushing tilting mode is estimated according to Eqn. (4.27) [98].

$$\omega_{crit} = \sqrt{\frac{k_t}{J_{Ttot}}} \quad (4.27)$$

,where k_t is the combined tilting stiffness of the membrane and the gas film and J_{Ttot} is the total transverse moment of inertia of the bearing bushing. Assuming the stiffness of the gas film to be negligible compared to the tilting stiffness k_t of the membrane and inserting the total transverse moment of inertia $J_{Ttot} = 12.19\text{e-}08 \text{ kgm}^2$ and the experimentally determined tilting stiffness $k_t = 4.3 \text{ Nm/rad}$ (refer to section 4.6.3) of the mounted membrane Var19 into Eqn. (4.27), results in a critical angular frequency for the bushing tilting mode of $\omega_{crit} = 5340 \text{ rad/s}$ (945 Hz), corresponding to a rotational speed of 57 krpm. The deviation of 6.6% most probably stems from neglecting the stiffness of the gas film and the fact that the stiffness of the flexible membrane presents some uncertainties due to inconsistent manufacturing, as discussed in section 4.6.3. Nonetheless, the good match between estimation and measurement confirms the presence of a critical bush tilting speed, which is passed at 61 krpm for the bearing bushing flexibly supported on membrane Var19.

A further increase in speed (points (5) and (6)) leads to an increasing cylindrical bushing motion amplitude, while the tilting motion amplitudes remain largely constant, until after 110 krpm, where they start to increase gradually again. Note that the cylindrical motion of the bearing bushing, represented by the gray orbit in Fig. 4.33, retains a circular shape whose diameter grows with speed due to the increasing imbalance force of the rotor acting on the bushing through the stiffness of the gas film.

At 116 krpm (7), where the onset speed of bush tilting instability has been identified, the center plane of the bearing bushing retains a circular shape, whereas the orbits of the front and back bushing planes present a typical half frequency whirl [99]. Figure 4.34 presents the orbits of the front, center and back bearing bushing planes projected in the direction of the rotor axis during approximately four rotor revolutions.

As suggested by the orbit plots of the front and back bushing plane, shown in Fig. 4.34, the front and back orbits present a half-frequency whirl manifesting itself by a whirl orbit of different amplitude appearing every second revolution of the rotor shaft, typical in the presence of an instability. The fact that the center plane orbit remains circular with constant amplitude is clearly indicating the bushing instability to be of tilting nature.

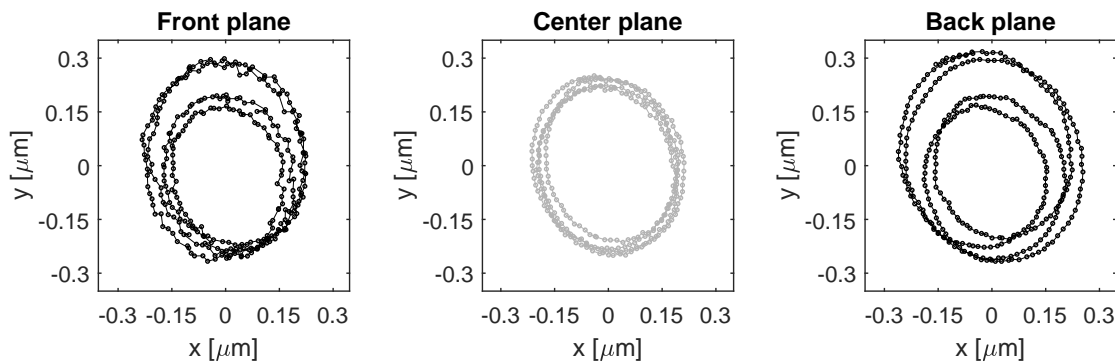


Figure 4.34 – Orbits of front, center and back bushing plane at the onset of instability located at a rotational speed of 116 krpm.

4.6.9 Influence of the bearing bushing inertia on the vibration response and the bush tilting stability

Due to the non-conductivity of the used ceramic material for the bearing bushings, they are equipped with a metal split ring (see Ring 1 in Fig. 4.35) in order for the capacitive LionPrecision probes to capture a signal. In case the additional optical Philtec D20 probes are used, a target surface of high optical reflectivity is needed in order to get a good signal-to-noise ratio, which is why an additional reflective target is fitted on the other side of the flexible membrane support (see Ring 2 in Fig. 4.35) in the measurement plane of the optical Philtec D20 probes.

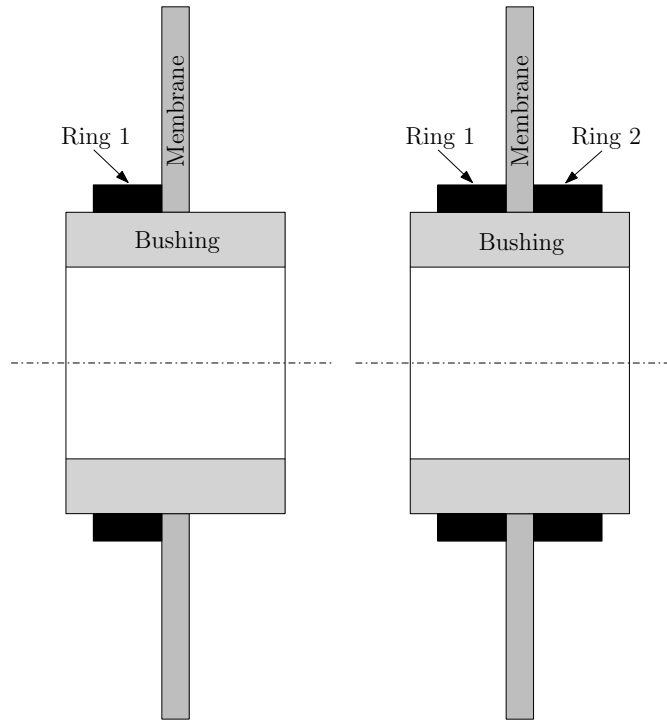


Figure 4.35 – Setup for measurements with optical probes: a) Standard setup containing one ring; b) Additional target ring fitted

Figure 4.36 shows the back side of the prototype. Visible are the outer housing, the electric stator package featuring the flexible membrane support attached with clamp ring and screws and the back bearing bushing, whose movement is captured by two optical Philtec D20 probes on the near side of the membrane and two LionPrecision displacement probes (not pictured) on the far side of the membrane. Figure 4.36 further presents the two options of additional reflective targets chosen to be fitted to the bearing bushings. The options consist of a polished metal foil of thickness $t = 50 \mu\text{m}$ glued to the OD of the bearing bushing (see Fig. 4.36 a)) or a polished metal ring (see Fig. 4.36 b)) of $D_i = 14.2 \text{ mm}$, width $w = 3.5 \text{ mm}$ and thickness $t = 1 \text{ mm}$ fitted. The difference between the two is the transverse inertia added by the reflective target. The very thin metal foil adds negligible additional inertia, whereas the metal ring increases the total transverse moment of inertia $J_{T_{tot}}$ of the bearing bushing by 37%.

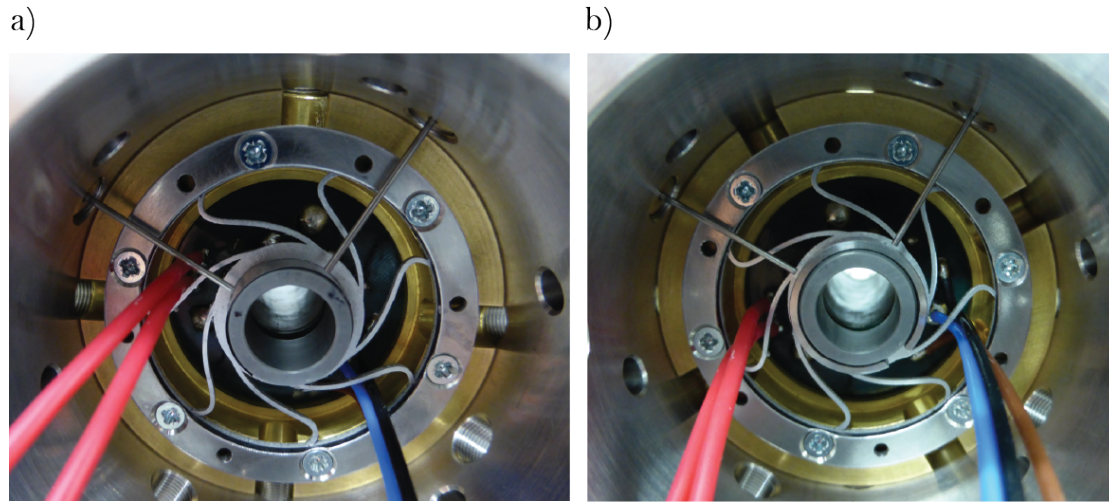


Figure 4.36 – Reflective target options for measurements with optical probes: a) Low inertia metal foil target; b) Polished metal ring target

Assuming the metal ring to be a thin-walled cylinder of mean radius $r_m = 7.6$ mm, mass $m = 1.3$ g and width $w = 3.5$ mm, the determination of the split ring transverse moment of inertia around the center of the bearing bushing is performed by applying the parallel axis theorem, also known as Steiner's theorem [98]. Table 4.7 presents the masses m and transverse moments of inertia J_T of the bearing bushing, the split ring target and the center ring of the membrane connected with the bushing. The mass moment of inertia for the center ring is evaluated for both investigated membrane materials aluminium AL6082-T6 and steel 1.4310.

Table 4.7 – Masses and transverse moments of inertia of bearing bushing, target ring and membrane center ring

Component	Mass m in kg	Inertia J_T in kgm^2
Bearing bushing	2550e-06	6.83e-08
Metal split ring	1292e-06	4.517e-08
Membrane inner ring in AL6082-T6	259.5e-06	0.843e-08
Membrane inner ring in 1.4310	754.4e-06	2.451e-08

The effect of the transverse moment of inertia of the bearing bushing has been investigated during a speed sweep of the prototype compressor featuring the flexible membranes Var19 (for details refer to Fig. 4.12 and Tab. 4.5) without damping measures applied. The tilting stiffness k_t of these membrane is 4.3 Nm/rad according to the measurements performed in section 4.6.3.

Figure 4.37 presents the motion amplitude of the back bearing bushing supported on

membrane Var19 using the thin foil target and compares it to the motion amplitude of the same bushing with the additional metal ring fitted (J_{Ttot} increased by 37%).

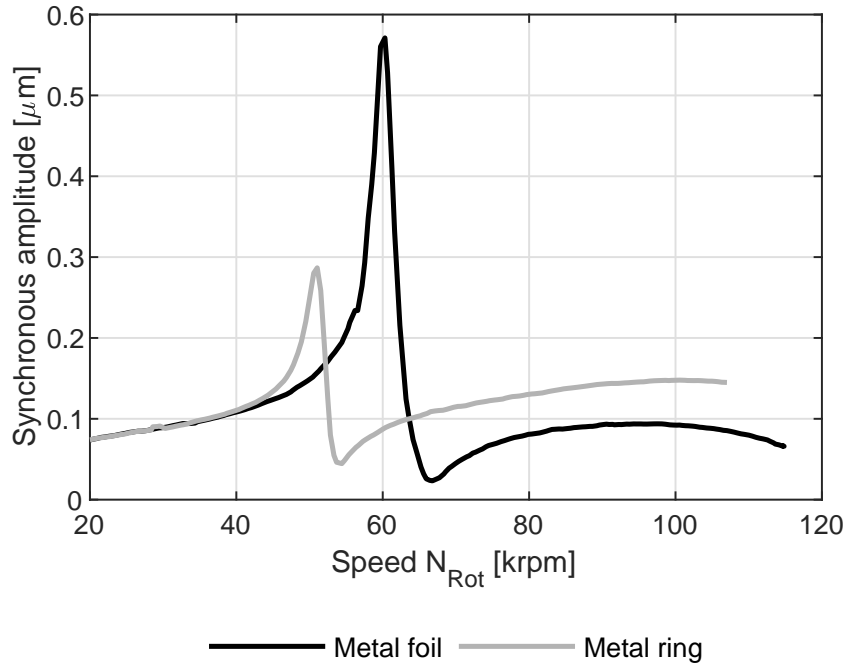


Figure 4.37 – Comparison of back bearing bushing motion amplitudes for metal foil and metal ring target

The prominent peak at 60 krpm, presented in Fig. 4.37 for the measurement with metal foil, has previously been identified as the critical speed of the bearing bushing tilting mode. As suggested by the measurement data, the critical speed of this tilting mode decreases from 60 krpm to 51 krpm due to the increased transverse mass moment of inertia caused by the added ring. Assuming the stiffness of the gas film to be identical at 51 krpm and 60 krpm and using Eqn. (4.27), allows to show that the ratio $\left(\frac{\omega_{crit1}}{\omega_{crit2}}\right)^2$ is only dependent on the ratio of transverse moment of inertia $\frac{J_{Ttot2}}{J_{Ttot1}}$ for the two tests, as presented in Eqn. (4.28).

$$\left(\frac{\omega_1}{\omega_2}\right)^2 = \left(\frac{6283 \text{ rad/s}}{5341 \text{ rad/s}}\right)^2 = 1.38 \stackrel{!}{=} \frac{J_{Ttot2}}{J_{Ttot1}} \quad (4.28)$$

Evaluating $\frac{J_{Ttot2}}{J_{Ttot1}}$, with J_{Ttot2} and J_{Ttot1} being the total transverse moment of the bushing with and without additional ring, respectively, using the inertia data presented in Tab. 4.7 results in a ratio $\frac{J_{Ttot2}}{J_{Ttot1}} = 1.37$, as shown in Eqn. (4.29).

$$\frac{J_{Ttot2}}{J_{Ttot1}} = \frac{6.83e-08 + 2(4.517e-08) + 0.843e-08}{6.83e-08 + 4.517e-08 + 0.843e-08} = \frac{16.707e-08}{12.19e-08} = 1.37 \quad (4.29)$$

The result matches very well with the ratio of critical speeds obtained in Eqn. (4.28), which confirms the assumption that the stiffness of the gas film is reasonably constant in the speed range from 51 krpm to 60 krpm.

Figure 4.38 presents the frequency spectrums obtained by FFT for the tilt angle θ of the flexibly supported back bearing bushing for a speed-sweep with and without additional ring. In both experiments, the speed is linearly increased until instability is detected by means of sub-synchronous vibrations in the FFT spectrum.

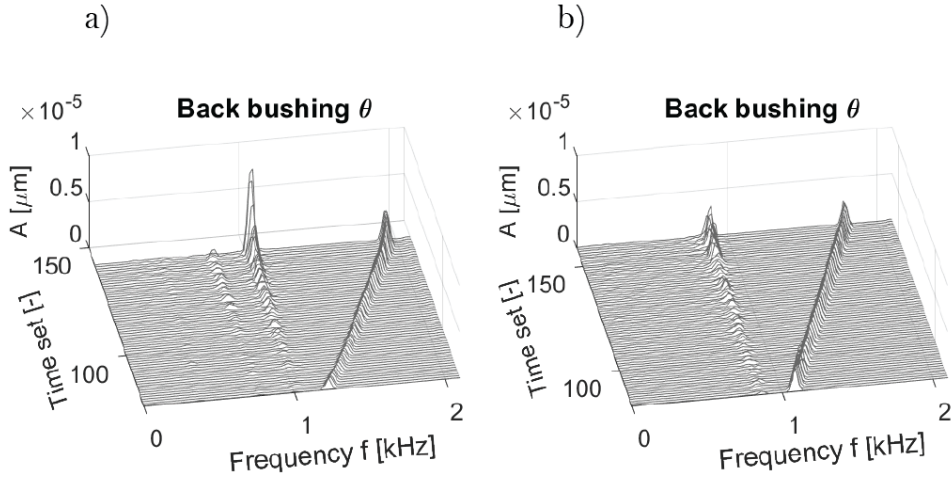


Figure 4.38 – FFT spectrum of back bushing tilt angle θ : a) with metal foil; b) with additional metal ring ($J_{Ttot} + 37\%$)

The FFT spectrums presented in Fig. 4.38 a) and Fig. 4.38 b) both show the proportional increase of the synchronous frequency with speed, which is due to the remaining imbalance of the rotor. Both frequency spectrums show the presence of sub-synchronous vibration in the tilting motion of the bearing bushing, however, the onset of instability is decreased for the bearing bushing featuring an additional ring, increasing the total transverse moment of inertia J_{Ttot} of the bushing. The spectrum of the test with the lower J_{Ttot} bushing (see Fig. 4.38 a)) presents the appearance of sub-synchronous bush tilting vibrations at a synchronous vibration frequency of 1930 Hz, corresponding to a speed of 116 krpm, whereas the sub-synchronous vibrations for the bushing with increased inertia (Fig. 4.38 b)) start appearing at 1783 Hz, which represents a rotational speed of 107 krpm. The sub-synchronous vibrations are at a frequency of 1000 Hz and 850 Hz for the low inertia and high inertia bearing bushing respectively, corresponding to the critical speed of 60 krpm and 51 krpm of the bush tilting mode, as presented in Fig. 4.37.

The critical bush tilting whirl speed ratio Ω_{crit} , defined as the ratio of sub-synchronous to synchronous vibration frequency at the onset of instability, is 0.52 and 0.48 for

the low inertia and high inertia bearing bushing respectively, representing a typical half-frequency whirl.

Figure 4.39 a) presents the predicted critical speed of the forward and backward bearing bushing tilting mode for the high and low inertia bearing bushing supported on membrane Var19, while Fig. 4.39 b) shows the corresponding evolution of the logarithmic decrement Γ_{Bush} with rotational speed.

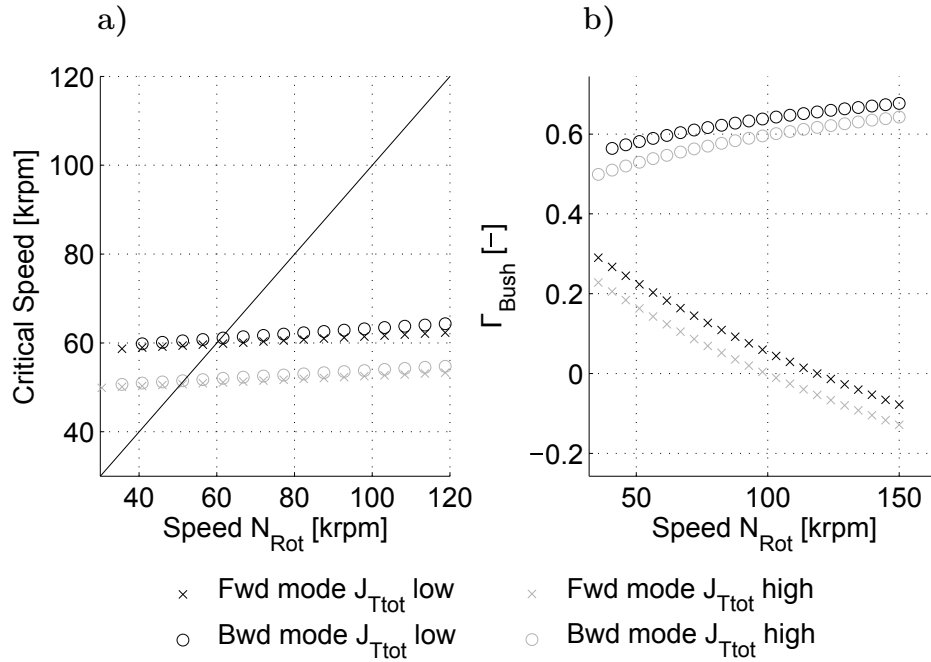


Figure 4.39 – Influence of the bushing transverse moment of inertia. a) Predicted critical speed of bearing bushing tilting mode; b) Logarithmic decrement Γ_{Bush}

As suggested by the predicted whirl speed map presented in Fig. 4.39 a), the critical speed of the bush tilting mode decreases from 60 krpm to 51 krpm if the transverse inertia of the bearing bushing is increased with an additional metal ring, corresponding to a 37% increase in total transverse inertia, matching exactly the observed critical speeds presented in Fig. 4.37. The predicted logarithmic decrement of the bushing motion Γ_{Bush} , representing the onset of instability when $\Gamma_{Bush} < 0$, suggests the bush tilting mode for membrane Var19 to become unstable at 119 krpm for the low inertia bushing. The prediction agrees very well with the observed start of sub-synchronous vibrations at 116 krpm, visible in the frequency spectrum in Fig. 4.38 a). The models predict the speed of instability onset for the bushing tilting motion to drop from 119 krpm to 100 krpm, if the bearing bushing inertia is increased by 37%. The measurement results suggest the onset speed of instability to be at 107 krpm for the high inertia bushing, slightly higher than the prediction obtained from the rotordynamic model.

4.6.10 Influence of the membrane tilting stiffness on the vibration response and the bush tilting stability

Table 4.8 presents the membrane designs and their corresponding radial and tilting stiffness that were tested in the new prototype featuring the flexible membrane support. The stiffness values detailed in Tab. 4.8 represent the design values except for the membranes, where measured values were available (marked with *). For more details on the design of these membranes, please refer to Fig. 4.12 and Tab. 4.5.

Table 4.8 – Radial and tilting stiffnesses of membranes tested in prototype. An asterisk * represents measured values with the designed value provided in brackets

Membrane design	Stiffness k_r in N/m	Stiffness k_t in Nm/rad
Var19	1.12e+06	4.3* (5.1)
Var8	1.12e+06	21.8* (35.2)
Var23	1.11e+06	28.3* (64.8)
Var6	1.14e+06	82.1

With a deviation of $\Delta k_r = 2.7\%$, the radial stiffness of the four membranes implemented in the prototype can be considered identical. The vibration amplitudes measured at the back bearing bushing for all four membranes featuring different tilting stiffnesses is presented in Fig. 4.40 for increasing rotational speeds of the rotor shaft. The investigated speed ranges for where measurements have been performed was restricted by the predicted onset of instability and not surpassed to avoid crashing of the prototype.

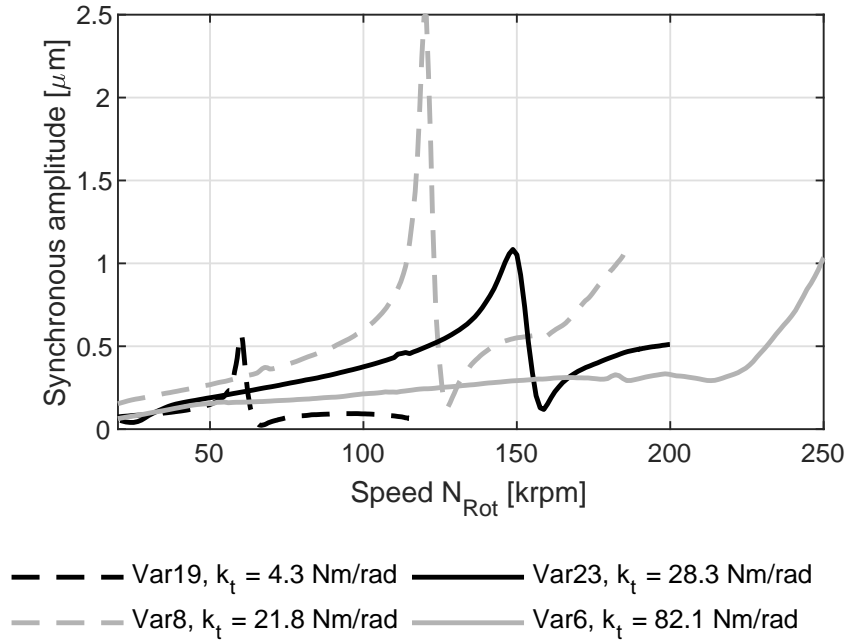


Figure 4.40 – Comparison of back bearing bushing motion amplitudes for membranes Var19, Var8, Var23 and Var6 offering different tilting stiffnesses k_t

As suggested by the measurement results presented in Fig. 4.40, the critical speed of the bearing bushing tilting mode increases with increasing tilting stiffness of the flexible membrane. The critical speed for the bearing bushing tilting mode is at 60 krpm (1000 Hz), 120 krpm (2000 Hz) and 148 krpm (2467 Hz) for membranes Var19, Var8 and Var23 respectively. The critical speed for membrane Var6, offering the highest tilting stiffness, has not been passed completely at 250 krpm (4167 Hz), but is expected to be localized at around 4200 Hz.

Evaluating Eqn. (4.27), under the assumption that the tilting stiffness of the membranes is considerably higher than the stiffness of the gas film, results in an estimated frequency of the bush tilting mode at 945 Hz for membrane Var19, 2000 Hz for Var8, 2280 Hz for Var23 and 4130 Hz for membrane Var6. This represents a relative deviation of -5.5%, 0%, -7.8% and -1.7% between predicted and observed critical frequency of the bush tilting mode for membranes Var19, Var8, Var23 and Var6 respectively.

Figure 4.41 a) presents the predicted critical speed of the forward bearing bushing tilting mode for membranes Var19, Var8, Var23 and Var6, featuring the tilting stiffnesses detailed in Tab. 4.8 and the corresponding bushing inertia in Tab. 4.7. The prediction results are based on the low inertia bearing bushing. Fig. 4.41 b) shows the corresponding evolution of the logarithmic decrement Γ_{Bush} with rotational speed. For illustrational purposes, only the critical speeds and the logarithmic decrements of the forward modes are plotted, since the backward modes are well damped and therefore do not present any concern for instability.

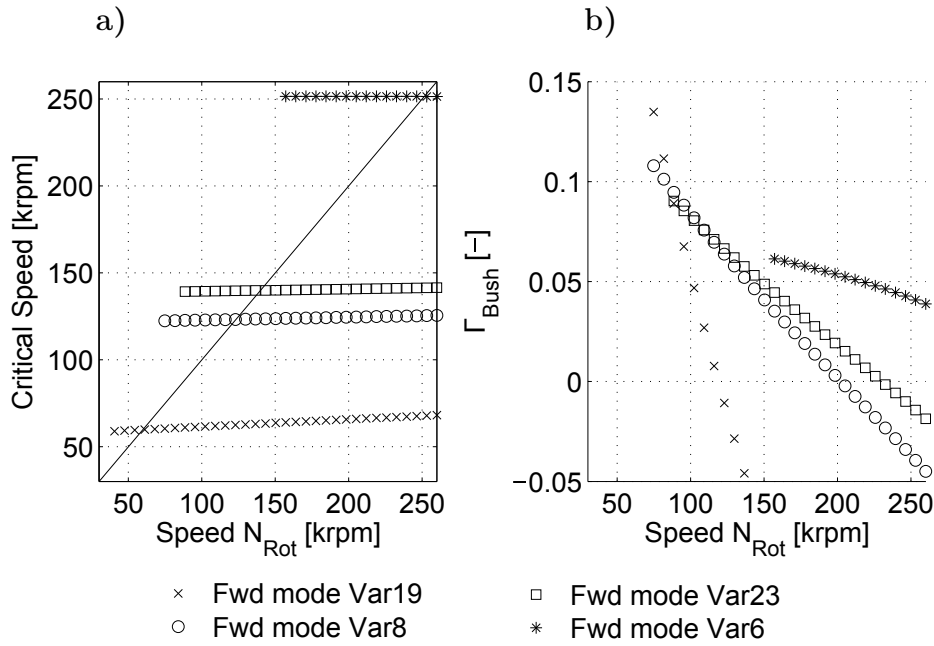


Figure 4.41 – Influence of membrane tilting stiffness for membranes Var19, Var8, Var23 and Var6. a) Predicted critical speed of bearing bushing tilting mode; b) Logarithmic decrement Γ_{Bush}

The predicted results suggest an increase in critical speed with increasing tilting stiffness of the membranes, which corroborates the obtained experimental results presented in Fig. 4.40, as well as the estimation performed using Eqn. (4.27). The rotordynamic model predicts the critical speed of the bushing tilting modes to be at 60 krpm, 123 krpm, 140 krpm and 251 krpm. The obtained prediction results match very well with the critical speeds observed during the measurements with the largest deviation between prediction and measurement being an under-prediction of 5.7% for membrane Var23.

The evolution of the logarithmic decrement Γ_{Bush} with rotational speed, presented in Fig. 4.41 b), suggests the speed of instability onset (SIO) of the bush tilting motion to increase with increasing tilting stiffness of the selected membrane. As stated before, the predicted tilting SIO for membrane Var19 at 119 krpm corroborates very well the experimentally determined SIO of 116 krpm. The predicted SIO for membrane Var8 is at 202 krpm. Due to the fatal consequences of a crash at such a high rotational speed, the SIO has not been experimentally verified, however, a speed of 185 krpm was obtained with these membranes and no sign of instability presented itself. Supporting the bearing bushings on membrane Var23, offering an even higher tilting stiffness than Var19 and Var8, allows stable operation up to 230 krpm according to the prediction presented in Fig. 4.41 b). Again, no experimental verification of the SIO was performed due to a high risk of crashing the prototype. A safe speed of 200 krpm was however reached and no sub-synchronous vibrations detected.

According to the model prediction, a minimum tilting stiffness of $k_t = 40 \text{ Nm/rad}$ is required to allow stable operation ($\Gamma_{Bush} > 0$) in the whole speed range up to 250 krpm. Membrane Var6 was designed with a tilting stiffness of $k_t = 82.1 \text{ Nm/rad}$, therefore offering a high margin against bush tilting instability in the nominal speed range up to 250 krpm.

Figure 4.42 a) and b) present the frequency spectrum of the measured bushing motion during a speed ramp from 0 to 250 krpm for the front and back bearing bushings supported on flexible membranes Var6 (designed $k_t = 82.1 \text{ Nm/rad}$).

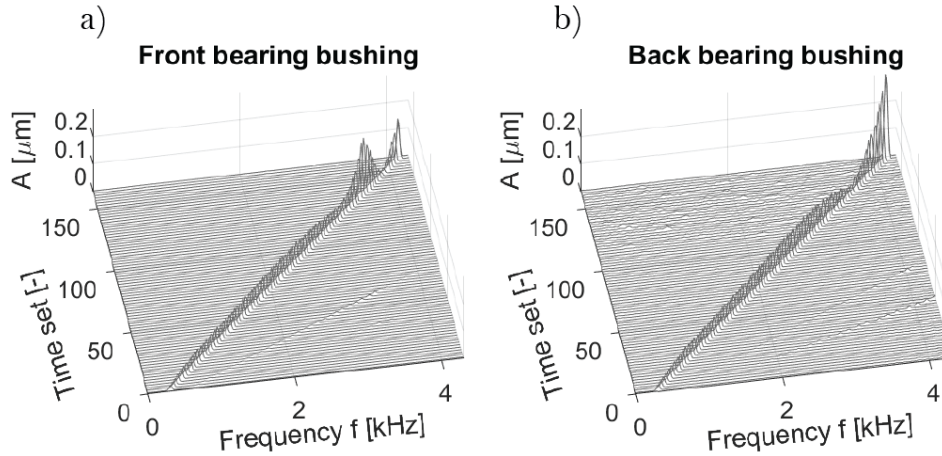


Figure 4.42 – Measured frequency spectrum of bushings supported on flexible membranes Var6 ($k_t = 82.1 \text{ Nm/rad}$): a) Front bearing bushing; b) Back bearing bushing

The absence of any sub-synchronous vibrations in the frequency spectrums presented in Fig. 4.42 suggests stable operation of the prototype up to 250 krpm, which is in agreement with the prediction of the rotordynamic model.

The whirl speed ratio of instability onset Ω_{crit} is generally ≤ 0.5 . It is therefore suggested that the criteria $\omega_{crit} > 0.5 \cdot \omega_{rot}$ has to be fulfilled in order to avoid the bush tilting mode to become unstable in the nominal speed range. The critical frequency ω_{crit} of the bush tilting mode can be evaluated according to Eqn. (4.27) and the stiffness of the gas film neglected, which results in a conservative design guideline.

4.6.11 Influence of the support damping on the bush tilting stability

From the three investigated damping concepts presented in section 4.6.4, the friction disk concept was chosen to demonstrate the effect of external damping on the stability of HGJBs. The friction disk concept allows to provide damping for both the

radial and the tilting motion of the bearing bushings, making it an ideal candidate to experimentally investigate a potential increase in the SIO of the bush tilting mode observed at 116 krpm for the bushings supported on membranes Var19. As suggested by the experimental results presented in section 4.6.4, the installation of the friction disk concept allows to increase the damping coefficient of the radial bearing bushing motion by up to 400%. Its capability of damping the instability in bush tilting motion previously observed at 116 krpm, however, is unclear and will be investigated here by means of a back-to-back comparison. The measurement results of a test run with the bearing bushings supported on membranes Var19 and no damping is performed and is compared to a test-run on the same membranes featuring the friction disk damping concept. Figure 4.43 a) presents the recorded frequency spectrum of the back bearing bush tilting angle θ for the test run without damping, which shows the onset of sub-synchronous vibrations at a synchronous frequency of 1933 Hz, corresponding to a rotational speed of 116 krpm. The measurement data featuring the same rotor, bearing bushings and membranes but including the friction disk concept, were recorded directly after the test run and its results presented in Fig. 4.43 b). As suggested by the obtained frequency spectrum of the back bush tilting angle, no sub-synchronous vibrations and therefore no signs of instability in the bush tilting motion was detected up to a synchronous frequency of 2667 Hz (160 krpm). However, at the maximum recorded speed of 160 krpm during this measurement, slight signs of sub-synchronous vibrations start appearing in the frequency spectrum indicating a soon-to-appear instability in bush tilting motion.

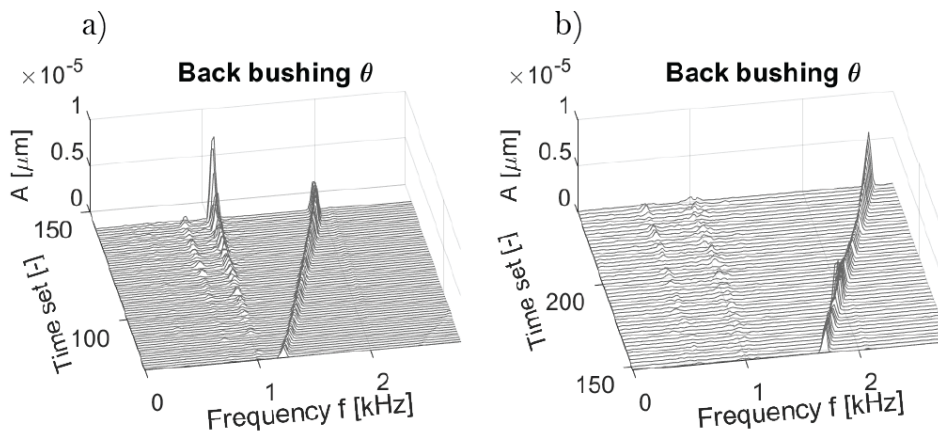


Figure 4.43 – Frequency spectrum of back bearing bushing tilt angle θ : a) Membrane Var19, no damping; b) Membrane Var19, friction disk damping concept installed

According to the presented measurement results, the external damping provided by

the friction disk concept allows to successfully increase the onset of instability of the bush tilting mode from 116 krpm to 160 krpm. This represents a relative increase of 38% and demonstrates the friction disk concept to be effective in damping both radial, as well as tilting bushing motions.

4.6.12 Assessment of long-term flexible support performance

As mentioned in section 4.2, misaligned bearing bushings cause increased low-speed frictional torque and non-repeatable lift-off speeds, which can lead to increased losses and wear on bushings and rotor. In addition to the non-repeatable alignment of O-Ring supported bearing bushings, as shown in Fig. 1.3, the alignment quality of O-Ring supported bushings also varies with operational time, as has been investigated by means of performing start-stop testing. Figure 4.44 a) shows the evolution of frictional torque with the number of performed start-stop cycles for a prototype featuring O-Ring supported bushings, while Fig. 4.44 b) presents the result of identical start-stop testing for the flexible membrane support developed in this chapter.

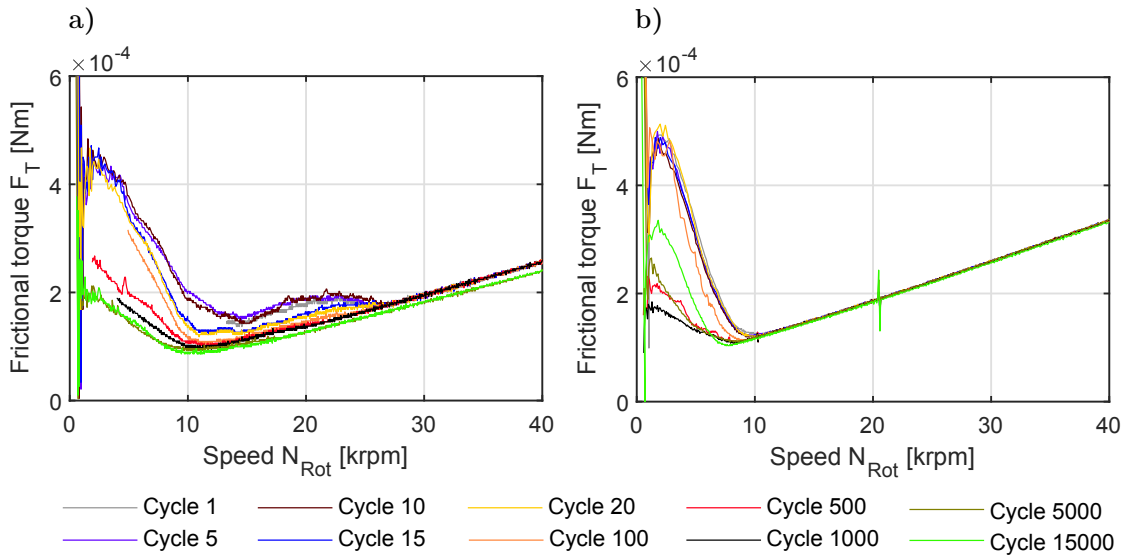


Figure 4.44 – Measured frictional torque during coast-down: a) O-Ring supported bearing bushings; b) Flexible membrane supported bearing bushings

As suggested by the results presented in Fig. 4.44 a), the point of minimum frictional torque, denoting the lift-off speed of the rotor in the radial bearings, changes with the number of performed start-stop cycles for O-Ring supported bearing bushings. It is evident that the alignment of the bearing bushings changes slightly with time, affecting the frictional torque and the lift-off speed of the rotor. Minimizing the lift-off speed of the rotor aims to reduce wear at start/stop since the amount of frictional energy absorbed by dry-friction is reduced. The slight increase in frictional torque at speeds as

high as 27 krpm, suggests that contact between rotor and bushing happens already at relatively high speed, suggesting a non-ideal alignment of the bearing bushings. After a total of 1000 start-stop cycles, the bearing bushings seem to have self-aligned and worn-in, resulting in the measured frictional torque curve to resemble the expected shape of a rotor supported on perfectly aligned bushings, which shows a clear minima, representing the lift-off speed, and a quadratic increase of frictional torque with speed thereafter.

Comparing the results from the O-Ring supported bushings to the ones obtained from the membrane equipped prototype, presented in Fig. 4.44 b), clearly shows that the membrane support offers a more reliable alignment quality that does not change with operational time and number of start-stop cycles. The measured frictional torque resembles the ideal curve from the first cycle and only shows a slight reduction in lift-off speed with the number of performed start-stop cycles, which is most likely caused by a polishing effect of the rotor and bushing surfaces during dry-friction contact at speeds below lift-off.

Presented in Fig. 4.45 a) and b) are photographs of the rotor shaft after 15000 start-stop cycles for O-Ring and flexible membrane supported bearing bushings respectively.

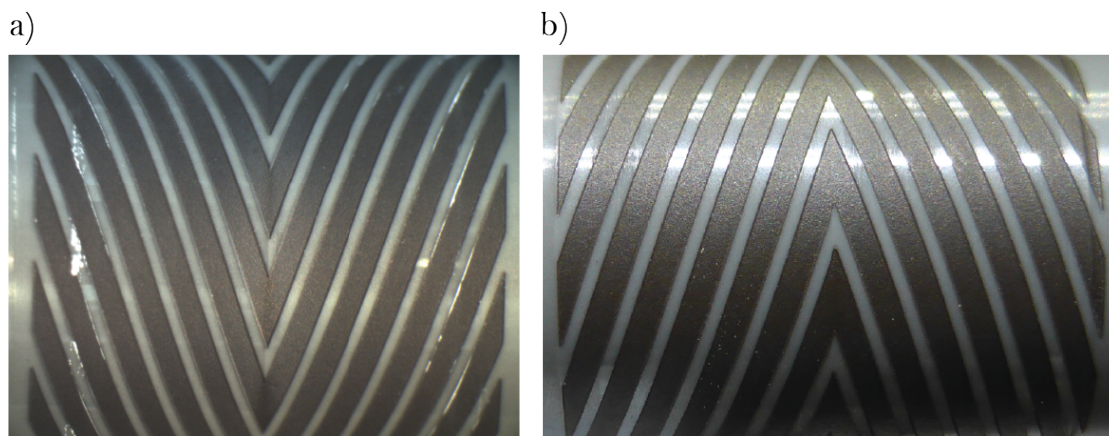


Figure 4.45 – Photograph of rotor shaft after 15000 performed start-stop cycles: a) O-Ring supported bearing bushings; b) Flexible membrane supported bearing bushings

As is evident from the accumulation of white dust in the bearing grooves, caused by dry-friction wear of the SiN rotor and bearing bushing, the rotor running in O-Ring supported bearing bushings presents significantly more wear after 15000 start-stop cycles than the rotor supported on flexible membranes. The rotor running in O-Ring supported bushings shows two zones of dust accumulation at $z = \pm 4L/5$, clearly indicating an angular misalignment of the bearing bushings, whereas the rotor running on membrane supported bearing bushings does not present any significant accumulation of wear particles, suggesting a near perfect alignment of the bushings, that is unaffected by operational time and the number of start-stop cycles performed.

After the successful completion of 15000 start-stop cycles, the prototype featuring membrane supported bearing bushings was subjected to further start-stop testing resulting in the successful completion of a total of 100000 start-stop cycles, corresponding to the number of cycles expected to be performed by a domestic heat-pump during a lifetime of 20 years. The results of the recorded frictional torque are presented in Fig. 4.46.

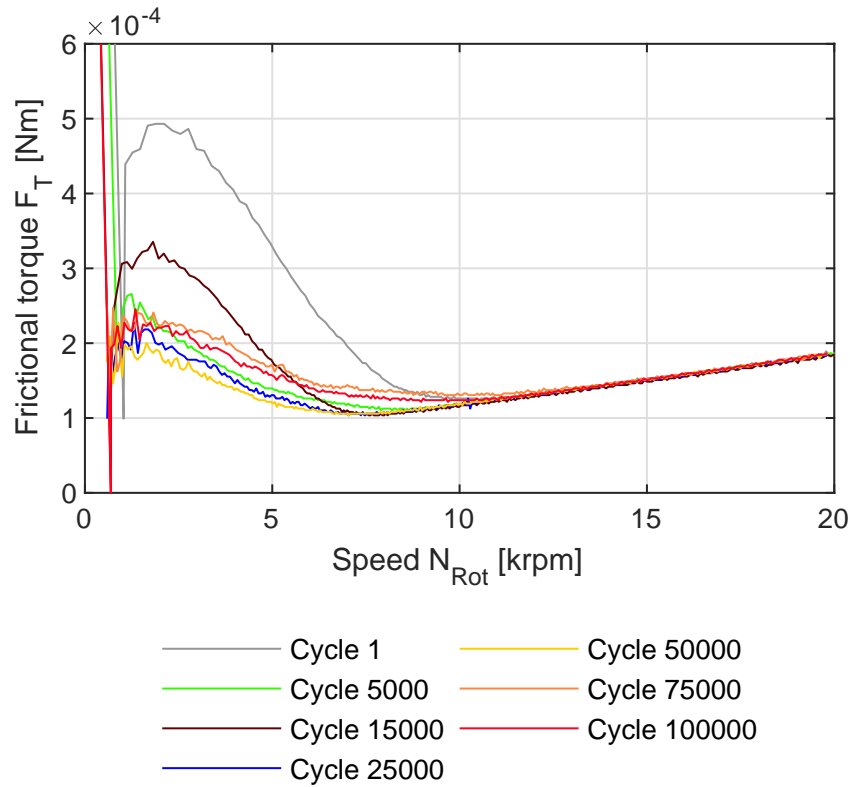


Figure 4.46 – Measured frictional torque during coast-down after 1, 5000, 15000, 25000, 50000, 75000 and 100000 start-stop cycles for membrane supported bearing bushings

As suggested by the recorded frictional torque during coast-down, the alignment quality of the novel flexible bearing bushing support does not change even after completing 100000 start-stop cycles. The only difference in the recorded coast-down frictional torque is a modest increase in rotor lift-off speed after 50000 performed start-stop cycles. This is most likely caused by slight wear of the bushing and rotor and the accumulation of the subsequent dust in the bearing grooves, resulting in a slight deterioration of the bearing performance.

The long term performance of the flexible membrane support has been further assessed by comparing the motion amplitudes of front and back bearing bushings after various number of performed start-stop cycles. Figure 4.47 presents the captured motion amplitudes after 1 cycle, acting as the reference, and a further 1000, 5000 and

Chapter 4. Flexible support for Herringbone-Grooved Journal Bearings

15000 start-stop cycles. Note that the first 1000 cycles were performed from 0-100-0 krpm, whereas the sequence for the remaining tests was 0-50-0 krpm.

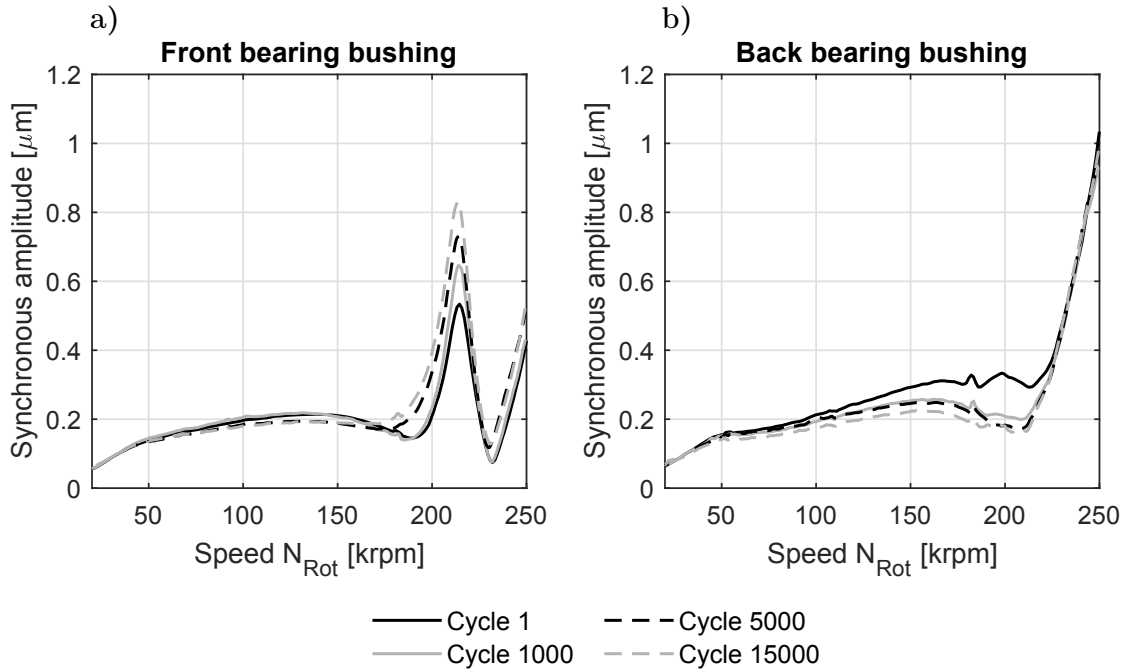


Figure 4.47 – Synchronous bearing bushing motion amplitudes after 1, 1000, 5000 and 15000 start-stop cycles: a) Front bearing bushing; b) Back bearing bushing

It is evident from Fig. 4.47 that the speed of where the highest motion amplitudes occur remains unchanged for both the front and the back flexible supports after 15000 start-stop cycles. The speed of where the motion amplitudes peak represents the critical speed of the bearing bushing tilting motion. The fact that this speed remains unchanged, suggests that the support tilting stiffness is unaffected by the number of performed start-stop cycles. Furthermore, the response of the flexible support in the speed ranges away from the critical bush tilting speed also remains unchanged, which suggests that the radial stiffness of the support does not deteriorate with the number of performed start-stop cycles. The peak response at a critical speed strongly depends on the acceleration rate of the rotor, as was investigated by Hassenpflug et al. [100]. The authors found that the peak response at a critical speed can be reduced by a factor of four or more by using high acceleration rates. Since the speed of the rotor for the experimental results presented in Fig. 4.47 was controlled manually, the acceleration rates differ, which leads to the peak responses not being comparable.

4.7 Summary and chapter conclusions

This chapter presents a flexible support concept for HGJB bushings that allows to independently vary radial and tilting stiffness and that can be coupled to various measures to include damping. The presented flexible support is easy and cheap to manufacture, offers dynamic characteristics that are largely independent of excitation frequency, temperature and age and offers a wide range of support stiffnesses (9 orders of magnitude) that enables the designer to choose the optimum characteristics depending on the application. The proposed flexible membrane concept can be used to support both, individual bearing bushings as well as bearing sleeves that contain both bearing planes within one part.

The FEM based parametric model developed in this chapter enables to quickly and accurately predict the radial and tilting stiffness of the novel flexible support whose output enabled the design of various flexible membrane geometries, which were manufactured and their dynamic characteristics in terms of radial and tilting stiffness experimentally investigated. Furthermore, three damping concepts were presented that offer independently tunable damping coefficient and that can be coupled to the flexible membrane support.

An alignment concept based on thermal expansion was presented and successfully applied numerous times to align two separate bearing bushings of considerable distance within the adopted prototype. The alignment quality of the bearing bushings was then assessed by means of coast-down tests and start-stop testing, which showed significantly better repeatability, no influence of operational time and less wear on rotor and bearing bushings compared to the previously used O-Rings to flexibly support the bearing bushings.

High-speed measurements of the new membrane supported prototype enabled the identification of an unstable bearing bushing tilting mode, whose existence is governed by the bushing transverse moment of inertia and the support tilting stiffness and whose onset speed of instability could be significantly increased by applying one of the presented damping concepts.

By selecting the correct tilting stiffness of the flexible membrane support, it was shown that the prototype can be safely operated up to its design speed of 250 krpm with no signs of rotor or bushing instability present.

A fatigue failure investigation performed on the novel flexible bearing bushing support clearly suggests that the stress level induced by the rotor motion is sufficiently low to achieve unlimited endurance. As a consequence, the flexible support concept presented in this chapter offers an easy to implement solution to introduce flexible and tunable support for fluid film bearings.

Chapter 4. Flexible support for Herringbone-Grooved Journal Bearings

The following conclusions have been drawn from the results obtained in this chapter:

- The Monte-Carlo results obtained using the parametric membrane model developed in this chapter suggest a design space covering 9 orders of magnitude in radial and tilting stiffness, even though the investigated range of design variables is comparatively small. This offers the designer a vast domain to select appropriate stiffness values of the flexible support.
- A deviation of less than 0.2% compared to 1D-models and less than 10% compared to a 3D-model clearly shows very good agreement of the parametric membrane model presented in this chapter with commercial FEM software.
- The parametric membrane model could easily be extended to feature flexible arms of varying width, which would further increase the design space of realizable radial and tilting stiffness.
- For some membranes, a substantial deviation between designed and measured radial and tilting stiffness has been observed. The deviations have been identified to be caused by thermal distortion and geometrical errors caused during the laser cutting process. Alternative manufacturing methods, e.g. water-jet cutting or wire-cut electric discharge machining, would probably lead to less thermal distortion and better geometrical accuracy of the membranes.
- Measurement results suggest that the membrane radial stiffness is independent of the excitation frequency, which makes their use as a flexible support for HGJB bushings significantly easier and more predictable than O-Rings.
- Flexible membranes manufactured from aluminum present less thermal distortion caused by the laser cutting process compared to steel. Furthermore, due to the lower elastic modulus of aluminum, the resulting flexible arms are thicker and wider for the same stiffness compared to steel membranes. For a given absolute manufacturing tolerance, this results in a less sensitive design in terms of manufacturing tolerances.
- The measured equivalent damping coefficients of the three presented damping concepts are in the same order of magnitude as the previously used silicone O-Rings, which offered favorable damping characteristics to support a Herringbone-Grooved Journal Bearing bushing. The investigated damping concepts are able to increase the damping coefficient of a membrane by up to 860%, which makes them viable candidates to be coupled with the modular flexible membrane support.
- The presented alignment concept, based on thermal expansion, offers reliable and accurate alignment of the bearing bushings. The alignment concept in combination with the presented flexible membrane structure allows to flexibly

support separate bearing bushings of considerable distance as well as bearing sleeves containing both bearing planes in one part. Furthermore, the flexible membranes can be replaced by solid disks in order to realize a rigid support structure with no trade-off in alignment quality.

- An unstable bushing tilting mode was discovered, whose appearance is primarily governed by the bushing transverse moment of inertia, the support tilting stiffness, the amount of damping and secondarily by the stiffness and damping properties of the gas film. Increasing the transverse moment of inertia of the bearing bushing leads to a decrease in the speed of instability onset, whereas a higher tilting stiffness of the flexible bushing support increases the onset speed of the bush tilting instability. Furthermore, it was shown that by introducing damping, the onset speed of the bush tilting instability could be increased from 116 krpm to 160 krpm.
- A method to determine the critical speed of the bearing bushing tilting mode was presented. It is suggested that the criteria $\omega_{crit} > 0.5 \cdot \omega_{rot}$ has to be fulfilled in order to avoid instability due to bush tilting. This results in a conservative design guideline since the stiffness of the gas film is neglected.
- The rotordynamic models available at LAMD reliably predict the onset of bearing bushing tilting instability. The effects of increased bearing bushing transverse moment of inertia, as well as the influence of the membrane support stiffness have been correctly predicted by the available tools.
- Lifetime assessment of a typical membrane geometry has been performed by means of an FEM analysis and a fatigue failure investigation. Assuming a radial vibration amplitude of 5 μm , induced by the imbalance of the rotor shaft, results in a safety factor for life of 1020 and a safety factor for stress of 2.4, suggesting unlimited lifetime of the presented novel flexible bearing bushing support.
- The proposed flexible support for HGJB bushings presents improved alignment of the bearing bushings, which is unaffected by operational time and is reproducible after dis-assembly and re-assembly of the prototype. Furthermore, wear after 15000 start-stop cycles is significantly reduced compared to O-Ring supported bearing bushings.

5 Enhanced groove geometries for Herringbone-Grooved Journal Bearings

This chapter presents the results of a theoretical and experimental investigation of the potential of enhanced groove geometries to increase the bearing clearance of a Herringbone-Grooved Journal Bearing supported rotor on rigidly support bearing bushings. Multi-objective optimizations are performed to study various groove geometries of different complexity and their effect on the stability of a particular rotor geometry. The theoretical results obtained from a rigid-body rotordynamic model suggest a possible increase of more than 300% in instability onset speed when enhanced groove geometries are used compared to the rotor featuring the same radial clearance but classical grooves. One rotor shaft with classical grooves, representing the base-line rotor, and four rotors of identical diameter and clearance, but with enhanced grooves of varying degrees of complexity are manufactured and experimentally tested. The experimental results show a significant increase of the instability onset for the rotors featuring enhanced grooves compared to the base-line rotor with classical grooves and identical bearing clearance. Experimental results of the classical rotor showed the onset of instability to be at a rotational speed of 56 krpm, whereas a speed of 180 krpm was achieved when enhanced groove geometries were applied to the rotor, agreeing very well with the theoretically predicted results. Furthermore, the rotor featuring only a varying groove angle along the rotor axis was found to perform similarly to fully enhanced grooves of varying groove width, depth and angle, hence representing a good trade-off between performance increase and design cost.

5.1 Introduction

Conventional HGJB groove geometries feature constant groove angle β , width ratio α and depth ratio H along the rotor axis and are usually engraved into the rotor by means of a laser.

As suggested by the results presented in chapter 2, the approach of directly altering the gas film itself by means of enhanced groove geometries offers a large potential

Chapter 5. Enhanced groove geometries for Herringbone-Grooved Journal Bearings

in increasing the stability of the rotor-bearing-system, hence allowing an increase in bearing clearance.

The approach of altering the gas film itself by means of optimized groove geometries was followed by a number of researchers, namely Ikeda et al. [53], who investigated the effect of non-uniform grooves by defining grooves that change linearly in axial rotor direction. The authors compare a rotor with classical grooves to a rotor featuring enhanced grooves of varying depth, width and angle along the rotor axis. The experimental investigation suggested that by using enhanced grooves, the maximum rotational speed before instability occurs could be increased by 20% compared to a classical groove pattern.

Schiffmann [26] performed multi-objective optimizations of enhanced groove geometries for a particular rotor geometry on rigidly supported bearing bushings, whose results suggest a possible increase in bearing clearance by up to 80%, while maintaining the same rotordynamic stability.

The potential of enhanced groove geometries was also investigated for spiral grooved thrust bearings, namely by Hashimoto and Ochiai [84], who found that a spline-shaped optimized groove geometry is able to significantly increase the stiffness and stability of a hydrodynamic gas film thrust bearing compared to conventionally used logarithmic Spiral-Grooved Thrust Bearings.

5.2 Motivation and nature of the issue

In addition to the previously presented benefits that come with an increase in bearing clearance, namely reduced windage losses and the relaxation of manufacturing and alignment tolerances, which yields a decrease in manufacturing cost and a reduction in waste from parts out of tolerance, the application of enhanced groove geometries offers the advantage of increased bearing performance for almost no additional cost.

Gas bearing supported rotors for high-speed turbomachinery are usually manufactured from materials like high-strength steel, ceramics or tungsten carbide due to their favorable ratio of elastic modulus to density, as well as high mechanical strength. The raw materials, manufacturing and assembly requires considerable financial investment and there is a clear interest in a reduction of waste parts not passing quality control.

The matching of rotors and bearing bushings is a viable option in the production of large series and can help to reduce waste by finding matching rotor-bushing pairs that present the required clearance, e.g. a rotor that is too large is matched to a bushing that is too large. However, remaining rotors or bushings that do not respect the manufacturing tolerances and can not be saved by part-matching due to too large clearances, could potentially be saved with the application of enhanced groove geometries, resulting in a further reduction in cost.

The theoretical investigation performed by Schiffmann [26] suggests very promising results for the application of enhanced groove geometries in Herringbone-Grooved Journal Bearing supported rotors. However, there is no experimental validation of the effect of enhanced groove geometries for HGJBs except the one by Ikeda et al. [53], who performed a theoretical and experimental investigation of one rotor featuring varying groove depth, width and angle simultaneously.

Multi-objective optimizations require high computational resources, which roughly increase linearly with the number of variables to be optimized [101]. The optimization of a fully enhanced groove design, featuring variable groove angle β , groove width ratio α and groove depth ratio H , whose values are defined at four interpolation points along the z-axis, requires the optimization of 12 design variables. In case the same performance enhancement is achievable with an enhanced groove design of reduced complexity, the computational resources could be reduced significantly. Furthermore, the manufacturing of fully enhanced grooves with varying α , β and H along the rotor axis can lead to an increase in cost of laser-grooving, if the average groove depth is deeper compared to classical grooves.

In order to save computational resources and design/manufacturing cost, the identification of the groove design variables that are offering the highest performance increase potential is of high interest, an important aspect that has not yet been treated in the current literature.

As was suggested by the results obtained in chapter 2, a flexible bearing bushing support does not always enhance the stability of a rotor-bearing-system. Below a certain threshold clearance, a rigid support offers higher performance than a flexible bushing support. Due to the fact that the application of enhanced grooves alters the behavior of the gas film directly, enhanced grooves offer a viable option to increase the stability and/or the bearing clearance for cases where a rigid bushing support is favorable.

5.3 Goals and objectives

The objectives to be treated in this chapter are listed below:

1. Theoretical investigation of the potential of enhanced grooves to increase bearing clearance while keeping rotordynamic stability for the rotor of a LAMD prototype.
2. Design and manufacturing of five rotors featuring varying degrees of enhanced groove complexity to be tested in a prototype previously equipped with a classically grooved rotor.
3. Experimental validation of LAMD simulation codes for gas bearings featuring enhanced groove geometries.

Chapter 5. Enhanced groove geometries for Herringbone-Grooved Journal Bearings

4. Experimental performance investigation and comparison of five rotors featuring varying degrees of enhanced groove complexity.
5. Identification of groove parameters suggested to offer the highest potential to increase stability and/or bearing clearance.

5.4 Methodology

5.4.1 Methodology for theoretical investigation

The theoretical investigations performed in this chapter are based on the same rotordynamic model presented in section 2.4.1 of chapter 2, however, since the current investigation focuses on enhanced groove geometries on rigidly supported bearing bushings, the support stiffness k_S is set to a very high value in order to simulate a rigid support.

Table 5.1 presents the rotor and bearing properties of the rotor to perform the theoretical and experimental enhanced groove geometry exploration.

Table 5.1 – Rotor design properties for theoretical and experimental enhanced groove geometry exploration

Bearing diameter D_{Brg}	8 mm
Bearing length-to-diameter ratio L_{Brg}/D_{Brg}	1
Rotor mass m_{Rot}	0.0271 kg
Polar rotor inertia J_P	6.073e-07 kgm ²
Transverse rotor inertia J_T	7.782e-06 kgm ²
Bearing distance l	24.78 mm
Distance front bearing mid-plane to rotor center of gravity l_a	8.65 mm
Distance back bearing mid-plane to rotor center of gravity l_b	16.13 mm
Nominal rotor speed N_{Rot}	180 krpm

Table 5.2 presents the boundary conditions of the multi-objective optimizations performed for the rotor with the design properties summarized in Tab. 5.1. The results of the multi-objective optimizations presented in this chapter have been obtained by using the same evolutionary optimizer as in chapter 2.

Table 5.2 – Range of design variables for the performed multi-objective optimizations

Groove width ratio $\alpha \in$	[0.35, 0.65]
Groove angle $\beta \in$	[110, 170] deg
Groove depth ratio $H \in$	[1.0, 6.0]
Bearing length ratio $\gamma \in$	[0.5, 1.0]
Radial bearing clearance $C \in$	[3, 20] μm

Multi-objective optimizations are performed for five groove patterns of varying degree of groove complexity. The list below presents the name of the rotors as referred to in this chapter, as well as the groove parameters that were held constant or varied along the rotor axis:

- *classic*: straight grooves of constant groove width ratio α , constant groove angle β and constant groove depth ratio H
- *alpha_var*: enhanced grooves with variable groove width ratio α , but constant groove angle β and constant groove depth ratio H
- *beta_var*: enhanced grooves with variable groove angle β , but constant groove width ratio α and constant groove depth ratio H
- *alpha_beta_var*: enhanced grooves with variable groove width ratio α and variable groove angle β , but constant groove depth ratio H
- *alpha_beta_hg_var*: enhanced grooves with variable groove width ratio α and variable groove angle β and variable groove depth ratio H

Note that the groove parameters that are left constant along the rotor axis are also optimized individually for each rotor. This results for example in different groove depth ratios H for the rotors *classic*, *alpha_var*, *beta_var* and *alpha_beta_var*.

5.4.2 Experimental methodology

The experimental measurement campaign aims to identify the performance of various enhanced groove patterns by comparing the results to a base-line rotor featuring classical grooves of constant groove angle β , width ratio α and depth ratio H . Five rotors are therefore manufactured with the groove patterns *classic*, *alpha_var*, *beta_var*, *alpha_beta_var* and *alpha_beta_hg_var* and their performance experimentally evaluated in terms of rotordynamic stability.

Chapter 5. Enhanced groove geometries for Herringbone-Grooved Journal Bearings

Description of test-rig

The rotor design properties presented in Tab. 5.1 correspond to the prototype rotor designed by P. Wagner during his PhD thesis [102] at EPFL. The prototype served as a proof-of-concept for a steam-driven micro-recirculation fan for solid oxide fuel cell systems and features a rotor shaft with classically grooved HGJBs.

The prototype is instrumented with four capacitive displacement probes, capturing rotor displacements in x- and y-direction both on the front (fan-side) and the back (turbine-side) of the rotor shaft. An optical displacement probe is mounted on the stator part of the prototype facing the thrust disk of the rotor and captures a trigger mark which provides information about the phase angles and rotational speed.

Figure 5.1 a) presents the fan-side of the prototype used to experimentally investigate the effect of enhanced groove geometries. Shown are the two nozzles that allow to drive the rotor by means of compressed air aimed at the fan, the optical Philtec probe aiming on a mark on the thrust disk and providing information about phase angles and rotor speed, as well as the four capacitance probes to measure the rotor orbits. The turbine-side of the prototype is shown in Fig. 5.1 b) with the turbine volute mounted. Supplying compressed air to the turbine inlet allows for a second driving-mode to power the rotor shaft.

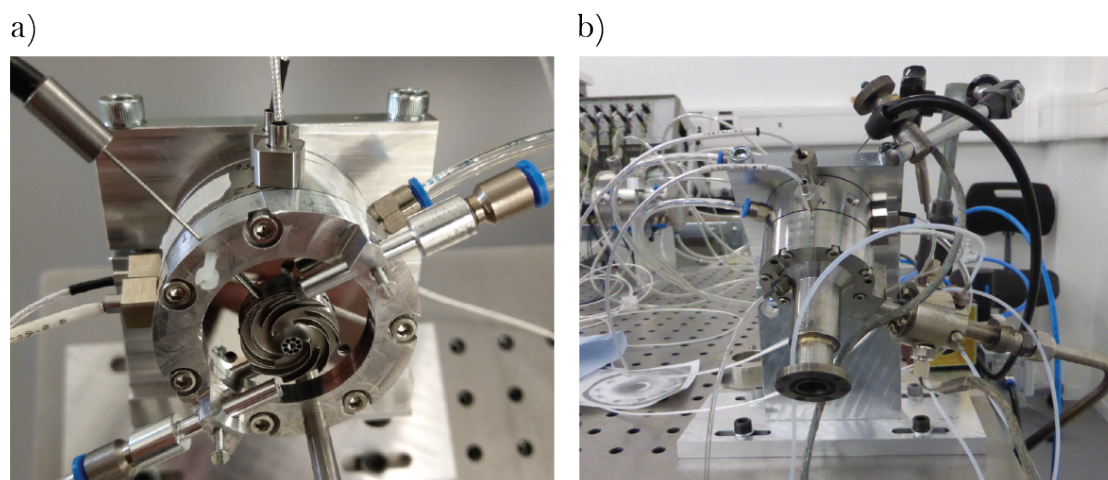


Figure 5.1 – Experimental setup for the enhanced groove exploration: a) Fan-side of rotor shaft; b) Turbine-side of rotor shaft

As was found during the experimental campaign, the fan-driven operational mode allows smooth starting of the rotor but induces unwanted noise in the frequency spectrum of the captured rotor motion. The turbine-driven operational mode does not induce any unwanted vibrations, however, controlling the rotational speed is difficult at low speeds. A coupled operational scheme was therefore adapted that allows to

smoothly start the rotor shaft by means of the fan and is then followed by a transition into the turbine-driven operational mode for high-speed measurements, free of any unwanted noise.

Table 5.3 summarizes the list of instruments used to perform the experimental enhanced groove exploration.

Table 5.3 – List of instrumentation for enhanced groove geometry exploration

Device	Model
Capacitive displacement probes	Lion precision C3S
Optical displacement probe	Philtec D20
Signal amplifier	Lion Precision CPL290
DAQ system	NI PXIe-1078/6356

The measurement data captured from the displacement probes is treated in LabView, where information about synchronous and sub-synchronous motion amplitudes are provided as well as the frequency spectrum of the rotor motion, which allows to identify sub-synchronous traces indicating a rotor instability.

5.5 Results and discussion

5.5.1 Results of multi-objective optimizations

Figure 5.2 a) presents the evolution of the groove width ratio α against radial clearance C for the rotors *classic* and *beta_var* that feature a constant groove width ratio α along the rotor axis. Figure 5.2 b) presents the same results for rotor *alpha_var* with varying groove width along the rotor axis. For information about the location of the interpolation points Pos1..Pos4, please refer to Fig. 2.2 in chapter 2.4.1.

The results presented in Fig. 5.2 a) suggest no clear trend for the groove width ratio α below a clearance value of 7 μm . At clearance levels above 7 μm , the optimizer converges towards wide grooves for both rotors *classic* and *beta_var*. As suggested by the optimizer results presented in Fig. 5.2 b), when the groove width ratio α is left to vary along the rotor axis, the optimizer favors broad grooves in the center region and grooves of reduced width ratio α towards the groove edges for low clearances, whereas for clearances above 8.5 μm the optimizer converges to a wide groove design for the whole groove length.

The evolution of the groove width ratio α for the rotors *alpha_beta_var* and *alpha_beta_hg_var* is presented in Fig. 5.3 a) and b) respectively.

Chapter 5. Enhanced groove geometries for Herringbone-Grooved Journal Bearings

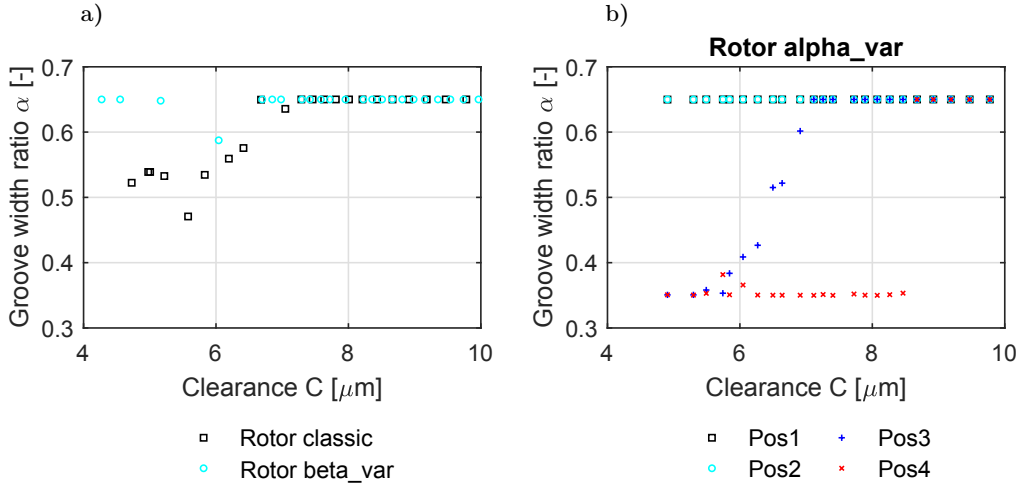


Figure 5.2 – Optimization results for groove width ratio α : a) Rotor *classic* and *beta_var* with constant groove width; b) Rotor *alpha_var* with varying groove width

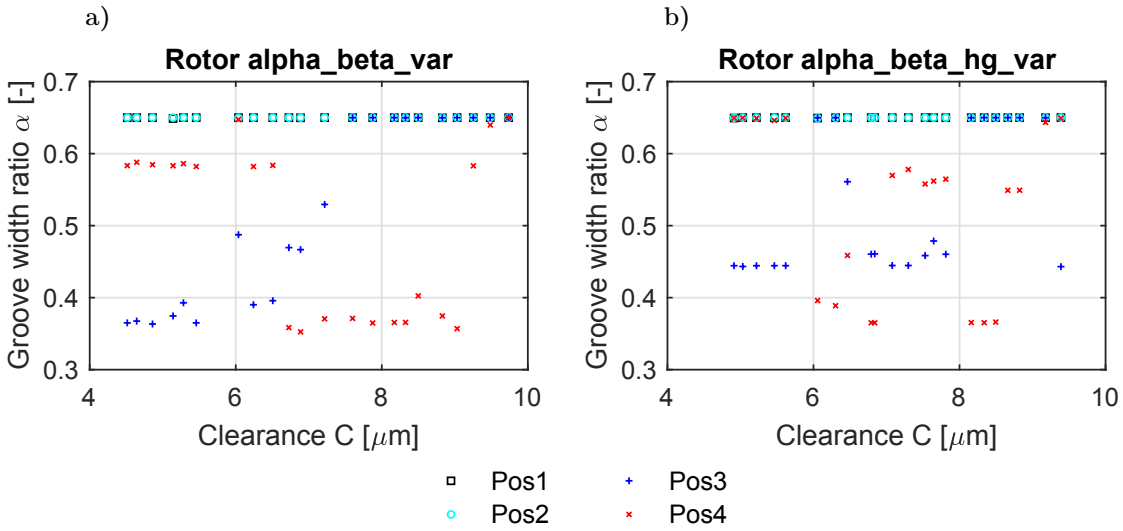


Figure 5.3 – Optimization results for groove width ratio α : a) Rotor *alpha_beta_var*; b) Rotor *alpha_beta_hg_var*

Similar to the results obtained for the rotor *alpha_var*, the results for rotors *alpha_beta_var* and *alpha_beta_hg_var* suggest α_{Pos1} and α_{Pos2} to converge towards the higher limiting bound of 0.65, regardless of the radial clearance C . This corresponds to a wide groove design in the center region of the bearing. For the groove width ratio towards the edge region of the bearing (Pos3 and Pos4), no clear trends can be deduced from the optimization results.

The evolution of optimum groove angle β as a function of the bearing clearance C for rotors *classic* and *alpha_var* is presented in Fig. 5.4 a), whereas Fig. 5.4 b) shows the

results for rotor *beta_var* at the four interpolation points along the rotor axis.

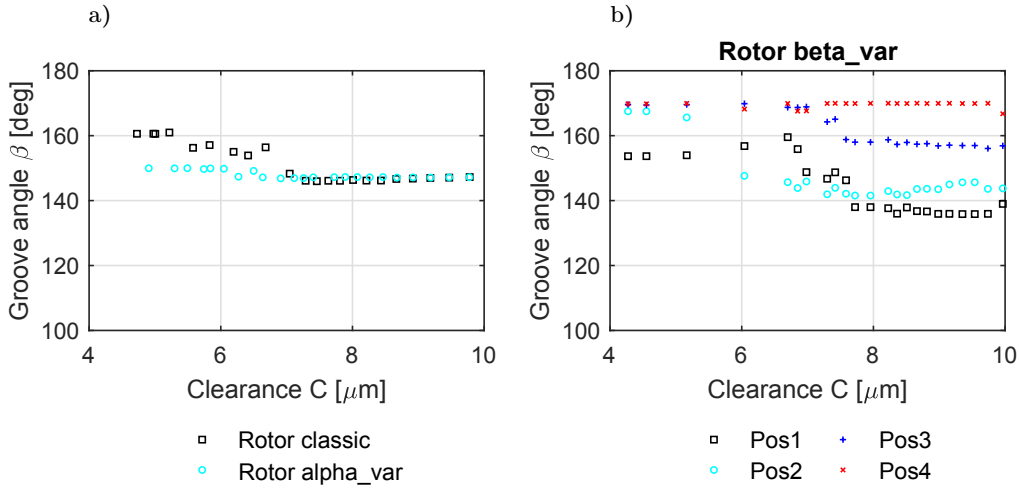


Figure 5.4 – Optimization results for groove angle β : a) Rotor *classic* and *alpha_var* with constant groove angle; b) Rotor *beta_var* with varying groove angle

Figure 5.4 a) suggests the optimized groove angle β to be larger for the rotor *classic* compared to rotor *alpha_var* for clearances below 7 μm . For clearances above 7 μm , the optimization results suggest the optimum groove angle β to be around 146 deg for both rotors. The optimized groove angles β at each interpolation point for rotor *beta_var* (see Fig. 5.4 b)) suggests the ideal groove angle to be steep at the edge region (Pos4) and flatter towards the center of the bearing. Furthermore, the optimization results for low clearances suggest the optimum grooves to be steep and straight at the edge region (same angles at Pos2, Pos3 and Pos4), to then flatten quickly towards the land region (Pos1). At higher clearances however, the transition from steep grooves at the edge region to flat grooves in the center becomes smoother due to the optimizer converging to a groove angle β that gradually decreases towards the center plane of the bearing.

The evolution of the groove angle β for rotors *alpha_beta_var* and *alpha_beta_hg_var* is presented in Fig. 5.5 a) and Fig. 5.5 b) respectively.

Similar to the results obtained for rotor *beta_var* (see Fig. 5.4 b)), the ideal groove angle is suggested to be steep at the groove edges and flat in the center region for clearances above 6 μm . For clearances below 6 μm , the optimizer suggests the ideal groove angle β for rotor *alpha_beta_var* to be flat in the edge region, get steeper in Pos2 and Pos3 to then become flatter again towards the center of the bearing. The rotor *alpha_beta_hg_var* presents a different trend below a clearance of 6 μm , favoring flat grooves at the edge that become steeper towards the center.

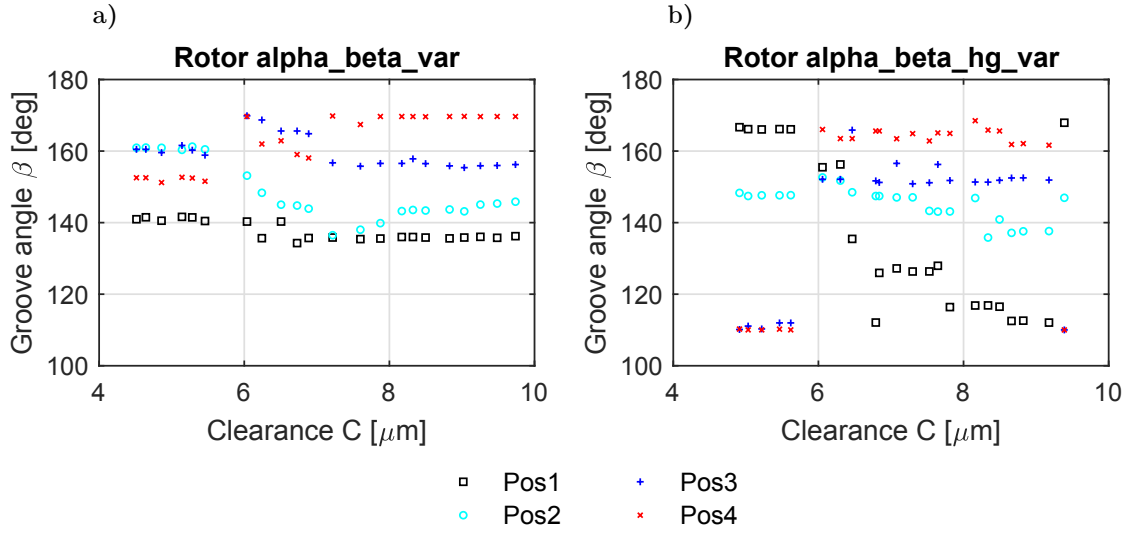


Figure 5.5 – Optimization results for groove angle β : a) Rotor *alpha_beta_var*; b) Rotor *alpha_beta_hg_var*

The results for the groove depth ratio H are presented in Fig. 5.6 a) for the rotors featuring constant groove depth along the rotor axis, while Fig. 5.6 b) shows the optimized results at each interpolation point for rotor *alpha_beta_hg_var*, which features variable groove depth along the rotor axis.

As is evident from the evolution of the groove depth ratio H presented in Fig. 5.6 a), the optimum groove depth seems to be largely independent of the radial clearance C as well as the groove pattern. The optimizer converges to a groove depth ratio of $H=2$ for all designs that feature a constant groove depth along the rotor axis. In the case of a variable groove depth, as presented for rotor *alpha_beta_hg_var* in Fig. 5.6 b), the optimizer suggests the optimum groove to be deep in the edge and land region and shallow in-between for clearances below $6 \mu\text{m}$. Above a clearance level of $6 \mu\text{m}$ however, the optimizer converges to a shallow groove design for almost the whole groove length, that deepens significantly towards the center region of the bearing.

Figure 5.7 presents the results obtained by multi-objective optimization for the dimensionless bearing length γ . As suggested by the results, all bearing designs converge to $\gamma = 1$, a fully grooved bearing with no land region.

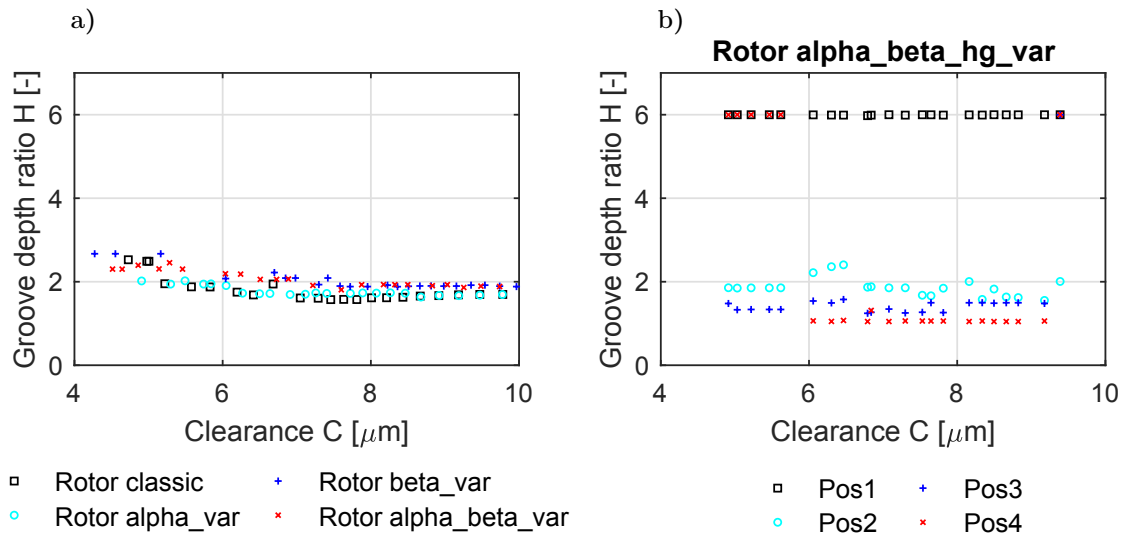


Figure 5.6 – Optimization results for groove depth ratio H : a) Rotor *classic*, *alpha_var*, *beta_var* and *alpha_beta_var* with constant groove depth; b) Rotor *alpha_beta_hg_var* with varying groove depth

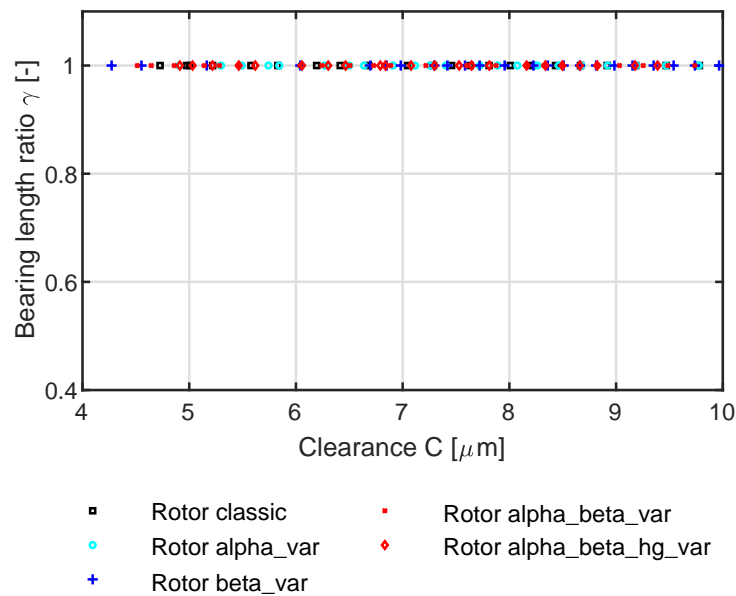


Figure 5.7 – Optimization results for bearing length ratio γ

These results agree with the results from Schiffmann [26] and the results obtained in chapter 2, where the results of the multi-objective optimizations also converged towards a fully grooved bearing design with no land region in the center.

To conclude the theoretical exploration of enhanced groove geometries, the optimization results suggest the optimum groove pattern to be fully grooved and features steep

Chapter 5. Enhanced groove geometries for Herringbone-Grooved Journal Bearings

and shallow grooves at the edge region which become flatter and deeper towards the center region of the bearing.

Figure 5.8 presents the Pareto front of the logarithmic decrement Γ against the radial clearance C for the rotor *classic* and the four rotors featuring enhanced groove geometries of increasing degree of complexity. The presented logarithmic decrement Γ corresponds to the lowest predicted logarithmic decrement in the whole speed range up to the nominal rotor speed of 180 krpm.

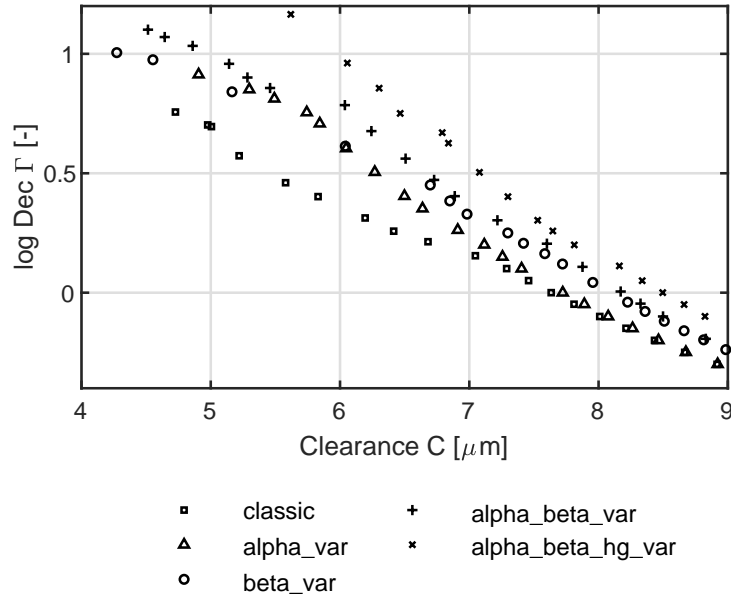


Figure 5.8 – Evolution of logarithmic decrement Γ for rotor *classic* and the four rotors featuring enhanced groove geometries of increasing degree of complexity

The results presented in Fig. 5.8 suggest a possible increase in bearing clearance from $7.6 \mu\text{m}$ to $8.5 \mu\text{m}$ (12%) for neutral stability, by using fully enhanced grooves. At lower clearances, fully enhanced grooves applied to this particular rotor geometry allow an increase in bearing clearance by up to 37%, while maintaining the same rotordynamic stability. This result is lower than the previously predicted increase of 50% in chapter 2 and the results obtained by Schiffmann [26]. The reason why enhanced groove geometries offer less potential for this particular rotor geometry is most likely because the instability is of conical nature, whereas the investigated rotor-bearing-systems in chapter 2 and by Schiffmann [26] exhibit instability of the cylindrical rotor mode.

As is evident from the results presented in Fig. 5.8, the groove geometry *alpha_var* offers increased performance compared to the classically grooved rotor for low clearance levels, however, its ability to improve stability vanishes almost completely at clearances above $7.5 \mu\text{m}$.

Furthermore, the groove geometry *beta_var*, while not offering any increased performance at low clearances compared to the geometry *alpha_var*, presents an almost identical performance as *alpha_beta_var* for clearances above $6.5\text{ }\mu\text{m}$.

Furthermore suggested by the results shown in Fig. 5.8, a maximum clearance C of $7.6\text{ }\mu\text{m}$ is required to ensure stable operation ($\Gamma > 0$) of the rotor *classic* up to the nominal rotor speed of 180 krpm. The maximum clearances for the enhanced groove geometries are $7.7\text{ }\mu\text{m}$, $8.1\text{ }\mu\text{m}$, $8.2\text{ }\mu\text{m}$ and $8.5\text{ }\mu\text{m}$ for the rotors *alpha_var*, *beta_var*, *alpha_beta_var* and *alpha_beta_hg_var* respectively.

In order to experimentally validate the theoretically obtained results, five rotor shafts of different diameter would need to be manufactured, resulting in the just mentioned specific bearing clearance for each rotor. It is evident that even by using the most modern technologies available, manufacturing of differences in rotor diameter as small as $0.1\text{ }\mu\text{m}$ is very challenging and expensive. It was therefore decided to design all five rotors with the same diameter, resulting in the same radial bearing clearance for all rotors, and experimentally compare the different groove designs by increasing the rotational speed of each rotor until instability occurs. The obtained maximum rotational speed of each tested rotor then allows to compare the performance of the different groove patterns.

5.5.2 Identification of common bearing clearance for experimental campaign

Figure 5.9 presents the speed of instability onset (SIO), defined as the rotational speed where the logarithmic decrement becomes zero, as a function of the bearing clearance C for the rotor *classic* and the four rotors featuring enhanced grooves. The maximum speed in the experimental setup is limited to a nominal speed of $N_{Rot}=180\text{ krpm}$ due to rotordynamic reasons, which is why all predicted speeds of instability onset (SIO) were limited to 180 krpm in case the instability onset was predicted to be higher than 180 krpm.

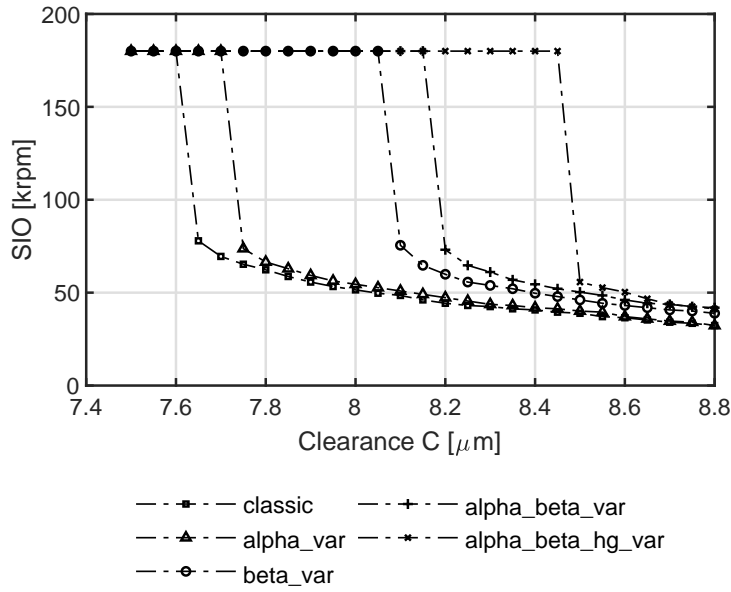


Figure 5.9 – Predicted speed of instability onset for the classically grooved rotor and the four rotors featuring enhanced groove geometries

As suggested by the results presented in Fig. 5.9, the speed of instability onset (SIO) increases with decreasing clearance C for all rotors. Similar to the results for the logarithmic decrement Γ presented in Fig. 5.8, the SIO increases with increasing complexity of the applied groove pattern. Using the theoretically predicted results presented here, the objective is to define an identical clearance for all rotors that offers to experimentally capture the different speeds of instability onset of the rotors and allows a comparison of their performance.

In order to facilitate the selection of a common clearance C for all five rotors, the results from Fig. 5.9 are plotted in a different style, shown in Fig. 5.10. Presented is the speed of instability onset (SIO) as a function of radial bearing clearance C for the rotor featuring classical grooves, as well as for the rotors featuring enhanced groove geometries.

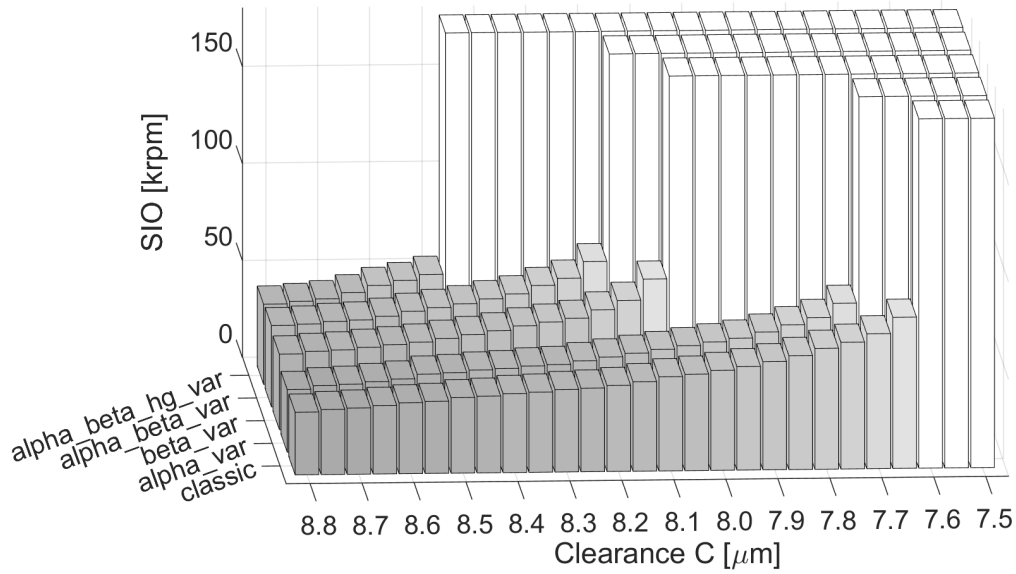


Figure 5.10 – Predicted speed of instability onset for rotor *classic* and the four rotors featuring enhanced groove geometries

The ideal clearance to be defined for all five rotors yields instability within the nominal speed range up to 180 krpm and ideally results in large enough differences in SIO to be captured in the experiment. Due to the fact that the nominal rotor speed of 180 krpm can not be exceeded during the experimental measurement campaign, the ideal clearance is therefore suggested to be $C=8.2 \mu\text{m}$. At this clearance, all rotors become unstable within the nominal speed range, except for rotor *alpha_beta_hg_var*, which is predicted to run in a stable manner up to the nominal speed of 180 krpm.

For an identical radial clearance of $C=8.2 \mu\text{m}$, the predicted speed of instability onset for all five rotors is presented in Tab. 5.4.

Table 5.4 – Predicted speed of instability onset (SIO) for all five investigated rotors with a radial clearance $C=8.2 \mu\text{m}$

Rotor name	SIO [krpm]
<i>classic</i>	44
<i>alpha_var</i>	47
<i>beta_var</i>	60
<i>alpha_beta_var</i>	73
<i>alpha_beta_hg_var</i>	>180

5.5.3 Manufacturing of bearing bushing and rotors

One bearing bushing, suitably designed to test all five rotors of different groove pattern, has been manufactured from a heat treated stainless steel of grade 1.4125. Measurements of the bearing bushing were performed, which resulted in an ID of 8.0106 mm, a roundness error of 0.2 μm and a parallelism error of 0.5 μm .

Five rotors were manufactured in an identical grade of steel to the diameter required for a clearance C of 8.2 μm . With respect to the measured bearing bushing ID, the OD of all five rotors is targeted to be $D_{Rot}=7.9942$ mm. Measurements of the rotor diameters after manufacturing, as well as the resulting clearances for all rotors are presented in Tab. 5.5. The measurement uncertainty for the rotor diameter is in the range of ± 0.3 μm and ± 0.5 μm .

Table 5.5 – Measurement results of rotor diameter

Rotor name	D_{rot} [mm]	Clearance C [μm]
<i>classic</i>	7.9938	8.4
<i>beta_var</i>	7.9938	8.4
<i>alpha_var</i>	7.9942	8.2
<i>alpha_beta_var</i>	7.9943	8.15
<i>alpha_beta_hg_var</i>	7.9943	8.15

As suggested by the measurement results of the rotor diameter presented in Tab. 5.5, the largest deviation from the target diameter of 7.9942 mm is found for the rotors *classic* and *beta_var* with a deviation of -0.4 μm from the designed dimension. With a maximum difference of 0.5 μm (6.1%) with respect to the nominal radial bearing clearance of $C=8.2$ μm , all rotors can be considered identical except for their groove pattern.

CAD files of the groove patterns were generated for all five rotors by transforming the optimized parameters for groove angle β , groove width ratio α and groove depth ratio H according to the selected clearance $C=8.2$ μm into absolute coordinates, which are then imported into a CAD software to generate splines. All groove geometries have been extrapolated by 0.5 mm on both edge regions in order to ensure complete coverage of the bearing surface.

Figure 5.11 presents the CAD geometry of the optimized groove patterns for rotors *classic*, *alpha_var*, *beta_var*, *alpha_beta_var* and *alpha_beta_hg_var* (from left to right), whereas Fig. 5.12 presents the realized groove patterns for the experimental enhanced groove geometry exploration after manufacturing by means of laser etching.

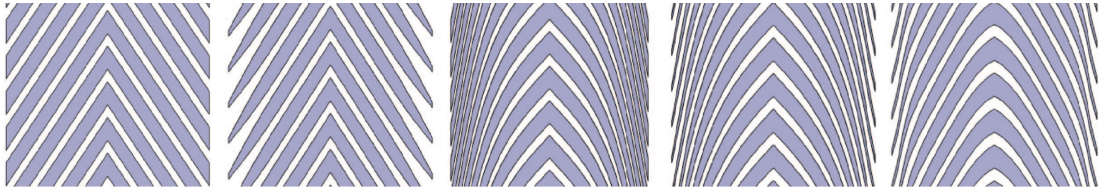


Figure 5.11 – Comparison of groove designs in CAD. From left to right: *classic*, *alpha_var*, *beta_var*, *alpha_beta_var*, *alpha_beta_hg_var*

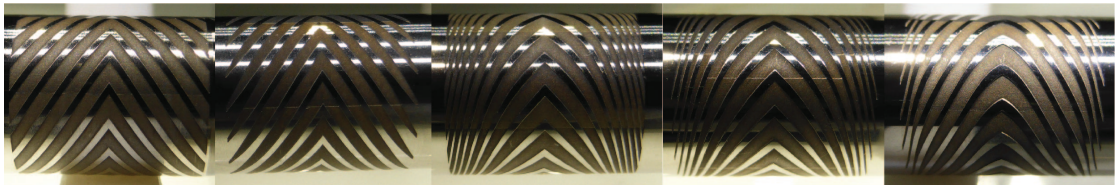


Figure 5.12 – Comparison of groove designs after laser etching onto rotors. From left to right: *classic*, *alpha_var*, *beta_var*, *alpha_beta_var*, *alpha_beta_hg_var*

Presented in Fig. 5.13 is the manufactured bearing bushing and the rotor components for the experimental investigation of enhanced groove geometries. The rotor components listed from left to right are: Turbine nut, turbine, shim, tie bolt, rotor *alpha_beta_var*, fan. The shim is required to adjust the axial rotor clearance.

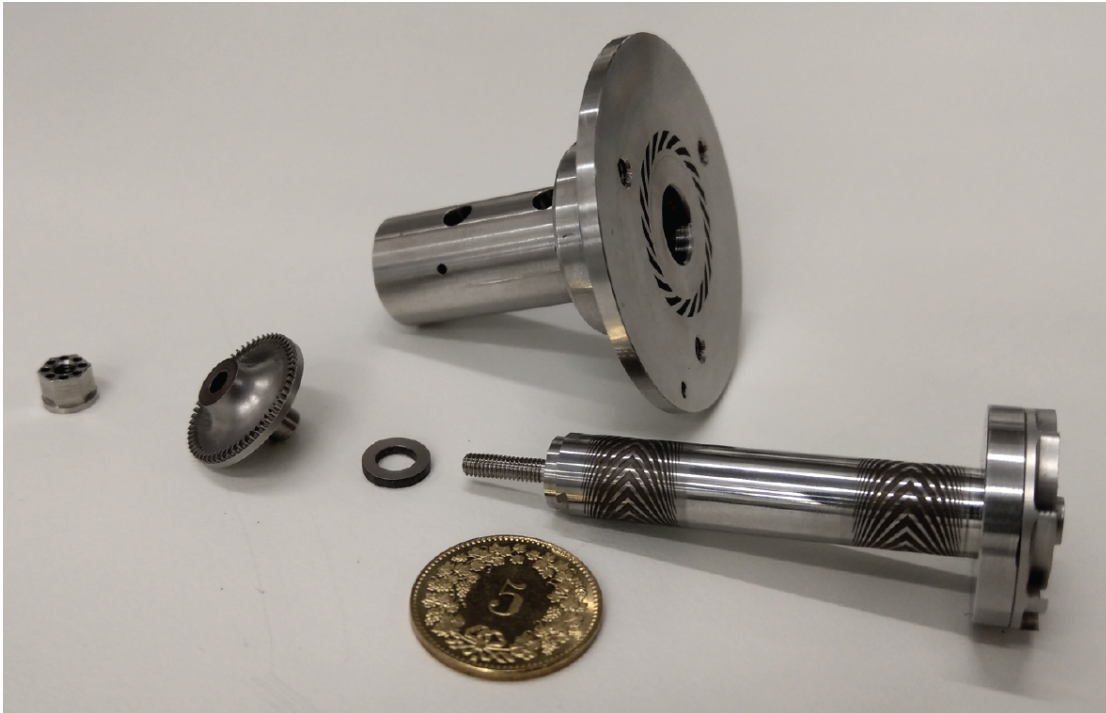


Figure 5.13 – Manufactured bearing bushing (top) and rotor (bottom) for enhanced groove geometry exploration. From left to right: Turbine nut, turbine, axial shim, tie bolt, rotor $\alpha_{\beta_{var}}$ with fan

5.5.4 Experimental results

Axial clearance measurement and adjustment

The axial rotor clearance is measured and adjusted using shims (see Fig. 5.13) manufactured from precision sheets of metal. Fig. 5.14 presents the procedure for measuring the axial clearance of the rotor when assembled and fitted to the prototype. The axial rotor clearance is measured by means of a digital dial test indicator and adjusted to the required axial clearance of $150\ \mu\text{m}$ by inserting shims of the required thickness.

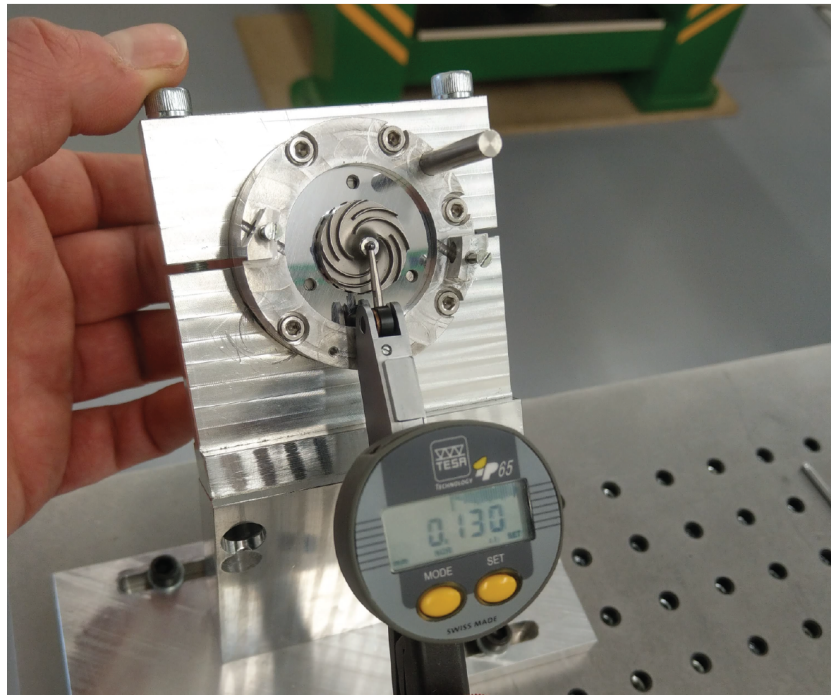


Figure 5.14 – Measurement of axial rotor clearance using a Tesa IP65 digital dial test indicator

Balancing

In order to obtain comparable measurement results, all rotors were balanced to a synchronous vibration amplitude of around $0.5 \mu\text{m}$ on the front and the back measurement location at a rotor speed of 40 krpm. The balancing procedure is based on the influence coefficient method [88] and is performed in-situ with the rotor mounted in the prototype. Three trial mass runs are executed in the following manner:

1. Rotor as received with no additional imbalance
2. Rotor with additional imbalance on the front balancing plane (near fan)
3. Rotor with additional imbalance on the back balancing plane (near turbine)

After performing the three trial mass runs, the results of the influence coefficient analysis provide information for both the front and rear balancing plane about the amount and the phase of where mass has to be added or removed.

Mass is then removed or added either by grinding off material on the turbine nut, or by inserting small masses into the balancing holes of the turbine nut or fan.

Experimental identification of the speed of instability onset

Figure 5.15 presents the captured synchronous and sub-synchronous motion amplitudes on the front and the back bearing plane for rotor *classic*. The rotor *classic* features constant groove angle β , groove width ratio α and groove depth ratio H along the rotor axis and serves as a base-line for the the performance evaluation of enhanced groove geometries.

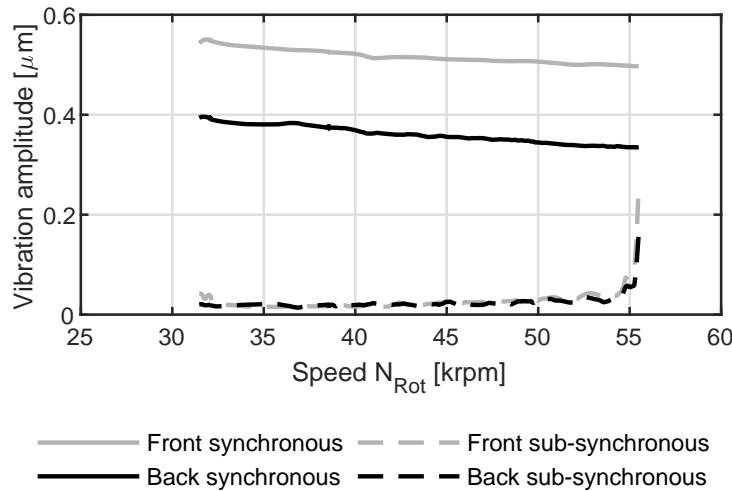


Figure 5.15 – Experimentally captured synchronous and sub-synchronous motion amplitudes of rotor *classic*

As suggested by the results presented in Fig. 5.15, the rotor *classic* shows a synchronous vibration amplitude on the front and the back bearing plane of about $0.5 \mu m$ at a rotor speed of 40 krpm after balancing. The evolution of the sub-synchronous motion amplitude shows very low values at low speed that slightly increase with increasing speed to then suddenly peak at 56 krpm. The captured sudden increase in sub-synchronous motion amplitude at the front and back of the rotor suggest the onset of instability of the rotor *classic* to be located at a rotational speed of 56 krpm.

Figure 5.16 shows the evolution of the synchronous and sub-synchronous rotor motion amplitudes captured for rotor *alpha_var*. The groove pattern of this rotor features a constant groove angle β , constant groove depth ratio H , but a variable groove width ratio α along the rotor axis.

As suggested by the recorded rotor amplitudes presented in Fig. 5.16, the rotor *alpha_var* exhibits elevated levels of sub-synchronous vibration on both, the front and the back bearing location already at low speeds, suggesting a low level of stability for this groove pattern. In general, operation of the rotor *alpha_var* proved to be challenging due to a difficult to regulate speed, most probably caused by the continuous onset and cessation of rotor instabilities. Nevertheless, a maximum rotational speed of 80 krpm was achieved with rotor *alpha_var* before the sub-synchronous vibration ampli-

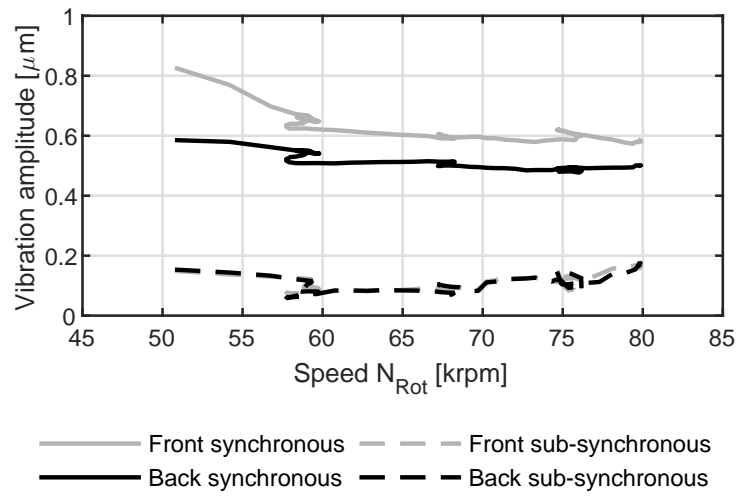


Figure 5.16 – Experimentally captured synchronous and sub-synchronous motion amplitudes of rotor *alpha_var*

tudes intermittently exceeded the synchronous motion amplitudes. The experiment was stopped at this point to avoid failure of the rotor or bearing bushing.

The recorded synchronous and sub-synchronous rotor amplitudes for rotor *beta_var*, featuring a variable groove angle but constant groove width and depth, are shown in Fig. 5.17.

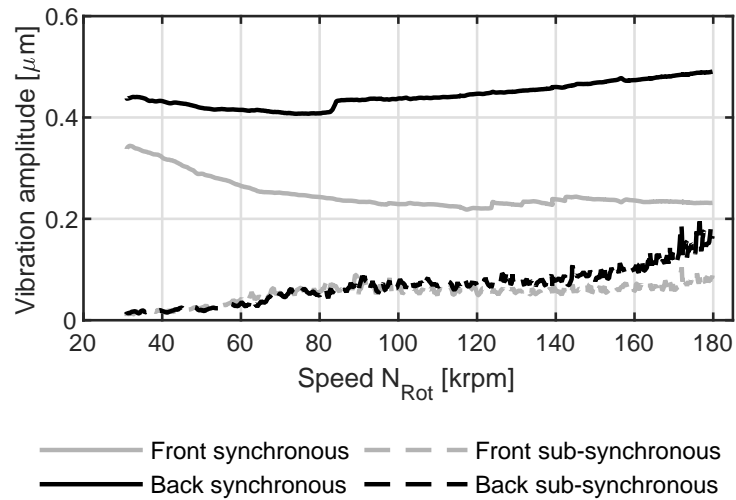


Figure 5.17 – Experimentally captured synchronous and sub-synchronous motion amplitudes of rotor *beta_var*

The evolution of sub-synchronous rotor amplitudes presented in Fig. 5.17, show an increase with increasing rotational speed for the front and the back bearing. At a rotational speed of 120 krpm, the sub-synchronous vibration amplitude of the back bearing starts to increase progressively and peaks at 0.2 μm for a speed of 180 krpm.

Chapter 5. Enhanced groove geometries for Herringbone-Grooved Journal Bearings

The sub-synchronous amplitude of the front bearing on the other hand levels out at a constant sub-synchronous amplitude of around $0.06 \mu\text{m}$. A maximum speed of 180 krpm was achieved with rotor *beta_var*, however, the increasing slope in the evolution of the sub-synchronous vibration amplitude on the back bearing after 160 krpm suggests the onset of instability to be situated at a rotor speed not far above 180 krpm.

The recorded results for rotor motion amplitude of rotor *alpha_beta_var* are presented in Fig. 5.18.

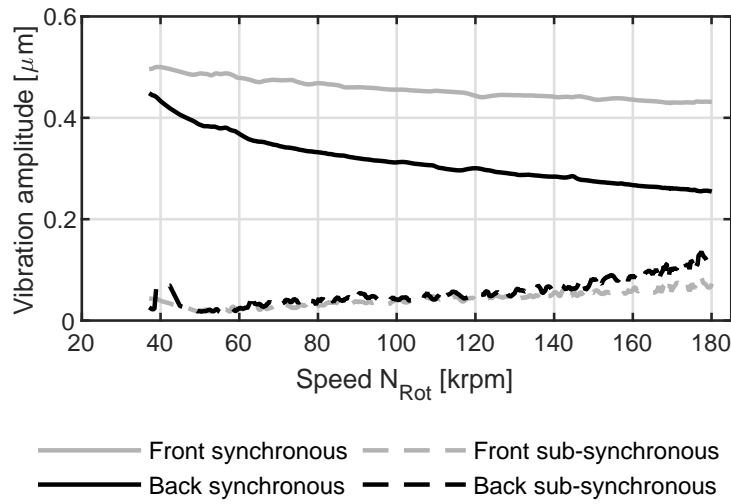


Figure 5.18 – Experimentally captured synchronous and sub-synchronous motion amplitudes of rotor *alpha_beta_var*

As suggested by the results presented in Fig. 5.18, a maximum rotational speed of 180 krpm was achieved with rotor *alpha_beta_var*. The sub-synchronous motion amplitudes of rotor *alpha_beta_var* are generally at a lower level compared to rotor *beta_var*, indicating a higher stability threshold of rotor *alpha_beta_var*. This corroborates the theoretical results presented in section 5.5.1, that predict a higher logarithmic decrement for the groove pattern *alpha_beta_var* compared to *beta_var* for the same radial clearance C .

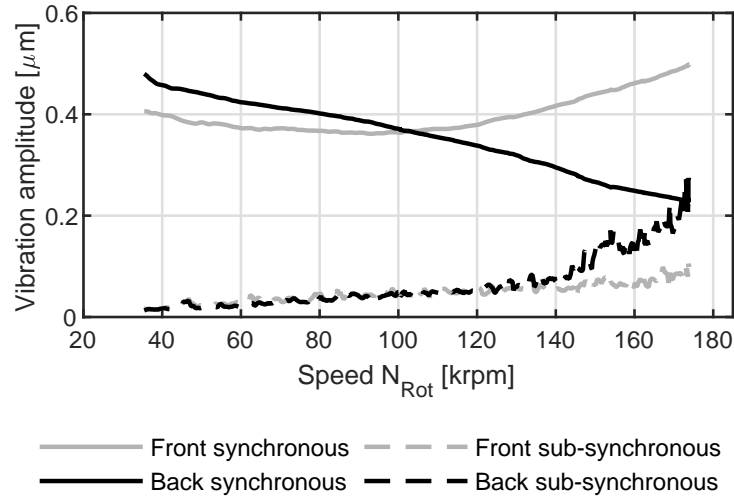


Figure 5.19 – Experimentally captured synchronous and sub-synchronous motion amplitudes of rotor *alpha_beta_hg_var*

The experimental results presented in Fig. 5.19 for rotor *alpha_beta_hg_var* show that the sub-synchronous motion amplitude recorded at the back bearing exceeds the synchronous amplitude at a rotational speed of 173 krpm, indicating the onset of instability. At this speed, the experiment was stopped in order to avoid failure of the prototype.

5.5.5 Comparison of predicted and experimental results

To account for the slight deviation between actual bearing clearance of the manufactured rotors (refer to Tab. 5.5) and the designed bearing clearance of $C=8.2 \mu m$, the rotordynamic stability predictions were repeated in order to compare the predicted with the experimentally determined speeds of instability onset. Furthermore, to account for measurement uncertainties in the measured rotor and bushing diameter and manufacturing uncertainties in the groove pattern, an uncertainty analysis was performed.

The uncertainty analysis is performed by evaluating the whirl speed maps for each rotor considering an uncertainty in measured rotor and bushing diameter of $\Delta C = \pm 0.4 \mu m$ and an uncertainty in the groove depth of $\Delta h_g = \pm 1 \mu m$. In order to take interactions of the two uncertainties into account, five rotordynamic calculations were performed for the combinations of clearance and groove depth uncertainty as shown in Fig. 5.20. The results from the five evaluations then serve to predict the nominal, maximum and minimum speed of instability onset for each investigated rotor.

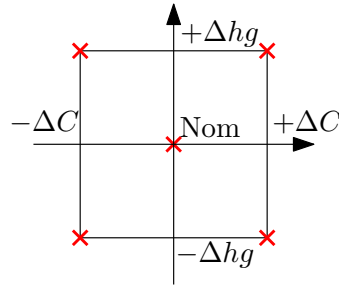


Figure 5.20 – Evaluated combinations of clearance uncertainty ΔC and groove depth uncertainty Δh_g in uncertainty analysis

Figure 5.21 presents the whirl speed map for the rotor *classic* considering the uncertainty in bearing clearance and groove depth.

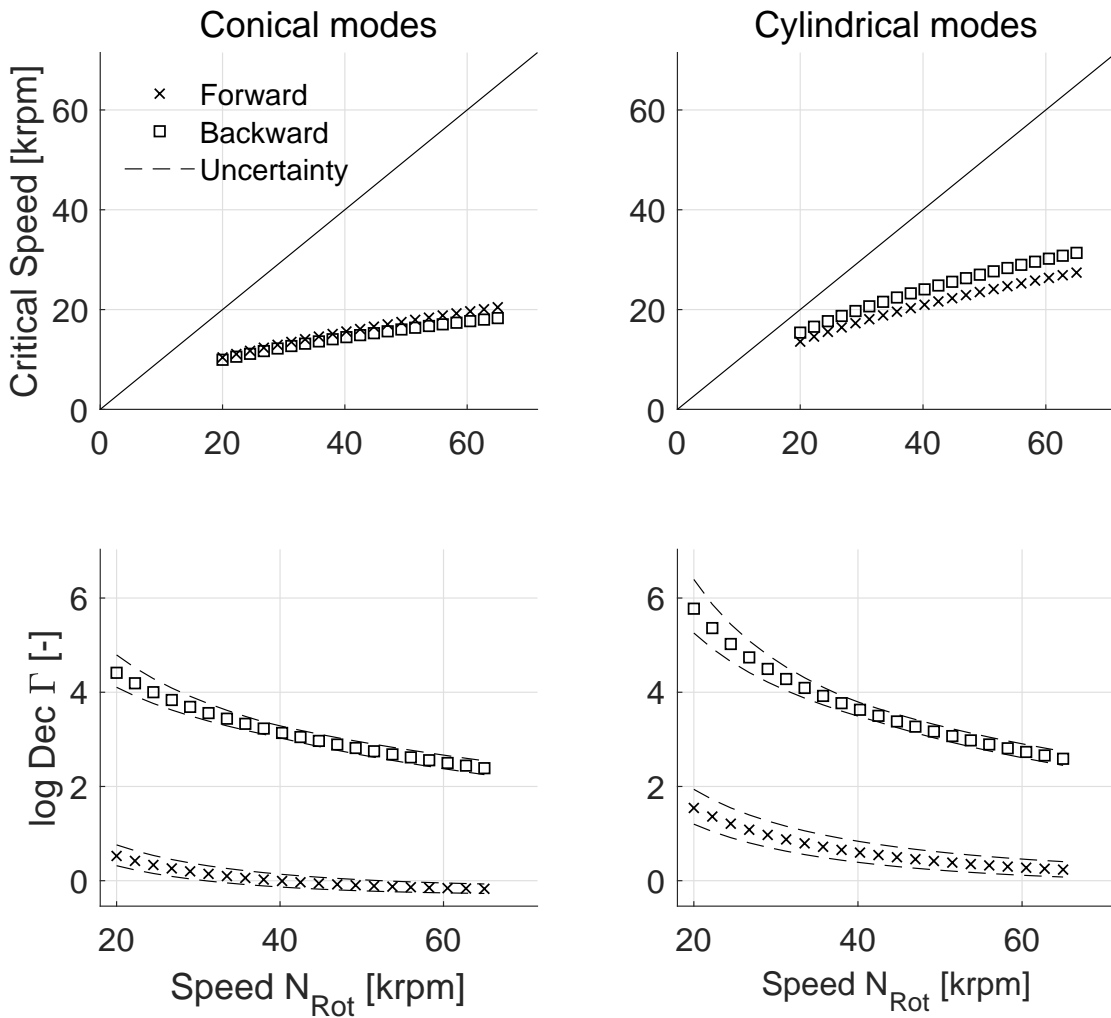


Figure 5.21 – Whirl speed map and evolution of logarithmic decrement Γ for rotor *classic* considering the uncertainty in bearing clearance and groove depth

As is evident from the whirl speed maps presented in Fig. 5.21, the rotor does neither encounter a conical nor a cylindrical critical speed in the tested speed range above 20 krpm. The cylindrical and conical backward modes do not cause concern since they are well damped and very rarely excited in general [103, 104, 105]. The results for the logarithmic decrement Γ suggest the expected instability to be a conical forward mode. To better capture the effect of the uncertainties in bearing clearance and groove depth on the speed of instability onset of the relevant conical forward mode, the evolution of the logarithmic decrement Γ as a function of rotor speed for rotor *classic* is plotted again in a larger format in Fig. 5.22.

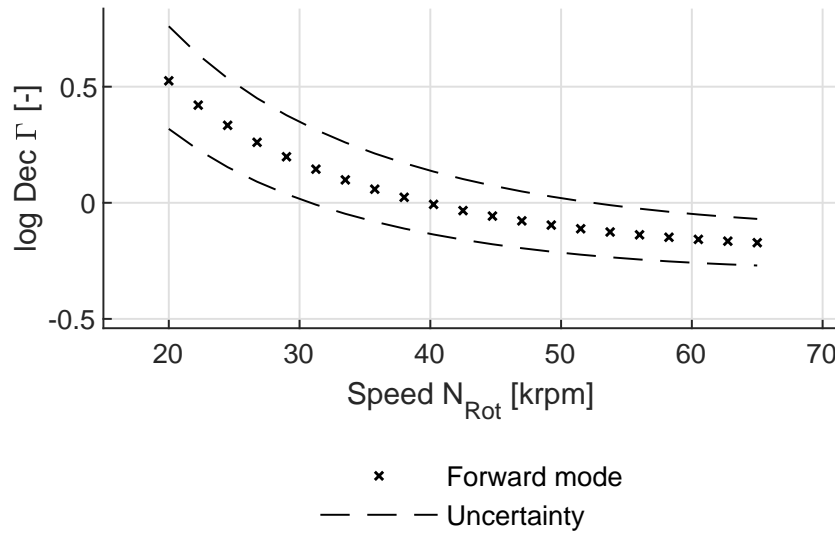


Figure 5.22 – Evolution of logarithmic decrement Γ for conical forward mode of rotor *classic*

As suggested by the results presented in Fig. 5.22, the nominal speed of instability onset (SIO) is predicted to be at around 40 krpm. This result is slightly lower than the previously predicted 44 krpm (refer to Tab. 5.4), since the actual clearance of the rotor is $C=8.4 \mu\text{m}$ instead of $C=8.2 \mu\text{m}$.

When considering an uncertainty of $\Delta C = \pm 0.4 \mu\text{m}$ and $\Delta h_g = \pm 1 \mu\text{m}$, the expected speed range of instability onset is between 31 krpm and 52 krpm for the rotor *classic*.

Identical evaluations have been performed for the four shafts featuring enhanced groove geometries, which enabled the identification of the nominal, minimum and maximum speed of instability onset due to measurement and manufacturing uncertainties. The detailed results for rotors *alpha_var*, *beta_var*, *alpha_beta_var* and *alpha_beta_hg_var* are attached in appendix D.

The comparison between experimentally identified and predicted speed of instability onset for all investigated groove patterns is presented in Fig. 5.23. The bar colors

Chapter 5. Enhanced groove geometries for Herringbone-Grooved Journal Bearings

represent the minimum, nominal and maximum predicted speed of instability onset, when considering the uncertainties in rotor/bushing diameter and groove depth. The red stars represent the speed where an instability was observed in the experiment and the red dots indicate the maximum achieved speed in the experiment with no clear onset of instability present yet.

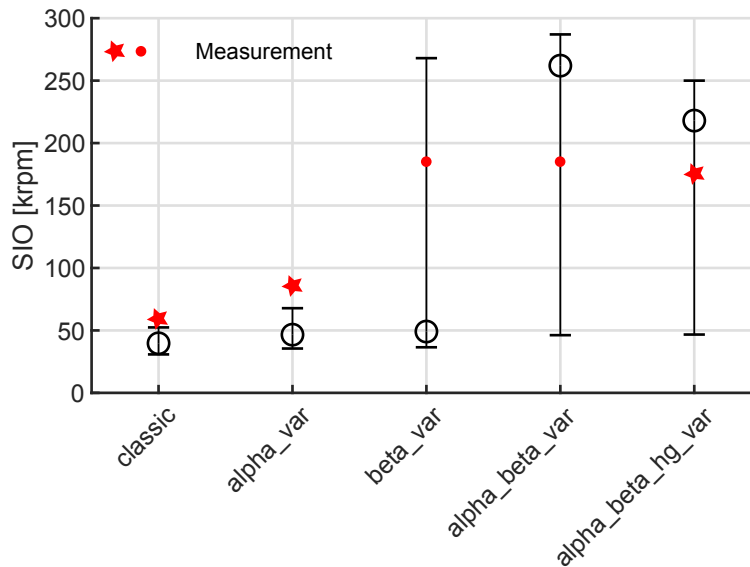


Figure 5.23 – Comparison of predicted and measured speed of instability onset. Red stars represent experimentally observed instability, red dots represent maximum achieved speed with no observed instability

As suggested by the comparison of predicted and measured data presented in Fig. 5.23, the theoretical results slightly under-predict the experimentally obtained results for rotors *classic* and *alpha_var*, even when considering the uncertainty in clearance and groove depth. For the rotors with the groove patterns *beta_var* and *alpha_beta_var*, the nominal speed of 180 krpm was predicted to be achievable, which was experimentally confirmed. Rotor *alpha_beta_hg_var* is suggested to have the highest performance according to the theoretically predicted results. The experimental data however suggests the performance of this rotor to be lower compared to rotors *beta_var* and *alpha_beta_var*. In general, the performance predictions of all rotors is slightly lower compared to the experimental results, except for rotor *alpha_beta_hg_var*, whose performance is slightly over-predicted by the models.

It is evident from the obtained experimental results that enhanced groove geometries are able to significantly increase the stability threshold of the rotor-bearing-system. Compared to a classically grooved rotor that becomes unstable at a rotational speed of 56 krpm, the application of enhanced grooves allowed to reach a speed of 180 krpm, representing an increase by more than a factor three.

5.6 Summary and chapter conclusions

This chapter summarizes the theoretical and experimental exploration of enhanced groove geometries for HGJBs. Multi-objective optimizations have been performed to determine the performance and optimum groove parameters for a classically grooved rotor, acting as the base-line rotor for the performance evaluation, and four rotors with enhanced groove geometries of different design complexity.

Resulting from the identified optimum groove pattern from the multi-objective optimizations, five rotors were manufactured with an identical radial clearance, whose performance was then experimentally evaluated and compared to the classically grooved base-line rotor. The experimentally obtained results showed good agreement with the models when considering measurement uncertainties of the bearing clearance and manufacturing uncertainties of the grooves.

The potential of enhanced grooves to increase the stability threshold of HGJBs was then experimentally demonstrated by achieving a rotational speed that is more than three times as high as the one achieved with the classically grooved base-line rotor featuring the same bearing clearance.

The following conclusions have been drawn from the results obtained in this chapter:

- The potential clearance increase offered by enhanced groove geometries is dependent on the rotor instability mode. The predicted results for the particular rotor geometry presented in this chapter are lower compared to the previously predicted results in chapter 2 and the results obtained by Schiffmann [26]. The reason is most likely because the instability of the particular rotor investigated in this chapter is of conical nature, whereas the investigated rotor-bearing-system in chapter 2 and by Schiffmann [26] exhibits instability of the cylindrical rotor mode.
- The optimum groove pattern is suggested to be fully grooved and features steep and shallow grooves at the edge region, which become flatter and deeper towards the center region of the bearing.
- The rotordynamic models developed at the LAMD reliably predict the onset of instability for rotors with enhanced groove geometries when measurement uncertainties in the bearing clearance and groove depth are considered in the theoretical analysis. It is evident that the manufacturing process of rotors and bushing, as well as the laser etching yields many more uncertainties than the two that have been considered. Further uncertainties stem from the groove angle, groove width, rotor and bearing roundness, extrapolated groove edge and land region, transverse and polar rotor inertia and rotor mass.

Chapter 5. Enhanced groove geometries for Herringbone-Grooved Journal Bearings

- The rotordynamic models slightly under-predicted the performance of all rotors that feature constant groove depth but over-predicted the performance of rotor *alpha_beta_hg_var*.
- The experimental exploration of enhanced HGJB geometries clearly suggest an increase in stability by using enhanced groove patterns, which is in agreement with the theoretically obtained results. The increase in stability was experimentally proven by achieving a rotational speed of 180 krpm with rotors *beta_var* and *alpha_beta_var*, which is an increase of more than a factor three compared to the classically grooved rotor with the same radial bearing clearance.
- The rotor *beta_var*, featuring enhanced grooves with variable groove angle β but constant groove width ratio α and constant groove depth ratio H , represents a good trade-off between performance increase and design/manufacturing costs.

6 Conclusions

Herringbone-Grooved Journal Bearings are a favorable bearing type for oil-free, small-scale turbomachinery due to their compactness, low losses, no need for lubrication, no need for auxiliary systems, low maintenance, low cost and very little wear. However, the exploitation of the various advantages of HGJBs in large production series is hindered by their main shortcoming: The requirement for very small clearance to diameter ratios in order to run stable and provide sufficient load capacity.

The main consequences of the small clearance ratios are increased bearing losses, very strict alignment tolerances and high cost due to expensive raw materials, complicated and time consuming manufacturing processes and the required extensive quality control.

Increasing the bearing clearance while maintaining the performance of the rotor-bearing-system allows to significantly reduce the disadvantages that result from the use of HGJBs to support high-speed rotors and helps to make their application in products less challenging. Two approaches have been investigated in this thesis that allow an increase in bearing clearance. The first approach uses enhanced groove geometries, whereas the second approach is based on a flexible bearing bushing support that provides external damping to the bearing bushing.

6.1 Potential of flexible bearing bushing support and enhanced groove geometries

In a first part of this thesis, a theoretical analysis of the potential of the two approaches to increase bearing clearance is conducted, based on a classically grooved rotor used in a LAMD prototype. Both approaches showed promising results. The performed multi-objective optimizations suggest a possible clearance increase of up to 50% for a classically grooved rotor on a flexible support and up to 50% for a rotor with enhanced grooves on a rigid support, compared to a rigidly supported rotor with classical grooves.

The combination of both approaches suggests to allow for even larger clearances and an improvement in bearing load capacity by up to 50%. Furthermore, the theoretical results suggested that below a certain clearance threshold, rigidly supported bearing bushings show better performance.

6.2 O-Ring model

In order to obtain a base-line for the dynamic characteristics of the flexible bushing support developed in this thesis, a test rig has been designed based on the Base Excitation - Resonant Mass method that allows to experimentally determine the stiffness and damping characteristics of the O-Rings implemented in the first generation LAMD prototype. In a second stage, the test-rig was adapted in order to investigate the effect of O-Ring diameter, cross-sectional diameter, squeeze, Shore A hardness and excitation frequency on the stiffness and damping of O-Rings. The governing variables have been identified using a DOE approach, which suggests that the Shore hardness has the largest effect on the stiffness, followed by the O-Ring diameter, the squeeze, the cross-sectional diameter and finally the excitation frequency. The order is identical for the damping coefficient, except for the excitation frequency, which is the only variable that has a reducing effect on the damping of the investigated O-Rings. Measurements of around 60 representative O-Ring geometries and installation specifications allowed to develop reduced-order models for stiffness and damping of O-Rings as a function of O-Ring geometry, Shore hardness, squeeze and excitation frequency. Contrary to the model presented by Green and English [62], it was found that the curvature ratio d/D does affect the stiffness and damping of the O-Rings investigated in this thesis. The developed reduced order model for stiffness presents an error of less than 30% between prediction and measurement, whereas the damping model yields slightly larger errors. Considering the hardness uncertainty of ± 5 Shore A given by the O-Ring manufacturer, the proposed models show a good agreement with the measurement results.

The shortcomings of using O-Rings to flexibly support HGJB bushings have been identified in this thesis. However, O-Rings do offer advantages, namely compactness, ease of availability and low cost, that can be profited from by flexibly supporting bearing sleeves, which are less sensitive to the geometrical O-Ring tolerances in terms of alignment, compared to two separate bearing bushings. The reduced-order models presented in this thesis are therefore very valuable for assessing and predicting the rotordynamic performance of rotors running in O-Ring supported bearing sleeves. Furthermore, thanks to the modeling approach of separating geometrical and material effects, the models are easily adapted to take further parameters like temperature or excitation amplitude into account, allowing the model to be used for example in predicting the dynamic characteristics of O-Rings applied in tuned mass dampers or as centering springs in squeeze film dampers.

6.3 Flexible support for HGJBs

A flexible bearing bushing support for HGJBs has been developed to address the shortcomings of the commonly used O-Rings to flexibly support the bearing bushings, namely alignment issues, insufficient assembly repeatability, limited lifetime at high temperatures and dynamic characteristics that are dependent on many parameters e.g. excitation frequency and temperature.

The developed flexible bearing bushing support is based on membrane shaped disks featuring specific cut-outs that allow to independently tune the radial and the tilting stiffness of the support. The presented novel bearing bushing support is cheap to manufacture, offers a vast domain to select appropriate stiffness values, can be coupled to various means to introduce damping and is largely independent of excitation frequency, amplitude and temperature, which makes its use as a flexible support for HGJB bushings significantly easier and more predictable.

Three damping concepts have been investigated that can be coupled to the flexible support and whose experimental results suggest damping coefficients of up to 23 Ns/m, which is almost 100% higher than the previously used O-Rings. The performed multi-objective optimizations for a classically grooved rotor on a flexible damped support with a damping coefficient of 3 Ns/m suggested a possible increase of more than 50% compared to a rigid bearing support. The obtained damping coefficient of 23 Ns/m should therefore allow for even larger clearances, while maintaining the same rotordynamic stability.

An alignment concept was presented that is based on a thermally expanding shaft and enables the accurate alignment of two separate bearing bushings at considerable distance, which allows to exploit the various advantages offered by using separate bearing bushings compared to bearing sleeves.

The novel flexible bearing bushing support was successfully implemented and aligned in a prototype, where its performance was assessed by means of high-speed measurements, coast-down tests and start-stop testing. The high-speed testing enabled the detection of an unstable bearing bushing tilting mode, a phenomena so far not treated in the literature and whose appearance was successfully predicted by the theoretical models. The appearance of the unstable bush tilting mode was found to be primarily governed by the bushing transverse moment of inertia, the support tilting stiffness, the amount of damping and secondarily by the stiffness and damping properties of the gas film. The introduction of damping by means of one of the proposed damping concepts allowed to significantly increase the onset speed of the bush tilting instability.

Coast-down tests have been performed to assess the alignment quality of two separate bearing bushings supported on the novel flexible support presented in this thesis, which showed significantly improved repeatability, lower lift-off speeds and less wear compared to O-Ring supported bearing bushings.

6.4 Experimental exploration of enhanced groove geometries

An experimental campaign was conducted to investigate enhanced groove geometries of different complexity and compare their performance to a base-line rotor featuring classical grooves. Five rotors have therefore been manufactured with an identical radial bearing clearance. One rotor was laser-etched with an optimized classical groove geometry, acting as the base-line rotor for the performance comparison with the four rotors featuring enhanced groove geometries.

A good agreement between experimentally determined speed of instability onset and prediction was found for the different groove patterns. It has been shown experimentally that enhanced grooves are able to significantly increase the onset speed of instability. Multiple rotors with enhanced grooves have been found to provide stable operation up to a speed that is more than a factor three higher than what was obtained with the base-line rotor, a clear proof of the potential of enhanced groove geometries. Furthermore, it was found that the rotor featuring only a variable groove angle, but constant groove width and depth along the rotor axis, represents a good trade-off between performance increase and design/manufacturing costs.

6.5 Future work

- It was found that the curvature ratio d/D does affect the stiffness and damping of Shore 70 and Shore 90 O-Rings in a different way. Additional measurements with O-Rings of an intermediate Shore hardness would allow to investigate the transition from Shore 70 to Shore 90 in more detail.
- The potential of flexibly supported rotors featuring enhanced grooves to increase bearing clearance has not yet been experimentally verified. With the tunable flexible support in combination with the tunable damping concepts presented in this thesis, all the required tools are present to perform such an experimental investigation.
- The parametric membrane model presented in this thesis could easily be adapted to predict the stiffness of membranes with flexible arms of variable width. Such a design can still be manufactured by laser or water-jet cutting and would result in an even larger design space.
- The materials investigated in this thesis to manufacture the flexible support have been limited to conventional metallic or polymer based materials. It would be worthwhile to investigate composite materials, e.g. polymer-metals or polymer-fibers, as materials to be used for the flexible support structure. This would yield increased degrees of freedom in the tuning of the material properties. The bushing supports may also be fabricated, in part or completely, by additive manufacturing procedures, which would allow the design of hollow and therefore

light structures. The inclusion of un-sintered powders in the hollow chambers would allow to tune the structural damping of the flexible support.

- The lifetime of the glue-connection between bearing bushing and flexible membrane is difficult to predict. A simple test-rig is suggested to be designed that allows to investigate the lifetime of the glue-connection subject to dynamic loading. This would yield important insights about the expected lifetime of the glue-connection and would not risk damaging the rotor, bushings and measurement equipment, as would be the case for testing in a high-speed prototype. Testing of the glue-connection at high temperatures should be included in the test program.
- The presented alignment concept has repeatedly shown very accurate alignment of the bearing bushings. The alignment procedure is, however, complicated and time-consuming. It is suggested to conduct further work dedicated to simplifying the alignment concept in order to enable its use in the manufacturing of larger production series.

A Detailed O-Ring stiffness and damping measurement results

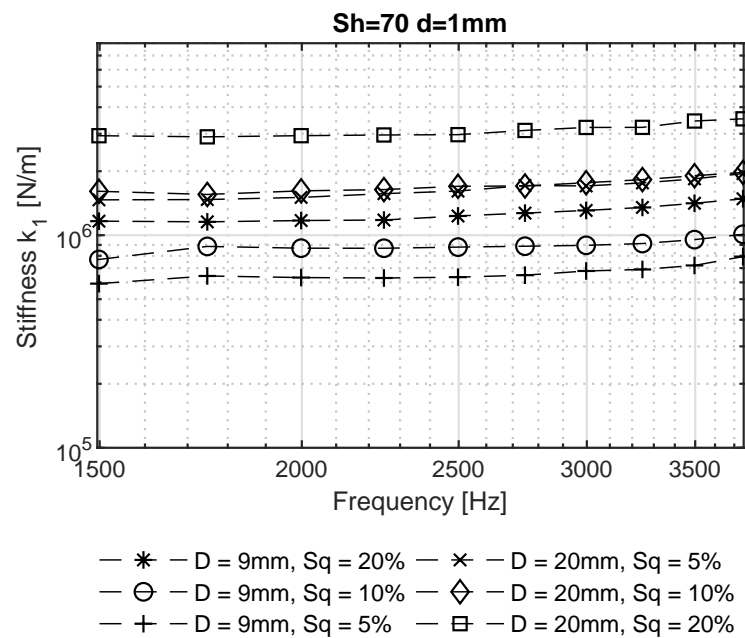


Figure A.1 – Measurement results for stiffness k_1 of a Shore 70 NBR O-Ring with d=1mm

Appendix A. Detailed O-Ring stiffness and damping measurement results

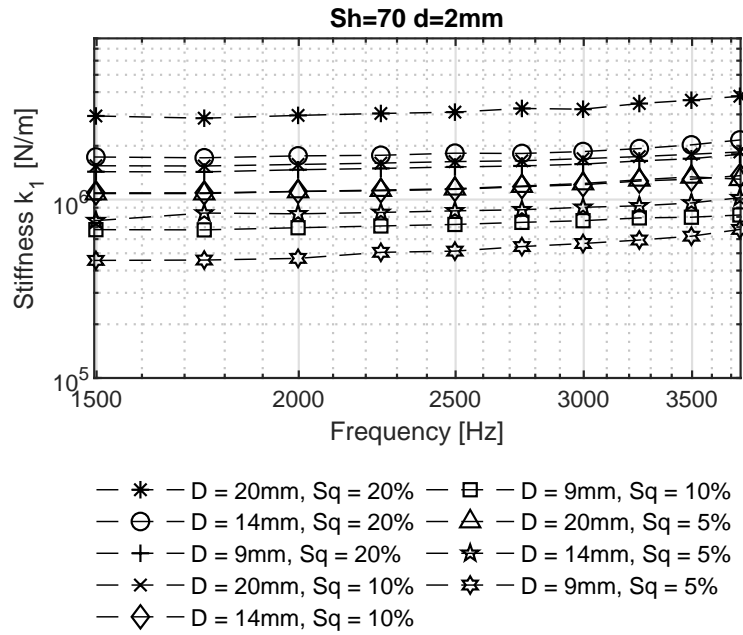


Figure A.2 – Measurement results for stiffness k_1 of a Shore 70 NBR O-Ring with d=2mm

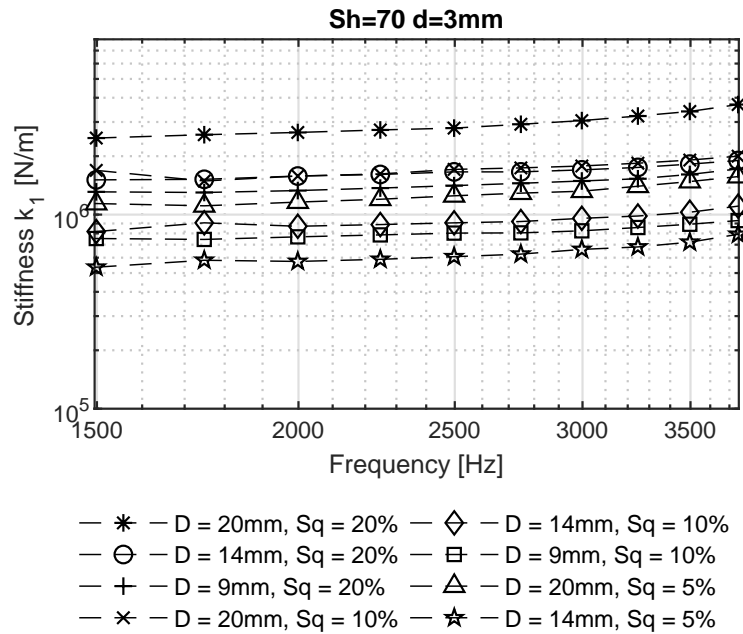


Figure A.3 – Measurement results for stiffness k_1 of a Shore 70 NBR O-Ring with d=3mm

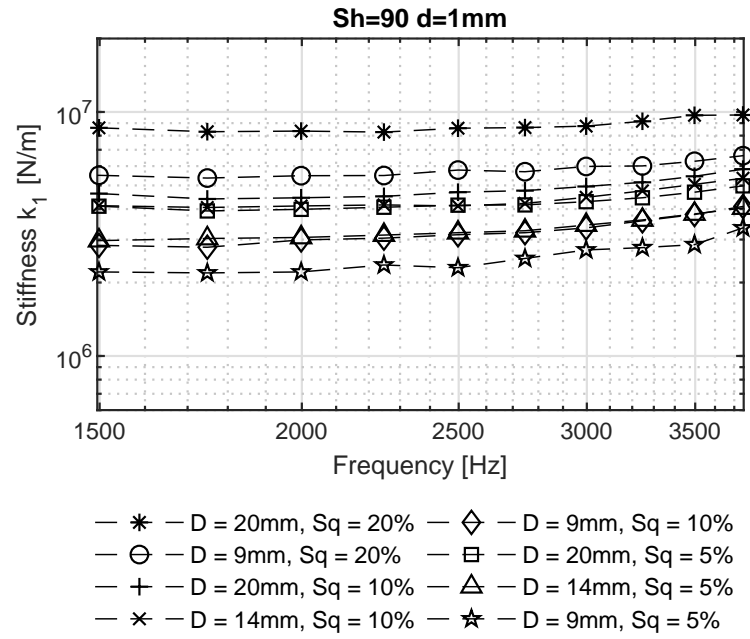


Figure A.4 – Measurement results for stiffness k_1 of a Shore 90 NBR O-Ring with d=1mm

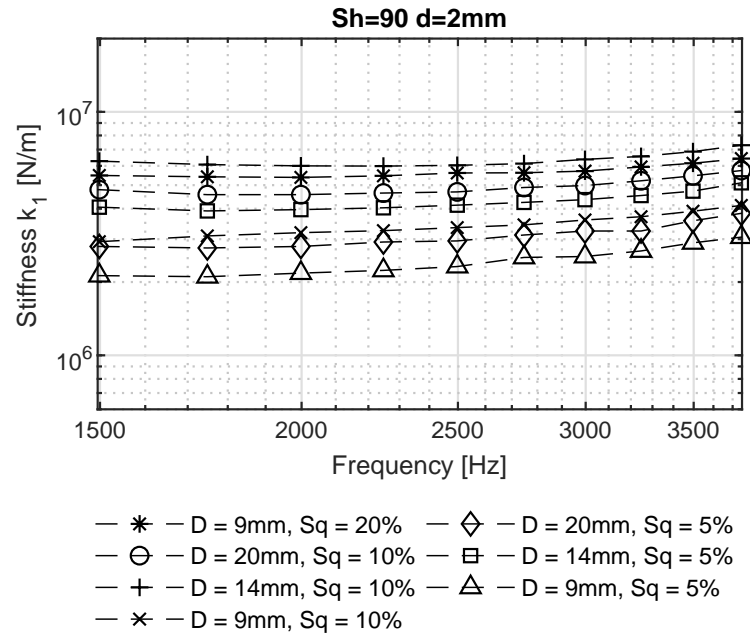


Figure A.5 – Measurement results for stiffness k_1 of a Shore 90 NBR O-Ring with d=2mm

Appendix A. Detailed O-Ring stiffness and damping measurement results

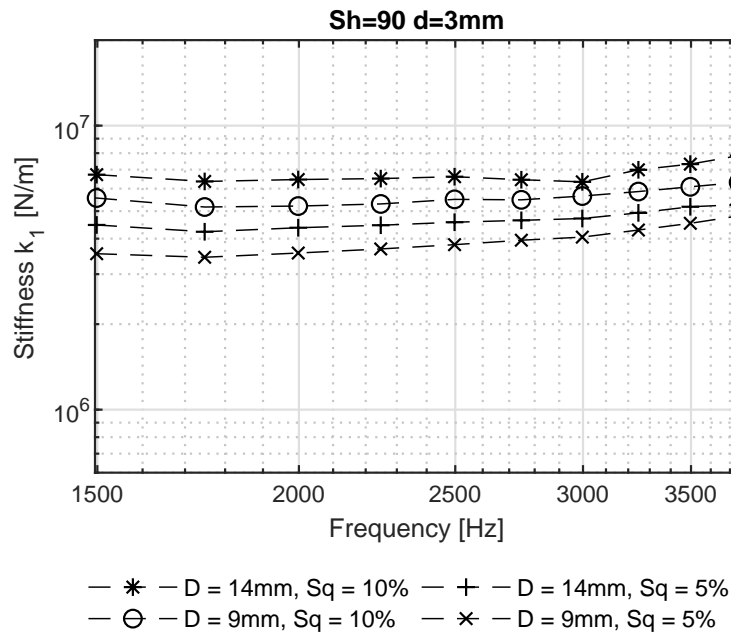


Figure A.6 – Measurement results for stiffness k_1 of a Shore 90 NBR O-Ring with d=3mm

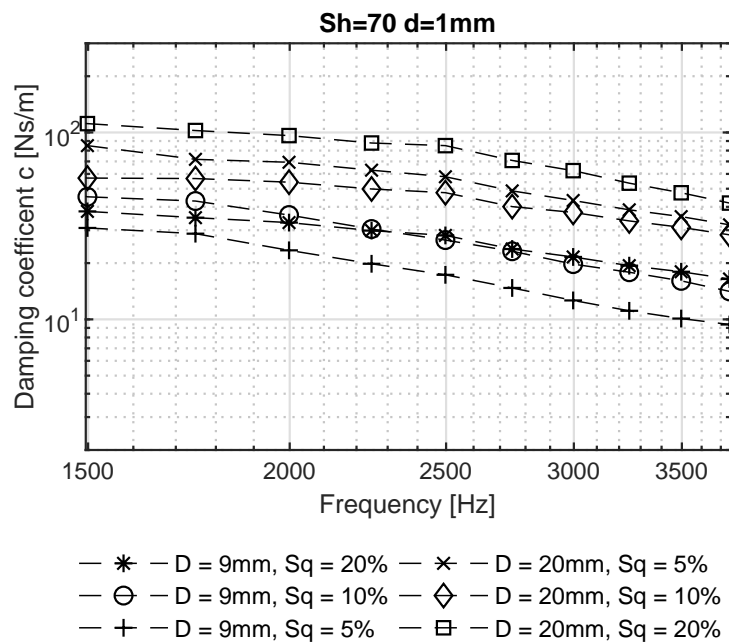


Figure A.7 – Measurement results for damping coefficient c of a Shore 70 NBR O-Ring with d=1mm

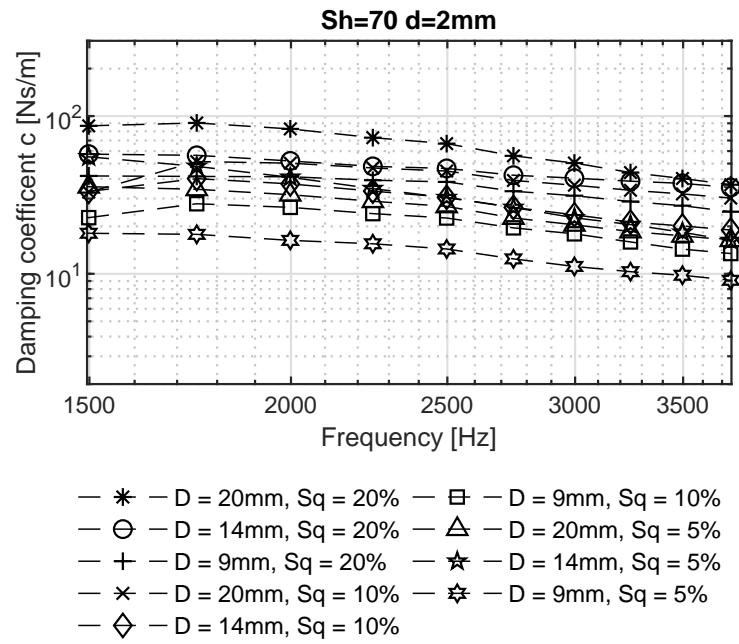


Figure A.8 – Measurement results for damping coefficient c of a Shore 70 NBR O-Ring with $d=2\text{mm}$

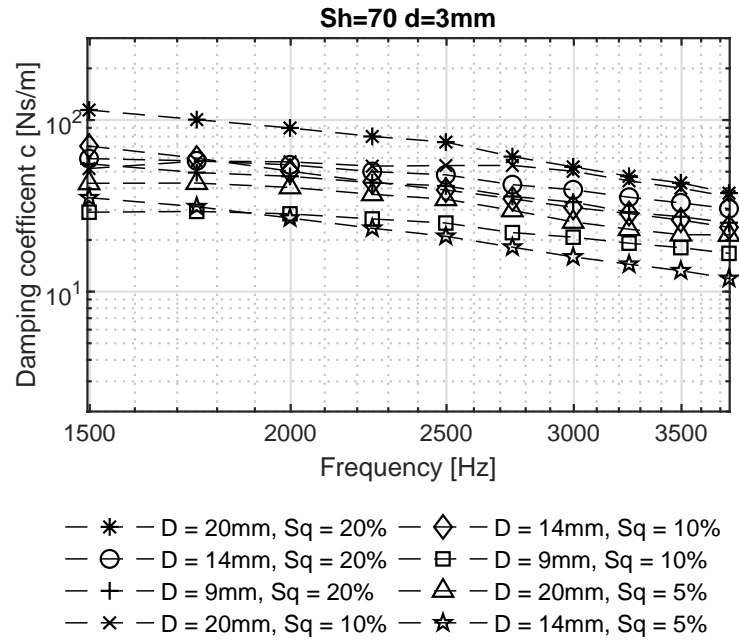


Figure A.9 – Measurement results for damping coefficient c of a Shore 70 NBR O-Ring with $d=3\text{mm}$

Appendix A. Detailed O-Ring stiffness and damping measurement results

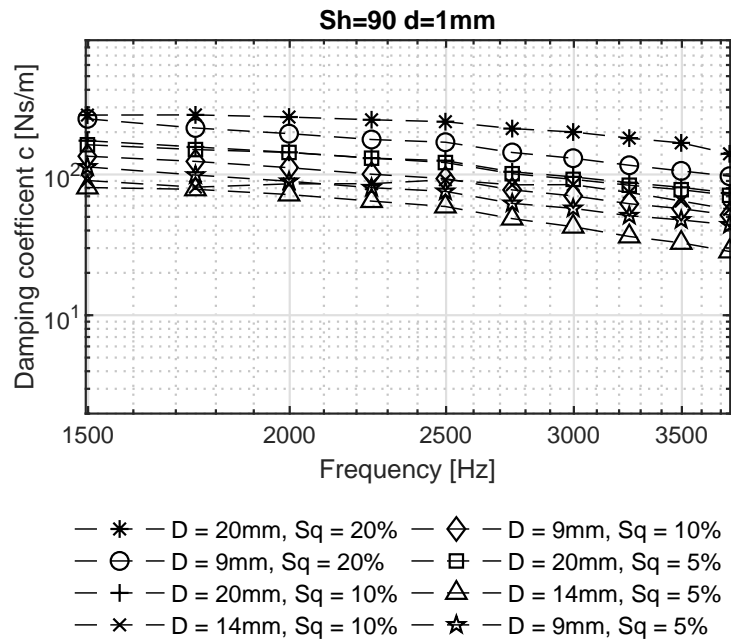


Figure A.10 – Measurement results for damping coefficient c of a Shore 90 NBR O-Ring with $d=1\text{mm}$

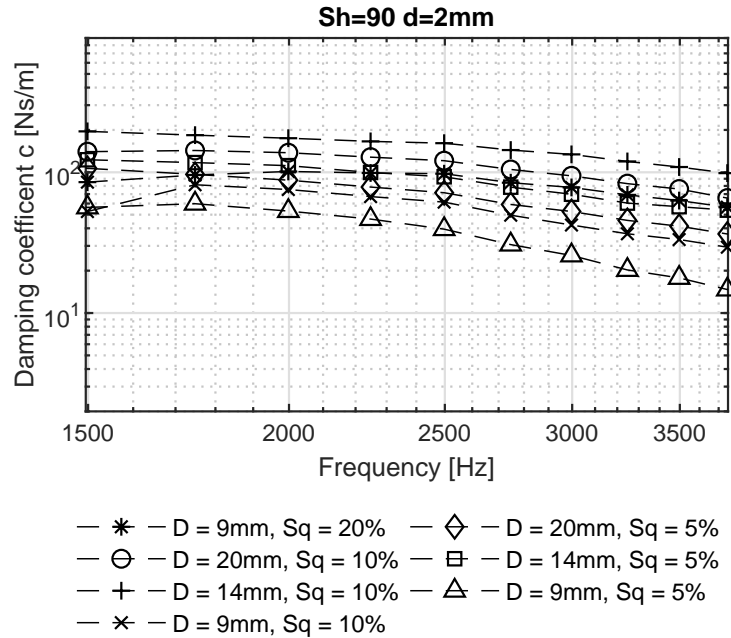


Figure A.11 – Measurement results for damping coefficient c of a Shore 90 NBR O-Ring with $d=2\text{mm}$

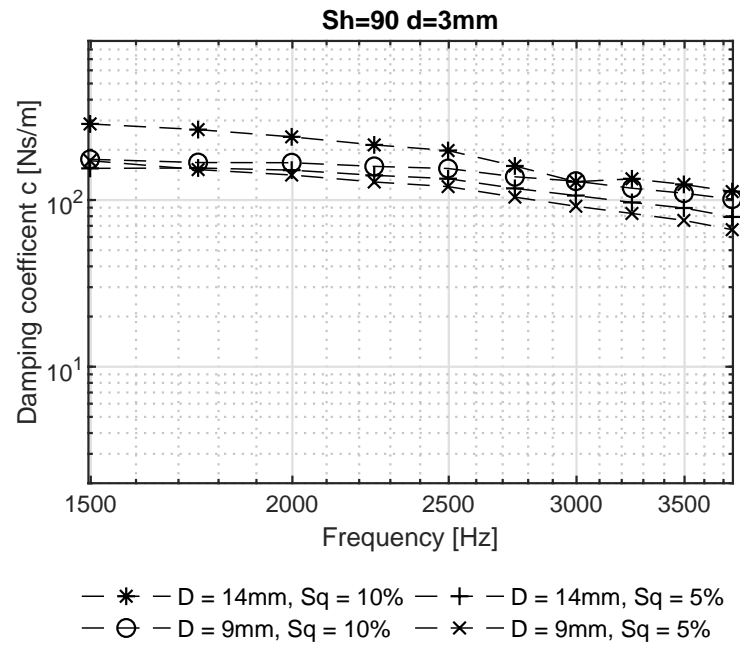


Figure A.12 – Measurement results for damping coefficient c of a Shore 90 NBR O-Ring with $d=3\text{mm}$

B Timoshenko stiffness matrix for beam element

The 12x12 element stiffness matrix K'_{el} for each finite element in local coordinates is constructed according to Timoshenko [91], with w being the width, t the thickness, l the length, E the Young's modulus and G the shear modulus of the finite element.

$$I = \frac{1}{12} \begin{pmatrix} 4wt^3 \\ wt^3 \\ w^3t \end{pmatrix} \quad c = \frac{12E}{Gwtl^2} \begin{pmatrix} 0 \\ 1.2I_3 \\ 1.2I_3 \end{pmatrix} \quad (\text{B.1})$$

$$a = \begin{pmatrix} \frac{Ewt}{l} \\ \frac{GI_1}{l} \\ \frac{12EI_3}{l^3(1+c_2)} \\ \frac{6EI_3}{l^2(1+c_2)} \\ \frac{EI_3}{l} \frac{4+c_2}{1+c_2} \\ \frac{EI_3}{l} \frac{2-c_2}{1+c_2} \\ \frac{12EI_2}{l^3(1+c_3)} \\ \frac{6EI_2}{l^2(1+c_3)} \\ \frac{EI_2}{l} \frac{4+c_3}{1+c_3} \\ \frac{EI_2}{l} \frac{2-c_3}{1+c_3} \end{pmatrix} \quad (\text{B.2})$$

Appendix B. Timoshenko stiffness matrix for beam element

$$K'_{el} = \begin{bmatrix} a_1 & 0 & 0 & 0 & 0 & 0 & -a_1 & 0 & 0 & 0 & 0 & 0 \\ 0 & a_3 & 0 & 0 & 0 & a_4 & 0 & -a_3 & 0 & 0 & 0 & a_4 \\ 0 & 0 & a_7 & 0 & -a_8 & 0 & 0 & 0 & -a_7 & 0 & -a_8 & 0 \\ 0 & 0 & 0 & a_2 & 0 & 0 & 0 & 0 & 0 & -a_2 & 0 & 0 \\ 0 & 0 & -a_8 & 0 & a_9 & 0 & 0 & 0 & a_8 & 0 & a_{10} & 0 \\ 0 & a_4 & 0 & 0 & 0 & a_5 & 0 & -a_4 & 0 & 0 & 0 & a_6 \\ -a_1 & 0 & 0 & 0 & 0 & 0 & a_1 & 0 & 0 & 0 & 0 & 0 \\ 0 & -a_3 & 0 & 0 & 0 & -a_4 & 0 & a_3 & 0 & 0 & 0 & -a_4 \\ 0 & 0 & -a_7 & 0 & a_8 & 0 & 0 & 0 & a_7 & 0 & a_8 & 0 \\ 0 & 0 & 0 & -a_2 & 0 & 0 & 0 & 0 & 0 & a_2 & 0 & 0 \\ 0 & 0 & -a_8 & 0 & a_{10} & 0 & 0 & 0 & a_8 & 0 & a_9 & 0 \\ 0 & a_4 & 0 & 0 & 0 & a_6 & 0 & -a_4 & 0 & 0 & 0 & a_5 \end{bmatrix} \quad (\text{B.3})$$

C Wiring diagram of heating cartridge system

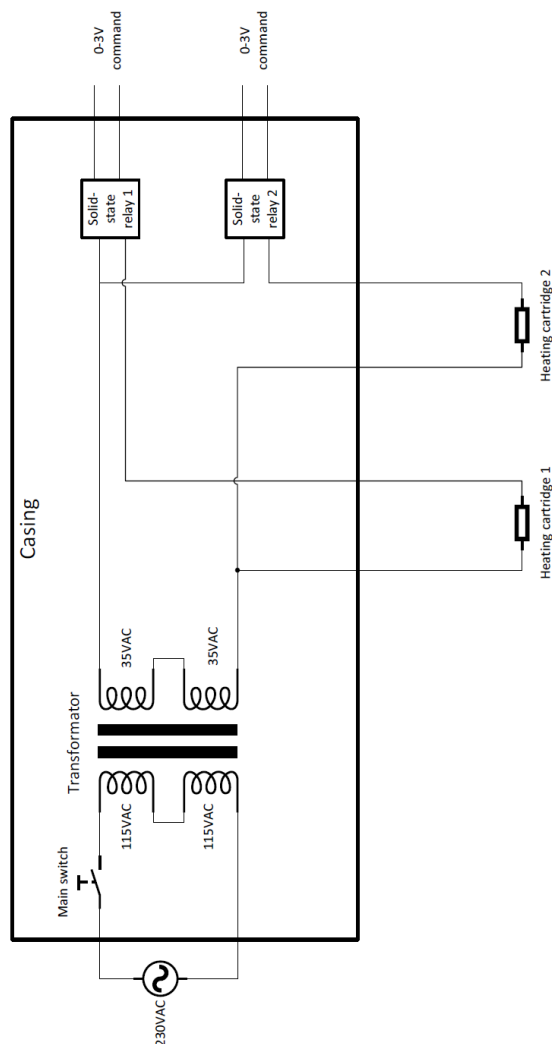


Figure C.1 – Wiring diagram of heating cartridge system

D Error estimation of SIO for enhanced groove geometries

Stability evaluation of shaft *alpha_var* Figure D.1 presents the evolution of the logarithmic decrement Γ for the shaft featuring enhanced grooves of varying groove width ratio α but constant groove angle and depth. The dashed lines represent the uncertainty band caused by measurement errors of shaft and bushing diameter, as well as the uncertainty in groove depth.

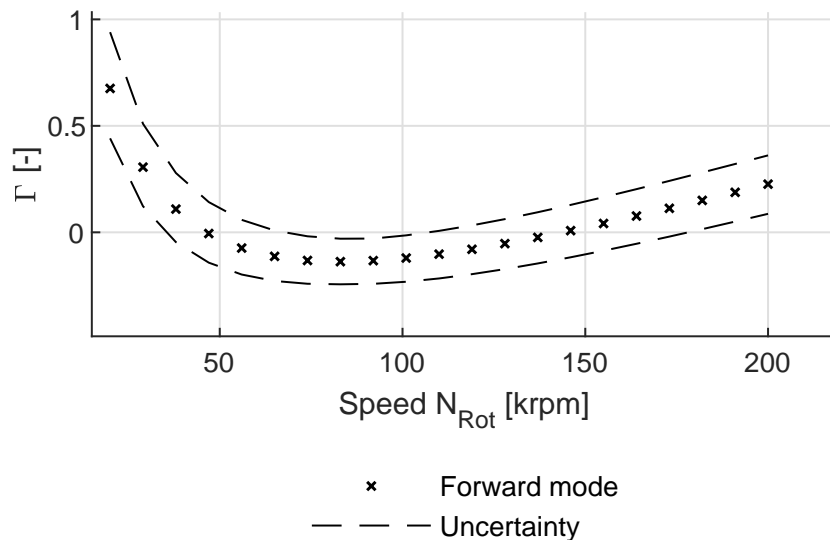


Figure D.1 – Whirl speed maps and evolution of logarithmic decrement for shaft featuring enhanced grooves α_{var} on rigid support

Stability evaluation of shaft *beta_var* Figure D.2 presents the evolution of the logarithmic decrement Γ for the shaft featuring enhanced grooves of varying groove angle β but constant groove width and depth.

Appendix D. Error estimation of SIO for enhanced groove geometries

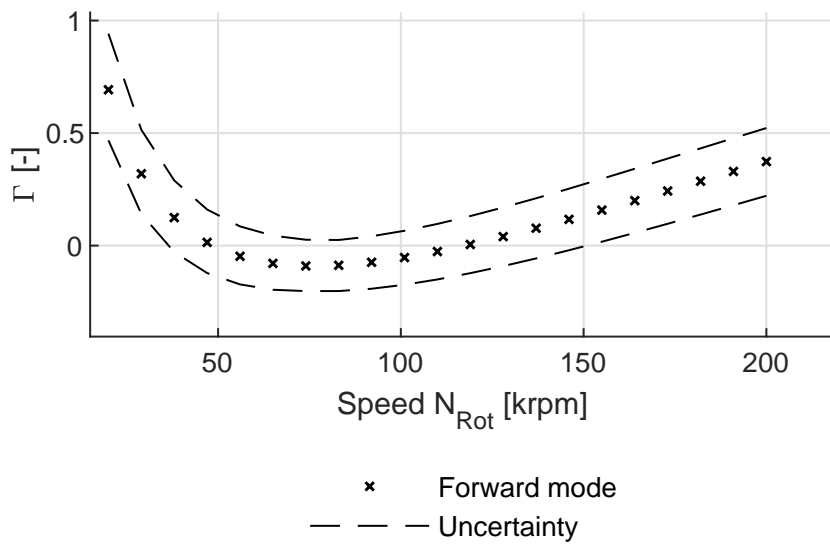


Figure D.2 – Whirl speed maps and evolution of logarithmic decrement for shaft featuring enhanced grooves β_{var} on rigid support

Stability evaluation of shaft α_{beta_var} Figure D.3 presents the evolution of the logarithmic decrement Γ for the shaft featuring enhanced grooves of varying groove width ratio α and groove angle β . The groove depth is held constant.

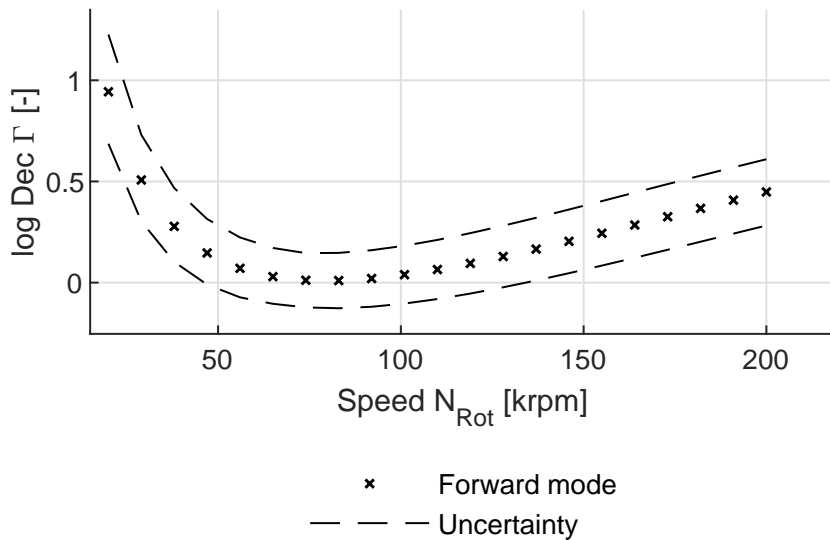


Figure D.3 – Whirl speed maps and evolution of logarithmic decrement for shaft featuring enhanced grooves α_{beta_var} on rigid support

Stability evaluation of shaft $\alpha_{beta_hg_var}$ Figure D.4 presents the evolution of the logarithmic decrement Γ for the shaft featuring fully enhanced grooves with varying groove width ratio α , groove angle β and groove depth hg .

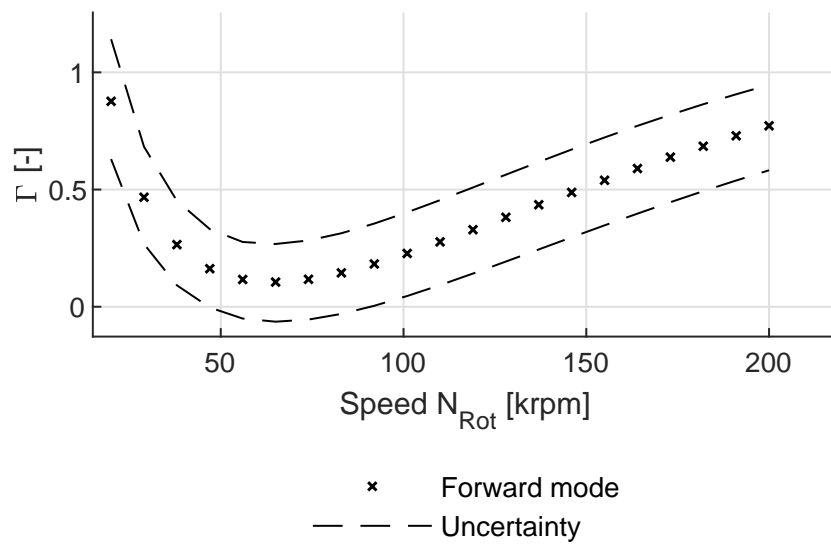


Figure D.4 – Whirl speed maps and evolution of logarithmic decrement for shaft featuring fully enhanced grooves $\alpha_{\beta_{hg_var}}$ on rigid support

Bibliography

- [1] O. Edenhofer, R. Pichs-Madruga, Y. Sokona, K. Seyboth, P.Matschoss, S. Kadner, T. Zwickel, P. Eickemeier, G. Hansen, S. Schlömer, and C. von Stechow. Special report on renewable energy sources and climate change mitigation. Technical report, Potsdam Institute for Climate Impact Research (PIK), 2012.
- [2] J.A. Turner. A realizable renewable energy future. *Science*, 285:687–689, July 1999.
- [3] D.P. Kaundinya, P. Balachandra, and N.H. Ravindranath. Grid-connected versus stand-alone energy systems for decentralized power—a review of literature. *Renewable and Sustainable Energy Reviews*, 13:2041–2050, October 2009.
- [4] P. Alstone, D. Gershenson, and D. M. Kammen. Decentralized energy systems for clean electricity access. *Nature Climate Change*, 5:305–314, March 2015.
- [5] V. Mounier and J. Schiffmann. Orc driven heat pump running on gas bearings for domestic applications: Proof of concept and thermo-economic improvement potential. In *12th IEA heat Pump Conference 2017*, Rotterdam, May 2017.
- [6] J. Demierre, A. Rubino, and J. Schiffmann. Modeling and experimental investigation of an oil-free microcompressor-turbine unit for an organic rankine cycle driven heat pump. *ASME Journal of Engineering for Gas Turbines and Power*, 137:032602, October 2014.
- [7] A.D. Hawkes and M.A. Leach. Cost-effective operating strategy for residential microcombined heat and power. *Energy*, 32:711–723, May 2007.
- [8] A.M. Andwari, A. Pesyridis, V. Esfahanian, A. Salavati-Zadeh, A. Karvountzis, and V. Muralidharan. A comparative study of the effect of turbocompounding and orc waste heat recovery systems on the performance of a turbocharged heavy-duty diesel engine. *Energies*, 10:1087, July 2017.
- [9] C. Carcasci, R. Ferraro, and E.Miliotti. Thermodynamic analysis of an organic rankine cycle for waste heat recovery from gas turbines. *Energy*, 65:91–100, February 2014.

Bibliography

- [10] K. Rosset, V. Mounier, E. Guenat, and J. Schiffmann. Multi-objective optimization of turbo-orc systems for waste heat recovery on passenger car engines,. *Energy*, 159:751–765, 2018.
- [11] J.O. de Veigh, N. Glynatsis, P. Gurung, and C. Wang. A comparative analysis of waste heat recovery systems in vehicles and their viability in real-world applications. *PAM Review: Energy Science Technology*, 6:88–109, May 2019.
- [12] M. Karlström. Local environmental benefits of fuel cell buses - a case study. *Journal of Cleaner Production*, 13, 2005.
- [13] B. Blunier and A. Miraoui. Proton exchange membrane fuel cell air management in automotive applications. *Journal of Fuel Cell Science and Technology*, 2010.
- [14] Z. Zhang, H. Mortensen, J. Vestervang-Jensen, and M. Andersenl. Fuel cell and battery powered forklifts. In *2013 9th IEEE Vehicle Power and Propulsion Conference, IEEE VPPC 2013*, pages 1–5, October 2013.
- [15] J. Shailendra A. Kirubakaran and R. Nema. A review on fuel cell technologies and power electronic interface. *Renewable and Sustainable Energy Reviews*, 13:2430–2440, April 2009.
- [16] J. Schiffmann. *Integrated design, optimization and experimental investigation of a direct driven turbocompressor for domestic heat pumps*. PhD thesis, École Polytechnique Fédérale de Lausanne, 2008.
- [17] C.H. Pan. Spectral analysis of gas bearing systems for stability studies. Technical report AD610872, Mechanical Technology Incorporated, Latham, New York 12110, December 1964.
- [18] D. Bonneau and J. Absi. Analysis of aerodynamic journal bearings with small number of herringbone grooves by finite element method. *Journal of Tribology*, 116(4):698–704, October 1994.
- [19] M.T.C. de Faria. *Finite Element Analysis of High Speed Grooved Gas Bearings*. PhD thesis, Texas A&M University, 1999.
- [20] E. Guenat and J. Schiffmann. Real-gas effects on aerodynamic bearings. *Tribology International*, 120:358–368, April 2018.
- [21] J.H. Vohr and C.H. Pan. On the spiral-grooved, self-acting gas bearing. Technical report MTI Technical Report MTI63TR52, Mechanical Technology Incorporated, Latham, New York, 1963.
- [22] S.B. Malanoski and C.H. Pan. The static and dynamic characteristics of the spiral-grooved thrust bearing. *Journal of Basic Engineering*, 87(3):547–558, September 1965.

-
- [23] L. Gu, E. Guenat, and J. Schiffmann. A review of grooved dynamic gas bearings. *Applied Mechanics Reviews*, July 2019.
- [24] R.E. Cunningham, D.P. Fleming, and W.J. Anderson. Experiments on stability of herringbone-grooved gas-lubricated journal bearings to high compressibility numbers. Technical report, Lewis Research Center, 1968.
- [25] J.H. Vohr and C.Y. Chow. Characteristics of herringbone-grooved, gas-lubricated journal bearings. *Transactions of the ASME: Journal of Basic Engineering*, 1965.
- [26] J. Schiffmann. Enhanced groove geometry for herringbone grooved journal bearings. *Journal of Engineering for Gas Turbines and Power*, 135:102501, October 2013.
- [27] G. Belforte, F. Colombo, T. Raparelli, and V. Viktorov. High-speed rotor with air bearings mounted on flexible supports: test bench and experimental results. *Journal of Tribology*, 130:021103, 2008.
- [28] T. Waumans, J. Peirs, F. Al-Bender, and D. Reynaerts. Aerodynamic journal bearing with a flexible, damped support operating at 7.2 million dn. *Journal of Micromechanics and Microengineering*, 21(10):104014, September 2011.
- [29] T. Waumans, J. Peirs, F. Al-Bender, and D. Reynaerts. Design, optimisation and testing of a high-speed aerodynamic journal bearing with a flexible, damped support. In *Technical Digest PowerMEMS*, pages 83–86, Washington DC, USA, December 2009.
- [30] N. Miyanaga and J. Tomioka. Effect of support stiffness and damping on stability characteristics of herringbone-grooved aerodynamic journal bearings mounted on viscoelastic supports. *Tribology International*, 100:195–203, August 2016.
- [31] J. Tomioka and N. Miyanaga. Measurement of dynamic properties of o-rings and stability threshold of flexibly supported herringbone grooved aerodynamic journal bearings. *Tribology Online*, 3(7):366–369, 2008.
- [32] J. Tomioka and N. Miyanaga. Stability threshold of herringbone-grooved aerodynamic journal bearings with external stiffness and damping elements. *Journal of Advanced Mechanical Design, Systems, and Manufacturing*, 7, 2013.
- [33] R. Liebich, A. Scholz, and M. Wieschalla. Rotors supported by elastomer-ring-dampers - experimental and numerical investigations. In *10th International Conference on Vibrations in Rotating Machinery*, pages 443 – 453. Woodhead Publishing, London, UK, December 2012.
- [34] A. Bormann. *Elastomerringe zur Schwingungsberuhigung in der Rotordynamik*. PhD thesis, Technische Universität Berlin, 2005.

Bibliography

- [35] N. Aktürk and R. Gohar. Damping the vibrations of a rigid shaft supported by ball bearings by means of external elastomeric o-ring dampers. *Proceedings - IMechE: J, Journal of Engineering Tribology*, 208:183–190, June 1994.
- [36] P. Bonello and H.M. Pham. An investigation into the dynamic response of a squeeze-film damped twin-shaft test rig. In *10th International Conference on Vibrations in Rotating Machinery*, pages 79 – 88. Woodhead Publishing, London, UK, December 2012.
- [37] A.Z. Szeri, A.A. Raimondi, and A. Giron-Duarte. Linear force coefficients for squeeze-film dampers. *Journal of Lubrication Technology*, 105(3):326–334, 1983.
- [38] F. Y. Zeidan, L. San Andres, and J.M. Vance. Design and application of squeeze film dampers in rotating machinery. In *Proceedings of the 25th Turbomachinery Symposium*, pages 169–188, Houston, Texas, USA, Sept 17-19 1996.
- [39] L. San Andrés and D. Lubell. Imbalance response of a test rotor supported on squeeze film dampers. In *Transactions of the ASME - Journal of Engineering for Gas Turbines and Power*, volume 120, pages 97–112, Orlando, Florida, June 2–5 1997.
- [40] S. Dousti, J.A. Kaplan, F. He, and P.E. Allaire. Elastomer o-rings as centering spring in squeeze film dampers: Application to turbochargers. In *Proceedings of the ASME Turbo Expo*, volume 7B, page V07BT30A018, San Antonio, Texas, USA, June 3-7 2013.
- [41] L. San Andrés and T.H. Kim. Thermohydrodynamic analysis of bump type gas foil bearings: A model anchored to test data. *Journal of Engineering for Gas Turbines and Power*, 132:042504–1–10, April 2010.
- [42] K-S. Kim and I. Lee. Vibration characteristics of a 75kw turbo machine with air foil bearings. *Journal of Engineering for Gas Turbines and Power*, 129(3):843–849, July 2006.
- [43] J. Schiffmann and Z.S. Spakovszky. Foil bearing design guidelines for improved stability. *Journal of Tribology*, 135:011103–1–011103–11, January 2013.
- [44] J. Park and K. Sim. A feasibility study of controllable gas foil bearings with piezo-electric materials via rotordynamic model predictions. *Journal of Engineering for Gas Turbines and Power*, 141:021027–1–021027–12, February 2019.
- [45] B.Z. Yazdi and D. Kim. Rotordynamic performance of hybrid air foil bearings with regulated hydrostatic injection. *Journal of Engineering for Gas Turbines and Power*, 140:012506–1–012506–8, January 2018.
- [46] B.Z. Yazdi and D. Kim. Effect of circumferential location of radial injection on rotordynamic performance of hybrid air foil bearings. *Journal of Engineering for Gas Turbines and Power*, 140:122504–1–122504–10, December 2018.

-
- [47] L. San Andrés and T.A. Chirathadam. Metal mesh foil bearing: Effect of motion amplitude, rotor speed, static load, and excitation frequency on force coefficients. *Journal of Engineering for Gas Turbines and Power*, 133:122503–1–122503–10, December 2011.
- [48] L. San Andrés and T.A. Chirathadam. A metal mesh foil bearing and a bump-type foil bearing: Comparison of performance for two similar size gas bearings. *Journal of Engineering for Gas Turbines and Power*, 134:102501–1–102501–13, October 2012.
- [49] K. Feng, X. Zhao, C. Huo, and Z. Zhang. Analysis of novel hybrid bump-metal mesh foil bearings. *Tribology International*, 103:529–539, August 2016.
- [50] K. Sim and J. Park. Performance measurements of gas bearings with high damping structures of polymer and bump foil via electric motor driving tests and 1-dof shaker dynamic loading tests. In *Proceedings of ASME Turbo Expo 2016: Turbine Technical Conference and Exposition GT2016*, page V07BT31A023, Seoul, South Korea, June 13–17 2015.
- [51] S. Morosi and I.F. Santos. Active lubrication applied to radial gas journal bearings. part1: Modeling. *Tribology International*, 44:1949–1958, 2011.
- [52] F.G. Pierart and I.F. Santos. Active lubrication applied to radial gas journal bearings. part1: Modelling improvement and experimental validation. *Tribology International*, 96:237–246, 2016.
- [53] S. Ikeda, Y. Arakawa, N. Hishida, T. Hirayama, T. Matruoka, and H. Yabe. Herringbone-grooved bearing with non-uniform grooves for high-speed spindle. *Lubrication Science*, 22:377–392, 2010.
- [54] K. Somaya, M. Miyatake, K. Okubo, and S. Yoshimoto. Threshold speed of instability of a herringbone-grooved rigid rotor with a bearing bush flexibly supported by straight spring wires. In *Proceedings of ASME Turbo Expo 2015: Turbine Technical Conference and Exposition GT2015*, volume 7A, page V07AT31A015, Montreal, Canada, June 15–19 2015.
- [55] S. Yoshimoto, M. Miyatake, and K. Nagata. Instability of herringbone grooved aerodynamic floating bush bearings flexibly supported by foils with hemispherical bumps. In *Proceedings of ASME/STLE International Joint tribology Conference*, pages 261–263, San Diego, California, USA, October 2007.
- [56] J.M. Vance and J. Li. Test results of a new damper seal for vibration reduction in turbomachinery. In *Transactions of the ASME - Journal of Engineering for Gas Turbines and Power*, page V005T14A001, Houston, Texas, June 5–8 1995.
- [57] G.B. Leyland. *Multi-objective optimization applied to industrial energy problems*. PhD thesis, École Polytechnique Fédérale de Lausanne, 2002.

Bibliography

- [58] A. Molyneaux. *A practical evolutionary method for the multi-objective optimization of complex energy systems, including vehicle drivetrains*. PhD thesis, École Polytechnique Fédérale de Lausanne, 2002.
- [59] A.J. Smalley, M.S. Darlow, and R.K. Mehta. The dynamic characteristics of o-rings. *Journal of Mechanical Design*, 100(1):132–138, January 1978.
- [60] I. Green and I. Etsion. Pressure and squeeze effects on the dynamic characteristics of elastomer o-rings under small reciprocating motion. *Journal of Tribology*, 108(3):439–444, July 1986.
- [61] F. Al-Bender and F. Colombo. Dynamic characterization of rubber o-rings: Squeeze and size effects. *Hindawii: Advances in Tribology*, 2017.
- [62] I. Green and C. English. Analysis of elastomeric o-ring seals in compression using the finite element method. *Tribology Transactions*, 35(1):83–88, 1992.
- [63] A. Javed, C. Arpagaus, S. Bertsch, and J. Schiffmann. Small-scale turbocompressors for wide-range operation with large tip-clearances for a two-stage heat pump concept. *International Journal of Refrigeration*, 2016.
- [64] T. Shoyama and K. Fujimoto. Calculation of high-frequency dynamic properties of squeezed o-ring for bearing support. *Mechanical Engineering Journal*, 5(2):17–00444, 2018.
- [65] G. E. P. Box, W. G. Hunter, and J. S. Hunter. *Statistics for Experimenters - Design, Innovation, and Discovery, 2nd Edition*. Wiley series in Probability and Statistics. J. Wiley & Sons, 2005.
- [66] P.K. Gupta, J.M. Tessarzik, and L. Cziglenyi. Development of procedures for calculating stiffness and damping properties of elastomers in engineering applications - part ii: Elastomer characteristics at constant temperature. Technical report CR-134704, Mechanical Technology Incorporated, NASA Lewis Research Center, April 1974.
- [67] G. E. Warnaka and H. T. Miller. Strain-dependent properties of polymers i. *Rubber Chemistry and Technology*, 39(5):1421–1427, November 1966.
- [68] A.R. Payne and R.E. Whittaker. Low strain dynamic properties of filled rubbers. *Rubber Chemistry and Technology*, 44(2):440–478, May 1971.
- [69] A. Lion, C. Kardelky, and P. Haupt. On the frequency and amplitude dependence of the payne effect: Theory and experiments. *Rubber Chemistry and Technology*, 76(2):533–547, May 2003.
- [70] Z. Kareaga. *Dynamic Stiffness and Damping Prediction on Rubber Material Parts, FEA and Experimental Correlation*. PhD thesis, London Metropolitan University, 2016.

-
- [71] L.P. Yarin. *The Pi-Theorem*. Experimental Fluid Mechanics. Springer-Verlag Berlin, 2012.
- [72] H.J. Qi, K. Joyce, and M.C. Boyce. Durometer hardness and the stress-strain behavior of elastomeric materials. *Rubber Chemistry and Technology*, 76(2):419–435, 2003.
- [73] A.N. Gent. On the relation between indentation hardness and young’s modulus. *Rubber Chemistry and Technology*, 31:896–906, 1958.
- [74] J. Boussinesq. *Application des potentiels à l’étude de l’équilibre et du mouvement des solides élastiques*. Gauthier-Villars, 1885.
- [75] J. Kunz and M. Studer. Determining the modulus of elasticity in compression via the shore a hardness. *Kunststoffe international*, 06, 2006.
- [76] M. Carfagni, E. Lenzi, and M. Pierin. The loss factor as a measure of mechanical damping. *Proceedings of SPIE - The International Society for Optical Engineering*, pages 580–, 1998.
- [77] M. Darlow and E. Zorzi. Mechanical design handbook for elastomers. Technical Report Contractor Report 3423, Mechanical Technology Incorporated, NASA Lewis Research Center, 1981.
- [78] Plastics – determination of dynamic mechanical properties– part 1: General principles. Standard, International Organization for Standardization, May 2011.
- [79] N. Miyanaga and J. Tomioka. Effect of dynamic properties of support o-rings on stability of herringbone-grooved aerodynamic journal bearings. *Tribology Online*, 11(2):272–280, April 2016.
- [80] J. Yan, Y. Wang, S Wang, and X. Su. Frequency dependence stiffness and damping of o rubber ring. *Advanced Materials Research*, 904:368–372, May 2014.
- [81] P. Bättig and J. Schiffmann. Data-driven model for the dynamic characteristics of o-rings for gas bearing supported rotors. *Journal of Applied Mechanics*, 86(8):081003, 2019.
- [82] K. Shalash and J. Schiffmann. On the manufacturing of compliant foil bearings. *Journal of Manufacturing Processes*, 25:357–368, 2017.
- [83] Q. D. Zhang and X. C. Shan. Dynamic characteristics of micro air bearings for microsystems. *Microsystem Technologies*, 14:229–234, October 2007.
- [84] H. Hashimoto and M. Ochiai. Optimization of groove geometry for thrust air bearing to maximize bearing stiffness. *Journal of Tribology*, 130(3):031101, 2008.

Bibliography

- [85] J. Schiffmann and D. Favrat. Integrated design and optimization of gas bearing supported rotors. *Journal of Mechanical Design*, 132:051007–1, May 2010.
- [86] R. Pampreen. Small turbomachinery compressor and fan aerodynamics. *Journal of Engineering for Gas Turbines and Power*, 95(3):251–256, July 1973.
- [87] J. J. Brasz. Investigation into the effect of tip clearance on centrifugal compressor performance. In *ASME 1988 International Gas Turbine and Aeroengine Congress and Exposition*, volume 1, page V001T01A066, Amsterdam, Netherlands, June 6-9 1988. ASME.
- [88] M. S. Darlow. Influence coefficient balancing. In *Balancing of High-Speed Machinery*, Mechanical Engineering Series, chapter 6, pages 81–106. Springer New-York, NY, 1989.
- [89] D.D. Fuller. A review of the state-of-the-art for the design of self-acting gas-lubricated bearings. *Transactions of the ASME: Journal of Lubrication Technology*, 1969.
- [90] O. Bottema and B. Roth. *Theoretical Kinematics*. Dover Books on Physics. Dover Publications, 2012.
- [91] S.P. Timoshenko and J.M. Gere. *Theory Of Elastic Stability*. Dover Civil and Mechanical Engineering. Dover Publications, 2 edition, 2012.
- [92] T. Gmür. *Méthode des éléments finis*. Presses polytechniques et universitaires romandes, 2007.
- [93] R.J. Guyan. Reduction of stiffness and mass matrices. *American Institute of Aeronautics and Astronautics*, 3(2):380–380, 1965.
- [94] W.C. Young and R.G. Budynas. *Roark's formulas for stress and strain*. McGraw-Hill, 7 edition, 2002.
- [95] Zapp Precision Metals GmbH, Unna, Germany. *Stainless Spring Steel Strip Zapp 1.4310*, February 2018.
- [96] Neno Torić, Josip Brnić, Ivica Boko, Marino Brčić, Ian W Burgess, and Ivana Uzelac. Experimental analysis of the behaviour of aluminium alloy en 6082aw t6 at high temperature. *Metals*, 7(4):126, April 2017.
- [97] A. Karolczuk, M. Kurek, and T. Lagoda. Fatigue life of aluminium alloy 6082 t6 under constant and variable amplitude bending with torsion. *Journal of Theoretical and Applied Mechanics*, 53(2):421–430, 2015.
- [98] K. Grote and J. Feldhusen, editors. *Dubbel – Taschenbuch für den Maschinenbau*. Springer, 22 edition, 2007.

- [99] E. J. Gunter Jr. Rotor-bearing stability. In *Proceedings of the first Turbomachinery Symposium*, pages 119–141, Texas, USA, 1972. Texas A&M University. Gas Turbine Laboratories.
- [100] H.L. Hassenpflug, R.D. Flack, and E.J. Gunter. Experimental study of the critical speed response, of a jeffcott rotor with acceleration. *Journal of the Franklin Institute*, 310(1):77–88, July 1980.
- [101] J. J. Durillo, A. J. Nebro, C. A. Coello Coello, F. Luna, and E. Alba. A comparative study of the effect of parameter scalability in multi-objective metaheuristics. In *IEEE Congress on Evolutionary Computation (IEEE World Congress on Computational Intelligence)*, pages 1893–1900, Hong Kong, China, June 1-6 2008. IEEE.
- [102] P.H. Wagner. *Integrated Design, Optimization, and Experimental Realization of a Steam-Driven Micro Recirculation Fan for Solid Oxide Fuel Cell Systems*. PhD thesis, École Polytechnique Fédérale de Lausanne, 2019.
- [103] L.M. Greenhill and G.A. Cornejo. Critical speeds resulting from unbalance excitation of backward whirl modes. In *ASME Design engineering technical conferences-Part B*, volume 3, pages 991–1000, 1995.
- [104] A.F. Jahromi, R.B. Bhat, and W-F Xie. Forward and backward whirling of a rotor with gyroscopic effect. In *Vibration Engineering and Technology of Machinery: Proceedings of VETOMAC X 2014*, volume 23, pages 879–887, Manchester, UK, Sept 9–11 2014.
- [105] P.T. Pedersen. On forward and backward precession of rotors. *Ingenieur-Archiv*, 42(1):26–41, January 1972.

Philipp Bättig

Curriculum vitae

Route de Prahins 3
CH-1409 Chanéaz
☎ +41 (0) 79 7426526
✉ philipp.baettig@gmx.ch



Personal details

Date of birth: 27.03.1986
Place of birth: Ufhusen LU / Switzerland

Education

- 2015–2019 **Doctoral student**, *Laboratory for applied mechanical design (LAMD/EPFL)*, Lausanne/Switzerland.
- 2010–2011 **Master of Science MSc**, *Imperial College*, London/United Kingdom, Applied Mechanical Engineering.
- 2005–2008 **Bachelor of Science BSc**, *University of Applied Sciences FHNW*, Windisch/Switzerland, Mechanical engineering.
- 2001–2005 **Apprenticeship as machinist with professional baccalaureate**, *Ferrum AG*, Rapperswil/Switzerland, Level E.

Professional experience

- 2011–2015 **Vibration calculation, Noise and Measurements Expert R&D**, *Wärtsilä Switzerland Ltd.*, Winterthur/Switzerland, Torsional vibration calculations of two-stroke marine diesel installations. Vibration, torque and noise measurements on customer engines.
- 2008–2010 **Scientific Assistant**, *University of Applied Sciences FHNW*, Windisch/Switzerland, Institute for Thermal and Fluid Engineering ITFE.

Language Skills

German **Mother tongue**
English **good in writing and speaking**
French **good in speaking, ok in writing**

Hobbies and interests

- Cars
- Cycling

